

# **Towards a new view of the photospheric magnetic field with the Polarimetric and Helioseismic Imager on Solar Orbiter**

Dissertation

zur Erlangung des mathematisch-naturwissenschaftlichen Doktorgrades

“Doctor rerum naturalium”

der Georg-August-Universität Göttingen

im Promotionsprogramm Physik

der Georg-August University School of Science (GAUSS)

vorgelegt von

**Jonas Sinjan**

aus Brasschaat, Belgien

Göttingen, 2024

### Betreuungsausschuss

Prof. Dr. Sami Solanki

Max-Planck-Institut für Sonnensystemforschung, Göttingen, Deutschland

Prof. Dr. Ansgar Reiners

Institut für Astrophysik, Georg-August-Universität Göttingen, Deutschland

Dr. Johann Hirzberger

Max-Planck-Institut für Sonnensystemforschung, Göttingen, Deutschland

### Mitglieder der Prüfungskommission

Referent: Prof. Dr. Sami K. Solanki

Max-Planck-Institut für Sonnensystemforschung, Göttingen, Deutschland

Korreferent: Prof. Dr. Ansgar Reiners

Institut für Astrophysik, Georg-August-Universität Göttingen, Deutschland

Weitere Mitglieder der Prüfungskommission:

Prof. Dr. Hardi Peter

Max-Planck-Institut für Sonnensystemforschung, Göttingen, Deutschland

Prof. Dr. Wolfram Kollatschny

Institut für Astrophysik, Georg-August-Universität Göttingen, Deutschland

Dr. Lakshmi Pradeep Chitta

Max-Planck-Institut für Sonnensystemforschung, Göttingen, Deutschland

Prof. Dr. Arnulf Quadt

II. Physikalisches Institut, Georg-August-Universität Göttingen, Deutschland

Tag der mündlichen Prüfung: 05.09.2024

© Jonas Sinjan



This work is distributed under a  
Creative Commons Attribution 4.0 License

Printed in Germany

**Cover figure:**

Solar Orbiter observing the Sun on 12th October 2023 at midnight, with Earth separated by approximately 80 degrees in longitude. The line-of-sight magnetogram by SDO/HMI at the same time is shown, with the FOV of SO/EUI-HRI (full disk) and SO/PHI-HRT (square) are outlined in red dashed lines. Created with JHelioviewer. The cartoon of Solar Orbiter is an adaptation of ESA image ID 431227, which is published with a CC BY-SA 3.0 IGO Licence. Image Credit: ESA, Acknowledgements: Work performed by ATG under contract for ESA. The cartoon of Earth is an adaptation of Adobe Stock Image #203849901 under a Standard licence.

# Contents

<b>Summary</b>	<b>9</b>
<b>1 Introduction</b>	<b>11</b>
1.1 The Sun . . . . .	14
1.1.1 Solar interior . . . . .	14
1.1.2 Solar atmosphere . . . . .	14
1.1.3 Solar magnetic field . . . . .	18
1.1.4 Solar poles . . . . .	21
1.2 Solar atmosphere diagnostics . . . . .	25
1.2.1 Zeeman effect . . . . .	25
1.2.2 Polarimetric Zeeman effect . . . . .	27
1.2.3 Stokes parameters and profiles . . . . .	28
1.2.4 Radiative transfer through the solar atmosphere . . . . .	32
1.2.4.1 Radiative transfer in the absence of magnetic fields . . . . .	32
1.2.4.2 Spectral Line Formation . . . . .	33
1.2.4.3 Eddington-Barbier approximation . . . . .	34
1.2.4.4 Local thermodynamic equilibrium . . . . .	35
1.2.4.5 Radiative transfer in the presence of magnetic fields . . . . .	36
1.2.4.6 Inversions . . . . .	37
1.3 Instrumentation . . . . .	38
1.3.1 SO/PHI . . . . .	38
1.3.2 SDO/HMI . . . . .	40
1.4 Magnetohydrodynamics . . . . .	41
<b>2 The on-ground data reduction and calibration pipeline for SO/PHI-HRT</b>	<b>45</b>
2.1 Abstract . . . . .	45
2.2 Introduction . . . . .	46
2.3 SO/PHI-HRT . . . . .	47
2.3.1 The instrument . . . . .	47
2.3.2 Flat-field acquisition . . . . .	47
2.4 SO/PHI-HRT on ground pipeline . . . . .	48
2.4.1 Pipeline overview . . . . .	48
2.4.2 Unsharp masking . . . . .	50
2.4.3 Flat-field correction . . . . .	50
2.4.4 Demodulation . . . . .	51

2.4.5	Limb detection and normalisation . . . . .	51
2.4.6	Cross-talk correction . . . . .	52
2.4.7	Special case: ISS off . . . . .	52
2.4.7.1	Modulation alignment . . . . .	52
2.4.7.2	$V$ to $Q, U$ cross-talk correction . . . . .	53
2.4.7.3	Wavelength alignment . . . . .	53
2.4.8	Radiative transfer equation inversion . . . . .	53
2.5	Early in-flight data . . . . .	54
2.5.1	February 2021 . . . . .	54
2.5.2	November 2021 . . . . .	57
2.5.3	Magnetogram Noise . . . . .	60
2.6	Conclusion . . . . .	60
<b>3</b>	<b>Magnetic fields inferred by Solar Orbiter: A comparison between SO/PHI-HRT and SDO/HMI</b>	<b>63</b>
3.1	Abstract . . . . .	63
3.2	Introduction . . . . .	64
3.3	Data . . . . .	65
3.3.1	SO/PHI-HRT magnetic field . . . . .	65
3.3.2	HMI magnetic field . . . . .	66
3.4	Method . . . . .	67
3.5	Comparison of SO/PHI-HRT and HMI magnetic field observations . . . . .	69
3.5.1	Comparison of SO/PHI-HRT and HMI LoS magnetograms . . . . .	69
3.5.2	Comparison of SO/PHI-HRT and HMI vector magnetic fields . . . . .	71
3.5.3	Comparison of SO/PHI-HRT and HMI LoS components of the full vector magnetic field . . . . .	76
3.6	Conclusions . . . . .	77
<b>4</b>	<b>Preliminary stereoscopic analysis with SO/PHI-HRT and SDO/HMI</b>	<b>79</b>
4.1	Introduction . . . . .	79
4.2	Data . . . . .	80
4.3	Method and alignment . . . . .	82
4.3.1	Alignment Performance . . . . .	91
4.3.2	17th March 2022 Comparison . . . . .	98
4.4	Conclusion . . . . .	102
<b>5</b>	<b>Magnetograms underestimate even unipolar magnetic flux nearly everywhere on the solar disk</b>	<b>105</b>
5.1	Abstract . . . . .	105
5.2	Introduction . . . . .	106
5.3	MURaM simulations . . . . .	108
5.4	Spectral Synthesis . . . . .	111
5.5	Stokes processing . . . . .	113
5.6	Inference of the line-of-sight magnetic field . . . . .	115
5.7	$\langle B_{LOS} \rangle$ centre-to-limb variation . . . . .	116
5.7.1	Fe I 6173.3 Å . . . . .	116

5.7.2	5250.2 Å versus 6173.3 Å . . . . .	122
5.7.3	Other $B_{LOS}$ retrieval methods . . . . .	124
5.8	Discussion . . . . .	126
5.9	Conclusions . . . . .	128
<b>6</b>	<b>Conclusions and Outlook</b>	<b>131</b>
6.1	Implications and further work . . . . .	135
	<b>Bibliography</b>	<b>139</b>
<b>A</b>	<b>Appendix to Chapter 5</b>	<b>157</b>
A.1	Validation of $B_{LOS}$ retrieval methods for a 1D atmosphere for all $\mu$ . . . . .	157
A.2	Stokes Profiles at $\mu = 0.5$ . . . . .	159
A.3	$\langle B_{LOS} \rangle$ centre-to-limb variation for Fe I 6173.3 Å derived by the weak-field approximation and centre-of-gravity technique. . . . .	160
A.4	$\langle B_{LOS} \rangle$ centre-to-limb variation for Fe I 5250.2 Å derived by the MDI-like algorithm, weak-field approximation and centre-of-gravity technique. . . . .	162
	<b>Publications</b>	<b>165</b>
	<b>Acknowledgements</b>	<b>167</b>



# Summary

Accurately determining the magnetic flux through the solar surface is incredibly important to understanding the dynamics of the Sun and its atmosphere. The magnetic field provides energy for heating the higher layers of the solar atmosphere, as well as controlling the dynamics of the plasma in this region. The number and strength of solar eruptive events, the amount of solar radiation, are all related to its magnetic field. Currently solar magnetographs, instruments that infer the solar magnetic field, can probe the magnetic field in the lowest layer of the solar atmosphere: the photosphere. Maps of the photospheric magnetic field are then used as an input for models to estimate the magnetic flux at higher layers of the solar atmosphere and beyond into the solar system.

These solar magnetographs have thus far been restricted to only observe the Sun from one direction, that along the Sun-Earth line. This singular view has its complications: there is a wide consensus that inference of the magnetic field near the edge of the solar disc is unreliable, as there the viewing angle with respect to the surface normal is highly inclined. The Polarimetric and Helioseismic Imager on board the Solar Orbiter spacecraft (SO/PHI), has become the first solar magnetograph to view the Sun from different positions. The new view provided by this instrument is the first opportunity to quantify the inaccuracy of inferring the photospheric magnetic field near the solar limb and in the polar regions.

To make this possible first a data reduction pipeline for the High Resolution Telescope of SO/PHI (SO/PHI-HRT) was developed to produce the first maps of the photospheric magnetic field, from raw data taken during the first phases of the mission. This effort determined the instrument's performance in different observational modes and produced magnetograms with noise levels between 6.5 – 8.5 G. Secondly, a comparison of the photospheric magnetic field inferred by SO/PHI-HRT with that from a space-based magnetograph orbiting Earth, the Helioseismic and Magnetic Imager on board the Solar Dynamic Observatory (SDO/HMI), is made when viewing the Sun from the same direction. The line-of-sight magnetograms aligned very closely, with offsets less than 1 G and a slope of 0.97 when performing linear fitting. Larger differences were found when comparing the vector magnetic field components, which can be mostly attributed due to the different noise levels between the instruments. With this knowledge we can later disentangle differences due to the viewing direction from those originating from differences between the instruments themselves.

A first attempt was made to compare the photospheric magnetic field from SO/PHI-HRT and SDO/HMI, when viewing from different positions in the ecliptic plane. Due to limitations in the reprojection algorithm, only the magnetic flux in sunspot umbrae could

be compared. There the total unsigned magnetic flux from the two directions, after dividing  $B_{LOS}$  by  $\mu$  to account for the different viewing direction (where  $\mu = \cos(\theta)$  and  $\theta$  is the heliocentric angle), did align closely. Nevertheless large differences in certain areas were found: near the centre of the umbrae, SO/PHI-HRT inferred stronger line-of-sight magnetic fields than SDO/HMI as it viewed the sunspots closer to disc centre, even after the  $\mu$ -correction is applied. The  $\mu$ -correction assumes the magnetic field to be radial everywhere, but even in the umbra and especially near its boundaries the field can be strongly inclined. Hence large differences were also found near the boundaries, which was further enhanced in areas where the boundaries did not agree, due to the Wilson depression and different instrument PSFs. To compare the magnetic fluxes over larger areas and from different magnetic features the reprojection algorithm must be developed to accurately resample magnetograms.

From investigations of inclined viewing angles on 3D magnetohydrodynamic simulations of the photosphere with a unipolar magnetic field, it was found that the line-of-sight magnetic field is underestimated at all angles and worsened with low spatial resolution at high  $\mu$ . Only at disc centre and with high spatial resolution was the ground truth magnetic flux within the simulation retrieved. Furthermore at  $\mu \leq 0.5$  the spatial resolution had very little impact. These results were found for two commonly used photospheric spectral lines and reproduced by four different methods of inferring the line-of-sight magnetic field.

The striking results from the simulations, together with preliminary observational evidence, imply that significantly different line-of-sight magnetic fields are retrieved when viewing from different directions. This may contribute to the resolution of the open flux problem, where the total solar open magnetic flux when propagated to 1 au is 2 – 3 times lower than that directly measured at 1 au.

# 1 Introduction

The impact of the Sun on our solar system cannot be overstated. It is the primary source of the energy required to sustain life. Furthermore the solar magnetic field is currently thought to have played a crucial role in angular momentum transport during the early formation of the solar system: the Sun holds 99.8% of the solar system mass, while the planets have 98% of its angular momentum (e.g. Balbus and Hawley 1998). Its magnetic field expands throughout the solar system; carrying plasma from the Sun's surface with it. This out-flowing mass is known as the solar wind. Indeed the edge of the solar system, the heliopause, is defined as the point at which the solar wind no longer balances the external pressure from the interstellar medium. This boundary is not circular due to the non-isotropic pressure from the interstellar medium. Only after 35 years of spaceflight in 2012 did Voyager 1 cross this boundary at approximately 123 AU, the first human made object to do so.

The solar magnetic field that permeates the solar system is known as the interplanetary magnetic field, or more recently as the heliospheric magnetic field. It controls much of the large scale physical phenomena within the solar system. In humanity's effort to understand and characterise the heliospheric magnetic field, we are predominantly concerned with regions on the Sun's surface where the magnetic field is open, i.e. they are not rooted in another foot point on the solar surface. These open magnetic fields instead extend into the interplanetary medium and form the heliospheric magnetic field. It is along these field lines that plasma from the Sun can leave and interact with Earth. The interaction between the heliospheric magnetic field and Earth's magnetic field is the reason why we observe shimmering green and red light near our North and South poles: the Aurora Borealis and Aurora Australis respectively. Furthermore solar eruptive events, which are introduced later in Sect. 1.1.4, expel vast quantities of solar plasma from the atmosphere, which can travel along open field lines towards Earth and initiate geomagnetic storms, known as space weather events.

Large areas where the magnetic field is open are coronal holes. These regions appear dark in extreme ultraviolet (EUV) wavelengths (see Cranmer 2009, for a review). They are dark because the plasma is cool and less dense than surrounding regions due to the rapid departure of plasma and birth of the solar wind. Three coronal holes are shown in Fig. 1.1 in an EUV image taken in 2022 from SDO/AIA (Atmospheric Imaging Assembly on the Solar Dynamics Observatory, see Lemen et al. 2012).

From long term observations of these open field regions on the surface, and monitoring of the open magnetic flux at 1 au, i.e. Earth's distance from the Sun, there is a disagreement. The observations of the surface suggest that a much lower open magnetic

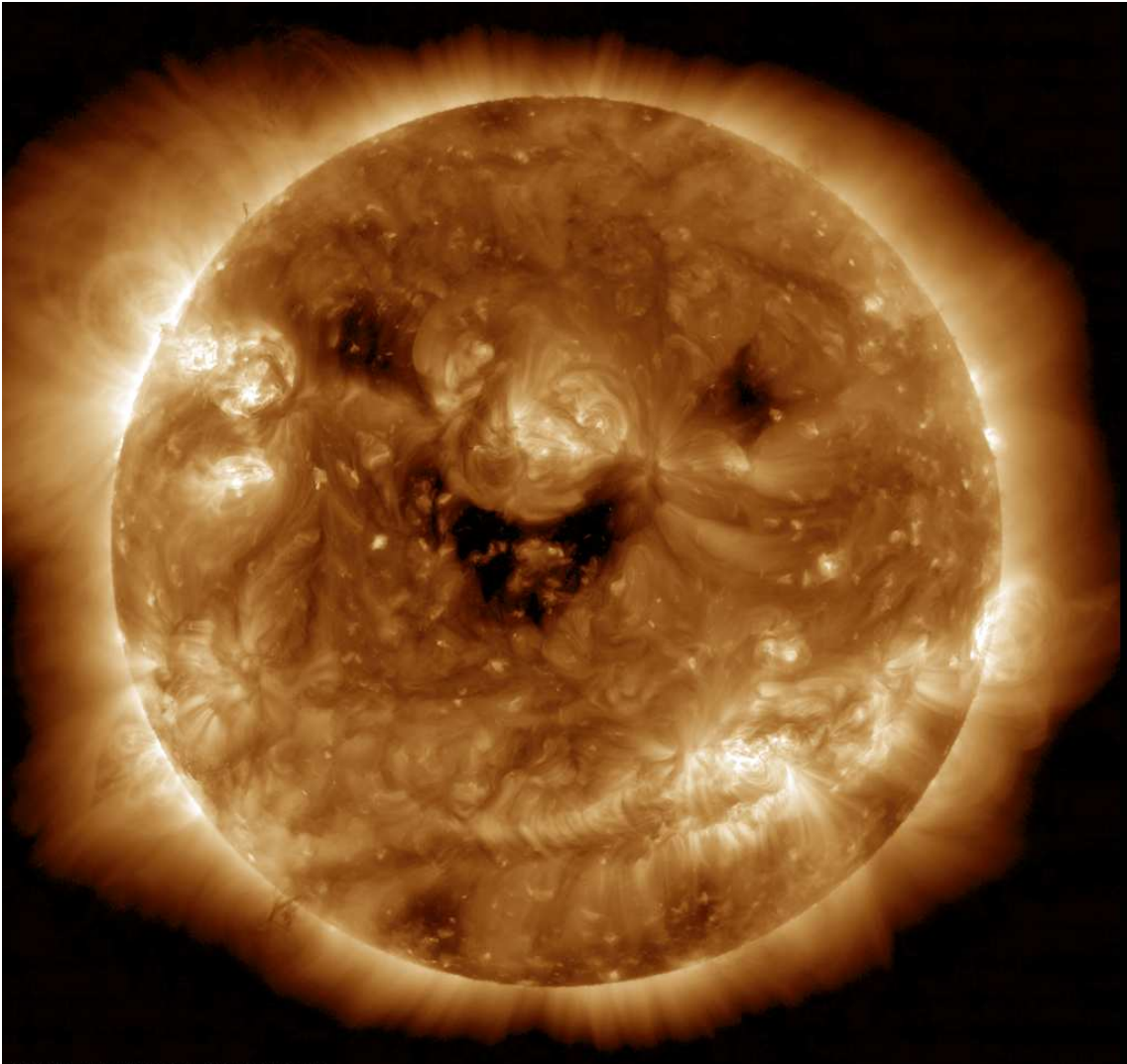


Figure 1.1: An image from SDO/AIA in the 193 Å channel on 2022-10-26 at 21:02UT. Three coronal holes stand out, with a large one at the disc centre. The Sun appears to be smiling. Image created with JHelioviewer (Müller et al. 2017).

flux should be measured at Earth's distance compared to what has actually been measured in-situ by spacecraft; in fact it is a 2 – 3 factor difference. This mismatch is known as the open flux problem (e.g. Linker et al. 2017).

There are several hypotheses, discussed in the literature, to explain this mismatch. One is that there is open flux emanating from regions that are not coronal holes. Coronal holes are typically found close to the poles, however their location does vary with the solar cycle: at solar minimum the coronal holes are closest to the Sun's poles, while at solar maximum they are furthest and closer to the equator. Another suggests that the magnetic flux at the Sun's surface, which we must remotely sense, is underestimated in the regions where coronal holes exist. It is this last hypothesis that motivates my work and is explored in this thesis. If the remotely sensed open magnetic flux is underestimated, when extrapolated to 1 au, a part, if not all of the 2–3 factor mismatch could be explained.

Observing these open flux regions is tricky however, especially during solar minimum when the coronal holes are nearest the poles. As past observatories have been ground-based, or space-based but in always in the ecliptic plane, the poles have always been observed very close to the edge of the solar disc. This creates many challenges for these observatories, which are discussed in further detail in Chapter 5. Even during solar maximum, when the coronal holes are closer to the equator, we often observe them away from disc centre, towards the limb, and like the poles, this is a challenging region to observe.

However a recently launched mission has changed the landscape: Solar Orbiter (SO, Müller et al. 2020). On board are a suite of remote sensing instruments, one of which infers the magnetic field at the solar surface: the Polarimetric and Helioseismic Imager (PHI, Solanki et al. 2020). Further details on the Solar Orbiter mission and the PHI instrument are described in Sect. 1.3.1. With Solar Orbiter’s highly elliptic orbit, for the first time, magnetic field measurements from different viewpoints are now possible, not just from Earth. With this additional viewpoint, stereoscopy can be performed for the first time and the regions that are near the limb from Earth can now be simultaneously observed near disc centre from a different vantage point. Additionally from 2025 onwards, Solar Orbiter will also steadily move out of the ecliptic plane, up to  $33^\circ$  in heliographic latitude in 2029, providing a view of the Sun’s poles that has never been possible before. Hence Solar Orbiter enables a much improved opportunity to observe open flux regions on the Sun where it has previously been difficult.

This thesis is organised in the following sections. In the rest of Chapter 1 the relevant basic physics is established: Sect. 1.1 introduces the solar interior, atmosphere, its magnetic field and the polar regions. Sect. 1.2 summarises key solar diagnostic techniques and Sect. 1.3 describes the salient instrumental specifications of SO/PHI and SDO/HMI (the Helioseismic and Magnetic Imager on SDO Scherrer et al. 2012), two instruments whose data are exploited in this thesis. Finally in Sect. 1.4 I outline the basics of magnetohydrodynamic theory - key to modelling the Sun.

To enable these new opportunities provided by Solar Orbiter, I have made the necessary groundwork, which are described in the next two chapters. The on ground data processing pipeline for the high resolution telescope (HRT, Gandorfer et al. 2018) of SO/PHI is detailed in Chapter 2 (published as Sinjan et al. 2022). This pipeline has enabled the fine detailed analysis of the SO/PHI-HRT data to study the performance of the instrument and improve the calibration of the data. This pipeline has now been integrated into the complete on ground processing software for SO/PHI. Subsequent to this, in Chapter 3 a comparison of the magnetic field inferences from SO/PHI-HRT with those from an Earth-based magnetograph SDO/HMI (The Helioseismic Magnetic Imager on board the Solar Dynamics Observatory, Scherrer et al. 2012, Pesnell et al. 2012) is presented (published as Sinjan et al. 2023). This comparison is crucial to allow us to perform stereoscopy, a first attempt of which is also laid out in Chapter 4 using SDO/HMI and SO/PHI-HRT data, when Solar Orbiter is out of the Sun-Earth line. Finally in Chapter 5 results from numerical simulations of inferring the longitudinal magnetic field from a unipolar region are presented. These simulations give insight on the impact of radiative transfer effects at inclined viewing positions and guide us with future observations. Chapter 6 concludes the work presented in this thesis and provides an outlook.

## 1.1 The Sun

In this section the phenomena and basic physics of the Sun relevant to the work in this thesis is laid out. First the inner structure of the Sun is discussed, followed by a brief overview of the Sun's surface and its constituent features. Finally the Sun's ever important magnetic field, including the polar regions are introduced.

### 1.1.1 Solar interior

The Sun is thought to consist of many layers. At its centre, lies the core, a sphere of hot dense plasma thought to be rapidly rotating (García et al. 2007), within which nuclear fusion occurs, creating that energy that drives all processes in our solar system. It is primarily through the  $p - p$  thermonuclear fusion chain that the core generates the energy in the form of gamma ray photons. The core extends up to approximately  $0.2 R_{\odot}$ , where  $R_{\odot}$  is the solar radius, and has a temperature of 15.7 million Kelvins. Directly surrounding the core is the radiative zone, the thickest layer of the Sun as it extends up to  $0.7 R_{\odot}$ , where the immense energy from the core is transported towards the surface via thermal conduction and radiative diffusion. Due to the high density the photons that carry the energy only travel a short distance before they are absorbed or scattered. It takes on average over 170,000 years for a photon to leave the radiative region (Elkins-Tanton 2006). Throughout the radiation zone, the temperature drops, until 1.5 million Kelvins at its upper limit. Further out is the convection zone, an unstable layer where the energy is transported to the exterior via convection. A cross-section of the Sun is shown in Fig. 1.2, with additional properties displayed.

### 1.1.2 Solar atmosphere

As the Sun is a massive ball of plasma, it is not straightforward to define its surface as one does for the Earth. Towards the upper layers of the convection zone, the density and temperature has decreased sufficiently, that there exists a region where the optical depth ( $\tau$ , the degree of light absorption) reaches 1. Beyond this point, the plasma becomes transparent (optically thin,  $\tau < 1$ ) where the majority of photons escape into space. The layer which is observed in white-light or continuum wavelengths of the visible electromagnetic spectrum, defines the top boundary of the convection zone: the solar photosphere. It is the deepest layer of the Sun that is visible. It is defined as the surface of unit optical depth at  $5000 \text{ \AA}$ . An image of the photosphere is shown in Fig. 1.3 taken by SO/PHI-FDT (Full Disc Telescope) in early 2022. The photosphere is very nearly in hydrostatic equilibrium and the pressure scale height is approximately 100 km, and the photosphere is around 500 km thick.

In Fig. 1.3 one can see several dark sunspots in the middle latitudes. Images like these also reveal a reddening as one looks away from disc centre and towards the limb: this is known as limb darkening. It is a projection effect wherein one observes more inclined to the surface normal and therefore probes higher in the photosphere, into a region which is cooler. A day earlier, the Sun was also imaged by SO/PHI-HRT, the high resolution telescope, and the active region in the lower left was captured, which is shown in Fig. 1.4.

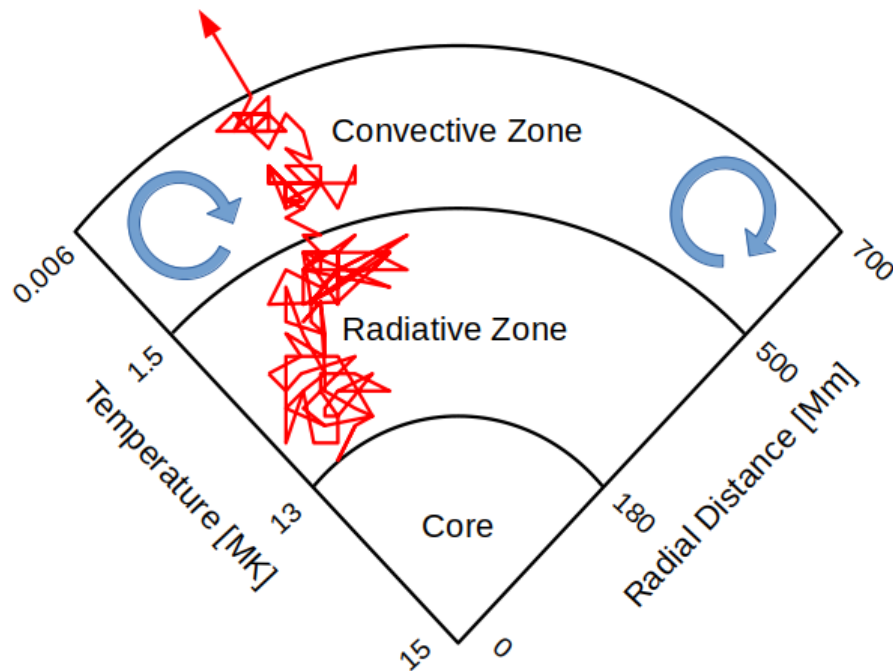


Figure 1.2: A cross-section of the solar interior, with the radial distance of the boundaries and typical temperatures indicated. An example random walk of a photon from the core to the surface is indicated in red, as well as the convective motion in the upper layer in blue. Adapted from Yeo (2014).

The Sun has a very strong global, and self sustaining magnetic field that permeates and drives all its activity; its global magnetic field is described in more detail in the next section: Sect. 1.1.3. An active region is an area of the Sun's surface with a particularly enhanced magnetic field, that contains one or more sunspots. The close up of this particular active region depicts several dark features, with one large sunspot on the right, several pores (small isolated dark patches) and one smaller sunspot on the left. The larger sunspot is shown in greater detail in the lower right panel. The darkest inner area of the sunspot is known as the umbra which harbours the strongest magnetic field concentration in the active region, while the region immediately surrounding it is known as the penumbra, also with very strong fields (albeit less than in the umbra). The umbra is dark as the intense magnetic field suppresses convection from below, thus leading to a cooler region. The field strength in the umbra is on the order of 2 – 4 kG, however much stronger fields, up to 8 kG have been detected in small features close to or in the umbra (e.g. in sunspot light bridges or at the edge of penumbral filaments, (see Siu-Tapia et al. 2019, Castellanos Durán et al. 2020, Castellanos Durán 2023). In the penumbra the field is around 1 kG. For more information on sunspots see Livingston (2002), Solanki (2003), Mathew et al. (2004), Borrero and Ichimoto (2011).

In the lower left panel of Fig. 1.4 a patch devoid of large features is highlighted. This is an area of quiet Sun, and upon further inspection one can observe many small bright cells, known as granules. These granules are formed due to convection. From the convective zone hot less dense plasma rises towards the surface, and is seen as small

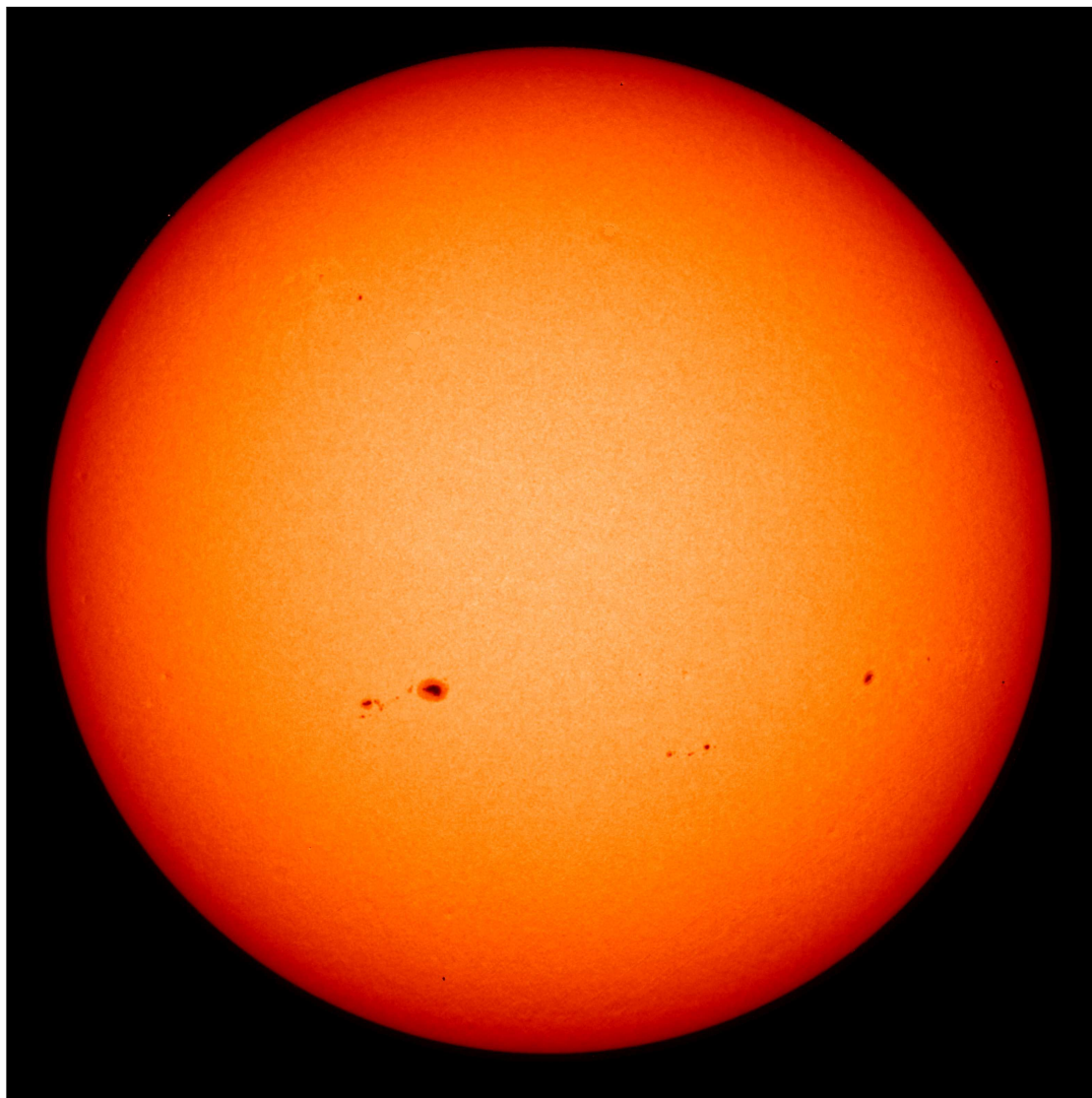


Figure 1.3: Continuum image of the solar photosphere taken with SO/PHI-FDT on March 8th 2022. The image is saturated from 0 to 1.2 arbitrary units of disc centre averaged continuum intensity. These data are only reduced in a preliminary manner.

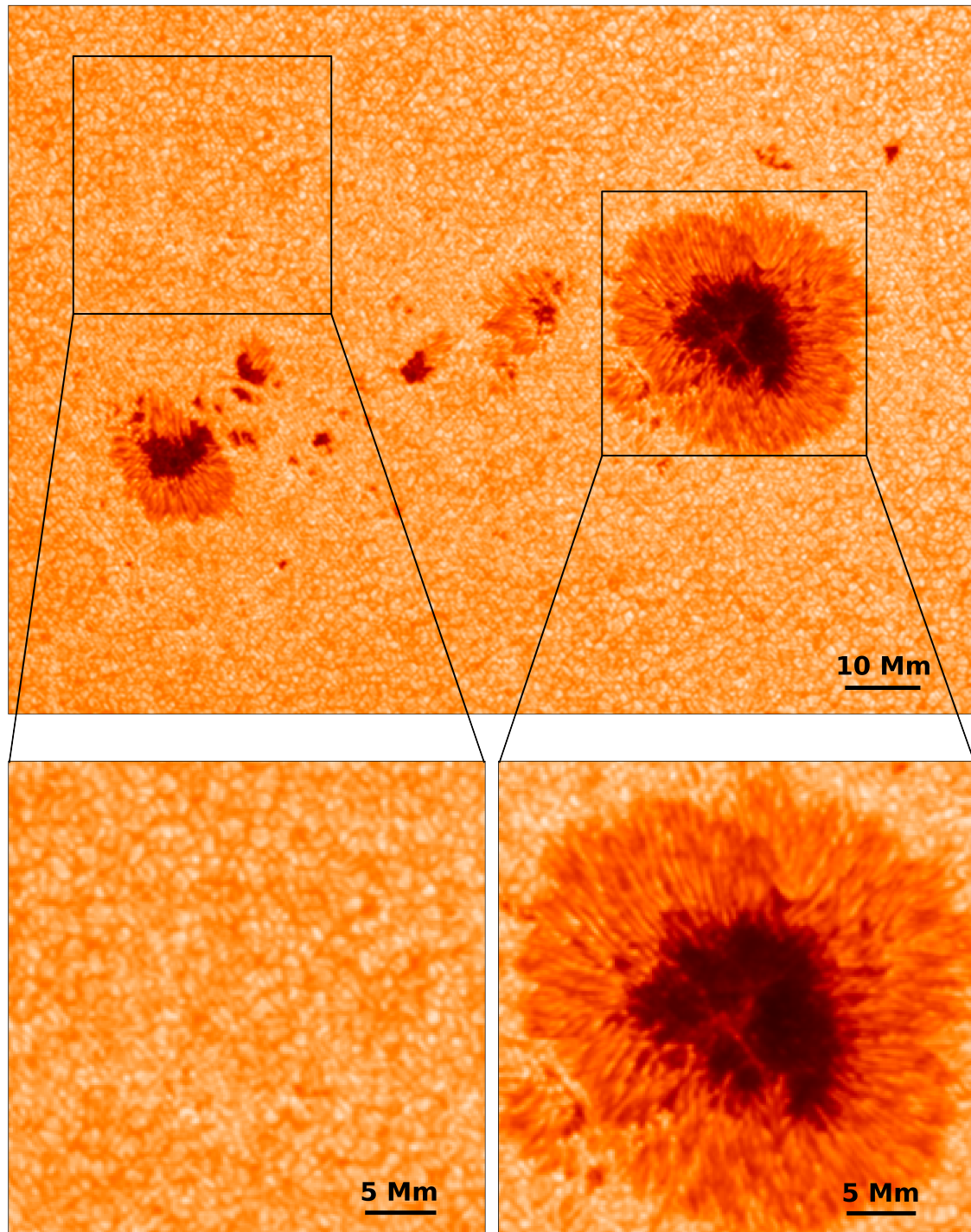


Figure 1.4: Continuum image of an active region taken with SO/PHI-HRT on March 7th 2022. The lower left panel shows a zoom in on a patch of quiet Sun, while the lower right plot shows a zoom in of the sunspot. The overlaid text highlights the scale in each panel. All panels are saturated from 0 to 1.2 arbitrary units of the mean disc centre continuum intensity. These data are only reduced in a preliminary manner.

bright features. The up-flowing plasma radiatively cools, and turn down along the sides defining the boundary of granules, in the intergranular lanes, which are the dark and hence cooler features that outline granules. A granule typically has a size on the order of 1 Mm (1000 km) and has a turnover time of approximately 5 – 10 minutes. The quiet Sun, while it may appear quiet, has important and complex magnetic field structures. In the following Section, the quiet Sun magnetic field is introduced.

The photosphere is just one layer of the Sun’s atmosphere, indeed it is considered the very bottom layer. Above the photosphere is the chromosphere, a transition region and the corona. The height range of these layers are typically defined by the temperature. The lower photosphere has a typical temperature of 6000 K, which lowers to approximately 4000 K in the upper photosphere (roughly 1 Mm above the surface) as the sun progressively cools via radiative processes. However, beyond the upper photosphere it slowly rises in the chromosphere, followed by a sharp increase in the transition region (at approximately 2 Mm on average) and finally a temperature of one or more million Kelvin is reached in the corona which can extend up to  $30 R_{\odot}$ . This counter intuitive increase in temperature with height is the source of great debate and is known as the coronal heating problem as no widely accepted explanation has been reached in the scientific community (e.g. Gomez 1990, Zirker 1993, Aschwanden et al. 2007, De Moortel and Browning 2015).

The plasma density also strongly drops in the transition region, such that in the corona, the magnetic field dominates the structure, while the opposite is true in the photosphere where plasma flows dominate. This can be expressed through the plasma beta parameter  $\beta$ :

$$\beta = \frac{p}{p_{\text{mag}}} = \frac{nk_bT}{B^2/2\mu_0}, \quad (1.1)$$

where  $\beta$  is the ratio of the plasma gas pressure  $p$  and the magnetic pressure  $p_{\text{mag}}$ . The plasma gas pressure is expressed via the number density  $n$ , Boltzmann constant  $k_b$  and temperature  $T$ . The magnetic pressure is a function of the magnetic field strength  $B$  and the permeability of free space  $\mu_0$  in SI units (in cgs units the magnetic pressure is  $B^2/8\pi$ ). In the photosphere and chromosphere the  $\beta$  is approximately 1, while in the lower corona  $\beta \ll 1$ .

### 1.1.3 Solar magnetic field

As early as 165 BC, Chinese and Korean astronomers recorded sightings of ‘black spots’ on the Sun, and since the 17th century regular observations of these sunspots have been made (Stephenson and Willis 1999, Chatzistergos et al. 2017). It was only until the discovery of the Zeeman effect in 1896 and the study of spectropolarimetry, did George Hale reveal in 1908 that the Sun harboured a magnetic field. Hale noticed a broadening of spectral lines and polarisation signature from the Zeeman effect when observing sunspots, and inferred the probable presence of strong magnetic fields. Further details on the Zeeman effect and its diagnostic capabilities are presented in Sect. 1.2.

The Sun’s large-scale magnetic field is thought to be generated via dynamo processes within the solar interior wherein the motions of electrically conducting plasma induce a magnetic field; for details on the dynamo process I refer the reader to Charbonneau

(2020) and the references therein. Small-scale dynamos, in the photosphere and convection zone, are thought to be responsible for the small-scale magnetic field, for a review see Rempel et al. (2023). In 1844 Heinrich Schwabe observed the number of sunspots over a period of 18 years and deduced that there appeared to be a cyclical increase and decrease in the sunspot number (Schwabe 1844). It is now known that over a roughly 11-year period the Sun undergoes a change in its number of sunspots and hence a change in its magnetic field. At solar minimum there are very few sunspots if all and the Sun is considered ‘quiet’, while at solar maximum sunspots regularly emerge and thus with them a flurry of associated activity such as flares and CMEs (coronal mass ejections), which we at Earth experience as space weather. For a review on space weather and the solar cycle see Temmer (2021) and Hathaway (2015) respectively.

In his study of sunspot numbers, Rudolf Wolf assigned the ‘first’ solar cycle to have started in February 1755 (Wolf 1861). We are currently in cycle 25, and in 2024 we find ourselves near solar maximum. This cycle started in December 2019: each cycle starts and ends in a period of solar activity minimum. While the sunspot number varies on an 11 year cycle, the magnetic field does so on a 22 year cycle. During each 11 year cycle, the magnetic field flips near solar maximum: the magnetic poles, which are well aligned with the rotational axis of the Sun, reverse, and only after 2 such 11 year cycles, is the global magnetic field configuration back in its original state.

A line-of-sight photospheric magnetogram from SO/PHI-FDT is shown in Fig 1.5 (the corresponding intensity image is displayed in Fig. 1.3). Fig. 1.5 reveals the magnetic field concentrations known as active regions in the middle latitudes, above and below the equator. These latitudinal bands are known as the activity belts. The classical picture of an active region consists of two sunspots with opposite polarities that are orientated in the East-West direction, i.e. one sunspot follows the other as the Sun rotates. The magnetic field in one sunspot is unipolar. However it is quite common for active regions to form complex magnetic structures with three or more sunspots, which are known as spot groups that are associated with the active region. Sunspots tend to emerge closer to the equator as one nears solar maximum known as Spörer’s law of zones (Spörer 1894), producing the famous ‘butterfly’ diagram published by Maunder (1904).

One distinct pattern is that the polarity of the leading sunspot of an active region (and the associated spot group) in the Northern hemisphere (i.e. the sunspot closer to the West limb) has the opposite polarity to the leading sunspot in the Southern hemisphere. After solar maximum when the global magnetic field reverses, the polarity of the leading sunspots that emerge is reversed in both hemispheres: this is known as Hale’s polarity law (Hale and Nicholson 1925). Additionally, the active regions (and the associated sunspot groups) are tilted, such that the leading sunspot is closer to the equator (Joy’s law, Hale et al. 1919). When an active region decays, most of the flux from the two polarities cancel, however some flux remains. A part of the trailing polarity flux is transported pole-ward while flux from the leading polarity can also cross the equator after which it is brought to the other pole through the meridional flow: this was first reported by Bumba and Howard (1969). This pole-wards transportation builds up opposite polarity flux in the poles and leads to the eventual reversal of the field near solar maximum. For more detail on pole-ward transport of active region flux see Petrie and Ettinger (2017).

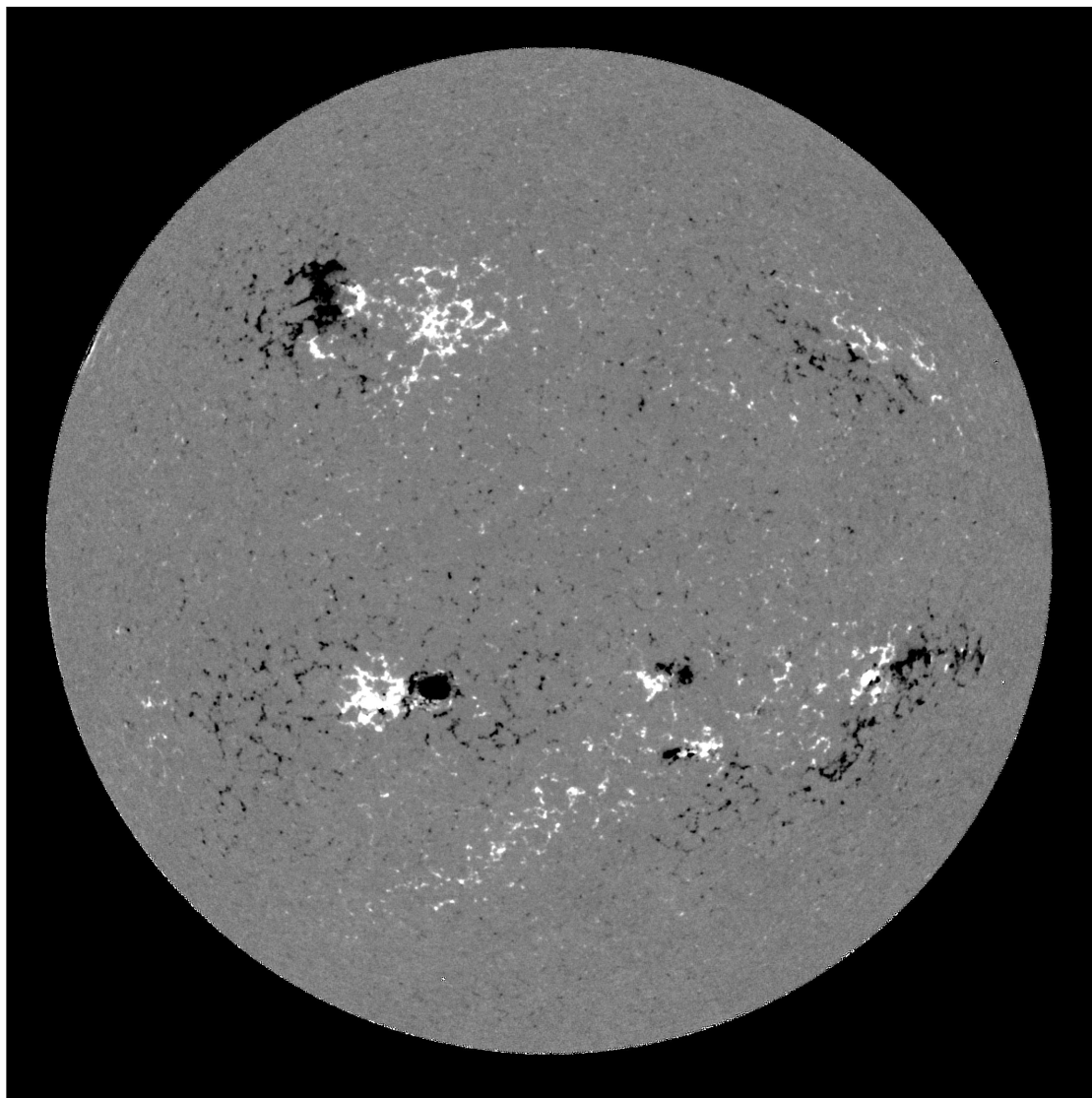


Figure 1.5: Line-of-sight magnetogram from SO/PHI-FDT on March 8th 2022. The image is saturated from  $-100$  to  $100$  G. The corresponding intensity image of the same dataset is shown in Fig. 1.3.

There are also concentrations of magnetic fields visible, that have no corresponding obvious dark features visible in the continuum image. Near the top left corner of Fig. 1.5 is a region of magnetic field enhancement. Upon inspection in the corresponding continuum image (Fig. 1.3, this region has patches which are slightly brighter than the neighbouring quiet Sun, and is known as a plage region and harbours kG fields. These make strong fields make up a fraction of the surface area of plage regions and thus when spatially averaged, the magnetic fields are on the order of hundreds of Gauss, weaker than that in a sunspot.

Elsewhere on solar surface, away from bright or dark features, and seemingly ubiquitous, is a salt and pepper appearance of the magnetic field. These fields are known as the quiet Sun fields. While the quiet Sun appears ‘quiet’ in a continuum image, it reveals a surprisingly complex magnetic structure. The quiet Sun magnetic fields can be separated into the network fields which surround regions of internetwork fields. The network fields can be of kG strength and are predominantly vertical, while the internetwork fields are much weaker, smaller in scale and more horizontal. The internetwork field regions align closely with supergranules. Supergranules are large areas of convection, up to 30,000 km in diameter, and last up to 1-2 days, and are described in detail in Rieutord and Rincon (2010). In contrast to the huge size of supergranules, the smallest scale quiet Sun magnetic fields, (that we can currently resolve) are only 100 km in size, and for a review on the small-scale magnetic features see Solanki (1993). While these fields can be small in size, the combined network and internetwork magnetic flux is extremely significant: it is on par to that carried by active regions during solar maximum (Gošić et al. 2014, Gosic 2015, Jin et al. 2011). For more details of the quiet Sun from an observational point of view see Bellot Rubio and Orozco Suárez (2019).

Another important cyclical variation, and one that is of particular relevance to this thesis, is the polar magnetic flux. The strongest flux at the poles is present during solar activity minima, while the opposite is true at solar activity maxima, due to the build up of opposite polarity flux from decayed active regions. The magnetic nature of the poles, and their importance are described in the next section: Sect. 1.1.4. In Fig. 1.6 are two images of the corona taken by the the Full Sun Imager of the Extreme Ultraviolet Imager on board Solar Orbiter (SO/EUI-FSI, Rochus et al. 2020). The image on the left depicts the Sun’s state near solar minimum in early 2021, while the image on the right is nearer solar maximum in late 2023. In the left panel there is a dearth of activity, in stark contrast to the right panel, with multiple bright active regions visible. On the left are also large darker areas, known as coronal holes, at the North and South poles, which is characteristic of solar minimum. As the cycle progresses towards maximum the coronal holes become more equatorial, and an equatorial coronal hole is visible in the right panel, below an active region.

### 1.1.4 Solar poles

Of high relevance to my thesis work is the polar magnetic field. For this reason in this section the properties and influence the polar region has on the solar dynamics are presented. For the basis of this section I have drawn heavily upon Petrie (2015) and references therein.

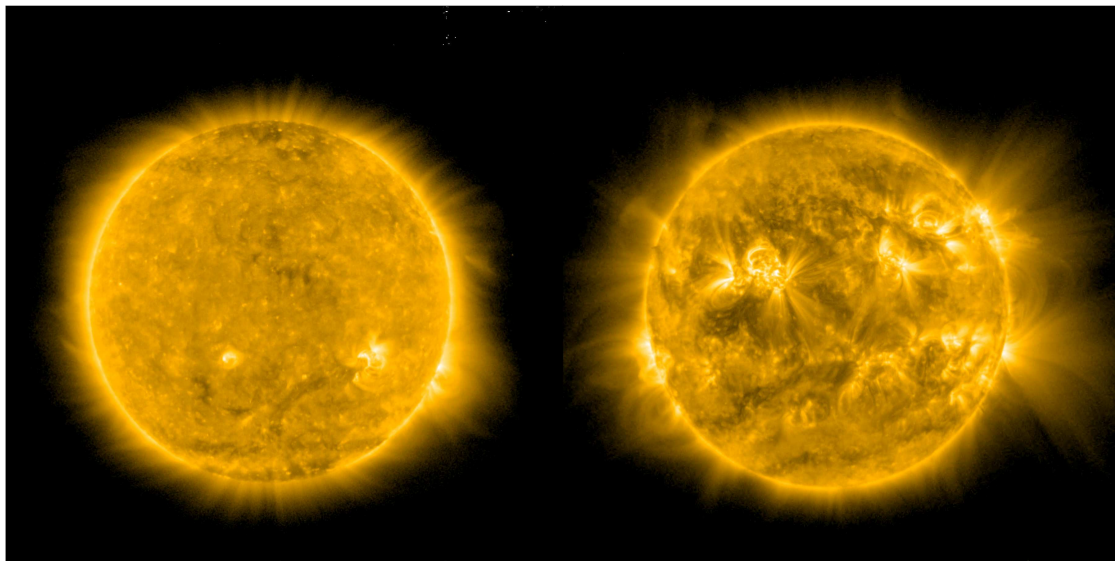


Figure 1.6: Images in the EUV taken by the EUV/FSI instrument on board Solar Orbiter. The image on the left depicts the Sun near Solar minimum (April 2021) while the right is closer to maximum (May 2023).

As alluded to in the previous section, the poles of the Sun are of critical importance and yet are one of the least-well understood regions on the solar surface. They are important due to the role they play in the dynamo process, source of solar wind, and strength of the solar activity. Nevertheless the region is poorly understood which is in great part due to the difficulty of observing the poles. At regular intervals, due to the  $7.5^\circ$  inclination of the solar rotation axis with respect to the axis of Earth's orbit, the North and South poles interchangeably move into view from Earth, just inside the solar disc. It is only from these opportunities that observations have been possible, albeit vastly restricted as one views them with an extreme amount of foreshortening.

The polar magnetic field is unlike any other region on the solar surface, apart from the magnetic field in coronal holes with which they share some similarities. At the poles, the magnetic field has a dominant unipolar polarity (i.e. a magnetic field mostly orientated in one direction), with opposite polarity at the two poles. Tsuneta et al. (2008a) observed the poles with the Solar Optical Telescope on board the Hinode spacecraft (Hinode/SOT, Tsuneta et al. 2008b) and found large unipolar patches, with fields up to 1 kG, and a magnetic field distribution that was predominantly radial. Prabhu et al. (2020) also found similar results, including an absence of strong horizontal fields, with the IMAX instrument on the SUNRISE balloon-borne mission (Solanki et al. 2010, Barthol et al. 2011, Martínez Pillet et al. 2011). While strong kiloGauss (kG) fields exist on the poles, the average flux density is low, on the order of  $5-10 \text{ Mx/cm}^2$ \*, much less than in an active region. This low flux density further complicates observations, as a very high signal to noise ratio is required to detect the low polarisation signals (for details on the polarisation

---

\*the cgs unit for flux density,  $\text{Mx/cm}^2$  is equivalent to 1 Gauss, which is used for the magnetic field strength. Hence, confusingly, in literature the two are often used interchangeably. For the remainder of this thesis, Gauss will be used to express both the flux density or magnetic field strength.

technique to detect magnetic fields see Sect. 1.2). Ito et al. (2010) compared the polar magnetic field with a patch of quiet Sun near the East limb, and inferred a slightly higher mean flux density in the polar region, as well as a larger total flux in the poles compared to the quiet Sun. Additionally they compared kG patches and found that they were larger and stronger in the polar regions.

A critical aspect of these polar fields, while they are low in mean flux density, is that they have widespread impacts on the strength of the solar activity and the solar system as a whole. They are believed to be a direct result of the poloidal fields within the solar interior, which act as the starting point for the dynamo process to generate the toroidal fields that create active regions and thus influence the solar activity. Therefore the strength of the polar magnetic field is a key component in predicting the strength of the next solar cycle (Cameron and Schüssler 2007, Petrovay 2020).

If there is polar coronal hole, the majority of the polar flux is open. This is visible in a potential field source surface (PFSS) model, shown in Fig. 1.7, of the Sun near the last solar minimum, which extrapolates the photospheric magnetic field (inferred by SDO/HMI see Sect.1.3.2 for details) up to the corona at  $2.5 R_{\odot}$ . Only magnetic field lines connecting the large magnetic structure are shown. There are open field lines at the poles in opposing polarities highlighted in red and blue, while the majority of the field in the mid latitudes is closed as shown in white. For more information about magnetic field extrapolations, including the PFSS model, see Régnier (2013), Wiegelmann et al. (2017). This open flux region forms the coronal holes that were introduced in the previous section, through which a majority of the solar wind is born.

As explained in Sect. 1, these open field lines form the bulk of the heliospheric magnetic field (HMF), along which the solar wind propagates into the solar system. This HMF interacts with the planets, including the magnetospheres of those planetary bodies that harbour global magnetic fields. The HMF brings with it solar and cosmic energetic particles, ejected in great numbers via flares or CMEs, and cause geomagnetic storms. These storms can temporarily disable radio communication, interrupt electrical power grids, and even prevent recently launched spacecraft from reaching their final orbits due to induced enhanced aerodynamic drag (Dang et al. 2022).

From the Ulysses mission we know that the HMF is broadly the same irrespective of the heliographic latitude and at either solar minimum and solar maximum (Smith and Balogh 1995). While the HMF is neither a potential field nor force-free as it is dragged out by the solar wind, close to the Sun the HMF is often simplified as a potential field (i.e. one that obeys Laplace's equation) and hence one can easily extrapolate the open flux inferred on the photosphere to any distance. This has also been confirmed by measurements from Parker Solar Probe, covering solar distances between 0.13 and 0.8 au (Badman et al. 2021). As demonstrated by Owens et al. (2008) it is possible to estimate the open magnetic flux at 1 au using a single-point measurement in-situ, which is currently provided by space missions such ACE and WIND (see Stone et al. 1998, Lepping et al. 1995).

Wang and Sheeley Jr. (1995) compared the predicted HMF extrapolated from Wilcox Solar Observatory data of the photosphere to that measured by Ulysses and reported a broad agreement. However they were only able to match the measured open flux using a correction factor which they justified as necessary to correct an instrumental

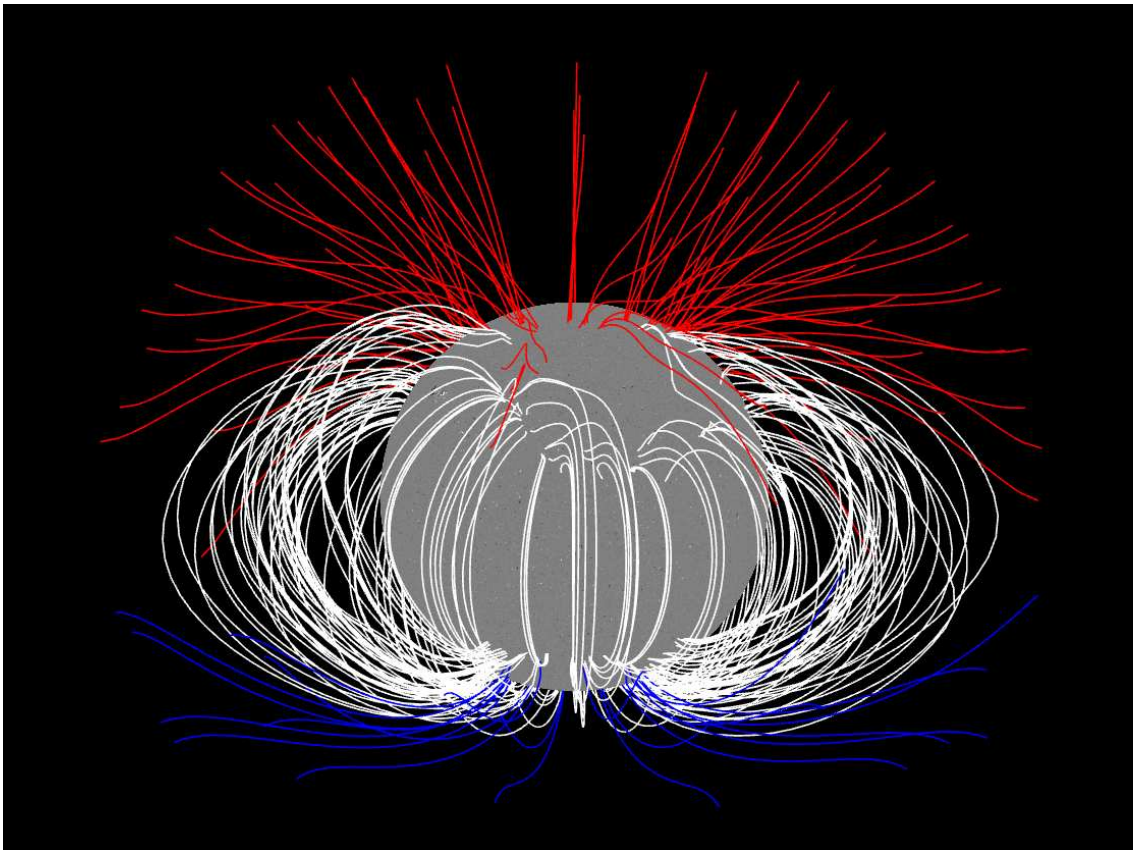


Figure 1.7: A SDO/HMI magnetogram in March 2020, with a PFSS model (restricted to the largest spatial scales) highlighting the global coronal magnetic field structure up to  $2.5 R_{\odot}$ . Image made with JHelioviewer.

effect of the observatory. Linker et al. (2017) more recently repeated the exercise using data from new observatories, which do not require an instrumental correction factor, together with a variety of models to extrapolate the field, and yet could not match the observed open flux with that extrapolated from photospheric magnetograms, leading to what is known as the ‘Open Flux Problem’. One recently proposed resolution to this problem is that strong magnetic fields near the boundaries of mid-latitude coronal holes close to active regions are the primary source of missing open flux when using a particular model (Arge et al. 2024).

As touched upon in Sect.1, this problem strongly motivates the work that I will present in this thesis. In particular it is the possible hypothesis that photospheric magnetograms underestimate the polar magnetic field which drives my work. This underestimation is hypothesised to stem from a combination of radiative transfer effects and the extreme viewing angle, which I explore with both observational data and numerical simulations in Chapters 3 and 5.

## 1.2 Solar atmosphere diagnostics

Now that the pertinent features of the Sun and its atmosphere, relevant to this thesis, have been introduced, I turn to the matter of how we are able to diagnose and retrieve information about the Sun and said atmosphere. I first describe the theory behind the quantum mechanical effect which leaves a trace of the magnetic field in the light, through polarisation, that we can observe: the Zeeman effect. This is followed by the mathematical formalism, the Stokes parameters, that we commonly use to describe polarised light. Next the basic radiative transfer equations, relevant approximations and solutions are presented. Finally the crucial technique we use to infer the magnetic field from the polarised light, Inversions, and method to synthesise Stokes parameters from a set of atmospheric conditions are introduced.

### 1.2.1 Zeeman effect

In 1896, Pieter Zeeman discovered that under the influence of a static magnetic field, spectral lines from an atom widened and later discovered that they split into doublets and triplets depending on the magnetic field (Zeeman 1897a,b,c). Zeeman also saw the polarisation signature of the effect named after him. A spectral line is a dip in intensity compared to the continuum due the absorption of photons at a specific wavelength, by an atom, as an electron transitions from a lower level to an excited upper level. The wavelength of this spectral line is determined by the energy difference between the lower and upper level in the atom.

Before we arrive at the quantum mechanical description, we first start with the classic Lorentz model of the Zeeman effect by considering the simple case of an electron circularly orbiting a nucleus in the  $x$ - $y$  plane. The magnetic moment is defined as  $\underline{\mu} = I\underline{A}$ , where  $I$  is the current and  $\underline{A}$  the area covered by the orbit. This can be reformulated as:

$$\underline{\mu} = \frac{-e}{2m_e} \underline{L}, \quad (1.2)$$

where  $e$  is the charge of an electron,  $m_e$  the mass of an electron and  $\underline{L}$  the orbital angular momentum vector ( $\underline{L} = m_e \underline{v} \underline{r}$ , where  $\underline{r}$  is the radius and electron velocity  $\underline{v}$ ). The magnetic potential energy,  $U$ , from the torque applied on the magnetic moment due to the magnetic field is:

$$U = -\underline{\mu} \cdot \underline{B}, \quad (1.3)$$

where  $\underline{B}$  is the external magnetic field vector. With a magnetic field aligned along the moment direction,  $z$ , the change in energy  $\Delta E$  of the split lines with respect to the zero field level is:

$$\Delta E = m_l \frac{e}{2m_e} L_z B = m_l \frac{e\hbar}{2m_e} B = m_l \mu_B B, \quad (1.4)$$

where  $B$  is the magnetic field strength,  $\mu_B = e\hbar/2m_e$  is the Bohr magneton and  $m_l$  is the quantum number of the orbital angular momentum, which takes the values  $m_l \in \{0, 1, -1\}$ . This  $\Delta E$  describes the energy levels of the uniformly spaced triplet, the Zeeman triplet, of spectral lines, due to the ‘Zeeman effect’. We see here a clear dependence of the size of the splitting on the magnetic field strength; the larger the  $B$ , the wider the lines are moved apart.

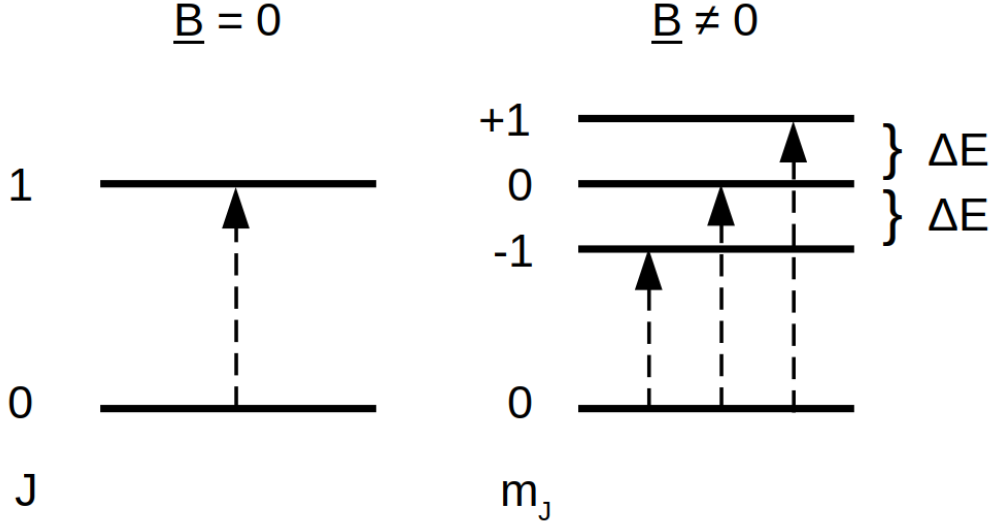


Figure 1.8: Transitions between an upper and lower level of an atom for the magnetic-free and magnetic field case for a Zeeman triplet. Adapted from Crutcher and Kemball (2019).

When the splitting is found not to be this equally spaced triplet, either with more split lines, or spacing of different widths, it is referred to as the ‘anomalous Zeeman effect’. This in fact describes the general case where the total angular momentum,  $\underline{J}$ , is considered, and the ‘Zeeman triplet’ is only one specific scenario. Assuming LS-coupling, the total angular momentum is the coupling of the electron spin angular momentum,  $\underline{S}$  with orbital angular momentum,  $\underline{L}$ . The general case, which requires a complete quantum mechanics treatment and ignoring higher order terms in  $\underline{B}$ , is as follows:

$$\Delta E = \frac{e}{2m_e}(\underline{L} + 2\underline{S}) \cdot \underline{B} = \mu_B B(g_L m_j - g'_L m'_j), \quad (1.5)$$

where ‘ denotes the upper level,  $g_L$  is the Landé factor, and  $m_j$  is the quantum number of the magnetic sublevels: the component of  $\underline{J}$  along the magnetic field direction, which takes the values  $-J, -J + 1, \dots, J + 1, J$ . The Landé factor is a dimensionless quantity that arises from the quantum numbers of a particular energy level. The Zeeman triplet is the scenario where  $g_L = g'_L$ , or  $J = 0$ , or  $J' = 0$ , such that one of the energy levels is not split. The appropriate selection rules for electric dipole transitions between the two levels are  $\Delta m_j = m'_j - m_j = 0, \pm 1$ . Therefore the spectral lines are observed to be split into three separate lines, as there are now three possible transitions from the lower to the upper level: hence a Zeeman triplet. This is depicted in Fig.1.8. When the magnetic fields are extremely strong,  $\underline{L}$  and  $\underline{S}$  are no longer coupled and thus a different treatment is required, known as the Paschen-Back effect (Paschen and Back 1912).

Given that most transitions do not produce a Zeeman triplet, and instead are ‘anomalous’, a common way to compare different transitions is by their ‘effective’ Zeeman triplet. Rewriting  $\mu_B$  as  $e\lambda_0^2/4\pi m_e c^2$  via the Planck relation  $E = hc/\lambda$ , where  $\lambda_0$  is the reference line centre wavelength, the wavelength shift for the ‘effective’ Zeeman triplet is:

$$\Delta\lambda = \frac{e}{4\pi m_e c} \lambda_0^2 g_{\text{eff}}^2 B = 4.67 \times 10^{-13} \lambda_0^2 g_{\text{eff}}^2 B, \quad (1.6)$$

where the right equality holds when  $B$  is expressed in Gauss and  $\lambda$  is in units of  $\text{\AA}$ ;  $g_{\text{eff}}$  is the effective Landé factor:

$$g_{\text{eff}} = \frac{1}{2}(g_L + g'_L) + \frac{1}{4}(g_L - g'_L)[J(J+1) - J'(J'+1)]. \quad (1.7)$$

George Hale studied spectra from sunspot umbrae, and discovered that the individual spectra exhibited signs of splitting, indicating that strong magnetic fields exist on the Sun (Hale 1908). Not only does the magnetic field split or widen the spectral lines, it also polarises the light: the polarimetric Zeeman effect. With this realisation, the Zeeman effect became the most commonly used physical mechanism exploited by solar instruments to infer the strength and orientation of the magnetic field vector in the solar atmosphere.

To select a transition as an effective diagnostic for the magnetic field in the photosphere, there are certain conditions. Firstly, the Zeeman splitting must be greater than the thermal line width, which is caused by Doppler broadening due to the thermal velocities of the atoms. The thermal line width of a spectral line at wavelength  $\lambda_0$  can be expressed as:

$$\Delta\lambda_D = \frac{\lambda_0}{c} v_T = \frac{\lambda_0}{c} \sqrt{\frac{2k_b T}{m_e}}, \quad (1.8)$$

where  $v_T = \sqrt{2k_b T/m_e}$  is the thermal velocity. This demonstrates that the line width is proportional to wavelength; however as Eqn. 1.6 demonstrates, the Zeeman effect is quadratic in wavelength and hence atomic transitions at longer wavelengths tend to be more effective as spectral line candidates. Secondly the spectral line must have a strong response to the magnetic field (large  $g_{\text{eff}}$  values). The two particular spectral lines selected for study here are the Fe I 6173.3  $\text{\AA}$  and Fe I 5250.2  $\text{\AA}$  spectral lines as they have strong effective Landé factors:  $g_{\text{eff}} = 2.5, 3$  respectively, and are formed approximately 150 km above the  $\tau = 1$  surface: i.e. the lower photosphere. Thanks to their Zeeman sensitivity, they have been employed for many studies of solar magnetism. For a recent overview of Zeeman sensitive photospheric lines and their diagnostic capabilities see Quintero Noda et al. (2021).

There are other fundamental methods to diagnose the magnetic field strength. The Hanle effect is one such example, which instead relies on the scattering of the polarised light, and the resulting change in orientation of the polarisation vector to provide information on the magnetic field. It however relies on much weaker polarisation signals and typically senses weak field strengths (10 – 100 G). It is useful where large Doppler broadening and low plasma density inhibits the use of Zeeman effect (high temperature); the corona is one such region (for more detail see Stenflo 1994).

## 1.2.2 Polarimetric Zeeman effect

With the Zeeman effect we can gauge the strength of the magnetic field, however, we can also determine the orientation of the magnetic field by studying the polarisation of the split lines. Recall Fig.1.8 from Sect.1.2.1, the allowed electric dipole transitions for the  $\underline{B} \neq 0$  case between the upper and lower level is described as follows:

$$\Delta m_j = m'_j - m_j = \begin{cases} +1 = \sigma_b \\ 0 = \pi \\ -1 = \sigma_r \end{cases}, \quad (1.9)$$

where the transition to the sublevel whose energy is independent of the magnetic field are the  $\pi$ -components, and the transitions to the sublevels shifted to higher and lower energies are the  $\sigma_b$ - and  $\sigma_r$ -components respectively. The  $\sigma_b$  and  $\sigma_r$  subscripts represent the blue and red shifted nature of their respective energy level with respect to the zero-field level.

The polarimetric signal of the Zeeman effect is that depending on the orientation of the magnetic field with respect to the observer, the  $\pi$ - and  $\sigma$ -components will appear differently polarised and is shown in Fig.1.9, where the geometry is such that the magnetic field is along the  $\underline{z}$  axis. If an observer's line-of-sight is along the  $\underline{z}$  axis from  $+z$  down, i.e. along the magnetic field pointing towards the observer,  $\sigma_b$  and  $\sigma_r$  are circularly polarised in the clockwise and counter-clockwise directions, and no  $\pi$ -component exists: the longitudinal Zeeman effect. If the observer instead observes from  $-z$  up, i.e. the magnetic field pointing away, the circular polarisation of the  $\sigma$ -components flips. If the line-of-sight is transverse to the magnetic field ( $\underline{z}$  axis), the visible components are linearly polarised: the transverse Zeeman effect. An intrinsic characteristic of the transverse Zeeman effect is that it is not possible to discern whether the magnetic field is along the  $+z$  or  $-z$  axis, leading to the  $180^\circ$  ambiguity in plane of the sky (plane perpendicular to the line-of-sight). When viewing off-axis in this geometry, the components are elliptically polarised.

### 1.2.3 Stokes parameters and profiles

One formalism to describe the exact nature of how light is polarised is through the Stokes parameters; these are the four parameters  $I, Q, U, V$ , which can be described in the following scheme, where the observer faces the radiation source:

$$\begin{pmatrix} I \\ Q \\ U \\ V \end{pmatrix} = \begin{pmatrix} I_\downarrow + I_\leftrightarrow \\ I_\downarrow - I_\leftrightarrow \\ I_\nearrow - I_\searrow \\ I_\circ - I_\ominus \end{pmatrix}, \quad (1.10)$$

where  $I_\downarrow, I_\nearrow, I_\leftrightarrow, I_\searrow$  are linearly polarised intensities at  $0, 45, 90$  and  $135^\circ$  relative to the vertical  $+y$  axis in the plane normal to the line of sight, and  $I_\circ, I_\ominus$  are right-hand and left-hand circularly polarised light in the plane normal to the line of sight. In fact Stokes  $I$  is any addition of two orthogonal components of polarisation. When  $Q = U = V = 0$ , the light is completely unpolarised; if  $I^2 = Q^2 + U^2 + V^2$  the light is completely polarised. Otherwise the light is partially polarised. The degree of polarisation,  $p$ , can be defined as:

$$p = \frac{\sqrt{Q^2 + U^2 + V^2}}{I} \leq 1. \quad (1.11)$$

Other formalisms such as the Jones vector exist, but the Stokes formalism has the advantage that the parameters are directly described as sums and differences of intensities,

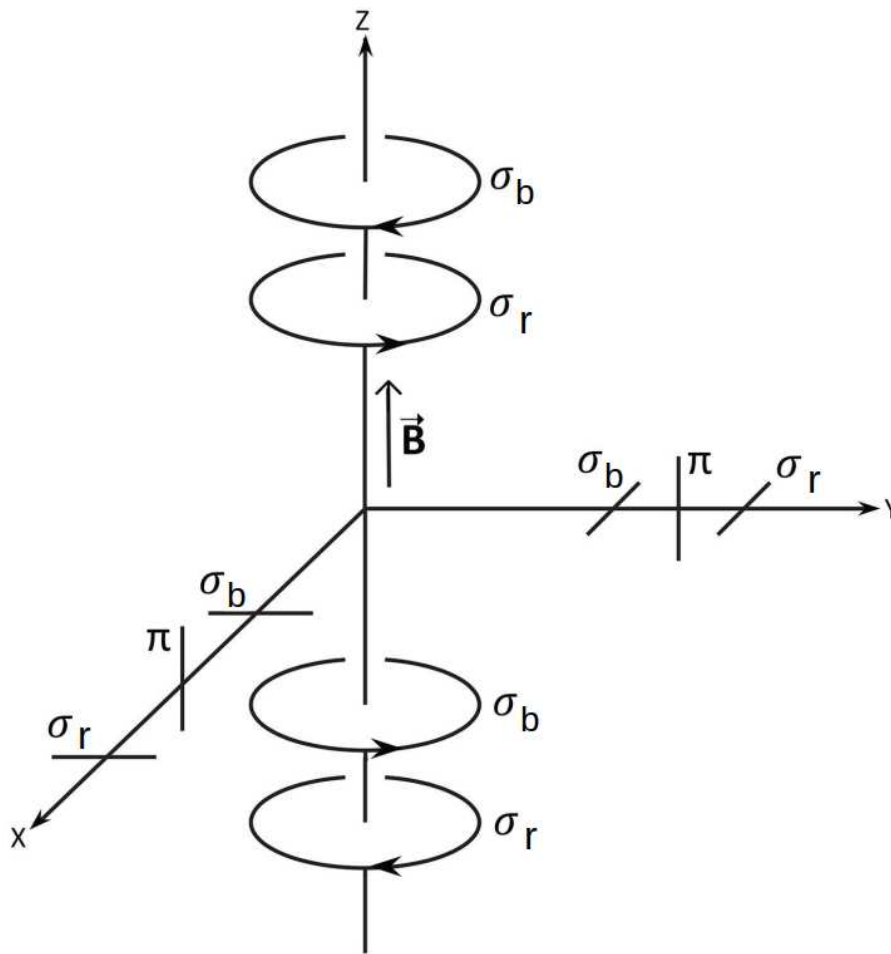


Figure 1.9: Polarisation of the Zeeman triplet components as seen from different angles, with a  $\underline{B}$  field along the  $+z$  axis. Adapted from Crutcher and Kemball (2019).

i.e. direct observables, and also can describe partial polarisation. It for these reasons, that the Stokes formalism is commonly deduced from the intensities measured by instruments to describe the polarisation state.

The longitudinal Zeeman effect is easily diagnosed with the Stokes  $V$  parameter. As explained in Sect.1.2.2, when the observer's line-of-sight is parallel (or anti-parallel) to the magnetic field, the  $\sigma$ -component transitions appear circularly polarised. As a ray of unpolarised light passes towards the observer, through a magnetised medium, the medium absorbs right- (left) circular polarisation, which results in excess left- (right) circular polarisation in the light beam when detected by the observer. This results in a negative- (positive) Stokes  $V$  signal.

The  $Q$  and  $U$  profiles are used to retrieve information about the transverse component of the magnetic field, such that the complete magnetic field vector can be inferred (albeit with a  $180^\circ$  ambiguity in the plane of the sky). However the transverse Zeeman effect is a second order effect compared to the longitudinal, as it is second order, the linear polarisation signals have a quadratic dependence on the magnetic field strength, while the circular polarisation is linear with respect to the magnetic field strength. If the magnetic

splitting is smaller than the field-free line width (which is typically the case on the Sun for most spectral lines), then the  $Q$  and  $U$  signals are typically weaker than Stokes  $V$ , while in very strong magnetic field regions with a significant horizontal component, the  $Q$  and  $U$  signals can be of similar magnitude to Stokes  $V$ . For more detail on the relative strengths of the transverse and longitudinal signals see Stenflo (1985).

An example of Stokes  $I, Q, U, V$  profiles are shown in Fig.1.10 from the Fe I absorption line at 6173.341 Å. These profiles were synthesised along vertical rays with the STOPRO module within SPINOR (see Sect. 1.2.4.5 for more detail and references) from a MURaM simulation (discussed in Sect. 1.4). The figure depicts 4 profiles, with the four Stokes parameters  $I, Q, U, V$  arranged from left to right column-wise. The top row depicts a profile which exhibits large Zeeman splitting. From Eqn. 1.6, the magnetic field strength, along the line of sight, is estimated at 2517 G purely from the splitting of the two Stokes  $V$  lobes which represent the two circular components. There is no  $\pi$  component as the field is close to parallel along the line of sight. The weak signals in  $Q$  and  $U$  also indicate that the magnetic field vector is close to vertical. This profile is a representative of a large flux concentration that can be found in a plage region. The second profile is representative of the middle of a granule, with a strong single absorption minimum in Stokes  $I$ , no  $Q$  and  $U$  signals (no horizontal fields) and very weak Stokes  $V$  signal (no strong vertical fields).

The two profiles in the top rows are considered typical profiles of their respective solar features, however the photosphere often produces atypical profiles, which are highlighted in the bottom two rows. From the Stokes  $I$  profile in the third row, one can observe that it is strongly blue shifted, implying a strong up-flow. Furthermore there are relatively strong  $Q$  and  $U$  signals, implying that the magnetic field vector has a significant horizontal component. Finally the last row illustrates an anomalous profile, with multiple lobes in Stokes  $V$ , which are the result several magnetic field components with different velocities along the line of sight.

The polarity of the magnetic field can be diagnosed with the longitudinal Zeeman effect: if the field is pointed towards the observer (positive polarity - which is the case in the top row of Fig.1.10), the blue lobe in Stokes  $V$  (first extremum) is positive, while the red lobe (second extremum) is negative. If the field is orientated away, the polarities of the two lobes are reversed.

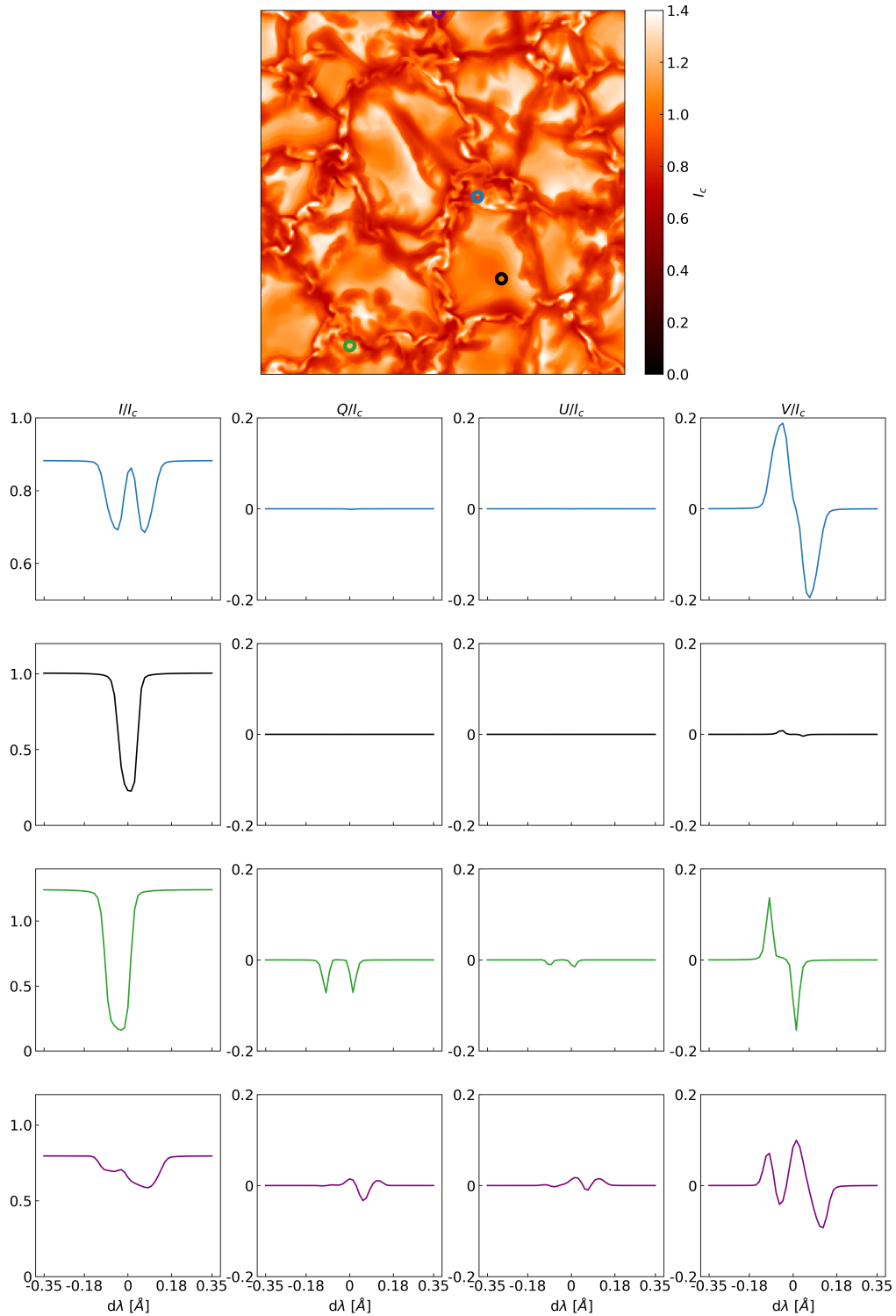


Figure 1.10: Stokes profiles, from left to right:  $I$ ,  $Q$ ,  $U$ ,  $V$  all normalised to the average continuum intensity of the entire 3D simulation. The continuum intensity of the simulation is shown above, with the locations of the profiles indicated by the circles of corresponding colour. The central wavelength is  $6173.341 \text{ \AA}$ .

## 1.2.4 Radiative transfer through the solar atmosphere

As explained in the previous section, polarised light is an excellent diagnostic tool of the solar atmosphere. To exploit this, magnetographs observe this polarised light and then infer the solar atmospheric conditions that generated the detected light. To do this one must employ a theoretical understanding of the light-matter interaction in the solar atmosphere: radiative transfer. In the following subsections, the basic theory and common methods or approximations to retrieve the solar atmospheric conditions are presented. Additionally a routine that I used in Chapter 5 which generates polarimetric spectra from a set of atmospheric conditions is presented. To form the basis of this section I drew heavily upon Stenflo (1994), Rutten et al. (2003) and del Toro Iniesta (2003).

### 1.2.4.1 Radiative transfer in the absence of magnetic fields

Consider first the specific intensity,  $I_\nu(\vec{r}, \vec{n}, t)$ , a quantity with cgs units:  $\text{ergs}^{-1}\text{Hz}^{-1}\text{cm}^{-2}\text{Sr}^{-1}$ . This quantity refers to the radiant flux per second per frequency per unit area per solid angle at a given position  $\vec{r}$ , through a unit area normal to  $\vec{n}$  and at a time  $t$ . Now consider a cylindrical medium in a plane parallel atmosphere, with its axis of symmetry along the vertical axis  $\vec{z}$ , and thickness  $Z$ . This setup is shown in Fig. 1.11, where the horizontal dashed grey lines indicate the horizontally constant layers in a plane parallel atmosphere. The change in specific intensity,  $dI_\nu$ , over a distance  $dz$  at a height  $z$  along  $\vec{z}$  can be derived

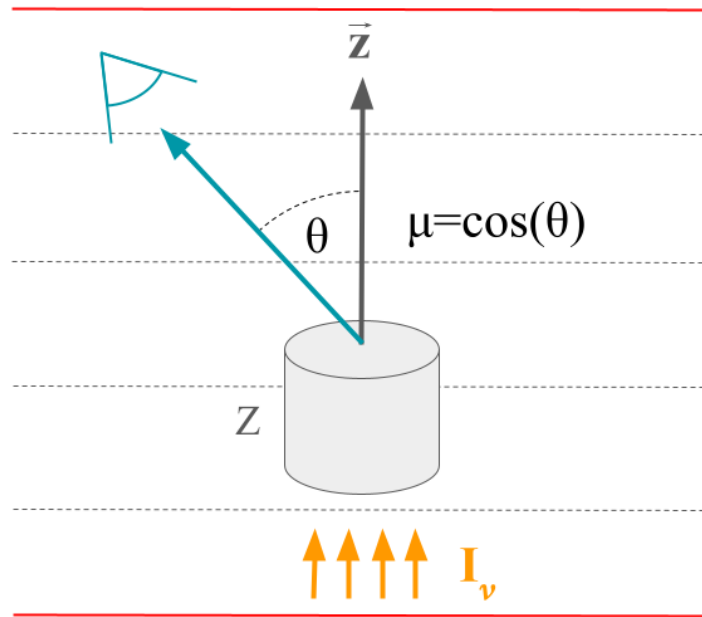


Figure 1.11: A cylindrical medium with thickness  $Z$  in a plane parallel atmosphere with its axis of symmetry along  $\vec{z}$  and incoming specific intensity  $I_\nu$ . The angle between the line-of-sight and  $\vec{z}$  is denoted with  $\theta$ .

from the difference between the light emitted by the medium (emission), and that taken away by the medium (absorption):

$$dI_\nu(z) = j_\nu dz - \alpha_\nu(z)I_\nu(z)dz, \quad (1.12)$$

where  $j_\nu(z)$  is the emission coefficient, and  $\alpha_\nu$  is the absorption coefficient of the medium. We can rewrite Eqn. 1.12:

$$\frac{dI_\nu}{\alpha_\nu dz} = \frac{j_\nu}{\alpha_\nu} - I_\nu = S_\nu - I_\nu, \quad (1.13)$$

where  $S_\nu = \frac{j_\nu}{\alpha_\nu}$  is the source function. The source function encompasses all the processes that contribute towards absorption or emission within the medium. The denominator in Eqn. 1.13 is equal to the optical path element  $d\tau_\nu$  along  $\vec{z}$ , where the optical thickness of a medium  $\tau_\nu$  with thickness  $Z$  is:

$$\tau_\nu = \int_0^Z \alpha_\nu(z) dz. \quad (1.14)$$

A medium is optically thick when  $\tau_\nu(Z) > 1$ , and optically thin when  $\tau_\nu(Z) < 1$ . In an optically thick medium, the absorption is considerable, such that photons do not travel very far before interacting with the medium, and hence we cannot ‘see’ through it, i.e. photons cannot travel through it towards us: it is opaque, while the opposite is true in an optically thin medium. However, in the context of observing the solar atmosphere, it is more practical to work in optical depth, which is considered from the observer along the line-of-sight rather than the propagation path of the light beam. Hence, the optical depth along  $z$  at a certain geometrical depth  $z_0$  with an observer at  $z = \infty$  is defined as:

$$\tau_\nu(z_0) = \int_\infty^{z_0} -\alpha_\nu dz = \int_{z_0}^\infty \alpha_\nu dz. \quad (1.15)$$

As indicated in Fig.1.11 the line-of-sight may not be along the  $\vec{z}$  axis so we can introduce  $\mu = \cos(\theta)$ , where  $\theta$  is the angle between the  $\vec{z}$  axis and the line of sight. The change in specific intensity is now over a distance  $dz/\mu$  along the line-of-sight. As this medium is in a plane parallel atmosphere  $\mu$  stays constant along the line-of-sight. Hence Eqn. 1.13 is more commonly presented in terms of  $d\tau_\nu$  and  $\mu$ :

$$\mu \frac{dI_\nu}{d\tau_\nu} = I_\nu - S_\nu. \quad (1.16)$$

This form of the radiative transfer equation is valid only in the absence of magnetic fields and a plane parallel atmosphere.

### 1.2.4.2 Spectral Line Formation

When analysing spectra from stellar atmospheres one observes many spectral lines, dips in the intensity due to absorption, across the ultraviolet, visible light and infrared spectrum. The formation of these spectral lines is described through the wavelength dependence of the absorption coefficient  $\alpha_\nu$ . A gray model atmosphere is a commonly used simplification where the absorption coefficient is independent of wavelength; such a stellar atmosphere does not exist but is used on occasion to vastly simplify radiative transfer computations. In Chapter 5 I use numerical simulations of the photosphere with a non-gray radiative transfer code to ensure an accurate representation of the emergent intensity.

In wavelength ranges where there are no spectral lines present, it is considered the background intensity, commonly referred to as the continuum. When treating the radiative

transfer of a spectral line formation, the line formation processes must be also included. The total optical depth therefore can be expressed in terms of the line and continuum absorption coefficients,  $\alpha_v^l$  and  $\alpha_v^c$  respectively:

$$d\tau_v^{tot} = -(\alpha_v^l + \alpha_v^c)dz = (1 + \eta_v)d\tau_v^c, \quad (1.17)$$

where  $\eta_v = \alpha_v^l/\alpha_v^c$  and  $\tau_v^c$  is the continuum optical depth.

The dependence of the line absorption coefficient on wavelength (or frequency), greatly impacts the height in the medium that is sensed at a particular wavelength of observation. The minimum at the line core  $\lambda_0$  in Stokes  $I$  profile in the second row of Fig. 1.10 indicates where the absorption coefficient of the atomic transition is the strongest. As the absorption is strongest at this wavelength, the line core is formed higher in the solar atmosphere (where it is slightly cooler), while further from the line core in the line wings, the profile is formed deeper, and the nearby continuum deeper still. Hence the Stokes  $I$  profiles contain information over a range of heights. The absorption profile of a spectral line can be described via a Voigt function  $H(a, u)$  (Voigt 1912):

$$H(a, u) = \frac{a}{\pi} \int_{-\infty}^{\infty} e^{-y^2} \frac{1}{(u - y)^2 + a^2} dy, \quad (1.18)$$

where  $u$  is a reduced variable equivalent to:  $(\lambda - \lambda_0)/\Delta\lambda_D$  ( $\Delta\lambda_D$  is the thermal line width),  $a$  is the damping parameter and  $y$  is an integration variable; see del Toro Iniesta (2003) for more details. A Voigt function is the result of a convolution of a Lorentzian and a Gaussian function. The spectral line is broadened by collisions and natural width of the line which have Lorentzian profiles while broadening due to thermal or bulk motions of the medium can be described by a Gaussian profile.

### 1.2.4.3 Eddington-Barbier approximation

There is a simple solution of the radiative transfer equation, Eqn. 1.16, for outward emerging intensity ( $\mu > 0$ ) at the point where the medium is completely optically thin ( $\tau_v = 0$ ):

$$I_v(\tau_v = 0, \mu) = \int_0^{\infty} S_v(t_v) e^{-(t_v)/\mu} dt_v / \mu, \quad (1.19)$$

where  $t_v = \int_{\infty}^z -\alpha_v(z) dz$  is an integration variable. Suppose we assume that the source function is a geometric series in terms of  $\tau_v$ :

$$S_v(\tau_v) = \sum_{n=0}^{\infty} a_n \tau_v^n = a_0 + a_1 \tau_v + a_2 \tau_v^2 + \dots \quad (1.20)$$

The emergent intensity  $I_v$  becomes:

$$I_v(\tau_v = 0, \mu) = a_0 + a_1 \mu + 2a_2 \mu^2 + \dots \quad (1.21)$$

If we ignore all terms of order 2 or higher we arrive at the Eddington-Barbier approximation:

$$I_v(\tau_v = 0, \mu) \approx S_v(\tau_v = \mu). \quad (1.22)$$

This solution for the emergent intensity is exact, when the source function varies linearly with  $\tau_v$ . This approximation implies that the emergent intensity at a given  $\mu$  is equal to the source function at an optical depth equal to  $\mu$ . The key result implied by this approximation is that when we view the surface of the Sun at disc centre ( $\mu = 1$ ), the intensity is equal to the source function of the medium at  $\tau_v = 1$ , while critically at inclined viewing angles, we probe shallower into the Sun:  $\tau_v = \mu$ . This, together with the decrease in temperature in the photosphere with height, explains the limb darkening that is shown in Fig. 1.3 in Sect. 1.1.2.

#### 1.2.4.4 Local thermodynamic equilibrium

Local thermodynamic equilibrium (LTE) describes the situation where the properties of matter in a medium can be characterised by the local temperature, and that there is no net energy exchange with its nearby surroundings. To be specific the salient properties are the electron level populations in the constituent atoms, ions and molecules. Under LTE conditions, these properties are given by the Saha-Boltzmann equations (see Rutten et al. 2003, for more details). LTE conditions can only hold when the radiation field is such that the electron level populations do not depart significantly from those expressed by the Saha-Boltzmann equations.

As introduced in Eqn. 1.13, the source function contains the emission and absorption properties of a particular energy level transition within an atom, ion or molecule. If there is complete frequency redistribution, the source function becomes a function of the ratio of the upper and lower population levels for the particular transition (as given by the Saha-Boltzmann equations). Complete frequency redistribution is the case where all the emission and absorption processes result in equal frequency distributions. Partial frequency distribution could for example occur due to a scattering process that results in a bias towards one particular frequency. Under LTE conditions, and a complete frequency redistribution, the source function  $\mathbf{S}_\lambda$  becomes  $(B_\lambda(T), 0, 0, 0)^\top$ , where  $B_\lambda(T)$  is the Planck Function:

$$B_\lambda = \frac{2hc^2}{\lambda^5} \frac{1}{\exp(\frac{hc}{\lambda k_b T}) - 1}, \quad (1.23)$$

where  $h$  is Planck's constant,  $c$  speed of light,  $\lambda$  wavelength and temperature  $T$ . This is a powerful equality as the source function at a given wavelength is now only a function of temperature.

To diagnose the solar atmosphere, neutral iron spectral lines are most often used. They dominate the available photospheric spectral lines, and have the additional benefit of not exhibiting hyperfine or isotopic splitting (Rutten 1988). As discussed in Sect. 1.2.1, the two photospheric lines of relevance to this work are two Fe I spectral lines: 6173.3 Å and 5250.2 Å. The source function of the two lines can be accurately modelled by a Planck function, as the scattering in the lines is weak. Hence these two lines are most commonly modelled under LTE conditions (e.g. Bello González et al. 2009, Felipe et al. 2017, Yadav et al. 2021) when performing spectral synthesis (Sect. 1.2.4.5) or inversions (Sect. 1.2.4.6). Nevertheless Fe I atoms in the solar atmosphere are over ionised by ultraviolet photons and consequently do exhibit some NLTE (non LTE) effects (see Smitha et al. 2023, for details on the 6173.3 Å spectral line).

### 1.2.4.5 Radiative transfer in the presence of magnetic fields

In Sect. 1.2.4.1 the general description of radiative transfer in a plane parallel atmosphere with no magnetic field was presented. However, in order to gain information about the magnetic structure in the solar atmosphere, the radiative transfer equation must be modified to include the effects on the polarisation state of the light when observing a spectral line that exhibits the Zeeman effect. Following del Toro Iniesta (2003), the radiative transfer equation, describing the full Stokes vector and including spectral line formation, becomes:

$$\frac{d\mathbf{I}_\lambda}{d\tau_\lambda^c} = \mathbf{K}(\mathbf{I}_\lambda - \mathbf{S}_\lambda), \quad (1.24)$$

where  $\mathbf{K}$  is the propagation matrix which is equal to  $(\mathbf{1} + \boldsymbol{\eta})$ , where  $\mathbf{1}$  is the identity matrix and  $\boldsymbol{\eta}$  is the line absorption matrix. The quantity  $\mathbf{I}_\lambda$  is now represents the full Stokes vector:  $\mathbf{I}_\lambda = (I_\lambda, Q_\lambda, U_\lambda, V_\lambda)^\top$ . Finally  $\mathbf{S}_\lambda$  is the source function for all four Stokes parameters. Note that I have changed from subscript  $\nu$  denoting frequency to  $\lambda$  signifying wavelength as is more commonly done in the context of Stokes profiles. The propagation matrix is as follows:

$$\boldsymbol{\eta} = \eta_0 \begin{bmatrix} \eta_I & \eta_Q & \eta_U & \eta_V \\ \eta_Q & \eta_I & \rho_V & -\rho_U \\ \eta_U & -\rho_V & \eta_I & \rho_Q \\ \eta_V & \rho_U & -\rho_Q & \eta_I \end{bmatrix}, \quad (1.25)$$

where  $\eta_0$  is the line-to-continuum absorption ratio. The  $\eta_I, \eta_Q, \eta_U, \eta_V$  terms describe absorption of the different polarisation states while the  $\rho_Q, \rho_U, \rho_V$  terms describe the magneto-optical effects that result in dispersion between the polarisation states. These seven elements that make up the propagation matrix are:

$$\eta_I = \frac{1}{2} \left\{ \phi_\pi \sin^2(\gamma) + \frac{1}{2} [\phi_{\sigma_b} + \phi_{\sigma_r}] (1 + \cos^2(\gamma)) \right\}, \quad (1.26)$$

$$\eta_Q = \frac{1}{2} \left\{ \phi_\pi - \frac{1}{2} [\phi_{\sigma_b} + \phi_{\sigma_r}] \right\} \sin^2(\gamma) \cos(2\chi), \quad (1.27)$$

$$\eta_U = \frac{1}{2} \left\{ \phi_\pi - \frac{1}{2} [\phi_{\sigma_b} + \phi_{\sigma_r}] \right\} \sin^2(\gamma) \sin(2\chi), \quad (1.28)$$

$$\eta_V = \frac{1}{2} \left\{ [\phi_{\sigma_b} + \phi_{\sigma_r}] \right\} \cos(\gamma), \quad (1.29)$$

$$\rho_Q = \frac{1}{2} \left\{ \psi_\pi - \frac{1}{2} [\psi_{\sigma_b} + \psi_{\sigma_r}] \right\} \sin^2(\gamma) \cos(2\chi), \quad (1.30)$$

$$\rho_U = \frac{1}{2} \left\{ \psi_\pi - \frac{1}{2} [\psi_{\sigma_b} + \psi_{\sigma_r}] \right\} \sin^2(\gamma) \sin(2\chi), \quad (1.31)$$

$$\rho_V = \frac{1}{2} \left\{ [\psi_{\sigma_b} + \psi_{\sigma_r}] \right\} \cos(\gamma), \quad (1.32)$$

where  $\phi$  and  $\psi$  are the absorption and dispersion profiles at the wavelength of the  $\sigma_b, \pi, \sigma_r$  Zeeman components. The absorption profiles are proportional to the Voigt function, discussed in Sect. 1.2.4.2, while the dispersion profiles are proportional to Faraday-Voigt functions. The angles  $\gamma$  and  $\chi$  are the inclination and azimuth of magnetic field in a spherical coordinate system where the line-of-sight is the radial component or zenith.

The set of equations, Eq. 1.26-1.32, together with the RTE in Eqn. 1.24, are known as the Unno-Rachkovsky equations (Unno 1956, Rachkovsky 1962, 1967).

The Unno-Rachkovsky equations can only be solved analytically in a few scenarios, in general it must be solved numerically, examples of such numerical RTE codes are: SIR (Ruiz Cobo and del Toro Iniesta 1992, Bellot Rubio 1998), STOPRO which is a module of SPINOR (Solanki 1987, Frutiger 2000) and RH (Uitenbroek 2001, Pereira and Uitenbroek 2015). These codes typically are initialised with a simple description of a stellar atmosphere: e.g. temperature profile, magnetic field vector, and line-of-sight velocity as a function of optical depth, and then produce a set of Stokes profiles as a function of wavelength. This is commonly referred to as spectral synthesis, and such calculations were performed in Chapter 5.

#### 1.2.4.6 Inversions

To remotely sense the magnetic field and other atmospheric conditions however, the inverse of spectral synthesis has to be performed. Stokes profiles are observed with spectropolarimetric instruments such as SO/PHI and SDO/HMI (see Sect. 1.3), and then the physical parameters must be inferred via the use of an inversion code. There are several codes in use which undertake a variety of approaches. These approaches can differ in the atmospheric modelling they assume or treatment of stray-light. Typically however, most inversion codes perform a minimisation problem: they strive to minimise the difference between the observed profiles  $\mathbf{I}_\lambda^{\text{obs}}$  and synthetic profiles  $\mathbf{I}_\lambda^{\text{syn}}$  that are generated via spectral synthesis, from a model atmosphere.

One common and simple assumption that some inversion codes make is the modelling of the solar atmosphere as a Milne-Eddington atmosphere. A Milne-Eddington atmosphere is one where all the physical parameters such as the magnetic field strength, magnetic field orientation, line-of-sight velocity and the line-to-continuum absorption coefficient ratio are all independent of optical depth. Furthermore the source function is assumed to only vary linearly in optical depth. With such an atmosphere an analytical solution can be found. A limitation of note when assuming a Milne-Eddington atmosphere is that due to the optical depth independence of the physical parameters, no vertical gradients in the line-of-sight velocity or magnetic field vector, which we know to be ubiquitous in the solar atmosphere, can be captured. These gradients reveal themselves in Stokes profiles through asymmetries around the line centre (e.g. Stenflo et al. 1984, Wiehr 1985, Sanchez Almeida and Lites 1992).

Examples of codes which use assume such a Milne-Eddington atmosphere are MILOS (Orozco Suárez and Del Toro Iniesta 2007a), VFISV (Borrero et al. 2011b), PyMilne (de la Cruz Rodríguez 2019), MERLIN (Lites et al. 2007) and HeLIx<sup>+</sup> (Lagg et al. 2004, 2009). For a comparison of some of these inversion codes see Borrero et al. (2014a). An example of a line-of-sight magnetogram from SO/PHI-FDT, generated with the MILOS code, is depicted in Fig. 1.5. A figure of all the data products of an observed sunspot, such as the magnetic field strength, its inclination and azimuth, as well as line-of-sight velocities that are generated with MILOS is shown in Fig. 2.10 in Sect. 2.5.2. Recall from Sect. 1.2.2 one important characteristic of the polarimetric Zeeman effect is that there exists a 180° ambiguity in the inferred azimuth: an azimuth of angle  $\chi$  and

$\chi + 180^\circ$  produce the same Stokes profiles. In Metcalf et al. (2006) various algorithms that seek to solve this ambiguity are discussed.

Inversion codes are not the only tool commonly used to extract information of the magnetic field from a set of observed Stokes profiles. Before the widespread availability of powerful computers simpler methods were commonly used. Such methods include the centre-of-gravity method (Rees and Semel 1979), weak-field approximation (e.g. Landi Degl’Innocenti and Landolfi 2004), and Fourier tachometer techniques such as the MDI-like algorithm (Couvidat et al. 2012a).

## 1.3 Instrumentation

Of particular relevance to this thesis are two spaced-based spectropolarimetric instruments: the Polarimetric and Helioseismic Imager (SO/PHI, see Solanki et al. 2020) and Helioseismic and Magnetic Imager (SDO/HMI, see Scherrer et al. 2012). These instruments both have the capability to observe a complete set of Stokes profiles from the same photospheric spectral line. In the following subsections the basic details of first SO/PHI and then SDO/HMI are presented. A short description of their respective space missions which host these instruments is also discussed.

### 1.3.1 SO/PHI

The SO/PHI instrument is on board the Solar Orbiter (SO, see Müller et al. 2020) mission. Solar Orbiter is a deep space mission that orbits the Sun in a highly elliptical orbit. It was launched in February 2020 and hosts 9 other instruments, with a total of 6 remote-sensing instruments and 4 in-situ instruments (for more detail on the full suite of instruments see Müller et al. 2020). At its closest approach Solar Orbiter will be at a distance of 0.28 au to the Sun. The unique property of Solar Orbiter’s orbit is that it will use successive Venus gravity assist manoeuvres (GAMs) to move out of the ecliptic, up to a maximum of  $33^\circ$  heliographic latitude. It will first start to exceed the maximum heliographic latitude of Earth ( $7.5^\circ$ ) in 2025. This will provide unprecedented opportunities to observe the solar poles. The heliographic latitude and solar distance are shown in Fig. 1.12.

The SO/PHI instrument observes the Fe I 6173.3 Å spectral line at 5 wavelength positions and an additional point in the nearby continuum, which are specified in Table 3.1 in Chapter 3.2. This spectral line was chosen due to its high magnetic sensitivity ( $g_{\text{eff}} = 2.5$ ) and a clean nearby continuum. SO/PHI uses a Fabry-Pérot interferometer, commonly referred to as an etalon, to accurately select the wavelength that is observed (Trosseille et al. 2008). SO/PHI cycles through 4 modulated polarisation states (different combinations of the 4 Stokes parameters) at the 6 wavelength positions to create the complete set of Stokes profiles. Modulated polarisation states are required as the Stokes parameters, described in Eqn. 1.10, are intrinsically defined as the difference of different polarisation states and hence cannot be directly measured. The method of extracting the Stokes parameters from these modulated states is described in the next Chapter.

SO/PHI has two telescopes, the Full Disc Telescope (FDT) and High Resolution Telescope (HRT, see Gandorfer et al. 2018). As their names suggest the FDT is designed

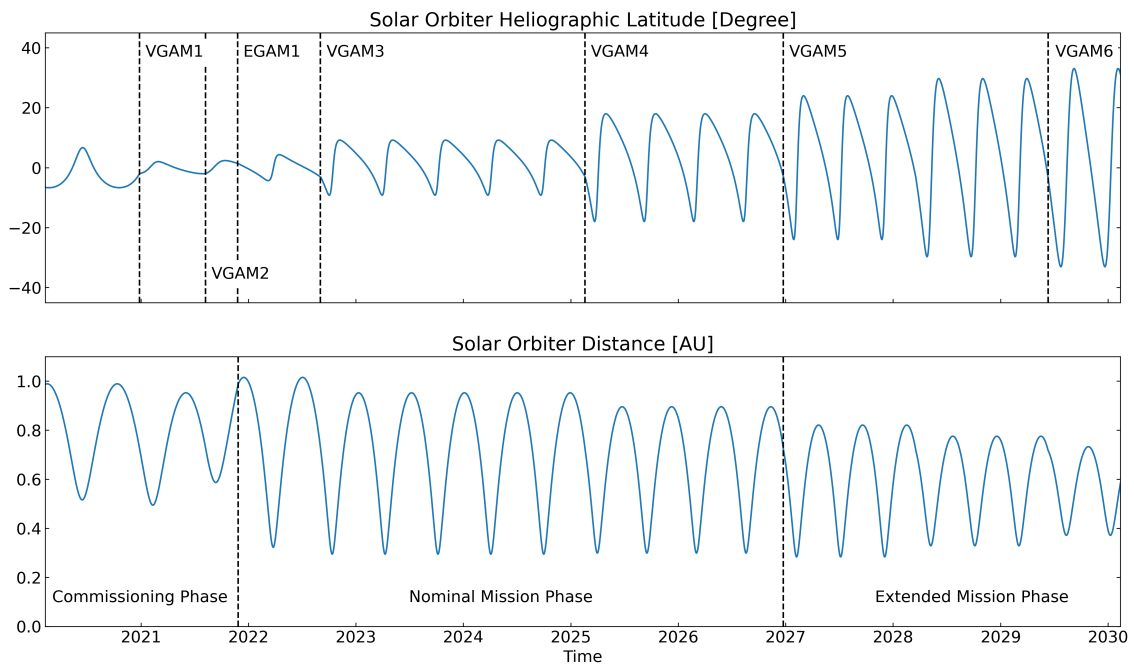


Figure 1.12: Solar Orbiter heliographic latitude and solar distance over the duration of the mission. In the top panel the seven gravity assist manoeuvres, 6 with Venus and 1 with Earth are highlighted with vertical dashed lines. The three mission phases: commissioning, nominal and extended phases are highlighted in the bottom panel with vertical dashed lines.

to always capture the full solar disc, irrespective of the solar distance, while HRT observes the photosphere at an unrivalled resolution for a space-based instrument (plate scale of 101.5 km during perihelia). An important characteristic is that the two telescopes cannot observe simultaneously as they share certain optical elements as well as the detector. A schematic of the HRT optical path and its elements is shown in Fig. 2.1 in Sect. 2.3.1. SO/PHI can operate at cadences as high as 1 minute and achieve a noise to signal ratio of below  $10^{-3}I_c$ .

The SO/PHI instrument uses the MILOS inversion code, mentioned in Sect. 1.2.4.6, to infer the magnetic field vector, line-of-sight velocity and continuum intensity. While the SO/PHI instrument has computers on board which can reduce the raw data and perform the inversion, most raw data is transmitted to ground for further analysis and calibration efforts. In the next Chapter, the on-ground data reduction pipeline for HRT that I developed, and first produced magnetograms are presented.

As SO/PHI is the first magnetograph outside the Sun-Earth line, fascinating results have already been published that only Solar Orbiter's orbit could enable. A first attempt to compare the disambiguated azimuth from algorithms such as the minimum energy method (Metcalf 1994) and that from stereoscopic analysis is presented in Valori et al. (2023). A stereoscopic observation of the same region on the photosphere allows for the first direct inference of an unambiguous azimuth. Furthermore, as Solar Orbiter at times can observe the 'back side' of the Sun with respect to Earth's view, much faster synoptic maps of the photospheric magnetic field can be produced: Löschl et al. (2024)

presented the first synoptic map which was recorded over a period of only 14 days as opposed to the standard 27 days that is required for the Sun to complete one revolution.

Due to its orbit and classification as a deep space mission, telemetry is highly restricted. Therefore the data intensive remote-sensing instruments are constrained to operate primarily in Remote-Sensing Windows (RSWs), which until now have been placed near the perihelion passes but in future will be placed near the maxima of heliographic latitude that Solar Orbiter reaches. <sup>†</sup>

### 1.3.2 SDO/HMI

Launched on 11 February 2010 and undergoing regular science operations from 1 May 2010, the Solar Dynamics Observatory (SDO, see Pesnell et al. 2012) hosts three remote-sensing instruments, one of which is SDO/HMI (Scherrer et al. 2012). As SDO's name suggests, the SDO mission is designed to be a solar observatory and provide near constant observations of the Sun. For this reason the SDO spacecraft is in a geosynchronous orbit at an altitude of 36,000 km, such that its solar distance remains close to 1 au. This close proximity to Earth enables high telemetry rates to support the GB/day of data that SDO's instruments provide. The prime mission phase of SDO ended on 30 September 2015 (Hoeksema et al. 2018), and currently the mission has been extended until at least 2030<sup>‡</sup>.

Like SO/PHI, SDO/HMI samples the Fe I 6173.3 Å spectral line but at 6 wavelength positions located in the line itself and without a point in the nearby continuum (see Table 3.1 in Chapter 3.2). SDO/HMI has two cameras, referred to as the front and side cameras, which share a common telescope aperture and SDO/HMI always captures the full solar disc. A diagram of the instrument layout is available in Couvidat et al. (2012b). The plate scale of both cameras of SDO/HMI is 0.5"/pixel which corresponds to approximately 362.5 km on the solar surface. Some basic specifications of the instrument are provided in Table 3.1. SDO/HMI utilises two successive Michelson interferometers and a Lyot-type filter to narrow the wavelength range to the desired position. SDO/HMI cycles through 6 polarisation states:  $I \pm Q$ ,  $I \pm U$ ,  $I \pm V$  and the 6 wavelength positions to create the complete Stokes vector. This procedure is sped up through the simultaneous use of both cameras.

From the complete Stokes profiles, the vector magnetic field can be inferred using the VFISV inversion code already mentioned (Borrero and Kobel 2011, Hoeksema et al. 2014, Liu et al. 2016). These data products are created at a 720 second cadence. However, SDO/HMI also produces line-of-sight magnetograms at a 45 and 720 second cadence without the need of an inversion code: instead the MDI-like algorithm (see Sect. 1.2.4.6) is applied to only the  $I \pm V$  filtergrams. This is an important distinction when comparing the vector and line-of-sight magnetograms from SDO/HMI with SO/PHI, and is fully explored in Chapter 3 wherein I directly compared SO/PHI data and SDO/HMI data, when Solar Orbiter had a near identical viewing angle of the Sun as SDO/HMI.

---

<sup>†</sup>For more information regarding the data products, publicly released data see [mps.mpg.de/solar-physics/solar-orbiter-phi/data-releases](https://mps.mpg.de/solar-physics/solar-orbiter-phi/data-releases) and for access to the Solar Orbiter archive see [soar.esac.esa.int](https://soar.esac.esa.int).

<sup>‡</sup>The data from SDO/HMI is available at <http://jsoc.stanford.edu/>.

## 1.4 Magnetohydrodynamics

Up until this point I have introduced the fundamental theory and salient methods by which we have observed the Sun's photosphere and inferred the atmospheric parameters. However we can also simulate the upper convection zone and photosphere and gain insight through that endeavour. In Chapter 5 I do exactly that and hence I now introduce the basic premise through which we can model the layer near the solar surface.

Magnetohydrodynamics, commonly referred to as MHD, is the description of fluids that harbour or interact with strong magnetic fields and have large scale slow dynamics. To be precise the exact approximations that enable treatment of a plasma via MHD is as follows:

1. The time over which we track quantities, such as the kinetic and thermal energy, vary slowly in comparison to the time scales of atomic interactions such as the ion gyroperiod and mean free path time.
2. The length scale through which we model the plasma must be larger than the ion gyroradius and mean free path length. The length scale must also be larger than the Debye length (shielding of charges), such that the plasma is quasi-neutral.
3. The plasma velocities (that of ions and electrons) are non relativistic.
4. The plasma must have a high electrical conductivity such that no strong electric fields can occur through the build up of charges.

These conditions, when fulfilled, also allow displacement currents to be neglected, which are present as Maxwell's addition to Ampere's law. As such, the solar atmosphere satisfies these aforementioned approximations. For more detail on the MHD approximations see Kippenhahn and Moellenhoff (1975), Priest (1982). We now turn to the equations that describe the MHD treatment:

1. The continuity equation,

$$\frac{\partial \rho}{\partial t} + \nabla \cdot (\rho \underline{v}) = 0, \quad (1.33)$$

where  $\rho$  is the density, and  $\underline{v}$  the plasma velocity and  $t$  is time.

2. The equation of motion,

$$\rho \frac{d\underline{v}}{dt} = -\nabla P + \underline{j} \times \underline{B} + \rho \underline{g} + \nabla \hat{\tau}, \quad (1.34)$$

where  $d\underline{v}/dt = \partial \underline{v}/\partial t + (\underline{v} \cdot \nabla) \underline{v}$  is the total or Lagrangian derivative,  $P$  the combined gas and magnetic pressure (introduced in Eqn. 1.1),  $\underline{j}$  the electric current,  $\underline{B}$  the magnetic field,  $\underline{g}$  gravity and finally  $\hat{\tau}$  the viscous tensor.

3. The induction equation,

$$\frac{\partial \underline{B}}{\partial t} = \nabla \times (\underline{v} \times \underline{B}) + \eta \nabla^2 \underline{B}, \quad (1.35)$$

where  $\eta$  is the magnetic diffusivity. This last term containing  $\eta$  describes non-ideal MHD behaviour when the fluid possesses electrical resistivity.

## 4. MHD energy equation,

$$\frac{\partial e}{\partial t} + \nabla \cdot \left[ \underline{v} \left( e + P \right) - \frac{\underline{B}(\underline{v} \cdot \underline{B})}{\mu_0} \right] = \frac{\nabla \cdot (\underline{B} \times \eta \nabla \times \underline{B})}{\mu_0} + \nabla \cdot (\underline{v} \cdot \hat{\tau}) + \nabla \cdot (K \nabla T) + \rho(\underline{g} \cdot \underline{v}) + Q_{\text{rad}}, \quad (1.36)$$

where  $e$  is the total energy,  $\mu_0$  is the permeability of free space,  $K$  the thermal conductivity,  $T$  the temperature and  $Q_{\text{rad}}$  is the radiative heating rate. The radiative term is required to model the transition from convective energy transport to radiative as the plasma becomes optically thin in the visible spectrum. These set of equations are in SI units.

To close these equations, equations of state are required to relate  $T$  and  $P$  to  $\rho$  and the internal energy density  $e_{\text{int}}$ . This set of closed equations, including the radiative term in the MHD energy equation, is known as radiative MHD.

There exist several numerical codes which solve the radiative MHD equations. Relevant examples include MURaM (MPS/University of Chicago Radiative MHD, see Vögler 2003, Vögler et al. 2005), Bifrost (Gudiksen et al. 2011), CO<sup>5</sup>BOLD (Freytag et al. 2010, 2012, Steiner et al. 2007), Stagger (Galsgaard and Nordlund 1996) and recently Mancha3D (Modestov et al. 2024).

In this study, I use MURaM, which has since received further extensions: Rempel and Cheung (2016) added the modelling of the corona, while Przybylski et al. (2022) included a NLTE (non local thermodynamic equilibrium) treatment such that the chromosphere too could be well simulated. However as I am interested in purely the upper convective zone and photosphere these extensions were not required. MURaM solves the set of closed radiative MHD equations in 3 spatial dimensions on a Cartesian grid and steps forward in time. To describe the equations of state, MURaM employs the first ionization state of the most common elements in the photosphere, which are provided by the Saha equation. To solve the radiative energy transport, the version of MURaM I used solves the radiative transfer equation (Eqn. 1.16) and assumes LTE conditions.

An example of a MURaM simulation, produced for the Riethmüller et al. (2014b) study, is shown in Fig. 1.13. The 3D simulation was first initialised under hydrodynamic conditions and allowed to evolve until it reached a statistically stationary state after 18 hours of solar time following which a homogeneous, unipolar vertical magnetic field of 50 G was introduced. Illustrated are horizontal slices from one snapshot in time of the three magnetic field components:  $B_x, B_y, B_z$ , the three plasma velocity components:  $V_x, V_y, V_z$ , as well as the Temperature and plasma density. These slices are at a geometric height close to where the spatially averaged optical depth  $\tau_{5000}$  is approximately 1. The grid cell sizes are  $20.8 \times 20.8 \times 14$  km, spanning a total area of size:  $6 \times 6 \times 1.4$  Mm. The box roughly covers 800 km below the visible surface and 600 km above, and these slices are at 910 km above the bottom of the box, close to the height of the visible surface. The simulation box has a free in- and outflow lower boundary condition and a closed top boundary, while conserving the total mass.

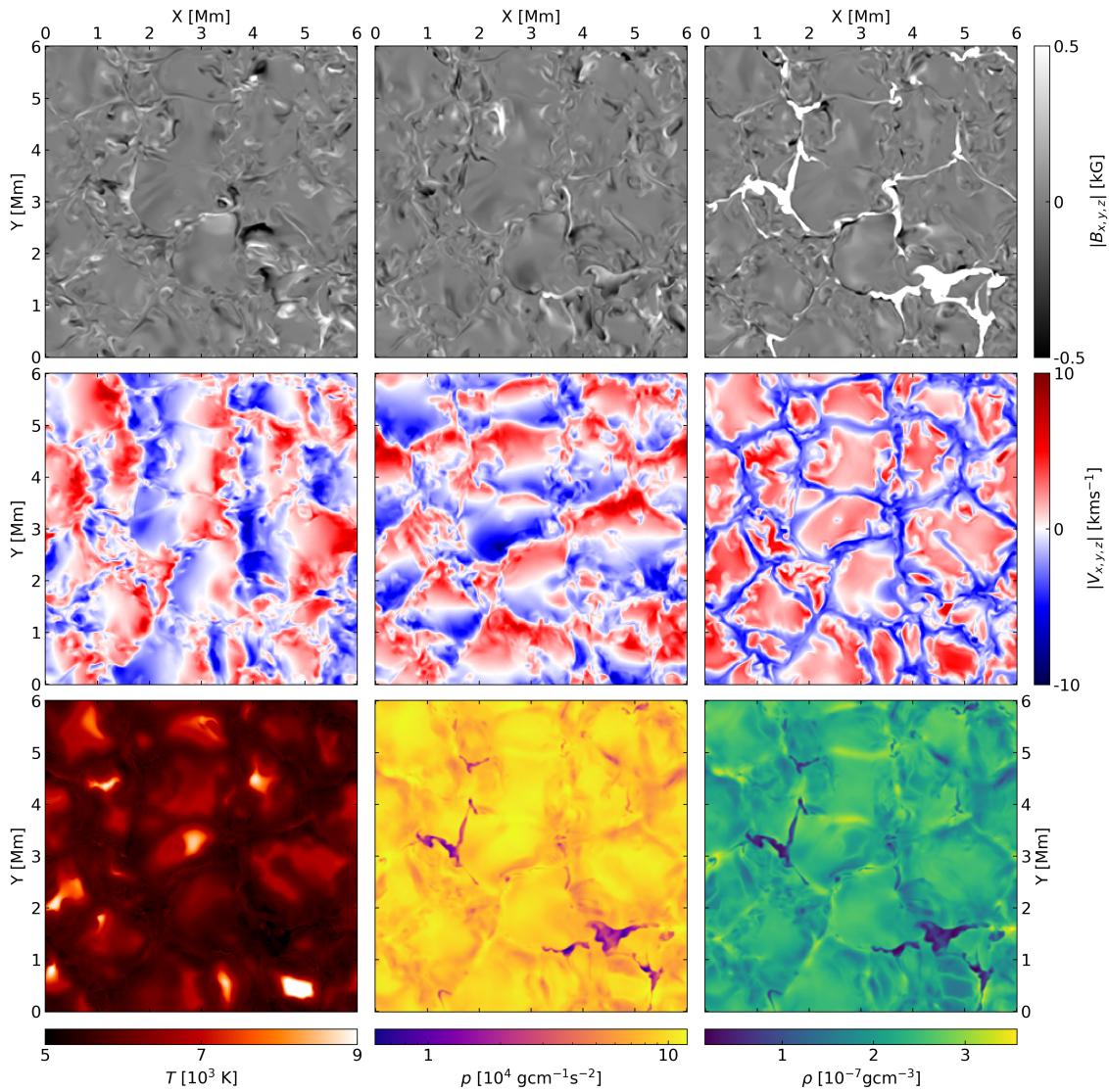


Figure 1.13: Physical quantities from a MURaM snapshot with  $\langle B_z \rangle = 50$  G. Top row: the magnetic field vector in cartesian geometry from left to right  $B_x, B_y, B_z$ , saturated to  $\pm 0.5$  kG. Middle row: the plasma velocity vector  $V_x, V_y, V_z$  saturated to  $\pm 10$  km/s. Bottom row: temperature  $T$  saturated between 5000 to 9000 K, the plasma gas pressure  $p$  and plasma density  $\rho$ .



## 2 The on-ground data reduction and calibration pipeline for SO/PHI-HRT

Sinjan, J. ; Calchetti, D. ; Hirzberger, J. ; Orozco Suárez, D. ; Albert, K. ; Albelo Jorge, N. ; Appourchaux, T. ; Alvarez-Herrero, A. ; Blanco Rodríguez, J. ; Gandorfer, A. ; Germerott, D. ; Guerrero, L. ; Gutierrez Marquez, P. ; Kahil, F. ; Kolleck, M. ; Solanki, S. K. ; del Toro Iniesta, J. C. ; Volkmer, R. ; Woch, J. ; Fiethe, B. ; Gómez Cama, J. M. ; Pérez-Grande, I. ; Sanchis Kilders, E. ; Balaguer Jiménez, M. ; Bellot Rubio, L. R. ; Carmona, M. ; Deutsch, W. ; Fernandez-Rico, G. ; Fernández-Medina, A. ; García Parejo, P. ; Gasent Blesa, J. L. ; Gizon, L. ; Grauf, B. ; Heerlein, K. ; Korpi-Lagg, A. ; Lange, T. ; López Jiménez, A. ; Maue, T. ; Meller, R. ; Michalik, H. ; Moreno Vacas, A. ; Müller, R. ; Nakai, E. ; Schmidt, W. ; Schou, J. ; Schühle, U. ; Staub, J. ; Strecker, H. ; Torralbo, I. ; Valori, G.

**Software and Cyberinfrastructure for Astronomy VII. Proc. of SPIE Vol. 12189, 121891J, 2022. SPIE Astronomical Telescopes + Instrumentation**  
DOI: [10.1117/12.2629323](https://doi.org/10.1117/12.2629323)<sup>§</sup>

### 2.1 Abstract

The ESA/NASA Solar Orbiter space mission has been successfully launched in February 2020. Onboard is the Polarimetric and Helioseismic Imager (SO/PHI), which has two telescopes, a High Resolution Telescope (HRT) and the Full Disc Telescope (FDT). The instrument is designed to infer the photospheric magnetic field and line-of-sight velocity through differential imaging of the polarised light emitted by the Sun. It calculates the full Stokes vector at 6 wavelength positions at the Fe I 617.3 nm absorption line. Due to telemetry constraints, the instrument nominally processes these Stokes profiles onboard, however when telemetry is available, the raw images are downlinked and reduced on

---

<sup>§</sup>The contents of this chapter are identical to the printed version of Sinjan, J. Calchetti, D., Hirzberger, J., Orozco Suárez, D., Albert, K., Albelo Jorge, N., Appourchaux, T., Alvarez-Herrero, A., Blanco Rodríguez, J., Gandorfer, A., et al., 2022, The on-ground data reduction and calibration pipeline for SO/PHI-HRT, in Software and Cyberinfrastructure for Astronomy VII, vol. 12189, pp. 612–628, SPIE, reproduced with permission from SPIE. I, Jonas Sinjan, completed all the underlying work on the pipeline, wrote the first draft text and created the figures for all sections of this publication except for Sect. 2.4.7.2 and Fig. 2.11 in Sect. 2.5.3, which were created by Daniele Calchetti. The remaining co-authors supported the development, engineering and operations of SO/PHI and provided comments on the draft text.

ground. Here the architecture of the on-ground pipeline for HRT is presented, which also offers additional corrections not currently available on board the instrument. The pipeline can reduce raw images to the full Stokes vector with a polarimetric sensitivity of  $10^{-3} \cdot I_c$  or better.

## 2.2 Introduction

The Solar Orbiter (SO) is the first selected medium-class mission from ESA's Cosmic Vision 2015-2025 Program. It is a collaborative effort with NASA, and the spacecraft was launched on February 10th 2020 (Müller et al. 2020). Its primary goal is to study the Sun and the inner heliosphere. To achieve this, the spacecraft carries a scientific payload of 10 instruments, 6 remote sensing and 4 in-situ. The Polarimetric and Helioseismic Imager (PHI) is one of the remote sensing instruments and it retrieves the continuum intensity, the vector magnetic field, and the line-of-sight velocity, both in the Sun's photosphere (Solanki et al. 2020). It does this by sampling four linear combinations of the four Stokes parameters of the magnetically sensitive Fe I absorption line at 617.3 nm at 6 wavelength positions. These samples are later transformed to the aforementioned physical quantities by inverting the radiative transfer equation for polarised light in the presence of a magnetic field.

The instrument has two telescopes: the Full Disc Telescope (FDT) and the High Resolution Telescope (HRT, Gandorfer et al. 2018). The FDT can capture the full solar disc, while the HRT is designed to capture photospheric features in more spatial detail. During normal operations to conserve telemetry, the raw images from the two telescopes are reduced onboard using field-programmable gate array (FPGA) computers, producing the data products which are downlinked to Earth (Lange et al. 2017, Albert et al. 2020).

However there are occasions during the nominal and extended mission phases when telemetry rates will be favourable such that raw images can be downloaded and reduced on-ground. The ability to reduce data on-ground provides more opportunities for fine-tuning the data reduction process, and therefore for producing higher quality data products. Furthermore it allows for the additional processing when the HRT's Image Stabilisation System is switched off. Since launch the spacecraft has been in its Cruise Phase until 27th November 2021, when the Nominal Mission Phase began (Zouganelis et al. 2020). During the cruise phase, predominantly raw images from HRT were downloaded and reduced on-ground, to allow for in-flight testing and investigate the instrument's performance. This paper outlines the current state of the on-ground pipeline for the HRT (V1.4 June 2022), written in Python3, which is used to reduce and calibrate these raw images. Finally early in-flight data reduced with this pipeline is presented and the telescope's high polarimetric sensitivity is shown.

## 2.3 SO/PHI-HRT

### 2.3.1 The instrument

A simplified description of the key optical components of the HRT is presented, following the optical path shown in Fig. 2.1 (Solanki et al. 2020, Gandorfer et al. 2018). The HRT is a Ritchey-Chrétien telescope with a decentred pupil. The HRT has a Heat Rejection Entrance Window (HREW) that allows in only 4 % of the incoming solar light power. The HRT uses its own Polarisation Modulation Package (PMP), consisting of Liquid Crystal Variable Retarders (LCVR) and a polariser to modulate the light in order to obtain the polarisation characteristics of the incoming light (Alvarez-Herrero et al. 2015). Once modulated, the light is split and a portion enters the Correlation Tracker Camera (CTC). The CTC is part of the Image Stabilisation System (ISS) which works to track a specific feature on the solar surface, calculating from the CTC images the steering signal for the M2 (tip-tilt) mirror, to accurately track the desired feature (Volkmer et al. 2012, Carmona et al. 2014). The ISS is also used to compensate for effects such as spacecraft jitter. After the beam splitter the light goes through the HRT Refocus Mechanism (HRM) and passes through the Feed Select Mechanism (FSM), which is used to switch between FDT and HRT, and towards the Filtergraph (FG). The FG contains two pre-filters and a tunable  $\text{LiNbO}_3$  Fabry-Perot etalon, an interferometer, which together allow for a transmission window with a mean full-width-half-maximum (FWHM) of  $(106 \pm 5)$  mÅ and free spectral range of 3.0 Å (Gandorfer et al. 2018, Dominguez-Tagle et al. 2014). The resultant light then illuminates an Active Pixel Sensor (APS) which reads out images with  $2048 \times 2048$  pixels. The re-imaging optics in the Focal Plane Assembly (FPA) provides a plate scale on the sensor of 0.5'' per pixel which corresponds to 102 km at 0.28 AU distance.

The imaging cadence is controlled by the modulation accumulation scheme in the PMP. While the HRT has the operational capability of a 60 second cadence, during the cruise phase a 96 second cadence was used. This was done using a PMP scheme of [4, 5]. At each wavelength position, 4 frames are taken for each modulation state, and this is cycled through each modulation state 5 times, resulting in 20 total frames for each modulation state at each wavelength position. The minimum number of frames to achieve the desired signal to noise ratio of  $10^3$  is 16 (Solanki et al. 2020).

### 2.3.2 Flat-field acquisition

A critical reduction process of the science data requires a flat-field. The flat-field contains the difference in gain of a given pixel with respect to the others, as well as information of other imperfections such as dust grains in the field of view (FOV). The HRT flat-fields are not acquired using off-pointing of the spacecraft (Kuhn et al. 1991). Instead, the solar surface evolution, is used to introduce differences between subsequent images, such that localised solar features are averaged out with enough acquisitions. Over a period of approximately 8 hours, 1500 images are accumulated at each polarisation state and wavelength. These flat-fields are acquired during every major campaign, to ensure the science data can be properly calibrated. However polarimetric structures remain in the flat-field that are smeared horizontally due to the solar rotation. This horizontal smearing leaves unwanted artefacts when applying the flat-field correction to the scientific data.

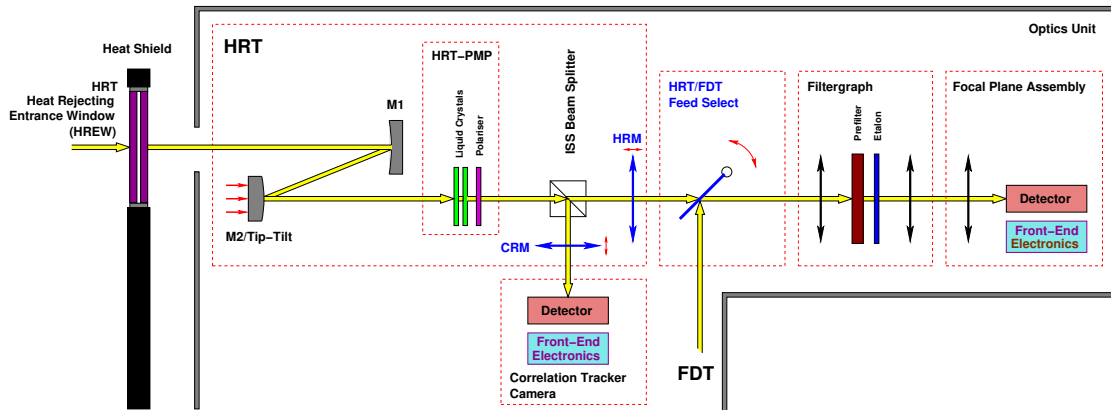


Figure 2.1: Schematic of the optics unit of SO/PHI-HRT. SO/PHI-FDT is located in the same optics unit but is not shown for clarity.

Therefore an additional flat-field processing procedure was implemented as part of the pipeline: unsharp masking, which is described in Sec. 2.4.2

## 2.4 SO/PHI-HRT on ground pipeline

### 2.4.1 Pipeline overview

The on-ground pipeline is developed in Python3 and reduces the raw data received from the SO/PHI-HRT instrument. The raw files downloaded from the instrument are classed Level 0 (L0) data. They become Level 1 (L1) data once necessary metadata are added, the data are scaled to the correct units (to account for the compression scheme used) and reflected in the  $Y$  axis to match the solar orientation convention. This on-ground pipeline converts the L1 data, into L2 data. This process is described in Fig. 2.2.

The inputs to the pipeline are the science data, raw flat-fields, and demodulation matrices (for each operating PMP temperature) from the polarisation calibration campaign performed prior to launch. The science data and flat-fields are first dark-corrected to remove the dark current (not shown in Fig. 2.2 for brevity). A key capability of the pipeline is the option to unsharp mask the flat-fields (see Sect. 2.4.2), however the width of the Gaussian distribution to be used must be known beforehand. The pipeline has the functionality to reduce multiple datasets at once, with the same flat-field, provided the image dimensions, PMP temperature and continuum position of all datasets agree. The pipeline is built to work with any cropped dataset provided the input is square. The pipeline can also reduce images when the ISS is locked to track the solar limb, using an automatic limb detection algorithm to account for limb darkening effects when normalising the Stokes parameter and applying the cross-talk correction. Furthermore additional steps are implemented to account for the case when the ISS is not operating. The output quantities are indicated with the dotted outlines in Fig. 2.2.

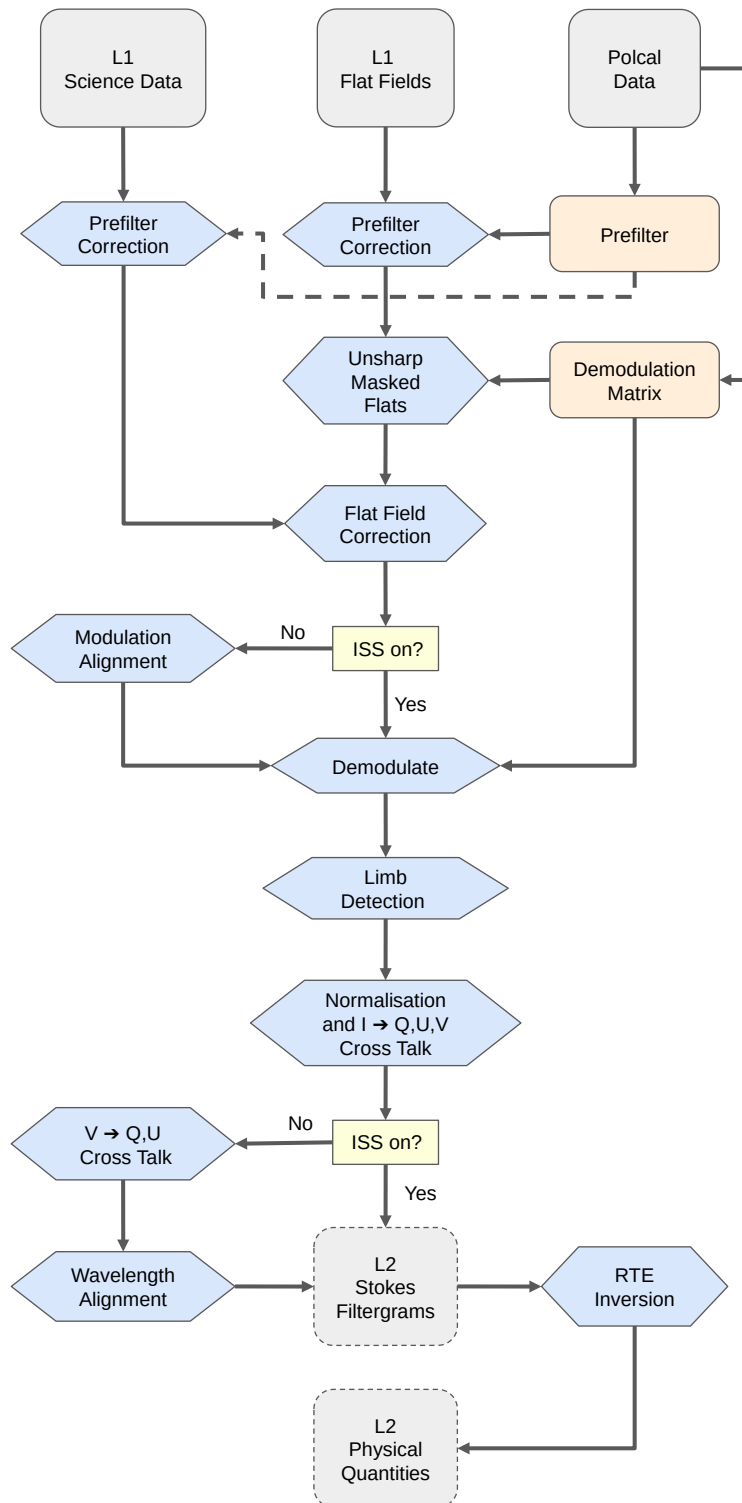


Figure 2.2: Flowchart of the on-ground pipeline, reducing Level 1 data to the Level 2 physical quantities. The dark field correction and field stop application has been omitted for brevity. ‘Polcal’ refers to the on-ground polarisation calibration campaign prior to launch.

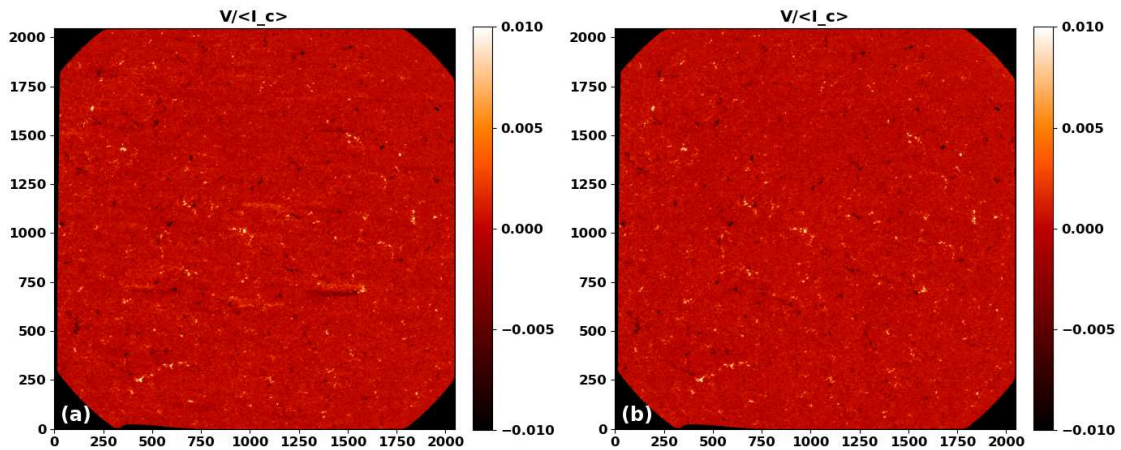


Figure 2.3: A Stokes  $V$  image in the line wing on 23 February 2021 17:00 UTC, taken at a Sun-spacecraft distance of 0.526 AU: a) result when using a flat-field without unsharp masking, b) result when unsharp masking is applied. The region outside the field stop is set to black for clarity.

### 2.4.2 Unsharp masking

Due to the method of flat-field acquisition as described in Sect. 2.3.2, horizontal polarisation elements exist in the flat-fields, which would contaminate the data. To remove this contamination unsharp masking is performed on the flat-fields. This is achieved by convolving the demodulated flat-fields with a 2D Gaussian distribution. The width of the Gaussian distribution was optimised such that the horizontal stripes were removed, but that any larger scale information was retained. The width of the Gaussian is a function of Solar distance and PMP temperature. For example, at a distance of 0.526 AU, a width of 59 pixels was used, while at 0.801 AU, 49 pixels was the appropriate width to be used. An example of the unsharp masking process is shown in Fig. 2.3.

### 2.4.3 Flat-field correction

From in-flight testing it was determined that a polarisation state dependent, and wavelength dependent flat-field must be applied to the science data. This is done in order to remove a polarimetric ghost that was detected, likely to originate from a reflection between the inner panel of the HREW and the highly reflective etalon. With an optical path of this nature, with many parallel optical surfaces, several measures were taken to suppress ghosts; however it was not possible to eliminate all of them. In particular those produced by the HREW, which is not mounted on the instrument but instead is a component of the heat shield of the spacecraft is prone to have large margins in the mechanical alignment. Nevertheless, with the proper treatment of the flat-fields, we are capable of removing the contribution from the detected ghost to below the noise requirement level. Finally, to correct for the cavities within the etalon, the flat-field must be normalised over the wavelength range, so that the spectral line profile is removed. This also has the effect of removing the solar rotation to at least first order. Thus the flat-fielded data,  $I_{ff}$ , is

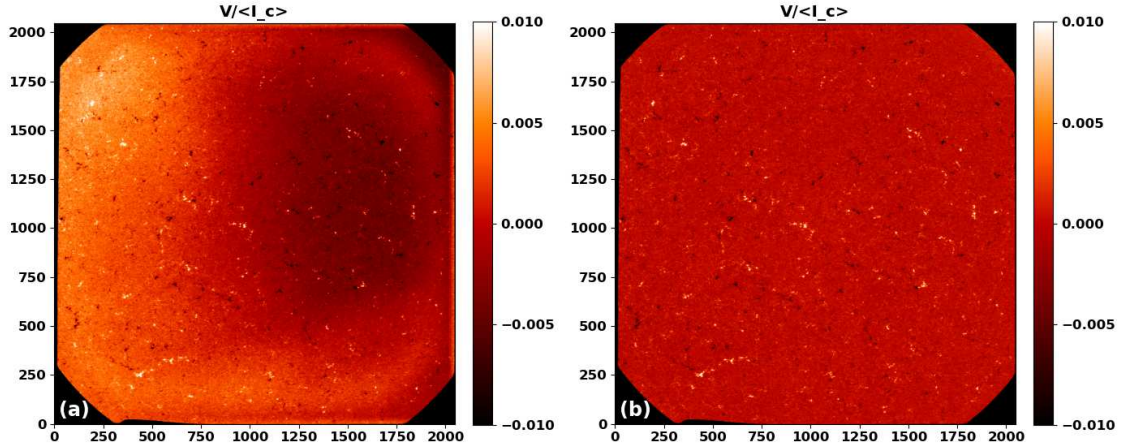


Figure 2.4: A Stokes  $V$  image in the ling wing on 23rd February 2021 17:00 UTC, with a distance of 0.526 AU and PMP temperature of  $50^\circ\text{C}$ : a) result when using the original demodulation matrix; b) result after using an averaged matrix.

calculated as follows:

$$I_{ff}(x, y, s, \lambda) = \frac{I_{df}(x, y, s, \lambda)}{I_{flat}(x, y, s, \lambda)}, \quad (2.1)$$

where  $I_{df}$  is the dark-corrected data,  $x$  and  $y$  are the spatial dimensions in the FOV,  $s$  is the polarisation state and  $\lambda$  denotes the wavelength.

#### 2.4.4 Demodulation

The raw images must be demodulated to remove the modulation applied by the PMP in the image acquisition process. This is obtained with the demodulation matrix:  $d_{11-44}$ , for a given pixel:

$$\begin{pmatrix} d_{11} & \dots & d_{14} \\ \vdots & \ddots & \vdots \\ d_{41} & & d_{44} \end{pmatrix} \begin{pmatrix} I_{ff1}(x, y, s, \lambda) \\ I_{ff2}(x, y, s, \lambda) \\ I_{ff3}(x, y, s, \lambda) \\ I_{ff4}(x, y, s, \lambda) \end{pmatrix} = \begin{pmatrix} I \\ Q \\ U \\ V \end{pmatrix}, \quad (2.2)$$

where  $I_{ff1..4}$  are the four flat-fielded intensities and  $I, Q, U, V$  are the Stokes parameters. The demodulation matrices acquired during the on-ground testing before launch, resulted in large gradients across the field of view in the Stokes parameters, an example of which are portrayed in Fig. 2.4. Averaging the central  $1024 \times 1024$  region of the demodulation matrix results in a demodulation matrix that removes the large scale FOV variations that were introduced using the matrix measured during the on-ground polarisation campaign.

#### 2.4.5 Limb detection and normalisation

For datasets where the limb is in the FOV, such as when the spacecraft is off-pointing to the poles, certain additional steps are needed. From the World Coordinate System (WCS) information in the fits header, the pointing (North, South, East, West) is determined, such

that a limb fitting algorithm can accurately detect the limb. First a mask is created, ensuring that all pixels outside the solar disc are set to 0 in the final data products. To prevent limb darkening from affecting the normalisation, the edge and radius of the limb are calculated. For limb images, the average of Stokes  $I$  at the continuum wavelength position is used as the Stokes normalisation factor, making sure to only include pixels which are less than 80 % of the solar radius in distance from disc centre. Under disc centre pointing, the average from the central  $1024 \times 1024$  region is found and used as  $I_c$ .

### 2.4.6 Cross-talk correction

Cross-talk between the Stokes parameters arises from three main sources: spacecraft jitter, imperfect instrument calibration, and modulation from the LCVRs. The strongest cross-talk, is that from Stokes  $I$  to the other Stokes parameters, as the absolute value of Stokes  $I$  is much greater than that of  $Q$ ,  $U$ ,  $V$  (del Toro Iniesta 2003). Due to cross-talk from sources described earlier, an ad-hoc correction is applied to the data (Sanchez Almeida and Lites 1992, Schlichenmaier and Collados 2002). A linear fit of  $Q$ ,  $U$ ,  $V$  against  $I$  is performed separately, on the continuum wavelength image, to find the gradient and offset parameters of the cross-talk from  $I$  to  $Q$ ,  $U$ ,  $V$ . When applying the cross-talk correction at each of the 6 different wavelength positions, the parameters are weighted by the respective averaged Stokes  $I$  value, relative to the continuum value. The cross-talk parameters from in-flight data are of the order of 1 % or lower, indicating that the ISS ensures there are no major contributions from the spacecraft jitter, the instrument calibration is accurate and that the demodulation matrices used are effective. After this step, provided the ISS is operational, the pipeline produces the L2 ‘Stokes’ filtergrams.

### 2.4.7 Special case: ISS off

The ISS of the instrument, as explained in Sect. 2.3.1, tracks features on the Sun and compensates for the spacecraft jitter. The latter is important for two reasons: it removes the cross-talks induced by the jitter and keep the 24 raw frames aligned between each other during the acquisition. In some occasions the ISS has to be turned off and three procedures have been implemented to compensate for the absence of this subsystem.

#### 2.4.7.1 Modulation alignment

The first procedure is the modulation alignment just before the demodulation of the data (see Fig. 2.2). For each wavelength we consider the first polarimetric modulation as a reference; the remaining three polarimetric modulations are then aligned to the chosen reference. This is performed by computing the gradient of the images, selecting a sub-region of  $512 \times 512$  pixels, and evaluating the cross correlation between them with sub-pixel accuracy (Guizar-Sicairos et al. 2008). This registration has to be performed before the demodulation in order to avoid the combination of pixels from different regions on the Sun. Figure 2.5 shows the effect of the spacecraft jitter on the data and the removal of the noise pattern with the modulation alignment step. The Stokes  $V$  noise level decreases from  $2.4 \times 10^{-3}$  to  $1.4 \times 10^{-3}$ .

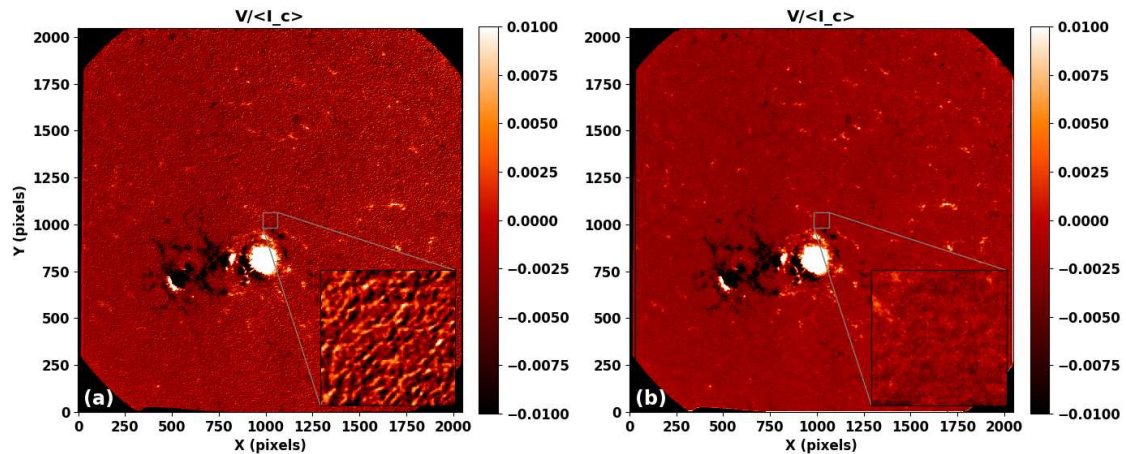


Figure 2.5: A Stokes  $V$  image in the line wing on 7 March 2022 00:00 UTC, at a Sun-spacecraft distance of 0.501 AU and PMP temperature of  $50^\circ\text{C}$ : a) result when using the standard pipeline procedure with ISS switched off, b) result when using the modulation alignment step.

#### 2.4.7.2 $V$ to $Q, U$ cross-talk correction

The spacecraft jitter is responsible for increasing the cross-talk both from  $I$  to  $Q, U, V$  and from  $V$  to  $Q, U$ . Similar to the correction of cross-talk from Stokes  $I$  (Sect. 2.4.6), this procedure performs a linear fit of Stokes  $Q$  and  $U$  against Stokes  $V$  immediately after the cross-talk correction from Sect. 2.4.6 is applied. The difference between the two methods is that here we consider points from all the wavelengths while computing the linear fit, so the parameters are not weighted by the continuum value. Despite the cross-talk parameters from  $I$  to  $Q, U, V$  being of the order of 1%, the parameters from  $V$  to  $Q, U$  can be up to 7%.

#### 2.4.7.3 Wavelength alignment

The last step before producing the L2 ‘Stokes’ filtergrams is the alignment of the frames at different wavelengths. Similar to that described in Sec. 2.4.4, we use the continuum Stokes  $I$  image as a reference, and after computing the gradient, we align the other frames to this reference. The only exception is for the line core wavelength image, for which a line wing image is used as a reference. This alignment has to be performed before the Radiative Transfer Equation is inverted to create cohesive Stokes profiles, where the different wavelength samples in a particular Stokes profile, come from the same spatial location on the Sun.

### 2.4.8 Radiative transfer equation inversion

To infer the physical quantities from the Stokes maps, a Radiative Transfer Equation (RTE) inversion is performed. Similar to the inversion code used by the HMI vector magnetic field pipeline [][][Hoeksema et al. (2014), Borrero et al. (2011b), a code assuming a Milne-Eddington (ME) atmosphere is used (del Toro Iniesta 2003, Landi Degl’Innocenti

and Landolfi 2004). A ME model assumes that the physical properties of the atmosphere remain constant with geometrical height, while the source function scales linearly with optical depth.

This pipeline uses the CMILOS code written in C, which utilises analytical response functions (Orozco Suárez and Del Toro Iniesta 2007a). This code is the same as that used by the FPGA devices onboard (Cobos Carrascosa et al. 2016) and it works by minimising the difference between the observed and synthetic profiles it produces, iterating the atmosphere’s parameters until convergence of the two profiles is achieved. The CMILOS code has three operating modes:

- RTE with default starting conditions
- RTE with Classical Estimates as starting conditions
- Classical Estimates only

With Classical Estimates (CE) enabled, either in CE only mode, or together with RTE, it estimates the line-of-sight magnetic field and velocity using the centre of gravity method (Semel 1967, Rees and Semel 1979). The transverse component of the magnetic field is estimated using the weak-field approximation (Landi Degl’Innocenti and Landolfi 2004). The CMILOS inversion code produces the following L2 data products: full magnetic vector, Dopplergram and continuum intensity. The azimuth is defined as the counter-clockwise rotation from the positive direction of the detector  $y$  axis. However, the intrinsic  $180^\circ$  ambiguity of the Zeeman effect is not removed at this stage.

## 2.5 Early in-flight data

### 2.5.1 February 2021

We first introduce reduced data from 23 February 2021 17:00 UTC. This data captured the quiet Sun at disk centre, allowing us to characterise the noise level well, given the lack of strong magnetic field signals. The distance of the spacecraft to the Sun was 0.526 AU, the PMP temperature was set to  $50^\circ\text{C}$  and the ISS was active. At this distance, the (two-pixel) spatial resolution is 382 km.

The Stokes filtergrams in Fig. 2.6 display high uniformity and low linear polarimetric signal as expected for a quiet Sun. This demonstrates the high effectiveness of the flat-field correction and additional cross-talk removal. The photospheric magnetic field network appears clearly in the Stokes  $V/I_c$  image. In Stokes  $U/I_c$  the remnants of a polarimetric ghost edge is present in the lower right corner. This ghost is most likely due to a reflection off the HREW (see Sect. 2.4.3). The flat-field correction removes the ghost to a large extent but the edge remains. From analysis of histograms of the four quadrants, the difference of the lower right corner distribution from the others is below the  $10^{-3} \cdot I_c$  noise level. Figure 2.7 displays the derived quantities from these Stokes filtergrams.

As expected by the uniformity of the filtergrams, the physical quantities in Fig. 2.7 display equal uniformity and low magnetic field strengths due to the quiet Sun being void of active regions. The edge of a polarimetric ghost is visible in the lower right corner of the azimuth due to the absence of signal. The continuum intensity map exhibits the

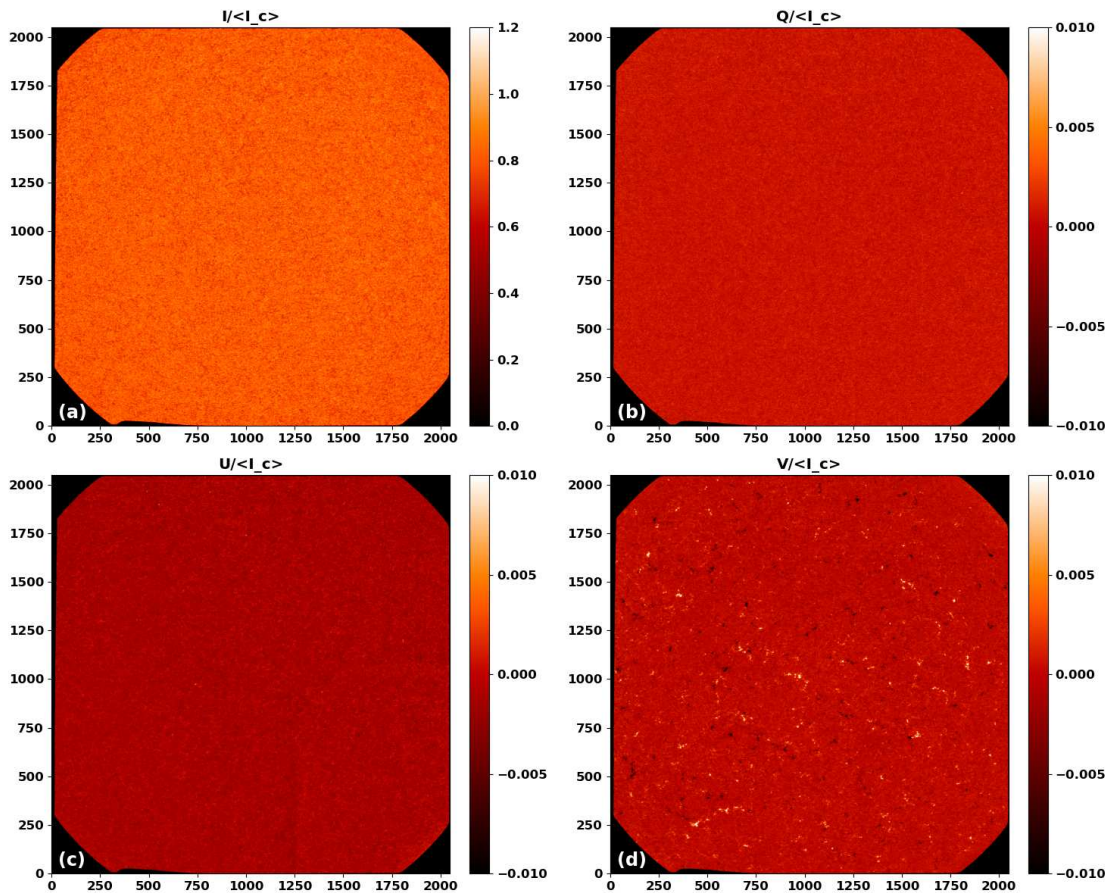


Figure 2.6: Stokes filtergram in the red line wing on 23 February 2021 17:00 UTC: a) Stokes  $I/I_c$ , b) Stokes  $Q/I_c$ , c) Stokes  $U/I_c$ , d) Stokes  $V/I_c$ .

granular structure of the photosphere. The inclination is centred on 90 degrees, and due to the very low linear polarisation signal, the azimuth contains mainly noise.

The Gaussian fit to the Stokes  $V$  histogram in Fig. 2.8 a) indicates that a polarimetric accuracy of  $< 10^{-3} \cdot I_c$  is achieved (Del Toro Iniesta and Martínez Pillet 2012), illustrating the high performance of the HRT instrument. It is also important to note that due to the tight telemetry budget, raw images from SO/PHI are compressed before download. The compression procedure, in this case to 6 bits/pixel (down from 32), increases the noise of the filtergrams: for example, data from the commissioning phase, which was downloaded without compression, had a Stokes noise level of  $8.5 \times 10^{-4}$ . Furthermore, using the same method as Liu et al. (2012), the line-of-sight magnetogram has an estimated noise level of 6.6 G, very similar to the noise level of the 720 second magnetogram images from HMI, but with almost eight times the cadence: 96 seconds.

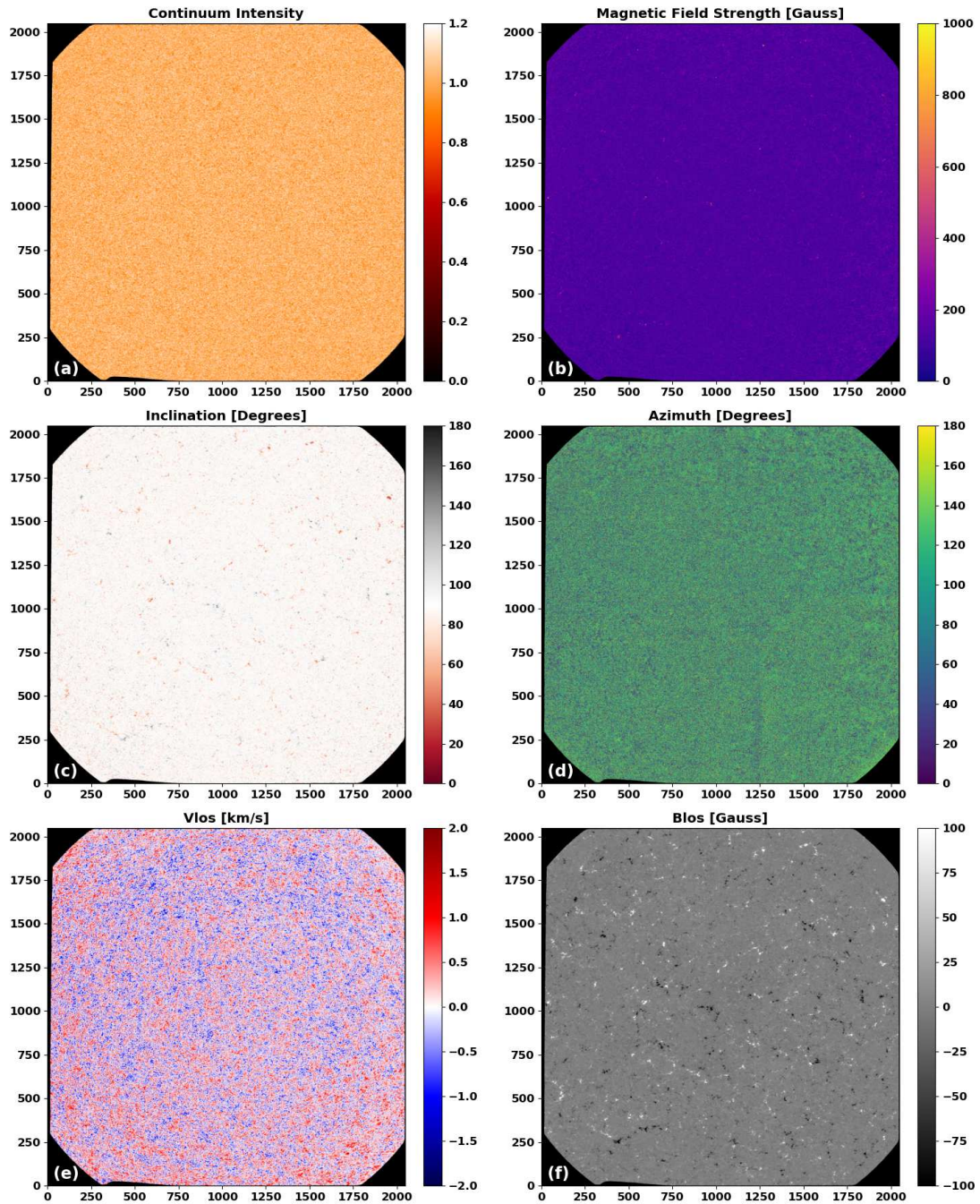


Figure 2.7: Derived physical quantities from data of 23 February 2021 17:00 UTC: a) continuum intensity, b) magnetic field strength, c) inclination relative to line-of-sight, d) azimuth relative to direction of rotation, e) Dopplergram, f) line-of-sight magnetogram. The region outside the field stop is set to black for clarity.

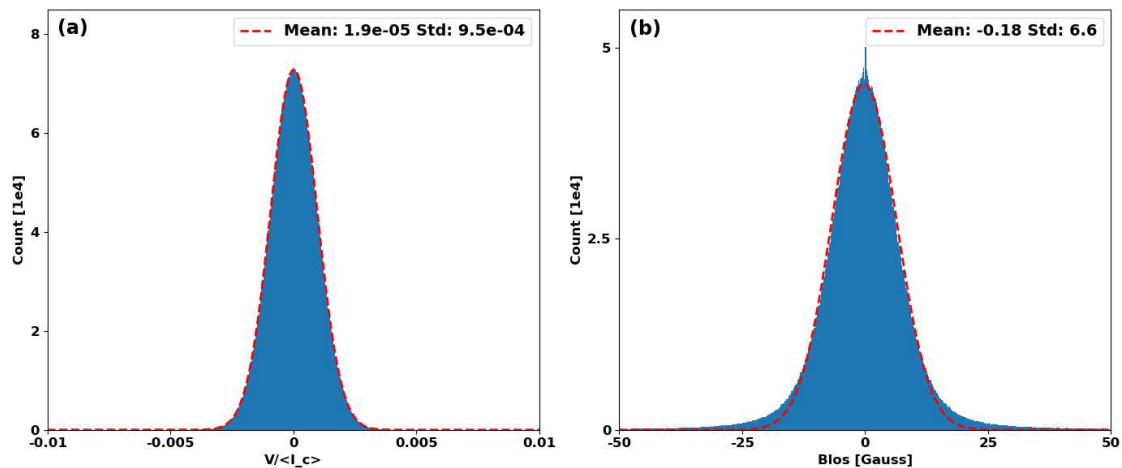


Figure 2.8: Histograms from data on 23 February 2021 1700 UTC: a) Stokes  $V/I_c$  at the continuum wavelength position, with a Gaussian fit (dashed red curve), b) the line-of-sight magnetogram, with a Gaussian fit.

## 2.5.2 November 2021

We present a reduced dataset of a sunspot captured by HRT, taken during the inferior conjunction in November 2021. The spacecraft was flying close to Earth, with a distance to the Sun of 0.858 AU, a PMP temperature set to 40 °C and was pointing to disc centre. At this distance the (two-pixel) spatial resolution is 624 km, and almost half the solar disk is within the FOV. As shown in Fig. 2.9 there are clear signals in Stokes  $Q/I_c$  and  $U/I_c$  that capture the linear polarisation from the sunspot, which highlights the instrument's sensitivity. The 45 degree offset in the signal pattern between Stokes  $Q/I_c$  and  $U/I_c$  is also finely highlighted.

Figure 2.10 displays the physical quantities computed from the Stokes filtergrams plotted in Fig. 2.9. Selecting the umbra region with a continuum upper threshold of 0.6, the mean magnetic field strength in the umbra is 1420 G. This is somewhat low for an umbra and may reflect stray light, or that the large Zeeman splitting within the umbra is not caught that well by the placement of the wavelength points in PHI. The azimuth is of particular interest with a strong signal. The line-of-sight velocity displays the expected redshift on the limb side of the spot, with the corresponding blueshift towards disc centre (Evershed flow, Evershed 1909).

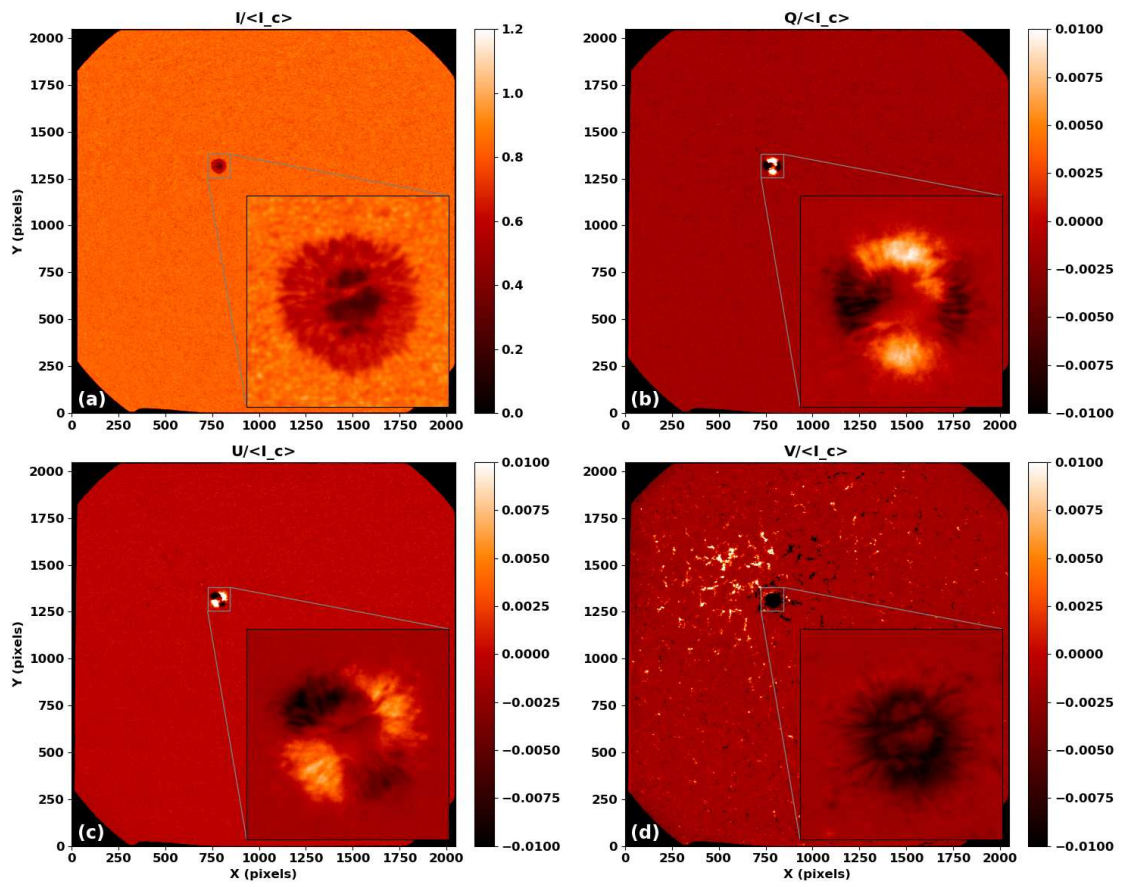


Figure 2.9: Stokes filtergram in the red line wing on 5 November 2021 20:21 UTC: a) Stokes  $I/I_c$  b) Stokes  $Q/I_c$  c) Stokes  $U/I_c$  d) Stokes  $V/I_c$ .

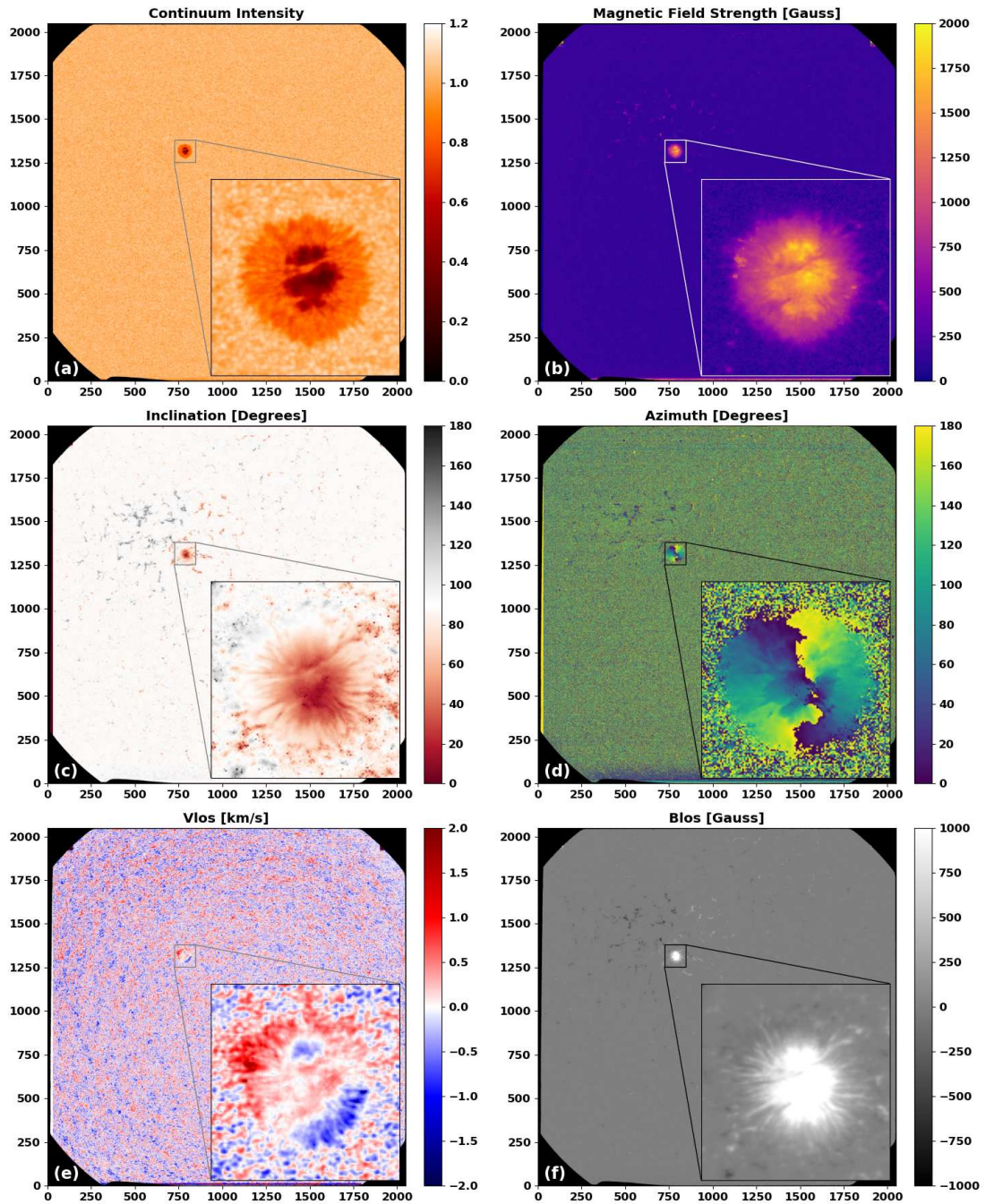


Figure 2.10: Derived physical quantities from data of 5 November 2021 20:21 UTC : a) continuum intensity, b) magnetic field strength, c) inclination relative to line-of-sight, d) azimuth relative to direction of rotation, e) Dopplergram, f) line-of-sight magnetogram. The region outside the field stop is set to black for clarity.

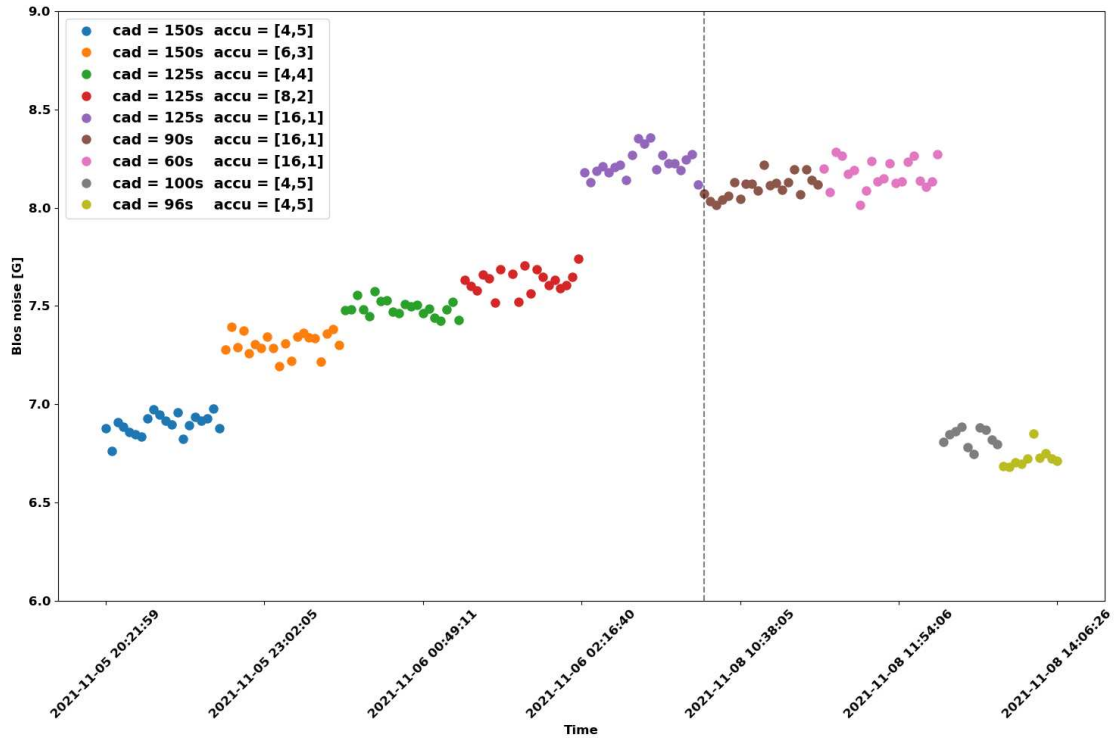


Figure 2.11: Noise from the central region of the magnetogram plotted against time. The different combinations of ‘cad’ (cadence) and ‘accu’ (PMP modulation accumulation scheme, see Sect. 2.3.1) are denoted by their marker colours. The vertical dashed line signifies the change in time from November 6th to November 8th.

### 2.5.3 Magnetogram Noise

Several datasets with different modulation schemes were acquired during a campaign in early November 2021 to test the cadence of the schemes. The noise from the line-of-sight magnetograms of these datasets at different cadences is presented in Fig. 2.11. The total number of frames per image is found from the multiplication of the two numbers in the accumulation scheme. A clear trend is visible: as the accumulation scheme changes from [4, 5] to [16, 1], less frames are being accumulated for each image, and therefore as expected the magnetogram noise increases from 6.8 G to 8.3 G. The last grouping, was the fastest the [4, 5] scheme could be executed by the instrument, with a cadence of 96 seconds. It is also clear that the higher the cycles of the modulation states (the second value in the accumulation scheme), the lower the magnetogram noise. It must also be noted that like the data from February 2021, the compression acts as the main driver of the noise.

## 2.6 Conclusion

An on-ground pipeline has been developed to reduce raw data from the HRT instrument to produce high quality data with a polarimetric accuracy  $10^{-3} \cdot I_c$  and infer physical parameters from the polarised light. The 96 second cadence line-of-sight magnetograms

are shown to have an excellent low level of noise, only 6.6 G, similar to the noise level of the HMI 720 second magnetograms. This was achieved by calibrating the flat-fields to remove unwanted artefacts from the acquisition process by use of unsharp masking. As a result of the analysis presented here, the unsharp masking procedure will be implemented onboard the spacecraft, such that the in-flight data will also produce data of the highest quality. The absence of the ISS has also been taken care by three more steps. Despite the increase in data quality, as shown in Fig. 2.5, noise levels remain slightly higher than in the standard configuration because of the spacecraft jitter. This pipeline will be embedded into a software tool which will automatically process all the SO/PHI science data that will arrive on ground and store them on the appropriate databases.



# 3 Magnetic fields inferred by Solar Orbiter: A comparison between SO/PHI-HRT and SDO/HMI

Sinjan, J. ; Calchetti, D. ; Hirzberger, J. ; Kahil, F. ; Valori, G. ; Solanki, S. K. ; Albert, K. ; Albelo Jorge, N. ; Alvarez-Herrero, A. ; Appourchaux, T. ; Bellot Rubio, L. R. ; Blanco Rodríguez, J. ; Feller, A. ; Gandorfer, A. ; Germerott, D. ; Gizon, L. ; Gómez Cama, J. M. ; Guerrero, L. ; Gutierrez-Marques, P. ; Kolleck, M. ; Korpi-Lagg, A. ; Michalik, H. ; Moreno Vacas, A. ; Orozco Suárez, D. ; Pérez-Grande, I. ; Sanchis Kilders, E. ; Balaguer Jiménez, M. ; Schou, J. ; Schühle, U. ; Staub, J. ; Strecker, H. ; del Toro Iniesta, J. C. ; Volkmer, R. ; Woch, J.

*Astronomy & Astrophysics*, Vol. 673, A31, 2023. DOI:10.1051/00046361/202245830<sup>¶</sup>

## 3.1 Abstract

*Context.* The High Resolution Telescope (HRT) of the Polarimetric and Helioseismic Imager on board the Solar Orbiter spacecraft (SO/PHI) and the Helioseismic and Magnetic Imager (HMI) on board the Solar Dynamics Observatory (SDO) both infer the photospheric magnetic field from polarised light images. SO/PHI is the first magnetograph to move out of the Sun–Earth line and will provide unprecedented access to the Sun’s poles. This provides excellent opportunities for new research wherein the magnetic field maps from both instruments are used simultaneously.

*Aims.* We aim to compare the magnetic field maps from these two instruments and discuss any possible differences between them.

*Methods.* We used data from both instruments obtained during Solar Orbiter’s inferior conjunction on 7 March 2022. The HRT data were additionally treated for geometric distortion and degraded to the same resolution as HMI. The HMI data were re-projected to correct for the 3° separation between the two observatories.

*Results.* SO/PHI-HRT and HMI produce remarkably similar line-of-sight magnetograms,

---

<sup>¶</sup>The contents of this chapter are identical to the printed version of Sinjan, J., Calchetti, D., Hirzberger, J., Kahil, F., Valori, G., Solanki, S. K., Albert, K., Albelo Jorge, N., Alvarez-Herrero, A., Appourchaux, T., Bellot Rubio, L. R. et al., 2023, Magnetic fields inferred by Solar Orbiter: A comparison between SO/PHI-HRT and SDO/HMI in *Astronomy & Astrophysics*, vol. 673, A31, with a CC-BY 4.0 licence. I, Jonas Sinjan, completed all the underlying work, wrote the first draft text and created the figures for all sections of this publication. The co-authors supported the development, engineering and operations of SO/PHI and provided comments on the draft text.

with a slope coefficient of 0.97, an offset below 1 G, and a Pearson correlation coefficient of 0.97. However, SO/PHI-HRT infers weaker line-of-sight fields for the strongest fields. As for the vector magnetic field, SO/PHI-HRT was compared to both the 720-second and 90-second HMI vector magnetic field: SO/PHI-HRT has a closer alignment with the 90-second HMI vector. In the weak signal regime ( $< 600$  G), SO/PHI-HRT measures stronger and more horizontal fields than HMI, very likely due to the greater noise in the SO/PHI-HRT data. In the strong field regime ( $\geq 600$  G), HRT infers lower field strengths but with similar inclinations (a slope of 0.92) and azimuths (a slope of 1.02). The slope values are from the comparison with the HMI 90-second vector. Possible reasons for the differences found between SO/PHI-HRT and HMI magnetic field parameters are discussed.

## 3.2 Introduction

The Solar Orbiter (see Müller et al. 2013, 2020) spacecraft was launched on 10 February 2020 and entered its Nominal Mission Phase in November 2021. The Polarimetric and Helioseismic Imager on the Solar Orbiter mission (SO/PHI; see Solanki et al. 2020) infers the photospheric magnetic field and line-of-sight (LoS) velocity from images of polarised light. It does this by sampling the Fe I 6173 Å absorption line at five wavelength positions and an additional point in the nearby continuum. Differential imaging is performed to acquire the Stokes ( $I, Q, U, V$ ) vector. SO/PHI has two telescopes: the High Resolution Telescope (SO/PHI-HRT; Gandorfer et al. 2018) and the Full Disc Telescope. In this paper only data from SO/PHI-HRT are discussed.

Solar Orbiter has a highly elliptic orbit with a perihelion as small as 0.28 au on some orbits. SO/PHI is the first magnetograph to move out of the Sun–Earth line. From 2025 on, with the help of Venus gravity assist manoeuvres, Solar Orbiter will reach heli-latitudes of  $33^\circ$ .

The Solar Dynamics Observatory (SDO; see Pesnell et al. 2012) was launched on 11 February 2010 and orbits the Earth in a circular geosynchronous orbit with a  $28^\circ$  inclination. Like Solar Orbiter, SDO carries a magnetograph: the Helioseismic Magnetic Imager (HMI; Scherrer et al. 2012, Schou et al. 2012). HMI has been in regular science operations since 1 May 2010. Similar to SO/PHI, it samples the 6173 Å Fe I line at six points but at somewhat different wavelength positions.

The relevant technical details of SO/PHI-HRT and HMI are shown in Table 3.1. As can be seen, SO/PHI-HRT and HMI share some technical specifications: the same working wavelength, aperture diameter, and plate scale. It is important to know that, unlike SO/PHI, HMI has two identical cameras. One is dedicated to the LoS observables – the LoS magnetic field ( $B_{\text{LOS}}$ ) and the LoS velocity – and is referred to as the ‘front camera’. The second camera, known as the ‘side camera’, is used together with the front camera to capture the full Stokes vector, in order to retrieve the vector magnetic field.

With SO/PHI and HMI now operating simultaneously, they provide excellent opportunities for new research that combines data from both instruments. For example, stereoscopy is now possible, allowing for simultaneous observations of the same feature on the solar surface from two different viewpoints. This can be used to investigate the

Table 3.1: SO/PHI-HRT and SDO/HMI instrument specifications.

Specification	SO/PHI-HRT	SDO/HMI
Working wavelength	6173 Å	6173 Å
Wavelength positions	-140, -70, 0, 70, 140, + or -300 mÅ	-172, -103, 34, 34, 103, 172 mÅ
Field of view	0.28° × 0.28°	0.57° × 0.57°
Aperture diameter	140 mm	140 mm
Spectral profile width	106 mÅ	76 mÅ
Detector size	2048 × 2048 pixels	4096 × 4096 pixels
Plate scale	0.5''	0.5''
Spatial resolution	203 km (0.28 au) - 725 km (1.0 au)	725 km

Wilson depression of sunspots (Romero Avila et al. 2024) and test disambiguation techniques for the magnetic field azimuth (Valori et al. 2022, 2023). These and many other applications build on the premise that the two instruments provide very similar measurements of the magnetic vector. Here we test this assumption and compare the magnetic fields inferred by SO/PHI-HRT and HMI and try to understand their similarities and differences.

In Sect. 3.3 the data from both instruments used in this study and their properties are presented. In Sect. 3.4 the detailed method for this comparison is given. The results of the comparison of the magnetic field data products from SO/PHI-HRT and HMI are discussed in Sect. 3.5, and in Sect. 3.6 we outline the conclusions reached from this work.

### 3.3 Data

The data used in this study are from 7 March 2022 (see Table 4.1) and thus from around Solar Orbiter’s inferior conjunction – that is, when Solar Orbiter was on the Sun–Earth line – which took place at 09:01:56 UTC (Coordinated Universal Time) on 7 March 2022. Solar Orbiter’s elevation from the ecliptic plane was 2.949° at inferior conjunction, and the effective angular separation between the two spacecraft during the observation period ranged from 3.006° to 3.024°. During this time, Solar Orbiter was at a distance to the Sun of between 0.493 au and 0.501 au. On the photosphere, the nominal spatial resolution of SO/PHI-HRT at this distance is 363 km. In the common field of view (FoV) was a sunspot with negative polarity located at a heliocentric angle of  $\mu = \cos \theta = 0.87$  as seen by SO/PHI-HRT.

#### 3.3.1 SO/PHI-HRT magnetic field

The SO/PHI-HRT data were collected to support a nanoflare and active region Solar Orbiter Observing Plan (see Zouganelis et al. 2020). The raw data from this observation campaign were downlinked to Earth and processed using the on-ground data reduction and calibration pipeline (Sinjan et al. 2022). In addition, the data were processed to remove residual wavefront errors, which originate mostly from the telescope’s entrance window. This was achieved using a point spread function (PSF) determined from phase

Table 3.2: Observation details of used SO/PHI-HRT and HMI data.

		SO/PHI-HRT			SDO/HMI
Start time		2022-03-07 00:00:09 UTC			2022-03-07 00:00:00 TAI
End time		2022-03-07 01:06:09 UTC			2022-03-07 01:12:00 TAI
Distance		0.493 – 0.501 au			0.992 au
ISS mode		Off			On
Processing		Ground			Ground
RTE mode		C-MILOS: CE+RTE			VFISV
		Vector	Line of sight		Vector
Cadence		60 s	45 s	720 s	90 s 720 s
Number of datasets		56	56	7	38 7

diversity analysis (Paxman et al. 1992). Additionally, in the same processing step as the PSF deconvolution, a convolution with the instrument’s theoretical Airy disc was performed. This produced data without optical aberrations, with increased contrast, and limited the noise that would otherwise be added by the deconvolution procedure. For further information regarding phase diversity analysis and the SO/PHI-HRT PSF, we refer the reader to Kahil et al. (2022, 2023). To determine the magnetic field vector, the radiative transfer equation (RTE) was inverted with C-MILOS (Orozco Suárez and Del Toro Iniesta 2007a) in the full vector mode, which assumes a Milne-Eddington (ME) atmosphere and uses classical estimates (CE) as the initial conditions for the inversion (Semel 1967, Rees and Semel 1979, Landi Degl’Innocenti and Landolfi 2004). For operational reasons, SO/PHI-HRT’s Image Stabilisation System (ISS) was switched off. The SO/PHI-HRT LoS magnetograms used in this study were generated from the vector magnetic field obtained from the RTE inversion:  $B_{\text{LOS}} = B \cos \gamma$ , where  $B_{\text{LOS}}$  is the LoS component of the magnetic field,  $B$  is the field strength, and  $\gamma$  is the angle of the field to the LOS.

The data from this campaign were recorded with a 60-second cadence. As shown in Sinjan et al. (2022), this mode results in quiet-Sun magnetograms with a noise of 8.3 G (with ISS on). Future investigations, using data planned to be gathered during Solar Orbiter’s next inferior conjunction in March 2023, will attempt to quantify the impact of non-ISS operation on the comparison.

### 3.3.2 HMI magnetic field

HMI treats its LoS and vector data products separately, each having two options for observing cadence. For this comparison study, all four possible data products were compared with SO/PHI-HRT (see Table 4.1). The vector data products were generated from the HMI vector pipeline (Hoeksema et al. 2014), while the LoS products were generated with an algorithm similar to that used by the Michelson Doppler Imager (MDI) on board the Solar & Heliospheric Observatory, hereafter referred to as the MDI-like algorithm (Couvidat et al. 2012a). The HMI LoS versus HMI vector has been compared by Hoeksema et al. (2014), who show that the MDI-like algorithm underestimates the field

strength in the strong field regime ( $|B_{\text{LOS}}| > 600 \text{ G}$ ) compared to the inversion result. The HMI 45-second and 720-second LoS magnetograms have a noise level in the quiet Sun, near disc centre, of 7–9 G and 3–4 G, respectively (Couvidat et al. 2016, Liu et al. 2012).

The 45-second magnetograms are produced every 45 seconds from an interpolation of Stokes  $I + V$  and Stokes  $I - V$  filtergrams from a 270-second interval (Liu et al. 2012, Couvidat et al. 2016). Since 13 April 2016, the full Stokes vector has been captured at a 90-second cadence and inverted to create the vector magnetic field data product. This cadence is achieved by combining images from both cameras (Liu et al. 2016). To produce the 720-second vector data product, a weighted temporal average is made every 720 seconds, combining 90-second Stokes vector maps collected over a period of more than 20 minutes and inverted using the very fast inversion of the Stokes vector (VFISV) ME code (Hoeksema et al. 2014, Borrero et al. 2011b). In Sect. 3.4 we describe the method by which we take the difference in interval and light travel time into account to ensure co-temporal observations are compared.

### 3.4 Method

We compared the magnetic field inferred by SO/PHI-HRT and HMI on a pixel-to-pixel basis. The HMI data were corrected for geometric distortion across the camera (Hoeksema et al. 2014), and the SO/PHI-HRT data were corrected using a preliminary distortion model, derived from calibration data pre-launch. The method we now describe has been applied to each comparison of the individual data products. We provide here an example for one pair of LoS magnetograms: First a SO/PHI-HRT 60-second magnetogram was selected and the closest HMI 45-second magnetogram in time was found (see the top panels in Fig. 3.1). This was done by comparing the average time of the observations, taking into account the different distances of Solar Orbiter and SDO from the Sun, and hence the different light travel times, as well as the difference between TAI (International Atomic Time) and UTC time. Secondly, the sub-region of the HMI FoV common to both telescopes, outlined in yellow in Fig. 3.1, was re-projected using the DeForest (2004) algorithm onto the SO/PHI-HRT detector frame of reference using the World Coordinate System (WCS) information (Thompson 2006).

Next, the SO/PHI-HRT data were resampled using linear interpolation to match the factor of two lower spatial resolution of the HMI data (SO/PHI-HRT was half the distance to the Sun at the time of observation). Applying boxcar binning or cubic interpolation makes no significant difference to the results of the comparison. As both SO/PHI-HRT and HMI have the same aperture diameter, their PSFs are similar. However, by resampling SO/PHI-HRT we change the effective PSF. The impact of this effect is left for future studies. Residual rotation and translation perpendicular to the normal of the SO/PHI-HRT image plane were found using a log-polar transform (cf. e.g. Sarvaiya et al. 2009) and corrected. The result of such corrections is shown in the bottom panels of Fig. 3.1. These corrections are due to inaccuracies in the WCS information. This process was repeated for each SO/PHI-HRT magnetogram.

Finally, the maps were cropped by 100 pixels at each side before the comparison was made, as outlined in orange in the lower panels of Fig. 3.1. This is because of

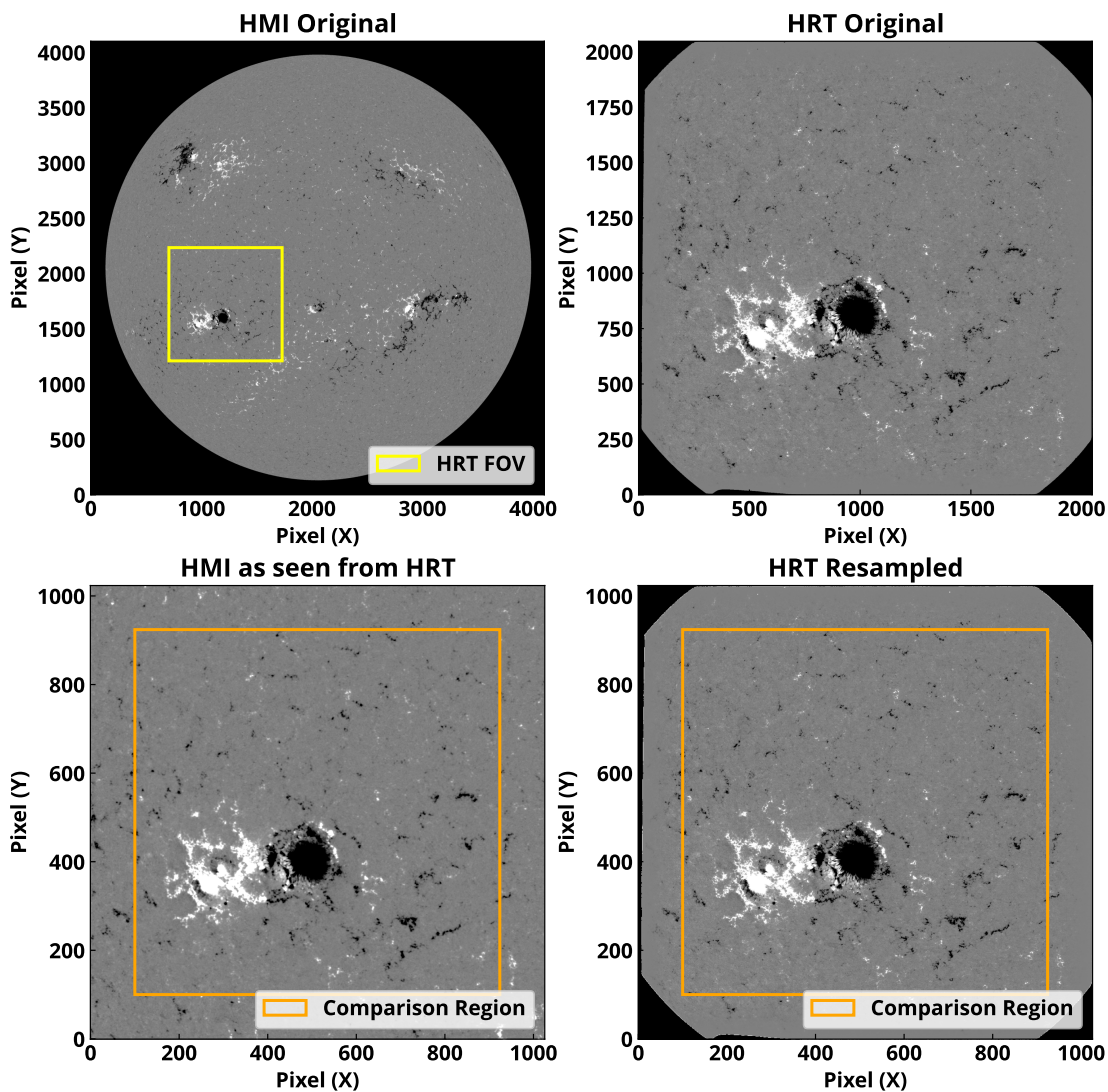


Figure 3.1: Magnetograms from HMI and SO/PHI-HRT on 7 March 2022. Top left: HMI 45-second LoS magnetogram at 00:01:30 TAI, with the SO/PHI-HRT FoV shown in yellow. The pixels outside the solar disc are set to black for clarity. Top right: SO/PHI-HRT 60-second magnetogram at 00:00:09 UTC. The pixels outside the field stop are set to black for clarity. Bottom left: Sub-region of the HMI magnetogram from the top-left panel, which has been re-projected to the SO/PHI-HRT frame of reference. Bottom right: SO/PHI-HRT magnetogram resampled to HMI resolution. The orange square outlines the regions used for the comparison. All magnetograms are saturated at  $\pm 200$  G.

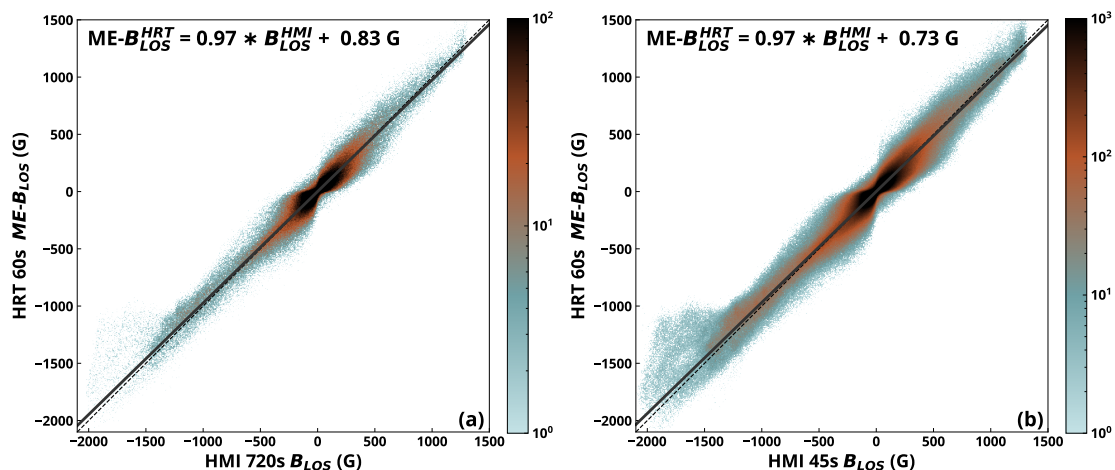


Figure 3.2: Scatter plot comparing pairs of SO/PHI-HRT 60-second  $ME-B_{LOS}$  and HMI  $B_{LOS}$ . The log density of the pixels is shown and saturated at 100 (a) and 1000 (b) pixels per plotted point for clarity. The averaged linear fit (of HMI vs SO/PHI-HRT and SO/PHI-HRT vs HMI) is shown with the solid grey line, and a one-to-one correspondence is indicated by the dashed black line. Panel (a): Seven pairs with HMI 720-second magnetograms. Panel (b): 56 pairs with HMI 45-second magnetograms. See the main text for a more detailed description.

the SO/PHI-HRT field stop, visible as the black region in Fig. 3.1, and because of the processing step to correct for residual wavefront errors. Within this procedure the image is apodised before the Fourier transform to ensure periodic boundaries, and the first 100 pixels at each side were affected. These regions therefore had to be excluded from the comparison with HMI.

For comparison with the HMI 720-second data products, a single SO/PHI-HRT dataset, the one closest to the average time of the HMI 720-second dataset, was used. This comparison was performed for the LoS magnetic field component,  $B_{LOS}$ , the magnetic field strength,  $|\mathbf{B}|$ , the inclination,  $\gamma$ , and the azimuth,  $\phi$ . Extra treatment was taken for the azimuth comparison: both HMI and SO/PHI-HRT define the azimuth anti-clockwise from the positive direction of the y-axis (Sinjan et al. 2022). After the re-projection of HMI, care was taken to ensure that both datasets used the same definition of the azimuth by taking the roll angle of each spacecraft into account.

## 3.5 Comparison of SO/PHI-HRT and HMI magnetic field observations

### 3.5.1 Comparison of SO/PHI-HRT and HMI LoS magnetograms

We stress here for clarity that, when discussing the LoS magnetograms from HMI, we refer to the LoS magnetic field derived using the MDI-like algorithm, referred to as  $B_{LOS}$ . However, the magnetograms from SO/PHI-HRT presented here are the LoS component of the full vector magnetic field (determined by RTE inversion): we refer to this as  $ME-B_{LOS}$ .

The scatter plot comparing the SO/PHI-HRT 60-second and HMI 720-second magnetograms is shown in Fig. 3.2a, where the logarithmic density of the points is indicated by the colour. This figure displays seven pairs of magnetograms; each of the SO/PHI-HRT 60-second magnetograms is recorded in the middle of the interval of time over which the HMI 720-second magnetogram that it is compared with is recorded. The solid black line is a linear fit to the distribution, which is the average of two linear fits, one of HMI versus SO/PHI-HRT and the other of SO/PHI-HRT versus HMI. This averaging removes statistical bias. As indicated by the fit, there is an excellent agreement between the two telescopes, with a slope value of 0.97 and an offset of 0.83 G. This offset could be an artefact of there being more very strong fields with negative polarity than with positive. The offset of the weak fields inferred by SO/PHI-HRT can be determined by histogram analysis: Sinjan et al. (2022) demonstrate that the SO/PHI-HRT  $B_{LOS}$  distribution in the quiet Sun is centred near zero with an offset of  $-0.18$  G. The Pearson correlation coefficient is 0.97. The linear fit, absolute error on the slope and offset, and Pearson correlation coefficient (cc) are shown in Table 3.3 for all compared quantities presented in this paper. In the case of Fig. 3.2, the errors on the slope and offset are negligible.

However, a difference is present for the strongest fields. We selected pixels where HMI 720-second  $B_{LOS} < -1300$  G, the point at which a large divergence between SO/PHI-HRT and HMI appears. The mean difference between them is  $+149 \pm 2$  G relative to the (negative) HMI values, which corresponds to 9% weaker LoS fields relative to HMI. The error here denotes the standard error in the mean; the scatter ( $1\sigma$ ) of the distribution of absolute differences is 197 G. The pixel selection threshold (HMI 720-second  $B_{LOS} < -1300$  G) corresponds to pixels only in the leading sunspot in the FoV, where 81 % are in the umbra and the remaining 19 % in the penumbra. The umbra and penumbra classification was determined using  $I_c < 0.55$  and  $0.55I_c < 0.95$  thresholds on the SO/PHI-HRT continuum intensity,  $I_c$ ; these thresholds are the same as those used in Sainz Dalda (2017), where the magnetic field between HMI and Hinode/SP is compared. It must also be noted that the distribution in Fig. 3.2 is not symmetric between fields of opposite polarity. This is because no strong fields above 1350 G were observed in HMI in the common FoV, while SO/PHI-HRT infers fields of up to 1500 G. Under similar conditions, we expect the comparison between the two telescopes in the positive strong field regime to be similar to that observed in the negative strong field regime, with SO/PHI-HRT measuring lower LoS field components compared to HMI.

The comparison with HMI 45-second magnetograms (Fig. 3.2b), where 56 pairs of data were compared, reveals very similar results. This was expected as the 45-second and 720-second HMI magnetograms are well inter-calibrated (Liu et al. 2012). For pixels where the HMI 45-second  $B_{LOS} < -1300$  G, there is a similar mean difference of  $+155.5 \pm 0.9$  G relative to the (negative) HMI values, which again corresponds to 9% weaker LoS magnetic fields inferred by SO/PHI-HRT in this regime.

In both Fig. 3.2a and b, all pixels are plotted, including those with signal below the noise. There is an hourglass shape around the origin present in both panels. This could be due to a mismatch in the alignment of the sets of magnetograms. As described in Sect. 3.4, we applied only a preliminary model to correct for geometric distortion in SO/PHI-HRT, which could explain inaccuracies in the alignment.

There are several effects that could explain the difference between SO/PHI-HRT and HMI for the strongest fields. Firstly, the two instruments use different methods to infer the LoS magnetic field: HMI uses the MDI-like formula, while SO/PHI-HRT uses a radiative transfer code. Additionally, the two instruments sample the Fe I line at different positions, and SO/PHI-HRT observes farther out in the continuum ( $\pm 300 \text{ m\AA}$  from the line core vs  $\pm 172 \text{ m\AA}$  for HMI). For the strongest fields, the very large Zeeman splitting results in the two instruments capturing different information from the true Stokes signal, which is then interpreted by the inversion routines differently. A detailed investigation of these effects is beyond the scope of this paper. Furthermore, the spectral profile width is different: SO/PHI-HRT has a full width half maximum (FWHM) of  $106 \text{ m\AA}$ , while the FWHM of HMI is  $76 \text{ m\AA}$ . There could also be a contribution from stray light, in particular for the pixels in the umbra, as neither HMI nor SO/PHI-HRT are corrected for stray light in their standard data pipelines.

Finally, it is known that HMI suffers from a 24-hour periodicity (Liu et al. 2012, Hoeksema et al. 2014, Couvidat et al. 2016) in its magnetic field observables due to the SDO orbit. The velocity relative to the Sun oscillates by  $\pm 3.5 \text{ km/s}$  on a 24-hour period, with further variation of hundreds of metres per second due to Earth's orbit. The SDO solar radial velocity for the data considered in this study started at  $3.249 \text{ km/s}$  and ended at  $3.291 \text{ m/s}$ . Couvidat et al. (2016) show that the  $B_{\text{LOS}}$ , calculated using the MDI-like algorithm, in the umbra depends quadratically on the magnitude of the velocity. A residual of between  $+50 \text{ G}$  and  $+100 \text{ G}$  was present when SDO had a radial velocity near  $\pm 3 \text{ km/s}$ . This residual is the value once the long-term variations ( $\geq 2 \text{ day}$ ) are removed. It explains approximately half of the observed difference in the strong signal regime. It is plausible, although not certain, that, when combined with the effects from the different wavelength sampling, different inversion codes, and stray light, it explains the observed discrepancy.

### 3.5.2 Comparison of SO/PHI-HRT and HMI vector magnetic fields

Here we compare the SO/PHI-HRT and HMI vector magnetic fields, both inferred by RTE inversions of the Stokes vector albeit using different inversion codes. We would like to highlight the  $3^\circ$  angular separation between SO/PHI-HRT and HMI, mentioned in Sect. 3.3. This has no impact on  $|\mathbf{B}|$ , and from a simple rotation test on SO/PHI-HRT data, we estimate that it does not significantly impact the magnetic field inclination or azimuth, except for producing an offset of a few degrees in the azimuth.

First we compared the magnetic field strengths,  $|\mathbf{B}|$ , as shown in the top row of Fig. 3.3. Both SO/PHI-HRT and HMI assume a magnetic filling factor of unity for the RTE inversion, so the field strength is averaged over the pixel. Consequently, we do not distinguish between magnetic field strength and magnetic flux density, as is sometimes done in the literature. In Fig. 3.3a the comparison between the SO/PHI-HRT and HMI 720-second  $|\mathbf{B}|$  is depicted, while in Fig. 3.3b the comparison with the HMI 90-second  $|\mathbf{B}|$  is shown. The slope is 0.84 and 0.89 in Fig. 3.3a and b, respectively. The higher slope value for the 90-second comparison is because the variance is more similar to that of the SO/PHI-HRT data than for the HMI 720-second data. The magnetic field strengths of the two instruments have a correlation coefficient of 0.85 and 0.84 for the 720-second and 90-second  $|\mathbf{B}|^{\text{HMI}}$ , respectively.

### 3 Magnetic fields inferred by Solar Orbiter: A comparison between SO/PHI-HRT and SDO/HMI

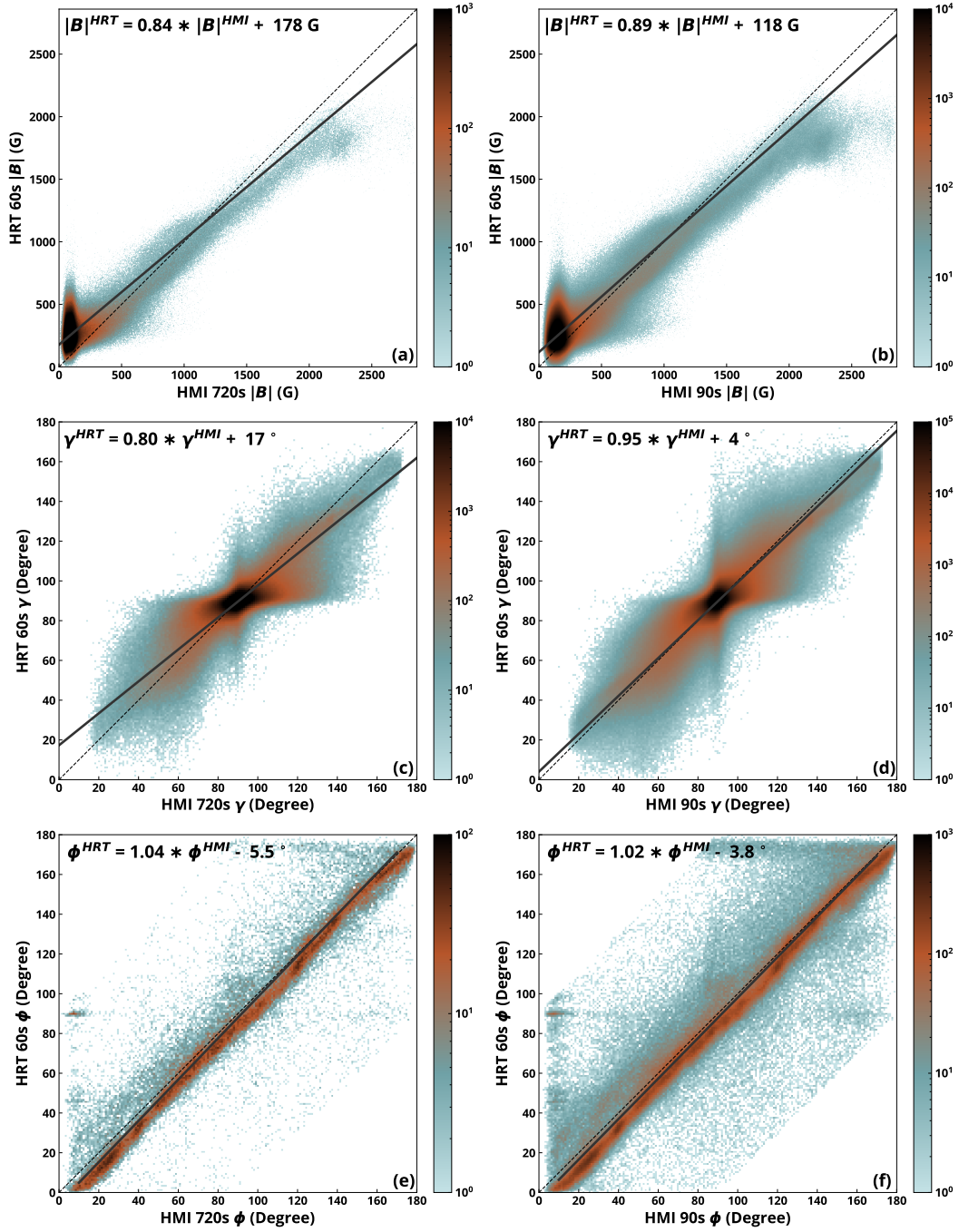


Figure 3.3: Scatter plots comparing SO/PHI-HRT and HMI vector magnetic field maps. The first column compares inversion results from seven pairs of SO/PHI-HRT 60-second and HMI 720-second datasets, while the second column does the same for 38 pairs of SO/PHI-HRT 60-second and HMI 90-second datasets. The log density of the pixels is given by the colour scale and is saturated for clarity. The averaged linear fit and  $y = x$  are given by the solid grey and dashed black lines, respectively. Panels (a) and (b): Magnetic field strength. Panels (c) and (d): Magnetic field inclination (relative to the LoS). Panels (e) and (f): Magnetic field azimuth. Pixels where  $|\phi_{HMI} - \phi_{HRT}| > 90^\circ$  and  $|B|_{HRT} < 600 \text{ G}$  are omitted and not included in the fit.

We observe here that in the weaker field regime, SO/PHI-HRT infers stronger fields. Following Liu et al. (2012), we arbitrarily used a boundary value of 600 G to define the weak signal regime. In this regime there is a dense distribution of pixels, seen in both Fig. 3.3a and b, which we refer to as the ‘hot zone’, that portrays a discrepancy between the two instruments. The offset is mainly due to this hot zone, with an offset of 178 G in Fig. 3.3a and a lower offset of 118 G in Fig. 3.3b. The difference in the offset perhaps reflects the noise difference between the 90-second and 720-second  $|\mathbf{B}|^{HMI}$ . The hot zone in Fig. 3.3b has a larger extent for HMI compared to that in Fig. 3.3a, which may be due to the difference in noise level. Borrero and Kobel (2011) have demonstrated that Stokes profiles with higher noise levels, when inverted, result in stronger but more inclined fields. We note the more horizontal dense field central patches in Fig. 3.3c, Fig. 3d, and Fig. 3.4a. The higher noise level in SO/PHI-HRT compared to HMI is due to the ISS non-operation and, crucially, the longer averaging time within the HMI data. Furthermore, the deconvolution of part of the PSF also increased the noise of the SO/PHI-HRT data by 20% (Kahil et al. 2023). Therefore, the noise levels of the original Stokes vector in SO/PHI-HRT are  $1.8 \times 10^{-3}$ ,  $2.2 \times 10^{-3}$ , and  $1.8 \times 10^{-3}$  for  $Q/I_c$ ,  $U/I_c$ , and  $V/I_c$ , respectively, where  $I_c$  denotes Stokes  $I$  in the continuum. In comparison, the noise in the HMI 720-second Stokes vector is  $9 \times 10^{-4}$  for  $Q/I_c$ ,  $U/I_c$ , and  $V/I_c$  (Couvidat et al. 2016). The noise in the 90-second Stokes vector, however, has not been quantified in the literature because this is a non-standard data product.

Now we turn to the strong signal regime in Fig. 3.3a and b. At approximately  $|\mathbf{B}| > 1300$  G for both HMI and SO/PHI-HRT, the distribution starts diverging from the  $y = x$  line. For pixels where the fields in HMI are stronger than this value, SO/PHI-HRT infers a lower field strength. The field strength threshold of 1300 G in HMI and SO/PHI-HRT corresponds to pixels where 38.1 % are in the umbra, 61.4 % are in the penumbra, and 0.5 % lie elsewhere. For fields stronger than 1300 G in SO/PHI-HRT or HMI, the mean difference between them was  $-247 \pm 1$  G and  $-246.8 \pm 0.4$  G relative to the HMI for the HMI 720-second and 90-second comparisons, respectively ( $\approx 13\%$  smaller relative to the HMI values in both cases). The error on the mean is the standard error. The scatter ( $1\sigma$ ) of the distribution of the differences is roughly 180 G in both cases, highlighting the large width of these distributions. While we cannot directly compare these mean differences to those presented in Sect. 3.5.1, because the strong magnetic field lines are not all along the LoS and we consider more pixels in the penumbra, we can still qualitatively deduce that we observe a larger separation between HMI and SO/PHI-HRT for the magnetic field strength. Important to note is that in Fig. 3.2 we compare the  $ME_{LOS}^{HRT}$ , which was derived from the full vector, while the  $B_{LOS}^{HMI}$  in Fig. 3.2 was calculated using the MDI-like formula. In Sect. 3.5.3 the LoS components derived from the full vectors are compared.

The inclination of the magnetic vector,  $\gamma$ , relative to the LoS, as deduced from the two instruments, is compared in the second row of Fig. 3.3. The slope is 0.80 and 0.95 for the HMI 720-second and 90-second comparisons, respectively. The correlation coefficient between SO/PHI-HRT and the HMI 720-second and 90-second magnetic field inclination is 0.81 and 0.85, respectively. It is clear that both instruments agree on the polarity of the magnetic field relatively well (there is a dearth of points in the upper-left and lower-right quadrants of Fig. 3.3c and d). We also note here that HMI has a somewhat

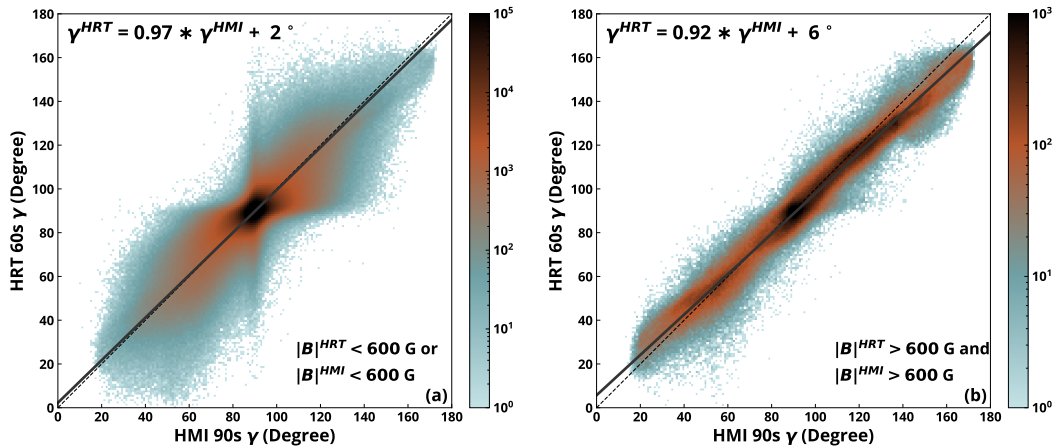


Figure 3.4: Scatter plots comparing SO/PHI-HRT 60-second and HMI 90-second magnetic field inclination. Panel (a): Pixels where  $|\mathbf{B}|_{\text{HRT}} < 600 \text{ G}$  or  $|\mathbf{B}|_{\text{HMI}} < 600 \text{ G}$ . Panel (b): Pixels where  $|\mathbf{B}|_{\text{HRT}} > 600 \text{ G}$  and  $|\mathbf{B}|_{\text{HMI}} > 600 \text{ G}$ . The log density of the pixels is shown and is saturated for clarity. The averaged linear fit and  $y = x$  are shown with the solid grey and dashed black line, respectively.

stronger tendency to infer inclinations close to  $90^\circ$  (the vertical streak at  $90^\circ$  is stronger than the horizontal one). The biggest difference between the inclinations inferred by the two instruments is, however, that SO/PHI-HRT data result in somewhat more horizontal fields (the slope of the solid black lines in Fig. 3.3c and d is less than unity). There is a closer agreement in Fig. 3.3d, with a slope of 0.95, as the variance in the HMI 90-second data is closer to the SO/PHI-HRT variance. The offsets shown in both Fig. 3.3c and d are not relevant here as the point of symmetry lies at  $(90^\circ, 90^\circ)$ . The averaged linear fit crosses  $(90^\circ, 90^\circ)$  with an offset of less than half a degree in both Fig. 3.3c and d. From the simple rotation test on SO/PHI-HRT data mentioned earlier, the  $3^\circ$  angular separation between SO/PHI-HRT and HMI could introduce an offset of  $< 1^\circ$ . Furthermore, a small part of the scatter – the distance of the points from the line of best fit – is likely due to the  $3^\circ$  difference in view direction.

In Fig. 3.4 we compare the inclination for the weak and strong field cases. In Fig. 3.4a pixels are shown where  $|\mathbf{B}|_{\text{HRT}} < 600 \text{ G}$  or  $|\mathbf{B}|_{\text{HMI}} < 600 \text{ G}$ , while in Fig. 3.4b pixels are shown where  $|\mathbf{B}|_{\text{HRT}} > 600 \text{ G}$  and  $|\mathbf{B}|_{\text{HMI}} > 600 \text{ G}$ . In Fig. 3.4b the distribution of the points is much closer to the line of best fit, with a correlation coefficient of 0.98, compared to a correlation coefficient of 0.80 in Fig. 3.4a. The slope in Fig. 3.4b, however, is slightly lower than that in Fig. 3.4a.

The comparison of the azimuth,  $\phi$ , is shown in the bottom row of Fig. 3.3. For this comparison, only pixels from and around the leading sunspot in the FoV, with  $B_{\text{HRT}} > 600 \text{ G}$ , were selected. Furthermore, for the linear fit, pixels where  $|\phi_{\text{HMI}} - \phi_{\text{HRT}}| > 90^\circ$  were not considered as they are affected by the intrinsic  $180^\circ$  ambiguity of the azimuth. Finally, the regions near  $0^\circ$  and  $180^\circ$  were excluded from the linear fits to avoid an artificial shift, as the end points were not periodic. There are strong correlation coefficients of 0.95 and 0.94 (HMI 720-second and 90-second comparisons, respectively). One reason why there is a strong correlation is that the HMI transverse magnetic field does not suffer from the

Table 3.3: Quantities compared, their linear fit, absolute errors on the slope and offset, and Pearson correlation coefficient (cc).

Quantities compared	Linear fit	Slope error	Offset error	Pearson cc
$ME-B_{LOS}^{HRT}$ 60 s vs $B_{LOS}^{HMI}$ 720 s	$ME-B_{LOS}^{HRT} = 0.97 * B_{LOS}^{HMI} + 0.83$ G	$9 \times 10^{-5}$	0.01	0.97
$ME-B_{LOS}^{HRT}$ 60 s vs $B_{LOS}^{HMI}$ 45 s	$ME-B_{LOS}^{HRT} = 0.97 * B_{LOS}^{HMI} + 0.73$ G	$3 \times 10^{-5}$	0.006	0.97
$ \mathbf{B} ^{HRT}$ 60 s vs $ \mathbf{B} ^{HMI}$ 720 s	$ \mathbf{B} ^{HRT} = 0.84 *  \mathbf{B} ^{HMI} + 178$ G	$3 \times 10^{-4}$	0.02	0.85
$ \mathbf{B} ^{HRT}$ 60 s vs $ \mathbf{B} ^{HMI}$ 90 s	$ \mathbf{B} ^{HRT} = 0.89 *  \mathbf{B} ^{HMI} + 118$ G	$1 \times 10^{-4}$	0.01	0.84
$\gamma^{HRT}$ 60 s vs $\gamma^{HMI}$ 720 s	$\gamma^{HRT} = 0.80 * \gamma^{HMI} + 17^\circ$	$4 \times 10^{-4}$	0.01	0.81
$\gamma^{HRT}$ 60 s vs $\gamma^{HMI}$ 90 s	$\gamma^{HRT} = 0.95 * \gamma^{HMI} + 4^\circ$	$1 \times 10^{-4}$	0.004	0.85
$\phi^{HRT}$ 60 s vs $\phi^{HMI}$ 720 s	$\phi^{HRT} = 1.04 * \phi^{HMI} - 5.5^\circ$	0.01	0.7	0.95
$\phi^{HRT}$ 60 s vs $\phi^{HMI}$ 90 s	$\phi^{HRT} = 1.02 * \phi^{HMI} - 3.8^\circ$	0.01	1.7	0.94
$\gamma^{HRT}$ 60 s vs $\gamma^{HMI}$ 90 s (weak-field)	$\gamma^{HRT} = 0.97 * \gamma^{HMI} + 2^\circ$	$1 \times 10^{-4}$	0.006	0.80
$\gamma^{HRT}$ 60 s vs $\gamma^{HMI}$ 90 s (strong-field)	$\gamma^{HRT} = 0.92 * \gamma^{HMI} + 6^\circ$	$2 \times 10^{-4}$	0.02	0.98
$ME-B_{LOS}^{HRT}$ 60 s vs $ME-B_{LOS}^{HMI}$ 720 s	$ME-B_{LOS}^{HRT} = 0.83 * ME-B_{LOS}^{HMI} + 1.0$ G	$1 \times 10^{-4}$	0.01	0.97
$ME-B_{LOS}^{HRT}$ 60 s vs $ME-B_{LOS}^{HMI}$ 90 s	$ME-B_{LOS}^{HRT} = 0.83 * ME-B_{LOS}^{HMI} + 1.0$ G	$5 \times 10^{-5}$	0.005	0.95

12- or 24-hour periodicity due to the SDO orbit (Hoeksema et al. 2014). As shown in Fig. 3.3e and f, the slope is 1.04 and 1.02, respectively, implying that SO/PHI-HRT infers azimuth angles slightly larger than that of HMI. There is also a negative, non-uniform offset of  $-5.5^\circ$  in the 720-second case, which is only  $-3.8^\circ$  in the 90-second case; this requires further investigation. The absolute errors on these offset values are 0.7 and 1.7, which are large relative to the computed offsets, as fewer points are considered relative to the other comparisons presented in this work. Were there an incorrect alignment of the +y detector between SO/PHI-HRT and HMI, which both define  $\phi = 0$ , an offset between  $\phi_{HMI}$  and  $\phi_{HRT}$  would exist. To the best of our knowledge, we have aligned the +y detector of both to solar north and thus rule this out as an origin of the observed offset. However, our rotation test also revealed that a rotation around axes orthogonal to the +y detector axis could also result in an offset of  $0^\circ$ - $2^\circ$ . Therefore, a part of the offset shown in Fig. 3.3 could originate from the angular separation between SO/PHI-HRT and HMI. In this test, the slope of the linear fit between the rotated and original SO/PHI-HRT,  $\phi$ , was 1.01, a change of 1%, which is reflected in the slope error for the  $\phi$  comparisons in Table 3.3. Additionally, a small part of the scatter may be due to the  $3^\circ$  angular separation.

Something that could explain the discrepancies seen in all three components of the magnetic vector is the different wavelength sampling and spectral resolution, as mentioned in Sect. 3.5.1. This, combined with the use of different inversion routines (VFISV applied to HMI data and C-MILOS to SO/PHI-HRT data), is certain to result in differences between the two instruments. As mentioned in the discussion of the weak magnetic field strength regime, the difference in noise levels, in part due to longer HMI integration times, is the reason for the different inferred fields. A non-perfect alignment of the data, as mentioned in Sect. 3.5.1, could also be a factor in explaining the noted difference.

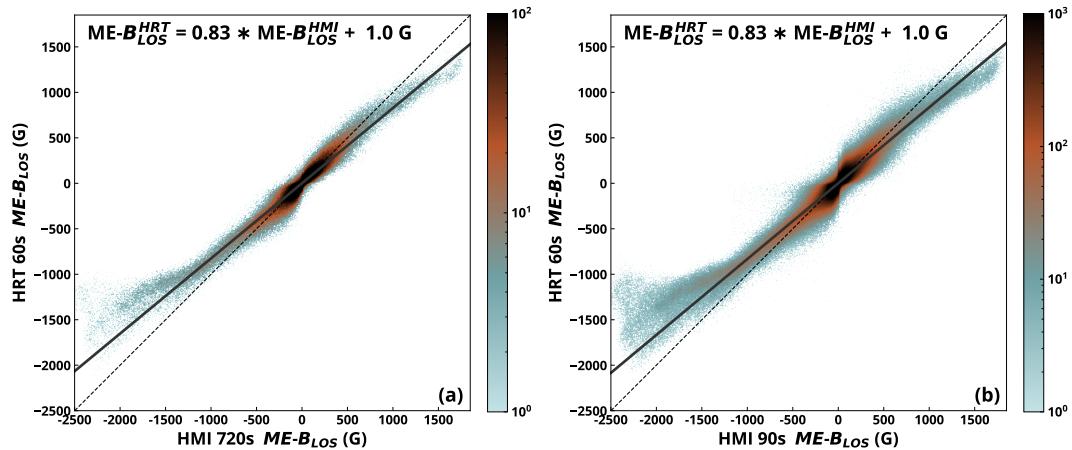


Figure 3.5: Scatter plots comparing the SO/PHI-HRT and HMI LoS components of the full vector magnetic field. ‘ME’ stands for Milne-Eddington and indicates that it is derived from RTE inversions. Panel (a): Comparison of inclinations from seven pairs of SO/PHI-HRT 60-second and HMI 720-second data. Panel (b): Same, but for 38 pairs of SO/PHI-HRT 60-second and HMI 90-second data. The log density of the pixels is shown by the colour and is saturated at 100 (panel a) and 1000 (panel b) for clarity. The averaged linear fit and  $y = x$  lines are plotted in solid grey and dashed black lines, respectively.

### 3.5.3 Comparison of SO/PHI-HRT and HMI LoS components of the full vector magnetic field

We compare the LoS magnetograms from SO/PHI-HRT (from RTE inversions) with those inferred by HMI (also from RTE inversions) in Fig. 3.5. The correlation coefficient is 0.97 and 0.95 for the 720-second and 90-second case, respectively, while the slope is 0.83 for both. We detect here a systematic difference in the strong field regime, with SO/PHI-HRT inferring weaker LoS fields. Hoeksema et al. (2014) report that the HMI MDI-like  $B_{\text{LOS}}$  underestimates the fields in comparison to the HMI ME- $B_{\text{LOS}}$ . Therefore, as the SO/PHI-HRT ME- $B_{\text{LOS}}$  agrees well with the HMI MDI-like  $B_{\text{LOS}}$ , as illustrated in Sect. 3.5.1, one expects to observe the same underestimation. We confirm this expectation here. Since the inclination is well correlated for strong fields (see Fig. 3.4), we can determine that this observed difference is due to the overestimation of  $|\mathbf{B}|$  by HMI (or equally, the underestimation by SO/PHI-HRT). In comparison with Fig. 3.2 from Sect. 3.5.1, we can see that HMI ME- $B_{\text{LOS}}$  infers stronger LoS fields, up to  $-2500$  G and  $1800$  G, than those inferred with the MDI-like formula. Furthermore, the mean difference where HMI ME- $B_{\text{LOS}} < -1300$  is  $486 \pm 2$  G and  $491 \pm 1$  G for the 720-second and 90-second cases, respectively. These are roughly three times larger than those found in Sect. 3.5.1. The scatter ( $1\sigma$ ) on these difference distributions is  $239$  G and  $247$  G, respectively.

Like the LoS magnetograms from HMI, the LoS component of the vector magnetic field, the ME- $B_{\text{LOS}}$  from HMI, is also affected by the radial velocity of SDO. However, while the residual of the  $B_{\text{LOS}}$  calculated using the MDI-like algorithm varies quadratically with radial velocity, the residual of the HMI vector LoS component varies linearly. At  $+3$  km/s, a residual of approximately  $-30$  G is determined, suggesting that HMI may

even be slightly underestimating the values compared to when SDO is at a radial velocity of 0 km/s (Couvidat et al. 2016). The effect from the radial velocity therefore cannot explain why HMI infers a stronger field than SO/PHI-HRT in this comparison.

## 3.6 Conclusions

In this paper we have compared the magnetic fields inferred by SO/PHI-HRT and HMI near the inferior conjunction of Solar Orbiter in March 2022. A comparison was made between the SO/PHI-HRT LoS component of the full vector magnetic field with both the HMI 45-second and 720-second LoS magnetograms computed with the MDI-like algorithm. The SO/PHI-HRT ME- $B_{LOS}$  and the HMI  $B_{LOS}$  have a high correlation coefficient of 0.97, a slope of 0.97, and an offset of less than 1 G. There is a difference, however, for the strongest fields ( $B_{LOS} < -1300$  G), where SO/PHI-HRT infers fields 9 % smaller. These LoS fields correspond to regions in the leading sunspot in the umbra and penumbra only. There are too few points with  $B_{LOS} > 1300$  G in the analysed dataset to determine if positive polarity fields recorded by the two instruments also display a difference. It is unclear what causes the difference at high field strengths. It could be that SO/PHI-HRT is saturated, or it could be due to the orbit-induced periodicity in HMI as SDO was near its maximum radial velocity relative to the Sun at the time of co-observation. Other factors, such as the different wavelength sampling positions, inversion routines, and stray light, likely also contributed.

The vector magnetic fields inferred by SO/PHI-HRT and HMI were also compared. Where  $|\mathbf{B}| > 1300$  G, SO/PHI-HRT inferred field strengths 13 % lower than HMI, but with similar field inclination. This field strength threshold corresponded to regions almost exclusively in the umbra and penumbra in the active region in the common FoV. This is apparent in the comparison between the LoS component of the full vector magnetic field from both SO/PHI-HRT and HMI. In the weak field regime ( $|\mathbf{B}| < 600$  G), SO/PHI-HRT inferred stronger field strengths than HMI. In this regime, the difference in field strength and inclination is mostly due to the difference in noise. The azimuth was compared by studying the large sunspot in the common FoV. It was shown to agree well, with a slope of 1.02–1.04; however, there was a non-uniform, negative offset that requires further investigation.

The differences found between SO/PHI-HRT and HMI, in both the LoS and vector magnetic fields, could be due to several factors. First of all, the two instruments sample different wavelength positions in the Fe I absorption line and use different inversion routines to infer the vector magnetic fields. Secondly, there could be a non-perfect alignment in the magnetic field maps due to residual geometric distortion in the SO/PHI-HRT data. Additionally, neither the HMI nor the SO/PHI-HRT data used in this study were corrected for stray light.



# 4 Preliminary stereoscopic analysis with SO/PHI-HRT and SDO/HMI

## 4.1 Introduction

With a robust data reduction pipeline now in place for SO/PHI-HRT, and a first understanding of the differences in the magnetic field inferences from SO/PHI-HRT and SDO/HMI, I can now attempt to compare the photospheric magnetic field from the two spacecrafts when observing from different directions. Given that Solar Orbiter does not move out of the ecliptic until 2025, there is, for now, no new access to the polar regions. Hence the hypothesis for explaining the open flux problem, that motivates the bulk of my thesis, i.e. that the open flux photospheric magnetic field is underestimated, cannot be conclusively tested yet. However, with SO/PHI as the first magnetograph out of the Sun-Earth line, stereoscopy in the ecliptic plane can now be performed. Stereoscopy typically refers to the determination of the three dimensional structure of an object by observing from different directions. When I use the term stereoscopy, I refer only to the concept of observing the same feature from two different directions, not the determination of the three dimensional structure which is explored by Romero Avila et al. (2024).

Stereoscopic inference of the photospheric magnetic field enables the first direct test of the ‘ $\mu$ -correction’, which is routinely applied to full disc or synoptic magnetograms when computing the total magnetic flux (e.g. Murray 1992, Fligge et al. 2000, Hagenaar 2001). This correction divides the line-of-sight magnetic flux in each pixel, by the cosine of the heliocentric angle, ( $\mu = \cos(\theta)$ ), of said pixel. This correction makes use of the common assumption that the photospheric magnetic field is radial, such that when the line-of-sight component of the magnetic field is inferred, the radial component can be retrieved via the  $\mu$ -correction. A broader overview of the reasons why the  $\mu$ -correction has often been implemented is given in the following Chapter in Sect. 5.2. Additionally, in Chapter 5, a simulation-driven approach to investigate the reliability of magnetograms to retrieve the flux from unipolar regions is made for a wide range of  $\mu$  values. This simulation also tests the efficacy of the  $\mu$ -correction in such regions.

In this chapter, a first attempt to perform stereoscopy on the photosphere is presented, with one view provided by SDO/HMI along the Sun-Earth line, and various observations provided by Solar Orbiter from different directions relative to the Sun-Earth line. The aim for this work can be broken down into several steps:

1. Accurately determine the region on the photosphere that SO/PHI-HRT observed in

the SDO/HMI data.

2. Reproject the SO/PHI-HRT magnetograms onto the SDO/HMI frame of reference to enable pixel to pixel comparison of the co-spatially observed regions
3. Compare the pairs of line-of-sight magnetograms and analyse their differences, including dependence on their respective  $\mu$  values and Earth-Sun-SO angles.

In Sect. 4.2, the SO/PHI-HRT data from early 2022 that I used, including their respective orbital positions and viewing geometry is introduced. In Sect. 4.3 an overview of the method that I implemented is outlined and the performance of the alignment method in Sect. 4.3.1 is shown. Finally, some preliminary results are presented in Sect. 4.3.2 and a conclusion is given in Sect. 4.4.

## 4.2 Data

As described in Sect. 1.3.1, SO/PHI-HRT operates primarily in Remote Sensing Windows (RSW), which are close to the perihelion passes. In these RSWs, Solar Orbiter regularly changes its pointing, to achieve the primary scientific objectives of a wide range of Solar Orbiter Observing Plans (SOOP, Zouganelis et al. 2020). In very few SOOPs has stereoscopy of the magnetic field been the primary objective: it is often a secondary objective.

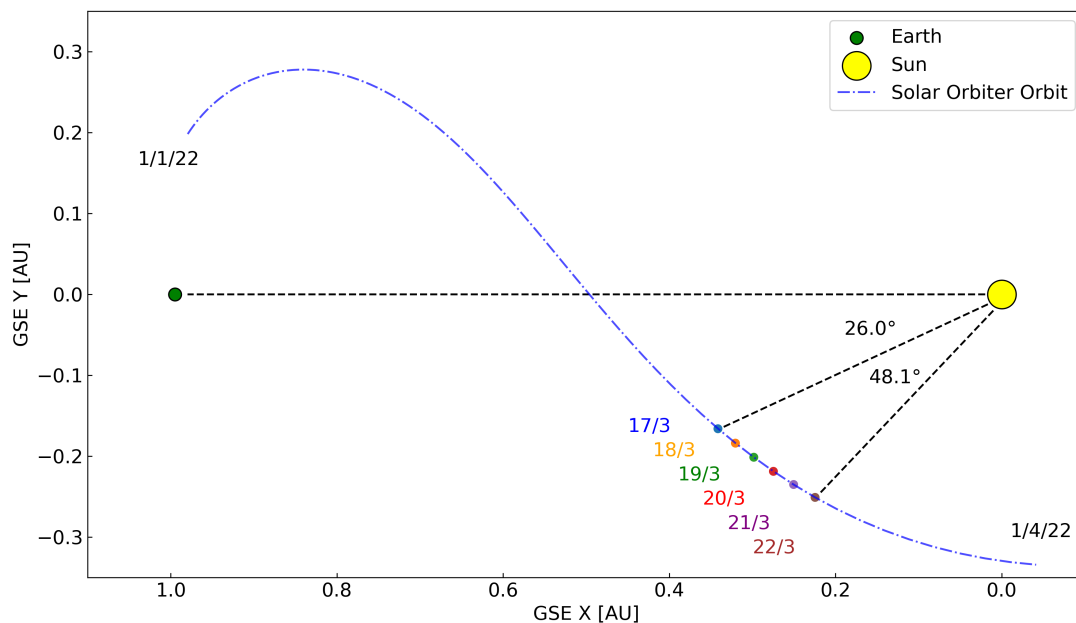


Figure 4.1: The orbital configuration of Earth, the Sun and Solar Orbiter from January 2022 until April 2022 in Geocentric Solar Ecliptic (GSE) coordinates. The orbit of Solar Orbiter is indicated in the dashed blue line. It starts from the top left and moves towards the bottom right. The 6 dates of Solar Orbiter observations that are explored in this chapter are highlighted in different colours. The start and end Earth-Sun-Solar Orbiter angles are indicated by the text and dashed black lines.

Table 4.1: Observation details of the SO/PHI-HRT data and HMI  $\mu$  values in the co-spatially observed regions.

Start Time	Angle [°]	Solar Orbiter Distance [au]	SO/PHI-HRT Pixel Size [km]	SOOP	Cadence	Datasets	HRT $\mu$	HMI $\mu$
2022-03-17 03:18:09	26.0	0.379	137	Nanoflares	1min	29	0.95-0.62	0.86-0.50
2022-03-18 10:10:09	29.9	0.366	133	Slow-Wind-Connection	5min	12	0.84-0.28	0.81-0.36
2022-03-19 10:36:09	34.0	0.356	129	Slow-Wind-Connection	5min	12	0.99-0.82	0.93-0.69
2022-03-20 11:27:09	38.5	0.348	126	Slow-Wind-Connection	5min	12	0.99-0.83	0.82-0.54
2022-03-21 11:36:09	43.2	0.340	123	Slow-Wind-Connection	5min	12	1.0-0.85	0.72-0.43
2022-03-22 09:40:09	48.1	0.335	121	Coronal Dynamics	100s	27	1.0-0.96	0.79-0.56

To perform stereoscopy well, an ideal observation from SO/PHI-HRT would be situated at an Earth-Sun-Solar Orbiter angle between 30 – 60°, and Solar Orbiter would be observing a region with many strong (kG) field elements or structures. Furthermore the stereoscopy would be in a particular configuration: with the region of the photosphere located near disc centre for one observer, while it is off centre and closer to the limb for the other. This would provide contrasting views of the same region. For the purposes of testing the  $\mu$ -correction the magnetic field data products of interest are the line-of-sight magnetograms from both instruments.

The first available SO/PHI data that broadly matched this criteria is just before the perihelion in March 2022. The orbit of Solar Orbiter a few months prior (Jan 2022) until April 2022 is indicated in the blue dashed line in Fig. 4.1. The Earth, Sun, and Solar Orbiter are shown in Geocentric Solar Ecliptic (GSE) coordinates. In this coordinate system, the Sun and Earth are stationary, while all other bodies move with respect to them. The  $x$ -axis points from Earth to the Sun and the  $y$ -axis is in the ecliptic plane. The dates of observation that are suitable for this stereoscopic analysis are highlighted in text for 6 separate dates, from 17 March to 22 March. The start and end Earth-Sun-SO angles are indicated with 26.0° and 48.1°. The distance of Solar Orbiter to the Sun starts at 0.379 au and reduces as Solar Orbiter approaches perihelion to 0.335 on the last day of consideration.

In Table 4.1, further details of the selected observations are given, including the distance of Solar Orbiter to the Sun, the range of  $\mu$  values of both SO/PHI-HRT and SDO/HMI of the region in the Solar Orbiter field of view (FOV)\*, the SOOP name, observing cadence of SO/PHI-HRT and number of datasets. Given the cadence of the SO/PHI-HRT observations are all faster than the 12-minute observations by SDO/HMI, instead the 45-second magnetograms from SDO/HMI are used.

\*I use FOV instead of FoV (as used in Chapter 3) to stay consistent with Chapter 2 and the rest of this thesis. As Chapter 3 is published I cannot resolve the inconsistency. The same applies to the abbreviation for line-of-sight, where I use LOS instead of LoS for the remainder of this thesis.

### 4.3 Method and alignment

Similar to Sect. 3.4, SDO/HMI data are retrieved that were recorded at the same time as the SO/PHI-HRT observations, taking into account the difference in light travel time and difference between International Atomic Time (TAI), which SDO uses, and Universal Coordinated Time (UTC) which SO uses. First however the WCS information in the SO/PHI-HRT data must be corrected. Inaccurate WCS information is not unique to SO/PHI-HRT, for example Hinode-SOT/SP (Spectropolarimeter on the Solar Optical Telescope Tsuneta et al. 2008b) also exhibits pointing errors when compared to SDO/HMI (Fouhey et al. 2023); it is a common issue for telescopes that have a limited FOV as they cannot use the solar limb to calculate accurate pointing information. The WCS information is corrected to first order by applying the following method (Xiahong Li 2024, private communication):

1. Reproject SDO/HMI magnetogram onto SO/PHI-HRT frame and up-sample to the SO/PHI-HRT pixel size using the SO/PHI-HRT WCS information.
2. Calculate the shift in the  $x - y$  plane (in SO/PHI-HRT pixels) between the reprojected SDO/HMI and SO/PHI-HRT magnetograms via a Fourier cross correlation technique.
3. Update the CRPIX and CRVAL keywords in the SO/PHI-HRT WCS information (see Pence et al. 2010, for details on these keywords).

To perform the reprojection I used the `reproject`<sup>†</sup> Python3 package, which is used by the leading solar python community package `sunpy`<sup>‡</sup> to reproject solar images and data. Like in Sect. 3.4, the DeForest (2004) algorithm was used to perform the reprojection.

To test the  $\mu$ -correction, and investigate if indeed any magnetic flux is ‘missing’ due to the observation at low  $\mu$  values, the magnetograms from SO/PHI-HRT and SDO/HMI must be treated such that the effect of foreshortening is considered. Through a reprojection and resampling of a magnetogram from one instrument to the coordinate frame and pixel size of the other, one can be sure that the pixels cover the same physical region on the solar surface. Therefore two possible approaches exist, reprojecting SO/PHI-HRT onto SDO/HMI or the reverse: SDO/HMI onto SO/PHI-HRT. I take the first approach here as it has the advantage that interpolation artefacts are minimised. These would be substantial with the latter approach as the spatial coverage of a pixel of SO/PHI-HRT on the Sun is much smaller due to its closer radial distance to the Sun. Furthermore during the dates considered here, SO/PHI-HRT observed predominantly near disc centre, while the region within the SO/PHI-HRT FOV is nearer the limb for SDO/HMI. This results in a large foreshortening effect for SDO/HMI and further increases the interpolation required if the latter approach is used. During our approach, the reprojection algorithm, at the same time as reprojecting the SO/PHI-HRT onto the SDO/HMI coordinate frame, resamples the data to the same pixel size as SDO/HMI.

However, the standard setup of the DeForest (2004) algorithm is not sufficient for accurate down-sampling of magnetograms. This algorithm was designed with astro-

---

<sup>†</sup><https://pypi.org/project/reproject/>

<sup>‡</sup><https://pypi.org/project/sunpy/>

nomical images in mind, for photometry. To circumnavigate this, I changed the input parameters to restrict the algorithm to only consider the SO/PHI-HRT pixels that make up one SDO/HMI pixel, and calculate the mean magnetic flux density of these constituent SO/PHI-HRT pixels when resampling.

Nevertheless, detailed testing revealed that some regions on the SO/PHI-HRT magnetogram, which each make up one SDO/HMI pixel, overlap. This occurs even though the DeForest (2004) algorithm conservatively truncates the input region when it has non-integer pixel dimensions: e.g. if the boundaries of the corresponding area on the SO/PHI-HRT magnetogram lie in middle of pixels, the algorithm disregards these sub-integer boundary pixels and only considers pixels that are wholly enclosed. This overlapping means that some SO/PHI-HRT pixels are being sampled twice. I want to clarify that when a pixel is 'sampled twice', the pixel contributes to the calculation of the mean in more than one region. From further tests, the overlapping of regions seems to occur more frequently and with larger overlaps where the SDO/HMI pixels are foreshortened the most. On average a SO/PHI-HRT pixel from a magnetogram on 17 March 2022 contributes to the calculation of the mean in 1.48 regions. In areas of the SO/PHI-HRT magnetogram where the magnetic flux density is unipolar and homogeneous, an overlap, has a much reduced impact on the calculation of the mean of these regions. The umbra of a sunspot could be considered such an area, and hence in Sect. 4.3.2 the total unsigned LOS magnetic flux of the two sunspot umbrae is cautiously compared.

Outside a unipolar homogeneous magnetic structure, the overlap can result in unnecessary flux cancellation, or the opposite, an incorrect inflation of the true flux. This means that with this algorithm the magnetic fluxes from the entire reprojected SO/PHI-HRT magnetograms cannot be compared with SDO/HMI. In Moreno Vacas et al. (2024), the authors faced a similar task, albeit only reconciling the different pixel sizes between SO/PHI-FDT and SDO/HMI with minimal differential foreshortening effects as the two instruments were observing the Sun at almost identical positions. In future work, a dedicated algorithm should be developed to resolve the issue of oversampling. For the purposes of the rest of this chapter, where there is no umbra, I will only compare these reprojected SO/PHI-HRT magnetograms to evaluate the alignment after correcting the WCS.

One pair of magnetograms (a SO/PHI-HRT dataset and the corresponding SDO/HMI 45-second magnetogram) from each of the 6 dates and results of the alignment procedure are depicted in Figs. 4.2, 4.4, 4.5, 4.6, 4.7 and 4.8. Each figure depicts the original SDO/HMI and SO/PHI-HRT line-of-sight magnetograms in the top row. The SO/PHI-HRT data shown in the top row have had 150 pixels cropped from each side. This is identical to the orange square depicted in Fig. 3.1. This is required due to apodisation affecting the very edges of the FOV. These edges are hence masked, and also contain the field stop region (black regions in second column of Fig. 3.1) and are taken into account when performing the reprojection. Furthermore in the top left panel of each figure, the outline of the SO/PHI-HRT observation is shown in the SDO/HMI FOV.

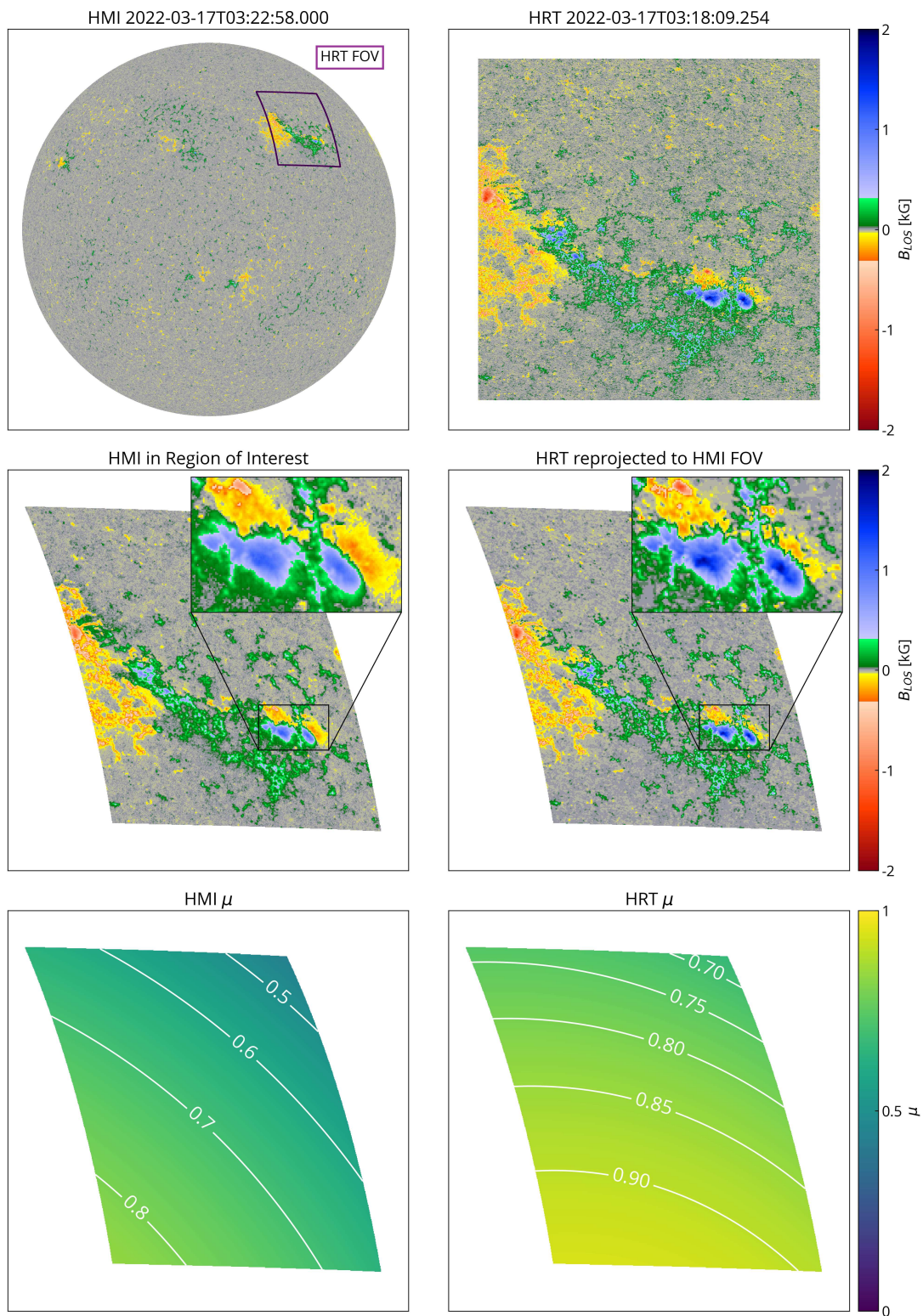


Figure 4.2: Top row: SDO/HMI (left column) and SO/PHI-HRT magnetogram (right column) from 17 March 2022 at 03:18:09 UTC, with the SO/PHI-HRT FOV outlined in purple. Second row: SDO/HMI magnetogram in the SO/PHI-HRT FOV is shown (left), while the reprojected SO/PHI-HRT data is shown (right). The magnetograms are saturated to  $\pm 2$  kG. Bottom row: the  $\mu$  values of each pixel are shown and saturated from 0 to 1.

In the second row of each figure, the SDO/HMI data, in the co-spatially observed region is shown in the left panel, while the reprojected SO/PHI-HRT data is shown in the right panel. Finally in the bottom row, the  $\mu$  values of each pixel from the middle row panels are shown, highlighted by contours. This indicates the difference in heliocentric angle of data recorded by the two instruments.

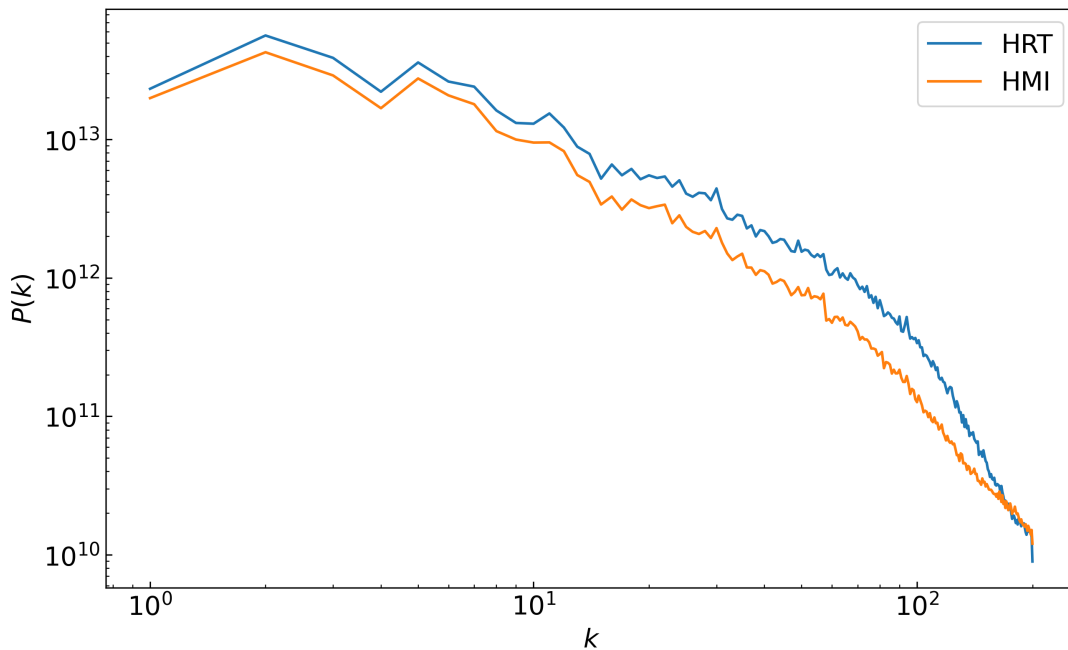


Figure 4.3: Power spectrum of the central region of the magnetograms shown in the middle row of Fig. 4.2.

Fig. 4.2 illustrates that SO/PHI-HRT observed an active region, with a large plage region, including a pore on the left side. In the middle rows, the pair of sunspots, are shown in enhanced detail. Even though SO/PHI-HRT has been down-scaled to the pixel size of SDO/HMI (from 137 km pixels to 362.5 km pixels - disregarding foreshortening), the reprojected SO/PHI-HRT magnetogram shows much higher contrast and finer detail. This is due to the fact that the PSF of SDO/HMI is broader than the PSF of SO/PHI-HRT due to the different distances to the Sun. From a comparison of the power spectrum of the central region in these pair of magnetograms, depicted in Fig. 4.3, SO/PHI-HRT has slightly more power across the full range of wavenumbers, which originates from the enhanced contrast in the original image.

The other dates under consideration will now be briefly discussed. Fig. 4.4 indicates that SO/PHI-HRT was pointing at a region near the South Pole, which merges with a coronal hole at the South Pole. The coronal images in the extreme ultraviolet of this merger are studied by Ngampoopun et al. (2023). For both instruments this region was far from their respective disc centre, albeit with the lowest  $\mu$  value for SDO/HMI in the bottom right corner, while it is in the bottom left corner for SO/PHI-HRT.

On 19 March, as shown in Fig. 4.5, SO/PHI-HRT observed a plage region that was magnetically connected to the active region closer to the West limb as seen by

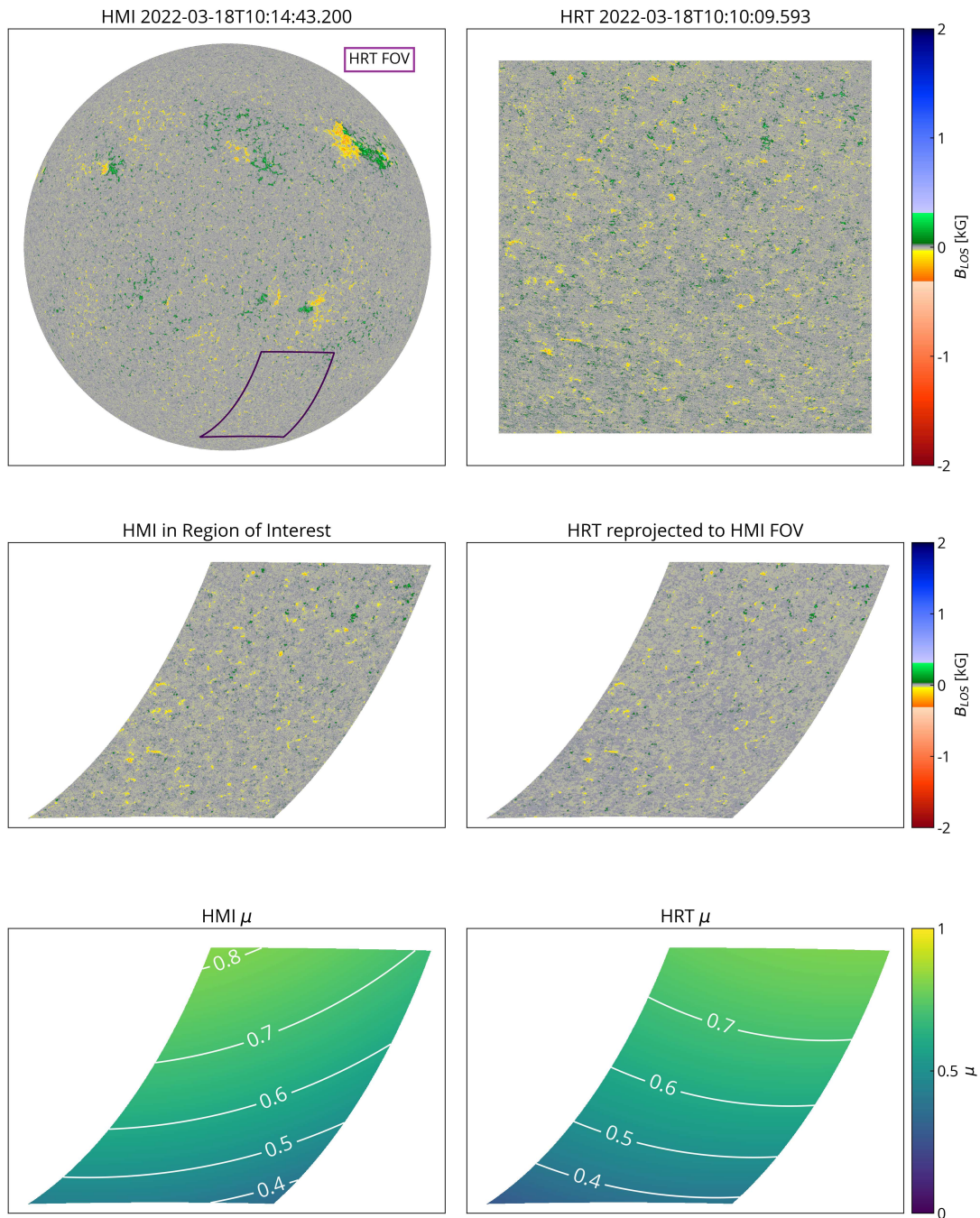


Figure 4.4: Same as Fig. 4.2 but for 18 March 2022 at 10:10:09 UTC.

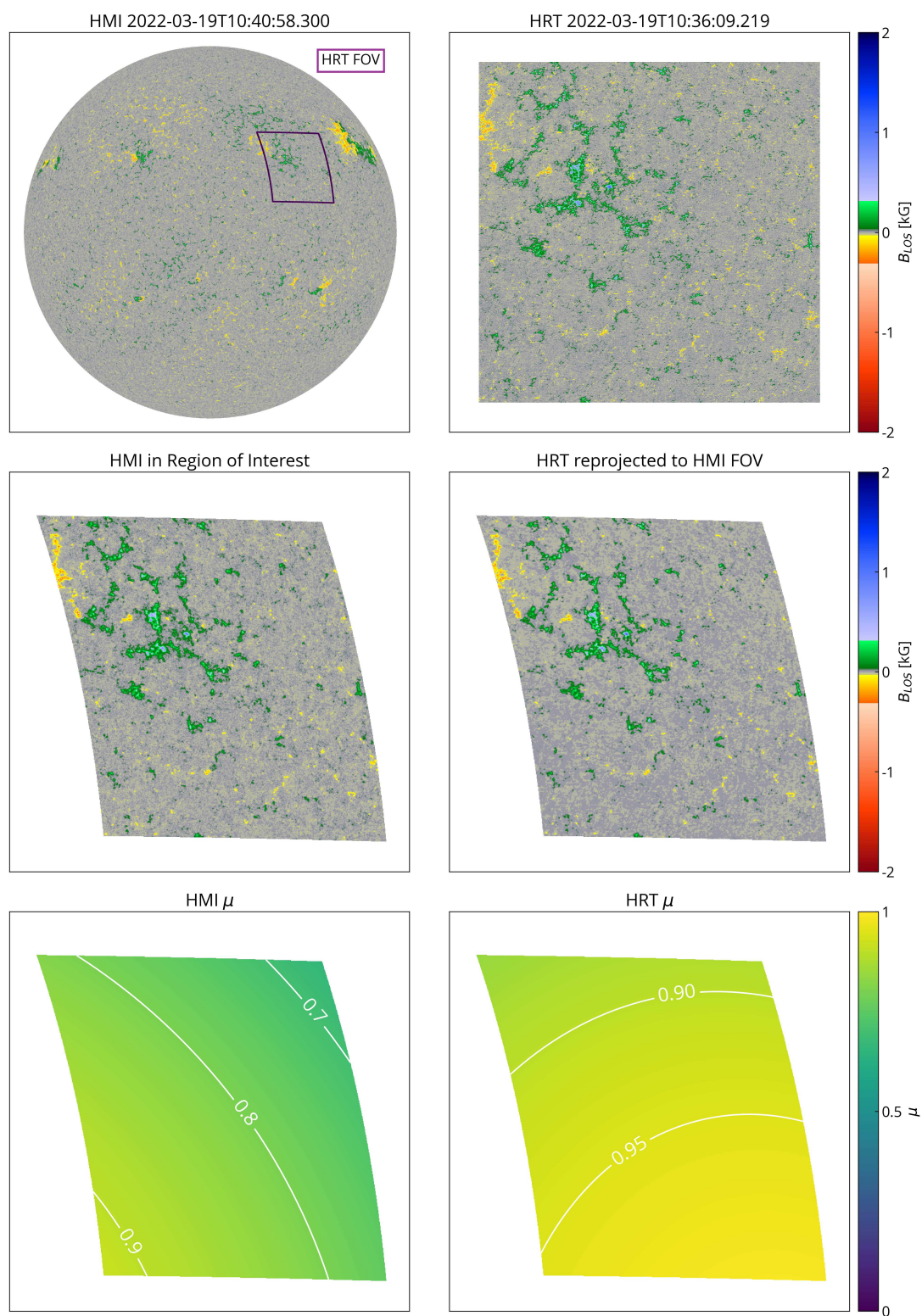


Figure 4.5: Same as Fig. 4.2 but for 19 March 2022 at 10:36:09 UTC.

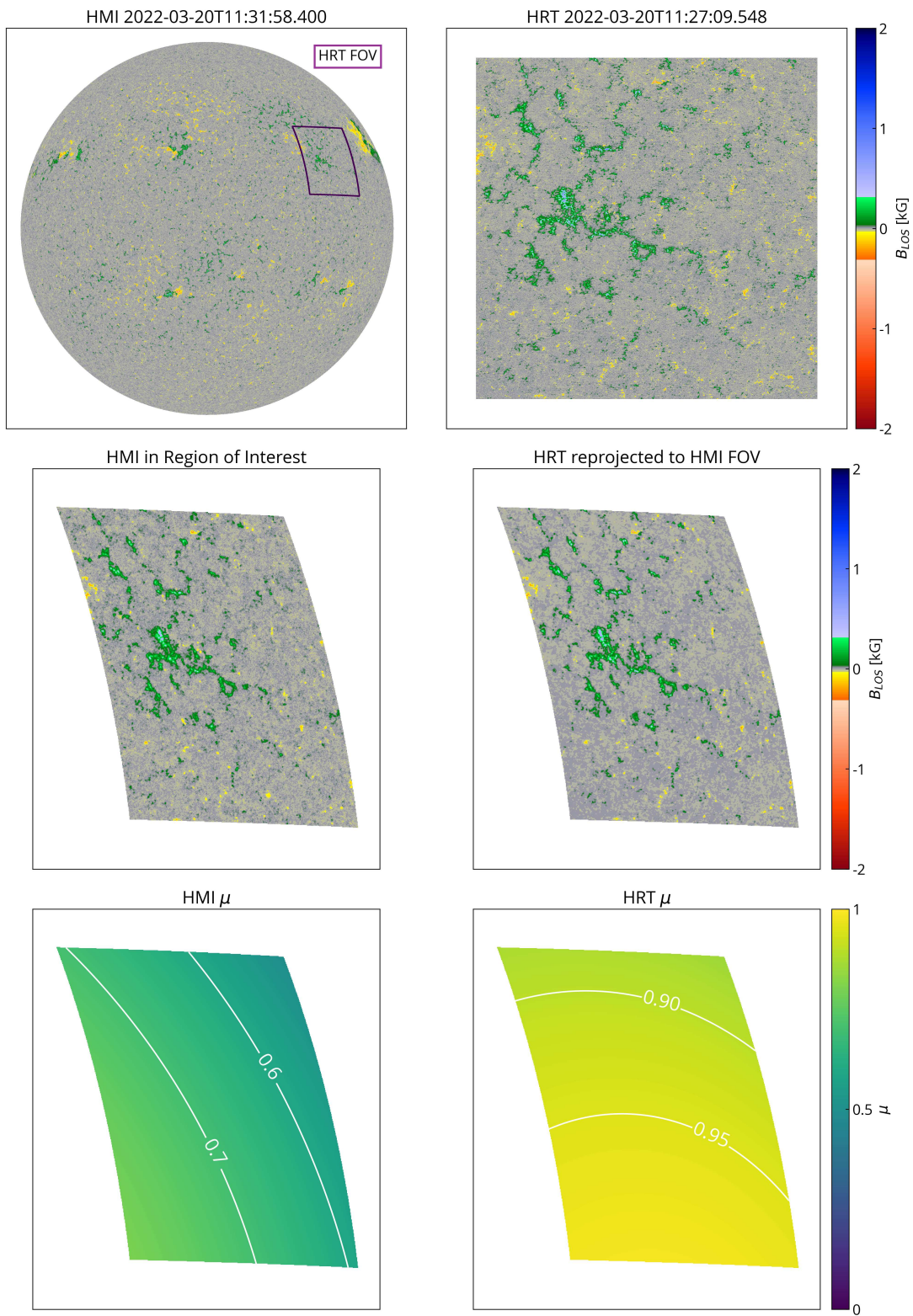


Figure 4.6: Same as Fig. 4.2 but for 20 March 2022 at 11:27:09 UTC.

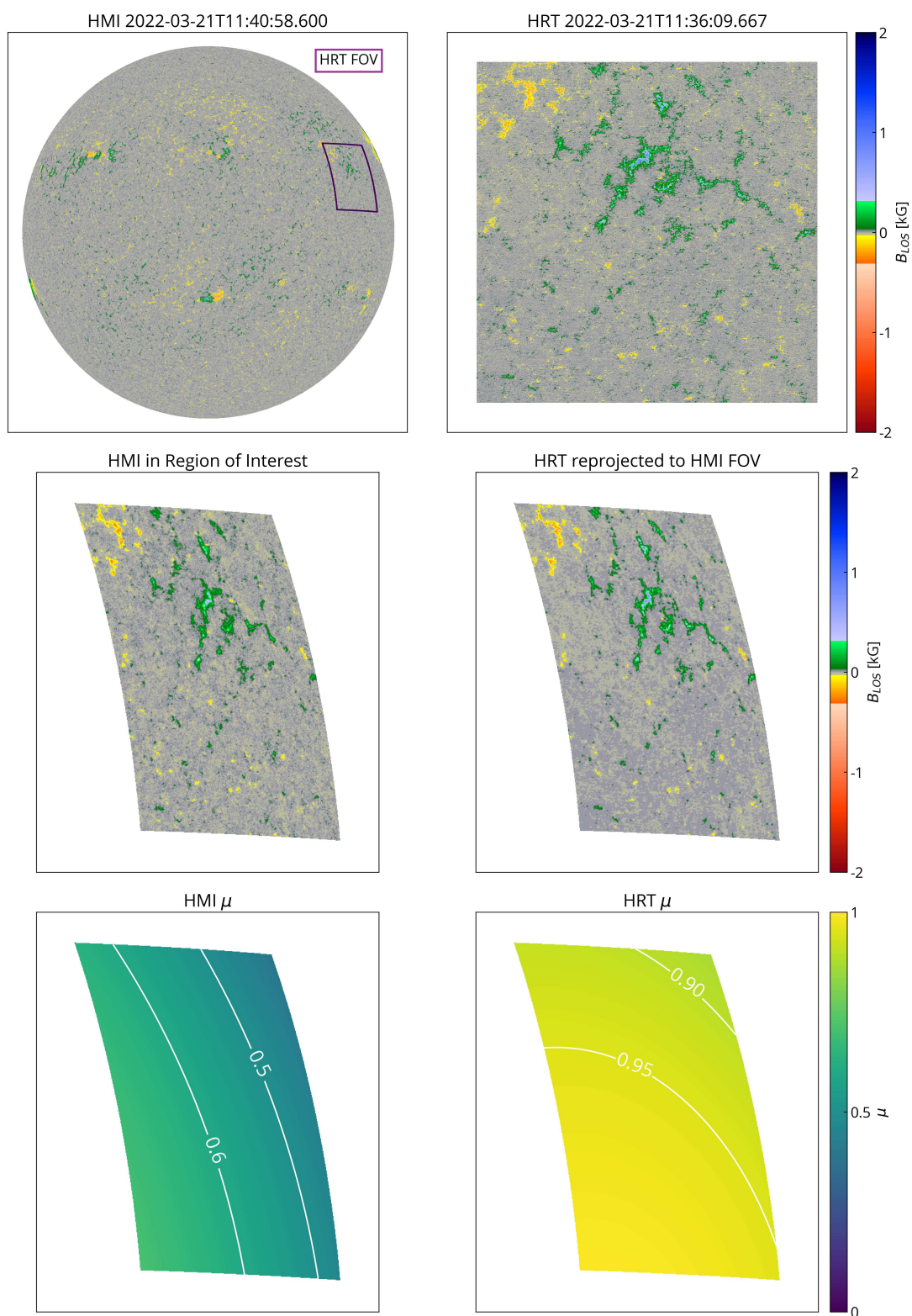


Figure 4.7: Same as Fig. 4.2 but for 21 March 2022 at 11:36:09 UTC.

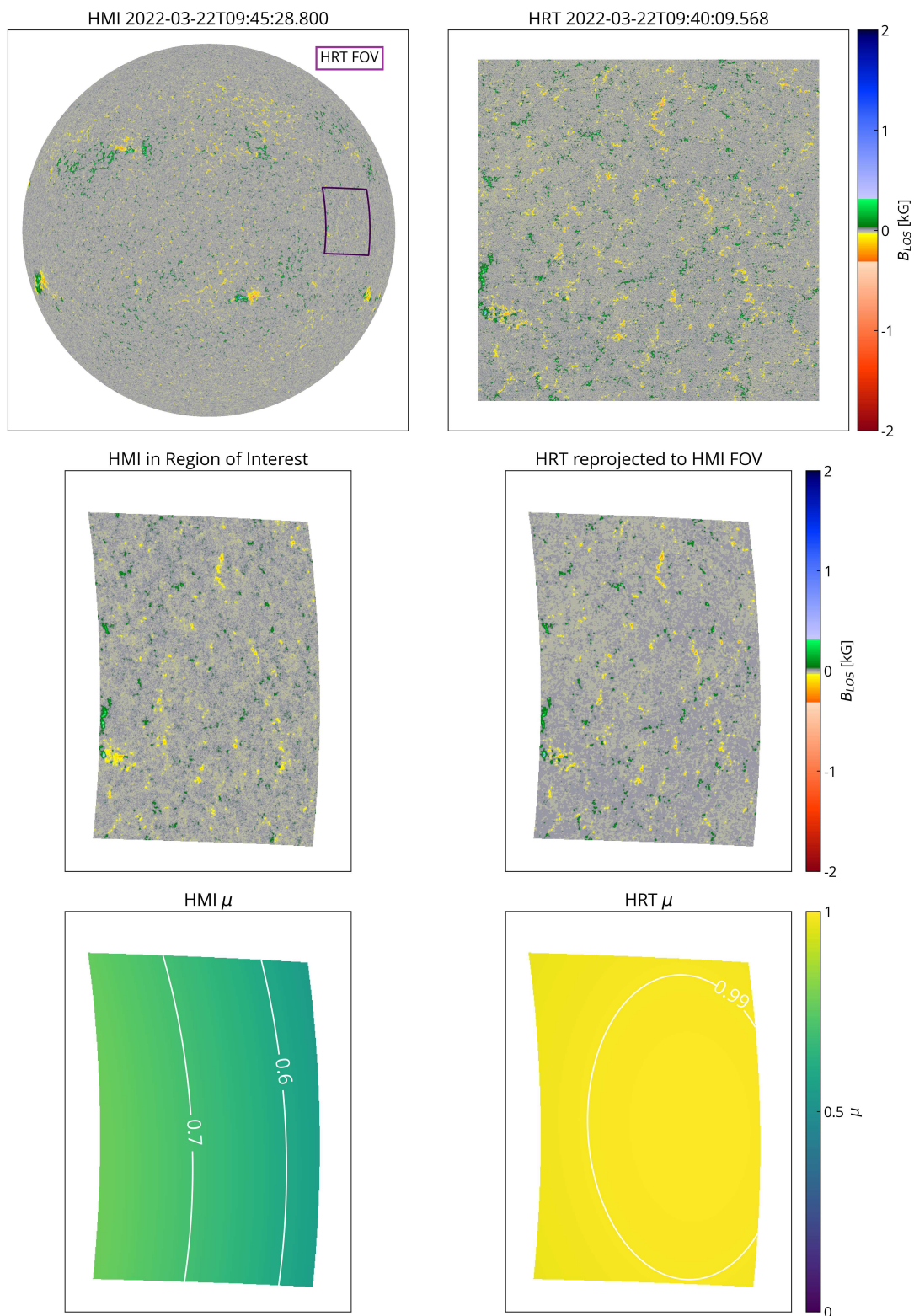


Figure 4.8: Same as Fig. 4.2 but for 22 March 2022 at 09:40:09 UTC.

SDO/HMI. As indicated in the lower row of Fig. 4.5 this region is almost at disc centre for SO/PHI-HRT while it is approximately at a  $\mu$  value of 0.8 in SDO/HMI.

For the next two days, this same region was observed and shown in Fig. 4.6 and Fig. 4.7. Over the course of these next two days, the region steadily moved to lower  $\mu$  values for SDO/HMI: at approximately 0.6-0.7 on 20 March and around 0.5-0.6 on 21 March. These three dates of observation are interesting to study as the same region was co-observed in three different stereoscopic configurations: in SDO/HMI it was observed at decreasing values of  $\mu$  as the region moved across the solar disc, while for SO/PHI-HRT it maintained a near identical viewing angle as Solar Orbiter nearly co-rotates with the Sun near its perihelion approach. Finally, on 22 March 2022, SO/PHI-HRT observed a region of quiet Sun, at exactly disc centre, while for SDO/HMI the region was at  $\mu$  values around 0.6-0.7.

### 4.3.1 Alignment Performance

To compare these pairs of SO/PHI-HRT and SDO/HMI data on a pixel-to-pixel basis, as in Chapter 3, the alignment must be correct. Upon detailed inspection of the reprojected SO/PHI-HRT and SDO/HMI magnetograms some residual shifts are still present. In Figs. 4.9, 4.10, 4.11, 4.12, 4.13 and 4.14, the difference between the reprojected SO/PHI-HRT and SDO/HMI magnetograms is displayed in the top row, while in the bottom row, the residual pixel shift of the sub-regions (outlined in black in the top right panel) in the  $x$  and  $y$  directions is shown. These sub-regions are  $80 \times 80$  pixels in size, except for Fig. 4.13 where instead sub-regions of  $69 \times 69$  pixels are used to maximise the coverage. The colour map used to indicate the difference in the magnetograms is a symmetric log scale with a linear behaviour between differences of  $\pm 50$  G. This log scale nature of the colour map visually enhances areas of strong difference while the linear behaviour around 0 increases the contrast in quiet Sun areas where the differences are much smaller in magnitude.

The top rows of Figs. 4.9, 4.10, 4.11, 4.12, 4.13 and 4.14 display significant differences between the reprojected SO/PHI-HRT and SDO/HMI magnetograms. A large portion of this difference is expected, due to the different lines of sight the component of the magnetic field vector towards the observing instrument will differ substantially. For example, this can be clearly seen near the bottom left corner of 4.14 or by comparing the magnetograms in the second row of Fig. 4.8. In this region there are magnetic patches that show different polarities as well as differences in their spatial distributions.

Furthermore, as touched upon in the previous section, the greater contrast in the SO/PHI-HRT magnetograms and less blurred appearance of the magnetic features results in some of the differences we observe here. Additionally, the different noise levels plays a factor: from Liu et al. (2012) the noise of the SDO/HMI 45-second magnetograms is approximately 10 G, while from Sect. 2.5.3 I have shown that the noise in SO/PHI-HRT magnetograms is approximately 6.5 – 8.5 G. The difference in noise, together with the different spatial resolution most likely explains the differences found in the quiet Sun areas. The largest differences are evident in Fig. 4.9 due to the presence of the strongest magnetic features from the 6 days of observations. The largest difference is found near the sunspot pair, with differences up to 786 G found in the sunspots. This area is discussed in further detail in the next section: Sect. 4.3.2. Here the major contributing factor is the

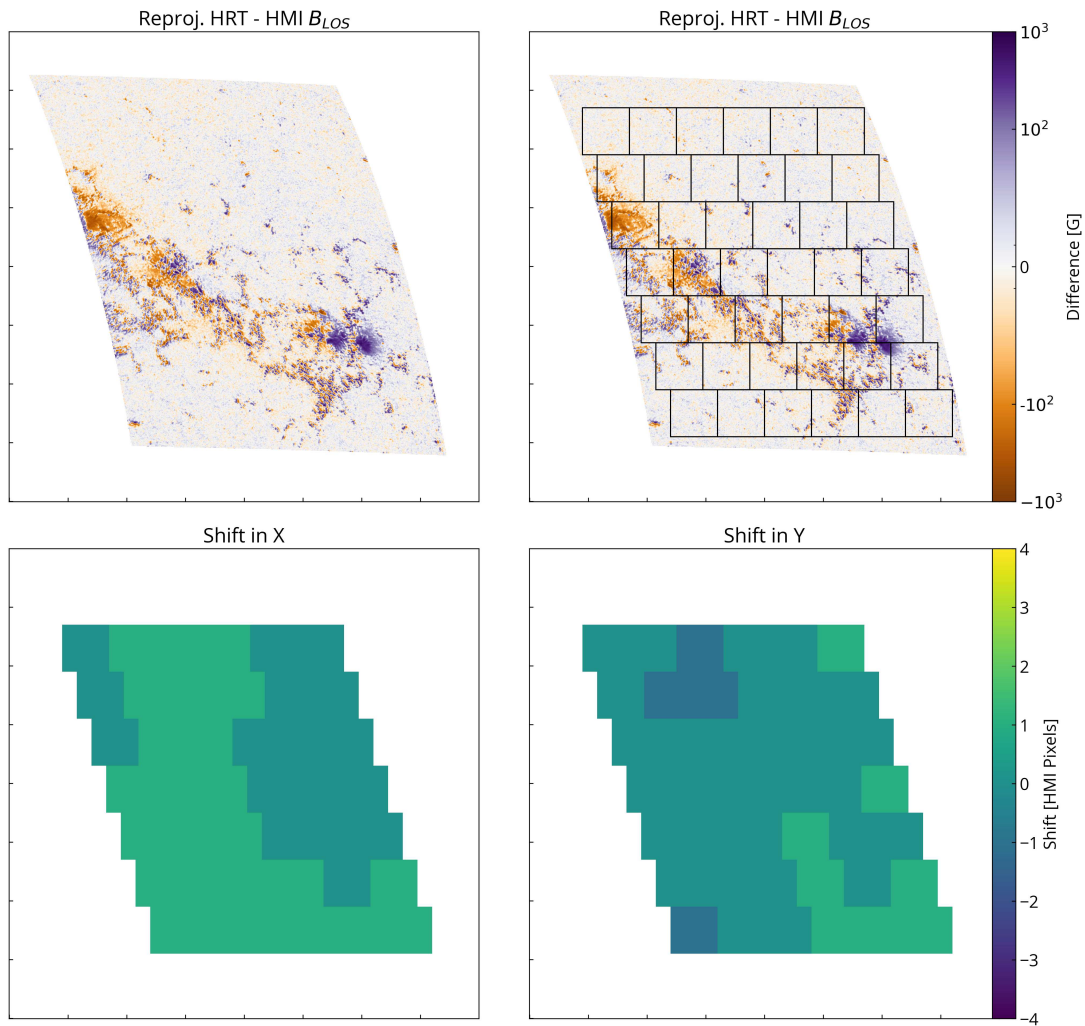


Figure 4.9: Top row: difference between the reprojected SO/PHI-HRT magnetogram and the corresponding SDO/HMI 45-second magnetogram (both panels) on 17 March 2022 at 03:18 UTC. On the right panel sub-regions are outlined in black squares of size  $80 \times 80$  pixels. The difference is saturated to  $\pm 1000$  G and a symmetric log scale is used for the colour map, with linear behaviour between differences of  $\pm 50$  G. Bottom row: residual  $X$  (left) and  $Y$  shifts (right) in the outlined sub-regions.

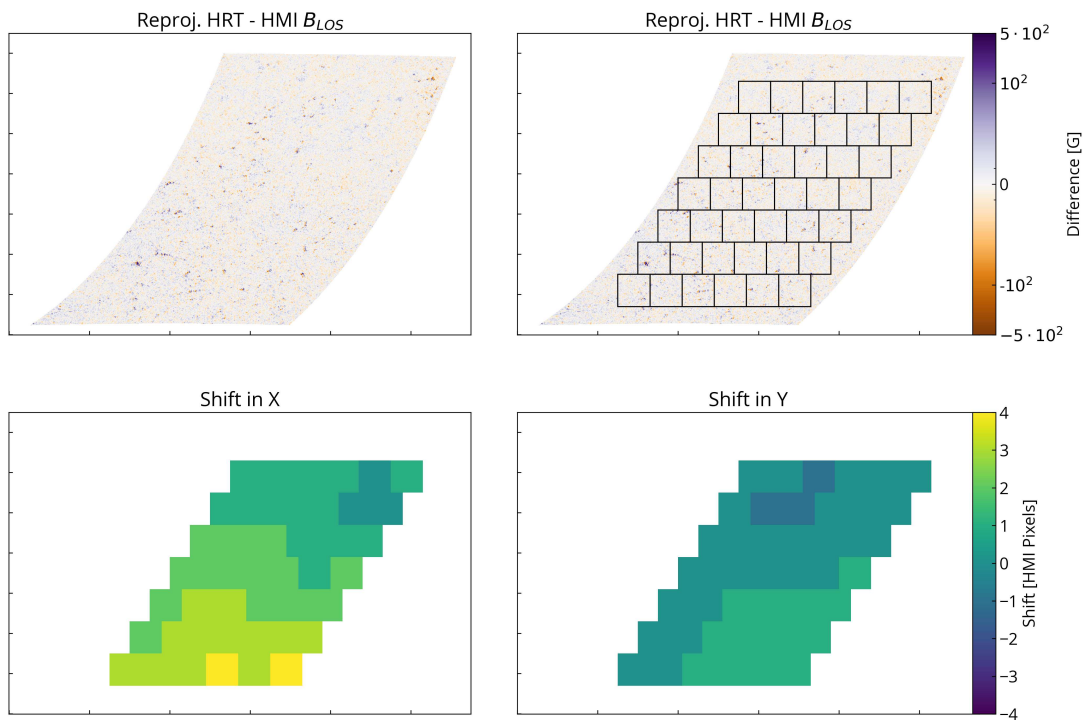


Figure 4.10: Same as Fig. 4.9 but for 18 March 2022 at 10:45 UTC. Furthermore the difference maps are saturated to  $\pm 500$  G.

different lines of sight. Outside the sunspots, throughout all 6 days of co-observations, near small to medium sized magnetic features, the non-perfect alignment (residual shifts) contributes heavily to a difference in the  $B_{LOS}$ . This can be seen by a feature with a negative difference in  $B_{LOS}$  immediately adjacent to an identically sized feature with a positive difference of equal magnitude.

While residual shifts exist, the majority of these sub regions for most of these dates have 0 or  $\pm 1$  HMI-sized pixel shifts. However on 18 March, when both telescopes were observing far off disc centre, the residual shifts were larger, up to 4 pixels in the  $x$  axis. Furthermore, on 21 and 22 March, the shifts in  $x$  increased by 1 when compared to 17 and 19 March. These results suggests, that the alignment performs worse when one or both of the telescopes are observing closer to the limb. There is one sub region in Fig. 4.13 where the residual shift is three pixels in  $y$  while all the neighbouring sub regions have no residual. This most likely stems from the the fact that this sub region is devoid of any strong magnetic features, and hence the Fourier cross correlation method may be more influenced by the noise in the magnetograms.

These residual shifts imply that there could be some distortion in one or both of the images. From a Venus transit Couvidat et al. (2016) show that the image distortion model for SDO/HMI is known with an error of approximately 0.1 SDO/HMI pixels. When using the same preliminary model of distortion as used in Chapter 3, these residual shifts slightly increase. This highlights that further work is required to understand the SO/PHI-HRT optical distortion, and will improve as more data becomes available. Efforts on this topic are currently underway and early results suggest that the plate scale

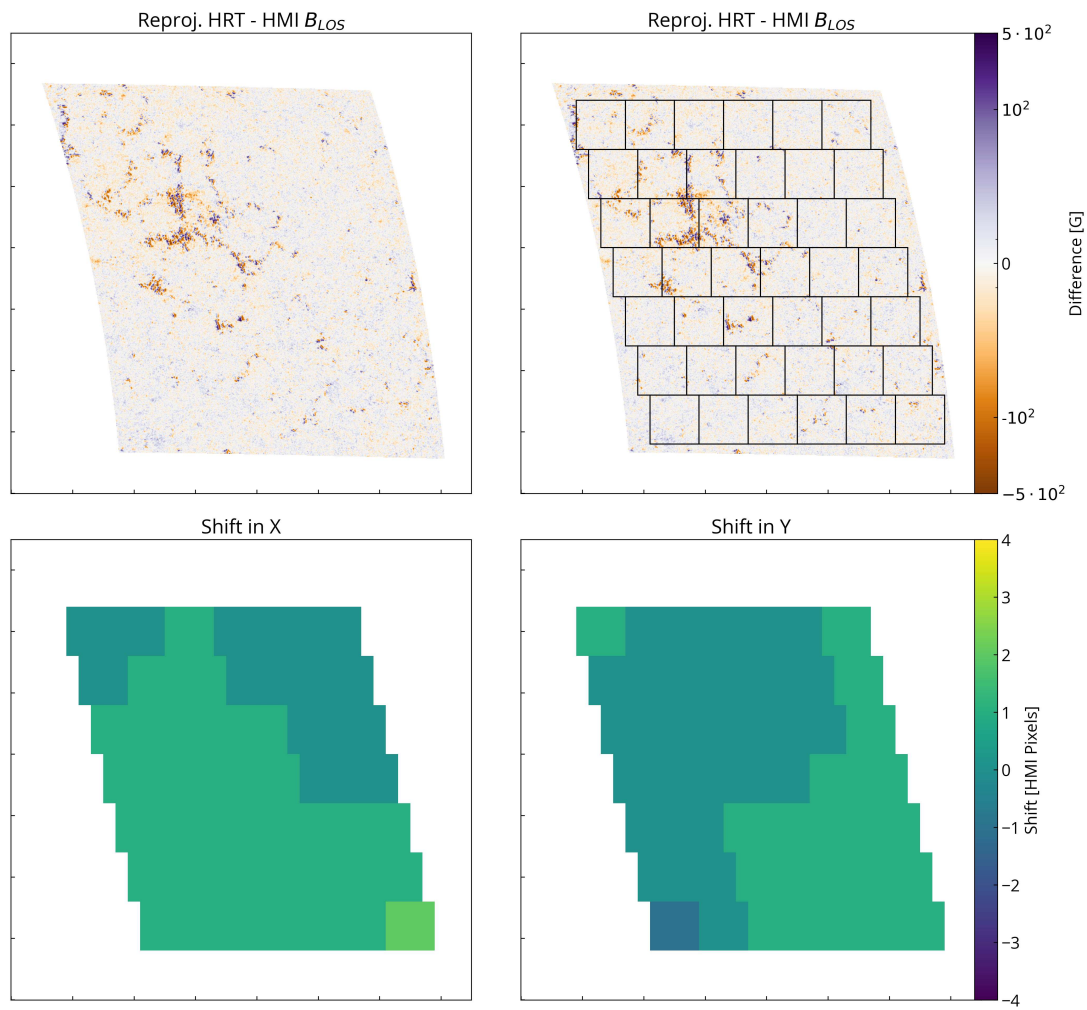


Figure 4.11: Same as Fig. 4.9 but for 19 March 2022 at 11:26 UTC. Furthermore the difference maps are saturated to  $\pm 500$  G.

varies with the focusing position of the SO/PHI-HRT refocusing mechanism (HRM, see Fig. 2.1). From 17 to 21 March 2022, the HRM of SO/PHI-HRT was set to the same position, however before the observations on 22 March, SO/PHI-HRT was refocused as Solar Orbiter approached perihelion.

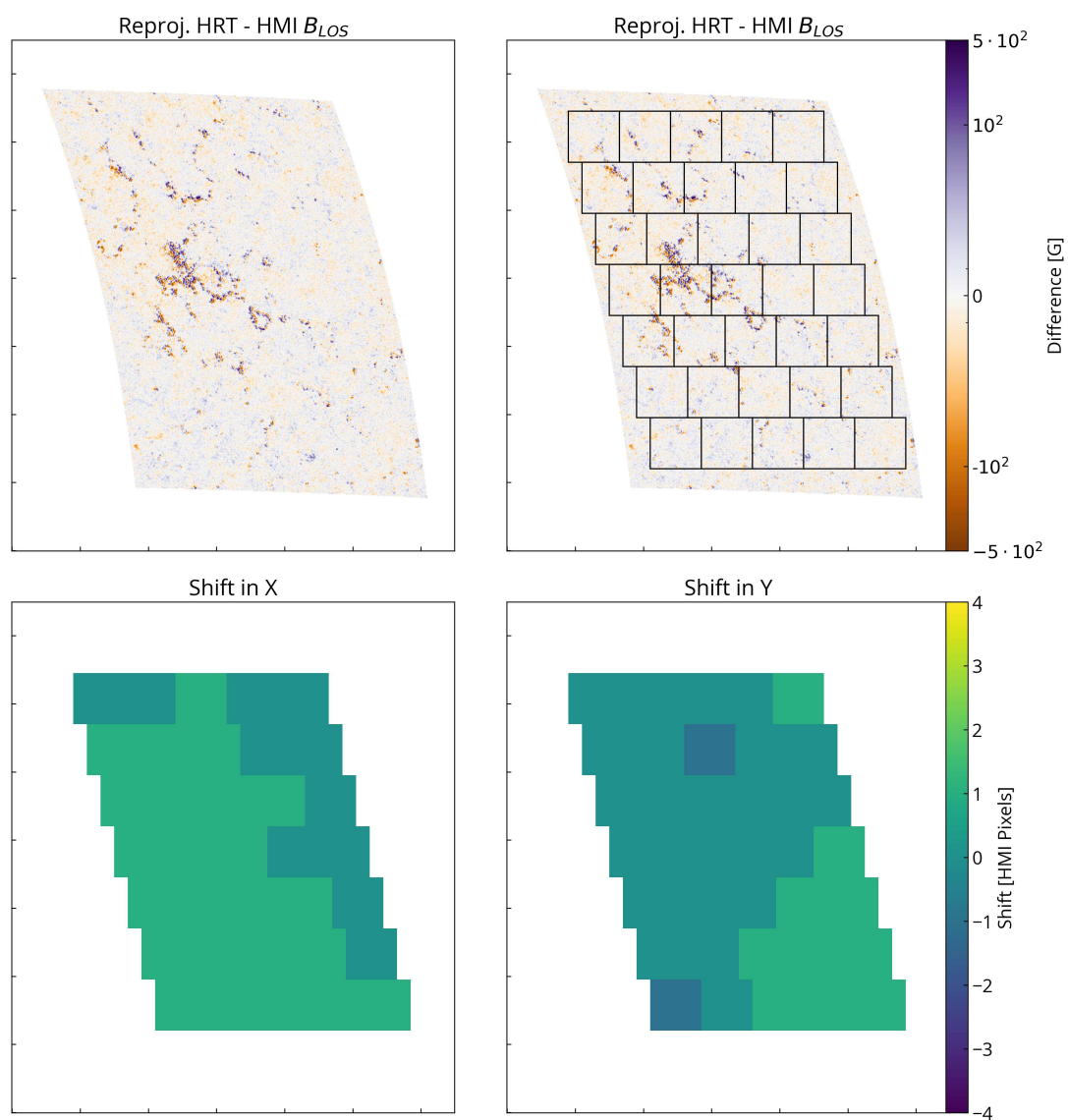


Figure 4.12: Same as Fig. 4.9 but for 20 March 2022 at 11:27 UTC. Furthermore the difference maps are saturated to  $\pm 500$  G.

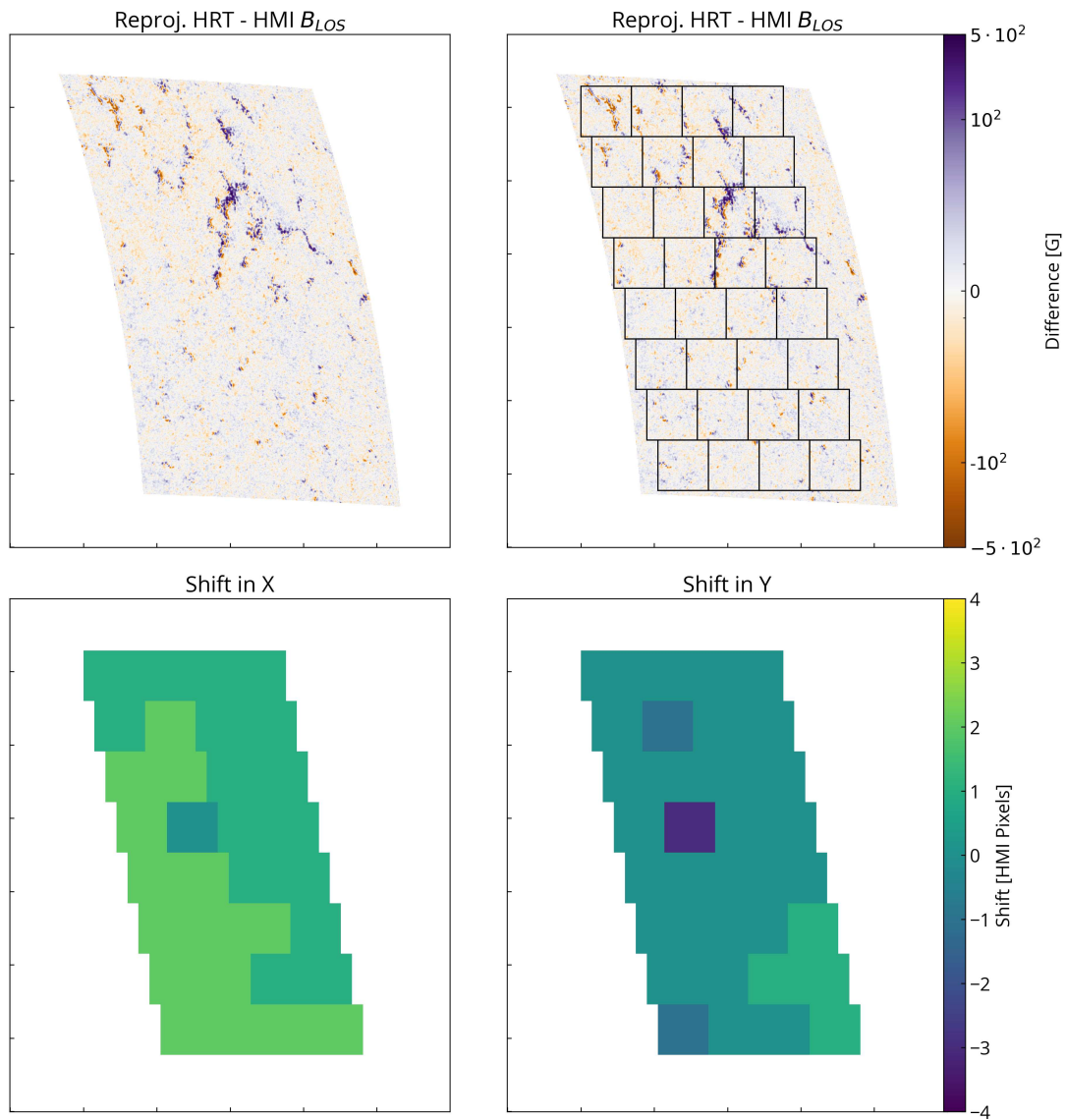


Figure 4.13: Same as Fig. 4.9 but for 21 March 2022 at 12:31 UTC. Furthermore the difference maps are saturated to  $\pm 500$  G, and the outlined sub-regions are  $69 \times 69$  pixels in size.

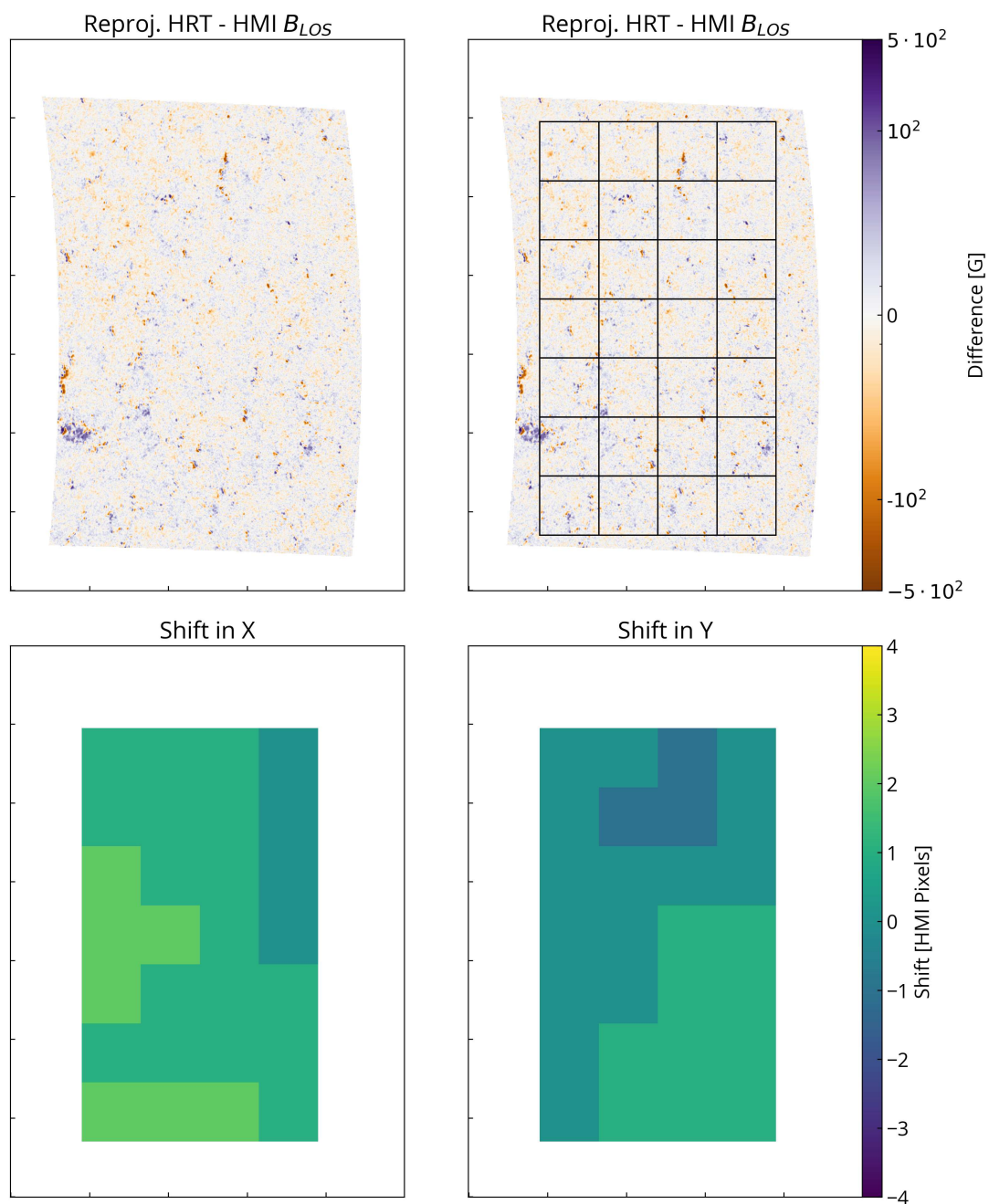


Figure 4.14: Same as Fig. 4.9 but for 22 March 2022 at 10:04 UTC. Furthermore the difference maps are saturated to  $\pm 500$  G.

### 4.3.2 17th March 2022 Comparison

Given the relatively uniform structure of the magnetic field in the umbra of the sunspot pair, I will cautiously present a preliminary comparison of the  $B_{LOS}$  inferred by both instruments in this region. In Fig. 4.15 the sub region of the respective continuum intensity images containing the sunspots is presented. Both continuum images are normalised to the nearby quiet Sun intensity. Like in the magnetograms, the reprojected SO/PHI-HRT continuum image displays greater contrast. As indicated earlier in Fig. 4.9 this region is aligned to within one SDO/HMI pixel in both the  $x$  and  $y$  axes. In the top panel of Fig. 4.15 are white contours which indicate the continuum intensity level of  $0.55 I_c$  in the SDO/HMI continuum image. Following Sainz Dalda (2017), this continuum intensity level is used to determine the boundary of the umbrae. These white contours are also plotted in the SO/PHI-HRT continuum image, and are shown to mostly agree with the green contours of the same intensity level in the reprojected SO/PHI-HRT image, further highlighting a good alignment. Residual differences result from the remaining misalignment, relative optical distortions between HMI and SO/PHI-HRT, differences in centre-to-limb variation of umbral and penumbral contrast and the Wilson depression.

In Fig. 4.16 the total unsigned line-of-sight magnetic flux in the sunspot umbrae from the reprojected SO/PHI-HRT and SDO/HMI magnetograms over the co-temporally observed time series is indicated. To clarify, I use here SDO/HMI magnetograms computed via the Fourier tachometer technique (the MDI-like algorithm, see Couvidat et al. 2012a), which has a close alignment with that from SO/PHI-HRT as shown in Chap. 3. The pixels in the umbrae were selected in both magnetograms using the white contours shown in Fig. 4.15. All pixels selected in both magnetograms were well above their respective noise level and hence the noise can be neglected.

One can see a clear increase in magnetic flux retrieved by SO/PHI-HRT: over  $1 \times 10^{20}$  Mx more flux. One also notices that the temporal variation of the magnetic flux inferred by both instruments agrees very closely. I can now also perform a direct observational test of the  $\mu$ -correction: the  $B_{LOS}$  values of both instruments are divided by  $\mu$  in each pixel and the total flux is calculated. These  $\mu$ -corrected total unsigned magnetic fluxes are indicated in Fig. 4.16 by the dashed lines. It is striking how well the two  $\mu$ -corrected fluxes agree. It was also found that the total unsigned flux from SO/PHI-HRT remained almost constant regardless of the input parameters to the reprojection algorithm, showing that indeed the shortcomings of the algorithm are mitigated in the umbrae.

While the two  $\mu$ -corrected fluxes agree very closely, there are many complex details to be considered. While the magnetic field in sunspot umbra is unipolar, its structure is not homogeneous. In the centre of a sunspot umbra, the magnetic fields are radially inclined, i.e. vertical to the solar surface (e.g. Solanki 2003) while near the umbral boundaries the magnetic fields can be inclined, reaching up to  $40^\circ$  to the surface normal. Given the  $\mu$ -correction relies upon assuming the magnetic field to be radial everywhere, we expect significant differences near the umbral boundary.

The histogram of the  $B_{LOS}$  values from the entire time series are illustrated in Fig. 4.17. This provides a detailed breakdown of the  $B_{LOS}$  distributions and the clear difference between the two instruments. SO/PHI-HRT retrieved much stronger magnetic fields, up to 2 kG, while SDO/HMI only inferred values up to approximately 1.2 kG.

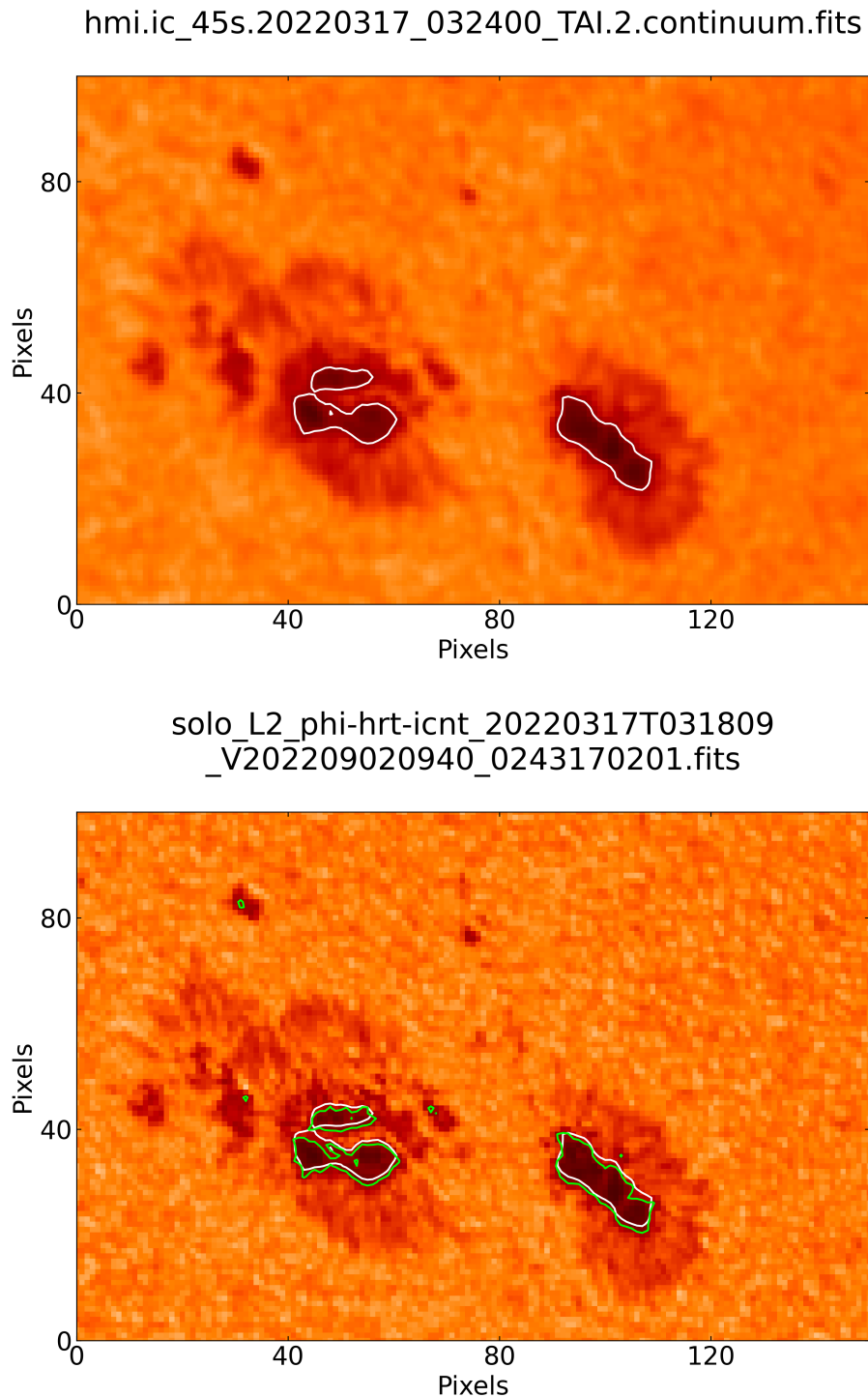


Figure 4.15: Continuum images of the sunspot pair co-spatially observed by SDO/HMI (top) and SO/PHI-HRT (bottom) on 17 March 2022. The SO/PHI-HRT continuum image is reprojected onto the SDO/HMI coordinate frame and resampled to the SDO/HMI pixel size. The contours indicate a continuum intensity level of  $0.55 I_c$ , where  $I_c$  is the nearby quiet Sun continuum intensity: (white contour: SDO/HMI, lime green contour: SO/PHI-HRT). Both contours are shown in the bottom panel to indicate the correct alignment of the two images.

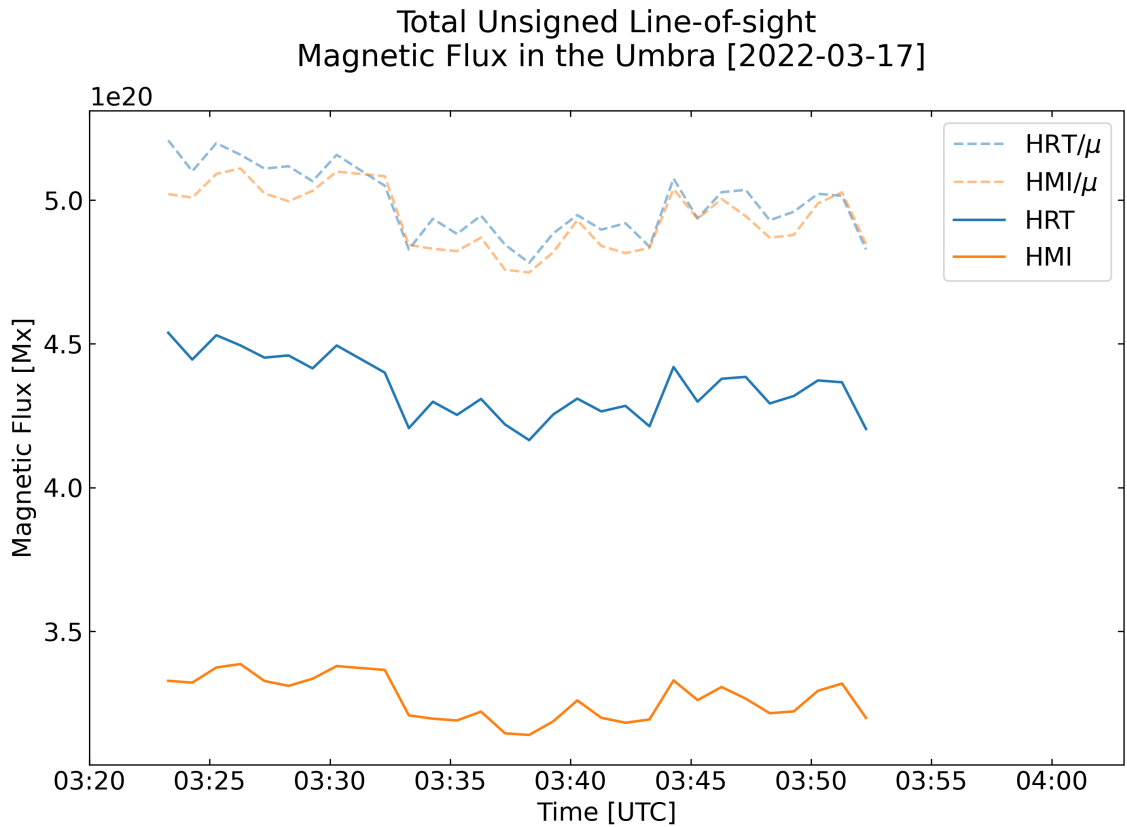


Figure 4.16: Total unsigned LOS magnetic flux in the umbra of the sunspot pair on 17 March 2022 over the co-temporally observed time series. The pixels in the SDO/HMI and reprojected SO/PHI-HRT magnetograms were selected using the white contours depicted in Fig. 4.15. The dashed lines indicate the total unsigned LOS magnetic flux with the  $\mu$ -correction applied to the  $B_{LOS}$  values.

SO/PHI-HRT inferred a wider distribution of line-of-sight field strengths, while SDO/HMI inferred values concentrated around 0.7 – 1 kG. The distributions of the  $\mu$ -corrected  $B_{LOS}$  values are also displayed, and while the total  $\mu$ -corrected magnetic fluxes closely agree, one notices some significant differences: the  $\mu$ -corrected SO/PHI-HRT distribution has a wider tail near 2 kG, while the  $\mu$ -corrected SDO/HMI  $B_{LOS}$  has more values near 1.7 kG.

As mentioned above, the magnetic field in the umbra is not perfectly vertical, which is the basic assumption behind the  $\mu$ -correction. Hence these differences noted when comparing the distributions likely stem from this fact. In some areas the field may be inclined towards the LOS of SO/PHI-HRT and so will observe much stronger fields whereas in other areas it will be preferentially inclined towards the LOS of SDO/HMI and hence will instead observe a stronger LOS magnetic field. Therefore, after dividing by  $\mu$ , large differences in the  $B_{LOS}/\mu$  values will arise.

The close agreement found between the magnetic fluxes after the  $\mu$ -correction is therefore not obvious given the difference in the distribution of the  $B_{LOS}/\mu$  values. A map of the difference in the  $B_{LOS}/\mu$  values for the first pair of magnetograms is shown in Fig. 4.18. While there are no significant differences between the green and white

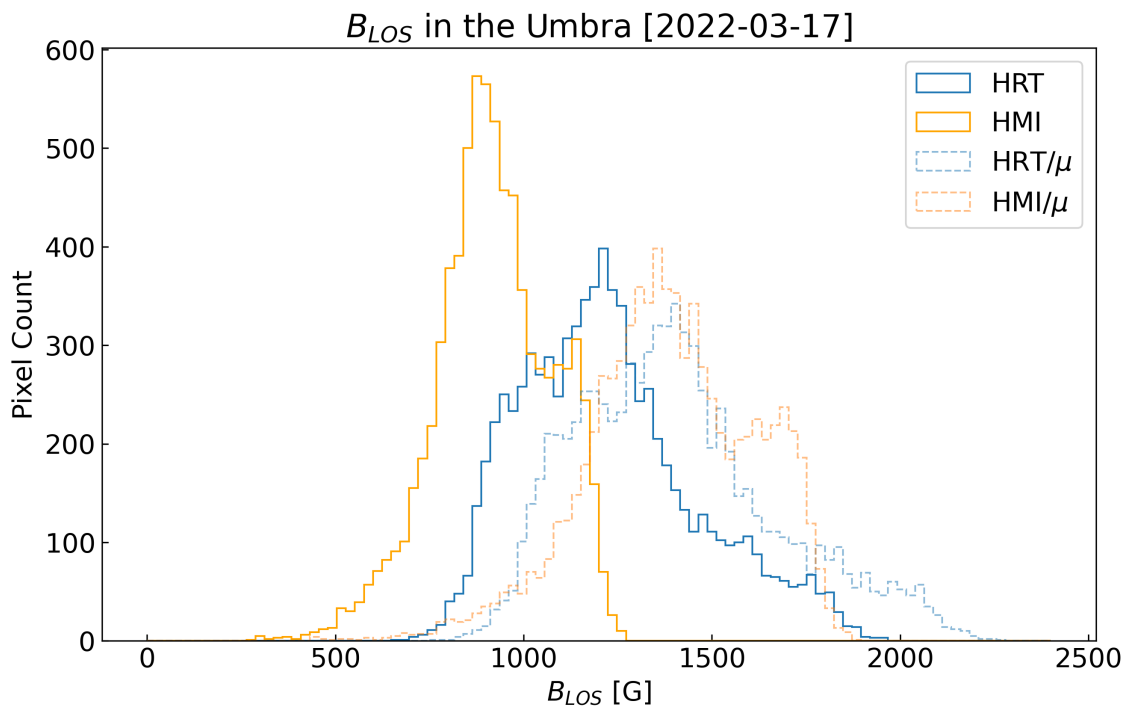


Figure 4.17: Histogram of  $B_{LOS}$  and  $B_{LOS}/\mu$  of SO/PHI-HRT and SDO/HMI in the umbra over the entire co-temporally observed time series, with 100 bins.

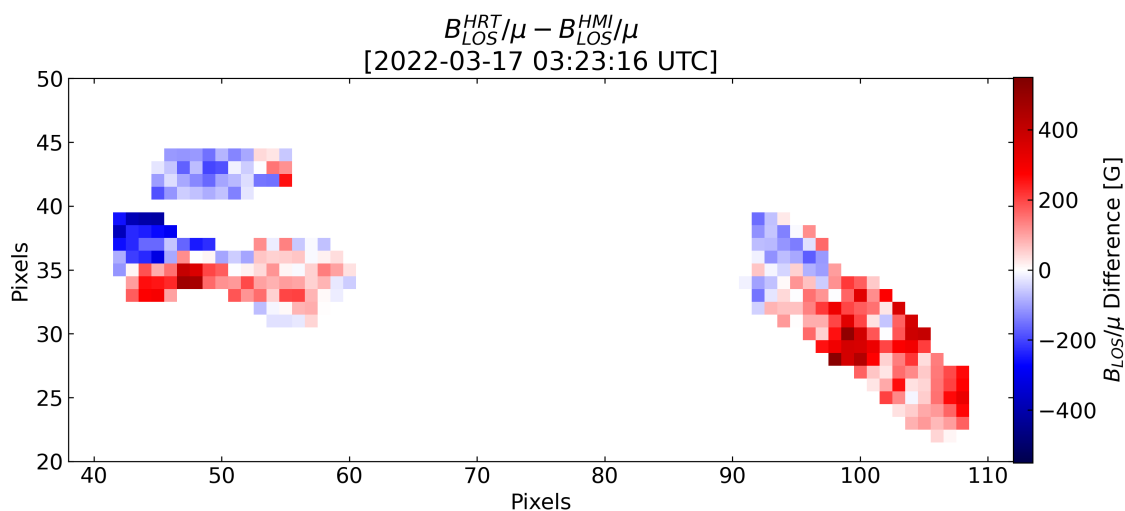


Figure 4.18: Difference in  $B_{LOS}/\mu$  between SO/PHI-HRT and SDO/HMI in the umbral boundary denoted by the white contours in Fig. 4.15 for the first pair of magnetograms on 17 March 2022. The pixels outside the white contours are set to 0. The disc centre in SDO/HMI is towards the bottom left.

contours shown in Fig. 4.15, they do not agree exactly. It is clear that in some areas SO/PHI-HRT resolves a different boundary to the umbra. Hence as the white contour is used in both the SDO/HMI and SO/PHI-HRT magnetograms, some of the pixels in SO/PHI-HRT in fact lie in the penumbra where the fields are weaker and more inclined. The pixels with the darkest blue shading in the left of Fig. 4.18 are in an area where the umbral boundary differs. Here the  $B_{LOS}/\mu$  values inferred by SO/PHI-HRT are up to 440 G lower. The different umbral boundaries may be attributed to the different effective point spread functions of the instruments, as well as their respective lines of sight.

The collection of red pixels near the centre of the umbrae, seen clearly in the right sunspot, indicate that there SO/PHI-HRT infers larger  $B_{LOS}/\mu$  values, up to 530 G more. These larger  $\mu$ -corrected line-of-sight magnetic fields are likely to be the result of the spectral line forming at a lower depth where the magnetic field is stronger, as SO/PHI-HRT observes the umbra closer to disc centre. The spatial distribution of these differences in the umbrae and their magnitude do not change significantly over the entire time series, indicating that these differences are not rooted in random processes.

Using the white contours to select the pixels in SDO/HMI and the green contours to select the pixels in SO/PHI-HRT is also not a satisfactory method to overcoming the different umbral boundaries. This is because some pixels in the neighbouring pores in SO/PHI-HRT also meet the umbral intensity criterion. This is further complicated by the time evolution of these pores, making it difficult to systematically ignore those pixels without manual intervention.

These myriad of details highlight the complicated nature of comparing the same magnetic feature in magnetograms from two different positions with two different instruments. While the shortcomings of the reprojection algorithm persist and the different effective PSFs are not accounted for, I cannot include the contribution that arises from the slight difference in  $B_{LOS}$  inferred by the two instruments ( $B_{LOS}^{HRT} = 0.97 \times B_{LOS}^{HMI} + 0.73$ ) determined in Chapter 3.

## 4.4 Conclusion

In this chapter I have presented 6 sets of co-observations with SO/PHI-HRT and SDO/HMI that are suitable for stereoscopic analysis of the line-of-sight magnetic field. These 6 co-observations were recorded two weeks after the co-observations that I used in Chapter 3 to investigate the differences between the two instrument's magnetic field data products, where Solar Orbiter was very close to the Sun-Earth line. The regions observed by SO/PHI-HRT covered a wide range of photospheric features, from sunspots and plage regions to the quiet Sun. For all but one of the 6 days SO/PHI-HRT observed regions near disc centre. Over the 6 days, Solar Orbiter progressively moved further away from the Sun-Earth line but remained in the ecliptic plane, and hence these co-observed regions were observed by SDO/HMI closer to the limb and therefore at lower  $\mu$  values.

After correcting the WCS information of the SO/PHI-HRT magnetograms, they were reprojected onto the SDO/HMI coordinate frame and resampled to SDO/HMI pixel sizes to disentangle any foreshortening from other effects caused by the different lines of sight. The performance of the reprojection was evaluated, and residual shifts between the

two were found to be on the order of one or two SDO/HMI pixels. This however seemed to increase up to  $\pm 4$  SDO/HMI pixels when one or both instruments were observing very close to the limb.

From detailed testing of the resampling method that is part of the reprojection algorithm, limitations were uncovered which prevented the comparison of the total LOS magnetic fluxes. By restricting a preliminary comparison of the magnetic fluxes to the sunspot umbrae these limitations were somewhat mitigated. In the sunspot umbrae, a preliminary observational test of the  $\mu$ -correction on  $B_{LOS}$  was made and shown to result in a very close agreement of the total unsigned line-of-sight magnetic fluxes between SO/PHI-HRT and SDO/HMI.

However the spatial distribution of the difference in the  $B_{LOS}/\mu$  values revealed clear differences, which is not surprising given that fields in sunspot umbrae are vertical typically only in a small part of the umbra and can reach inclinations up to  $40^\circ$  near the boundary of the umbra. Division by  $\mu$  clearly does not provide  $\mathbf{B}$  if the field is not vertical and can be responsible for a significant part of the discrepancy between the results obtained by the two instruments. After reprojection the umbral boundaries differed somewhat between the two instruments. Hence where these boundaries disagreed significant differences in the  $B_{LOS}/\mu$  were found. The inclined nature of the magnetic field near the boundaries together with the different lines of sight may also contribute. In the centre of the umbra, SO/PHI-HRT inferred much stronger line-of-sight fields even after applying the  $\mu$ -correction. The larger  $B_{LOS}/\mu$  values near the centre of the umbrae are most likely due to the different formation heights of the spectral line as a result of the different lines of sight. Once the resampling algorithm is further developed, other instrumental effects, such as the difference in effective PSFs and small difference between the two instrument's magnetograms that I characterised in Chapter 3 will need to be included and investigated.

This analysis has demonstrated that much more work is needed to thoroughly investigate how the different viewing angles impact the retrieved line-of-sight magnetic fields. It is clear that many more magnetograms, at different  $\mu$  values and simultaneously a wide range of difference of the  $\mu$  values between the two instruments, must be compared to build up a complete picture. Until Solar Orbiter moves out of the ecliptic to better view the poles, further tests can be undertaken while in the ecliptic. As evidenced by the comparison in Sect. 4.3.2, sunspots are excellent candidates to test the efficacy of the  $\mu$ -correction, as they consist of both radial and highly inclined strong magnetic fields. Hence a prime candidate of an observing campaign which meets these criteria is the "R\_SMALL\_MRES\_MCAD\_AR-Long-Term" SOOP<sup>§</sup>. This SOOP has been performed three times and is scheduled to run for a fourth time in October 2024. In Chapter 6 an outlook is provided that highlights preliminary data from the October 2023 instance.

---

<sup>§</sup>[https://s2e2.cosmos.esa.int/confluence/display/SOSP/R\\_SMALL\\_MRES\\_MCAD\\_AR-Long-Term](https://s2e2.cosmos.esa.int/confluence/display/SOSP/R_SMALL_MRES_MCAD_AR-Long-Term)



# 5 Magnetograms underestimate even unipolar magnetic flux nearly everywhere on the solar disk

Sinjan, J. ; Solanki, S. K. ; Hirzberger, J. ; Riethmüller, T. ; Przybylski, D.  
*Astronomy & Astrophysics*, Vol. 690, A341, 2024. DOI:10.1051/0004-6361/202450267<sup>¶</sup>

## 5.1 Abstract

*Context.* The amount of magnetic flux passing through the solar surface is an important parameter determining solar activity and the heliospheric magnetic field. It is usually determined from line-of-sight magnetograms.

*Aims.* We aim to test the reliability of determining the line-of-sight magnetic field from a 3D MHD simulation of a unipolar region. In contrast to earlier similar studies, we consider the full solar disk, by considering the full centre-to-limb variation, as well as regions with different averaged field strengths.

*Methods.* We synthesised Stokes profiles from MURaM MHD (magnetohydrodynamics) simulations of unipolar regions with varying mean vertical magnetic flux densities, ranging from quiet Sun to active region plage. We did this for a comprehensive range of heliocentric angles: from  $\mu = 1$  to  $\mu = 0.15$ , and for two commonly used photospheric spectral lines: Fe I 6173.3 and Fe I 5250.2 Å. The synthesised profiles were spatially foreshortened and binned to different spatial resolutions characteristic of space-based magnetographs currently in operation. The line-of-sight magnetic field was derived with a Milne-Eddington Inversion as well as with other commonly used methods.

*Results.* The inferred spatially averaged  $\langle B_{LOS} \rangle$  is always lower than that present in the MHD simulations, with the exception of  $\mu \approx 1$  and sufficiently high spatial resolution. It is also generally inconsistent with a linear dependence on  $\mu$ . Above  $\mu = 0.5$  the spatial resolution greatly impacts the retrieved line-of-sight magnetic field. For  $\mu \leq 0.5$  the retrieved  $B_{LOS}$  is nearly independent of resolution, but is always lower than expected from

---

<sup>¶</sup>The contents of this chapter are identical to the version of Sinjan, J. ; Solanki, S. K. ; Hirzberger, J. ; Riethmüller, T. ; Przybylski, D., 2024, Magnetograms underestimate even unipolar magnetic flux nearly everywhere on the solar disk, *Astronomy & Astrophysics*, vol. 690, A341, with a CC-BY 4.0 licence. I, Jonas Sinjan, completed all the underlying work, wrote the first draft text and created the figures for all sections of this publication. The co-authors provided comments on the draft text and created the MURaM simulations that I used.

the simulation. These trends persist regardless of the mean vertical magnetic field in the MHD simulations and are independent of the  $B_{LOS}$  retrieval method. For  $\mu \leq 0.5$ , a larger  $\langle B_{LOS} \rangle$  is inferred for the 5250.2 Å spectral line than 6173.3 Å, but the converse is true at higher  $\mu$ .

*Conclusions.* The obtained results show that with high spatial resolution observations, for instance those achieved with SO/PHI-HRT (High Resolution Telescope of the Polarimetric and Helioseismic Imager on Solar Orbiter) at close perihelion, the magnetic flux can be reliably retrieved at high  $\mu$  values, whereas in lower resolution observations, as well as at lower  $\mu$ , a significant fraction of the magnetic flux is missed. The results found here raise some doubts of the reliability of determining the radial field by dividing the line-of-sight field by  $\mu$  and are of considerable importance for deducing the total magnetic flux of the Sun. They may also contribute to the resolution of the open flux problem.

## 5.2 Introduction

Obtaining the correct amount of magnetic flux passing through the solar surface is important for many purposes. In mixed polarity regions, the flux and its density, that is the field strength, determine the total magnetic energy and hence are a guide to the heating of the upper solar atmosphere. In unipolar regions associated with open magnetic field lines, such as coronal holes, the magnetic flux contributes to the heliospheric magnetic field.

It is well known that in mixed polarity regions the measured magnetic flux density depends strongly on the spatial resolution (e.g. Krivova and Solanki 2004, Pietarila Graham et al. 2009, Chitta et al. 2017). For unipolar fields, however, it has often been assumed that the correct amount of magnetic flux in unipolar regions is determined more or less independently of spatial resolution of the observations.

At the same time, it has often been assumed that at least outside sunspots, most of the magnetic flux seen by full-disk magnetograms is vertical (i.e. radial), so that line-of-sight (LOS) magnetograms are sufficient to get the correct magnetic flux density, at least in unipolar magnetic regions. This assumption has been made in part due to the difficulty of retrieving a meaningful magnetic field vector outside of active regions. This in turn is because the signal in Stokes  $Q$  and  $U$  is typically much lower than in Stokes  $V$  outside sunspots and for spectral lines in the visible spectral range, making LOS fields the most reliably deduced component of the magnetic field. The vertical component of the field can be computed by dividing the LOS magnetic field,  $B_{LOS}$ , by the cosine of the angle of incidence,  $\theta$ , the heliocentric angle,  $\mu = \cos(\theta)$  (e.g. Murray 1992, Fligge et al. 2000, Hagenaar 2001). In the following we will refer to this practice as the ‘ $\mu$ -correction’.

Coronal holes are typical regions where unipolar magnetic fields are observed, with the most prominent being those located at the poles of the Sun around minima of solar activity cycles. Due to the geometry, retrieving the vector magnetic field is difficult there. Tsuneta et al. (2008a) observed large  $> 1$  kG unipolar patches on the poles with Hinode SOT/SP (Spectral-polarimeter on the Solar Optical Telescope) that were predominantly radial and Prabhu et al. (2020) also inferred large unipolar kG patches at the pole with the IMAx instrument on the SUNRISE balloon-borne observatory (Solanki et al. 2010, Barthol et al. 2011, Martínez Pillet et al. 2011, Gandorfer et al. 2011, Berkefeld

et al. 2011) but without the need of a magnetic filling factor.

The polar magnetic field is important for a variety of reasons. For example, the polar magnetic field has been shown to be a key element to predicting the strength of the next solar cycle (Schatten et al. 1978, Cameron and Schüssler 2007, Wang and Sheeley 2009). Furthermore the fast solar wind originates from large coronal holes, from around the poles during solar minima (Krieger et al. 1973). There is also a longstanding unsolved problem known as the open flux problem (e.g. Wang and Sheeley Jr. 1995, Linker et al. 2017). It consists of a 2 – 3 factor mismatch between the open flux directly measured in-situ at 1 au and that calculated from the magnetic flux at the solar surface in large coronal holes, and extrapolated to 1 au. Current ideas to explain this mismatch include: missing coronal holes, open magnetic flux not in dark EUV or X-ray emission regions or an underestimation of the open magnetic flux in synoptic LOS magnetograms. This last idea strongly motivates this study: if the radial field deduced from the LOS magnetic field measured over the solar disk underestimates the actually present field, then this could contribute to solving the open flux problem.

Retrieving the vector magnetic field in coronal holes is not straightforward, even more so when they are located at the limb, for example at the poles. To retrieve the complete magnetic vector full Stokes polarimetry is required. However the Stokes signals of the transverse component of the magnetic field are intrinsically lower than the longitudinal component as they are a second order effect for incomplete Zeeman splitting (which is typically the case outside sunspots for spectral lines in the visible spectrum), and therefore the signal to noise ratio is lower. First of all, coronal holes have relatively low spatially averaged field strengths, similar to quiet Sun regions, so that Stokes signals are typically small, those of Stokes  $Q$  and  $U$  particularly so.

Although cancellation of Stokes  $V$  profiles occurs to a much smaller degree, due to the dominance of one magnetic polarity (e.g. Wiegmann and Solanki 2004), near the limb foreshortening plays a major role as the projected area encompassed by one resolution element of the photosphere increases by  $1/\mu$ . The detected rays from these foreshortened areas travel a much longer path through the solar atmosphere, and when  $\mu$  is low enough, rays from magnetically strong regions pass through nearby non-magnetic regions where significant absorption can take place (Audic 1991, Solanki et al. 1998), which further reduces the polarised Stokes parameters. The lower intensity levels near the limb also result in lower signal to noise ratios. Finally, the fact that the lines are formed higher near the limb, where the field strength in magnetic features is reduced (due to horizontal pressure balance) implies smaller Zeeman splitting which results in even lower Stokes  $Q$  and  $U$  profiles relative to Stokes  $V$ .

When observing off disc centre, the spectropolarimetric signature of magnetic features near the limb has not been well characterised. Solanki et al. (1998) synthesised rays utilising different flux tube models over a range of  $\mu$  down to  $\mu = 0.2$  for a variety of spectral lines. They found that the amplitude of Stokes  $V$  need not follow the  $\mu$  linear dependence as expected by the  $\mu$ -correction. Near the limb, almost all diagnostics were greatly affected by the passage of rays through non-magnetic material, and by the width of the flux tubes in their models. They also suggested that the global magnetic flux may be underestimated near the limb.

Hinode SOT/SP (Tsuneta et al. 2008b) uniquely combines high spatial resolution and polarimetric sensitivity. However, even this may not be sufficient to reliably determine the magnetic vector close to the limb (Centeno et al. 2023). These authors simulated polar observations by Hinode SOT/SP at  $\mu = \cos(65^\circ) = 0.42$  and found strong biases in the retrieval of the inclination and azimuth. They point out that photon noise, projection effects, telescope spatial point spread function, spectral point spread function and the limitations of Milne-Eddington inversions (with a variable magnetic filling factor) all contribute towards the generation of these observed biases. They do, however, find that pixel-averaged quantities, such as  $B_{LOS}$  when assuming a filling factor of unity, highly correlate with the MURaM simulations they used to create the synthetic observations.

Furthermore Plowman and Berger (2020c) and more recently Milic et al. (2024) found that with reduced spatial resolution, the mean LOS magnetic flux is not accurately retrieved: it is underestimated. Plowman and Berger (2020c) explained this through correlations between magnetic flux density and continuum brightness (assuming that magnetic features are comparatively dark) while Milic et al. (2024) instead argue that this is due to non-linearity of the methods used to infer the magnetic field. The study by Milic et al. (2024) was limited to disk centre views (i.e.  $\mu = 1$ ), which means that their results are not applicable to fields in the polar coronal holes (at least not as seen from Earth, or even from Solar Orbiter at its maximum heliolatitude; see Müller et al. (2020).

Due to these challenges in determining the correct magnetic flux in coronal holes, we aim to use radiative MHD simulations of unipolar photospheric regions for a comprehensive range of  $\mu$  values to study how reliably the LOS field can be retrieved. In this way we not only test the  $\mu$ -correction to retrieve the radial magnetic field from unipolar regions away from disk centre, but also gain an idea of whether the dependence on spatial resolution of the magnetic flux obtained at disk centre is also valid closer to the limb, or if indeed magnetic flux may be generally underestimated in unipolar regions, such as coronal holes, including those near the solar limb. We do this for several spatial resolutions, mimicking those of SDO/HMI (Helioseismic Imager on the Solar Dynamics Observatory, Scherrer et al. 2012), SO/PHI-HRT and FDT (Full Disk Telescope of SO/PHI) and lower resolution magnetographs, and for several levels of magnetic flux density, ranging from relatively quiet Sun typical of coronal holes to strong plage regions.

In Sect. 5.3 we introduce the radiative magnetohydrodynamic (MURaM) simulations employed and in Sect. 5.4 we present the method we implemented to synthesise the Stokes profiles from the MHD simulations at a range of  $\mu$  values. The method to bin these profiles to different spatial resolutions is detailed in Sect. 5.5. The method by which the line of sight magnetic field is inferred is outlined in Sect. 5.6. In Sect. 5.7 we present the CLV (Centre-to-Limb Variation) of the inferred LOS magnetic field and discuss the limitations of our work in Sect. 5.8. We outline our conclusions in Sect. 5.9.

### 5.3 MURaM simulations

Three-dimensional magnetoconvection simulations of the photosphere were computed using the MURaM code (Vögler et al. 2005). MURaM solves the MHD equations along with radiative energy transport. The radiative energy exchange rate is computed via non-

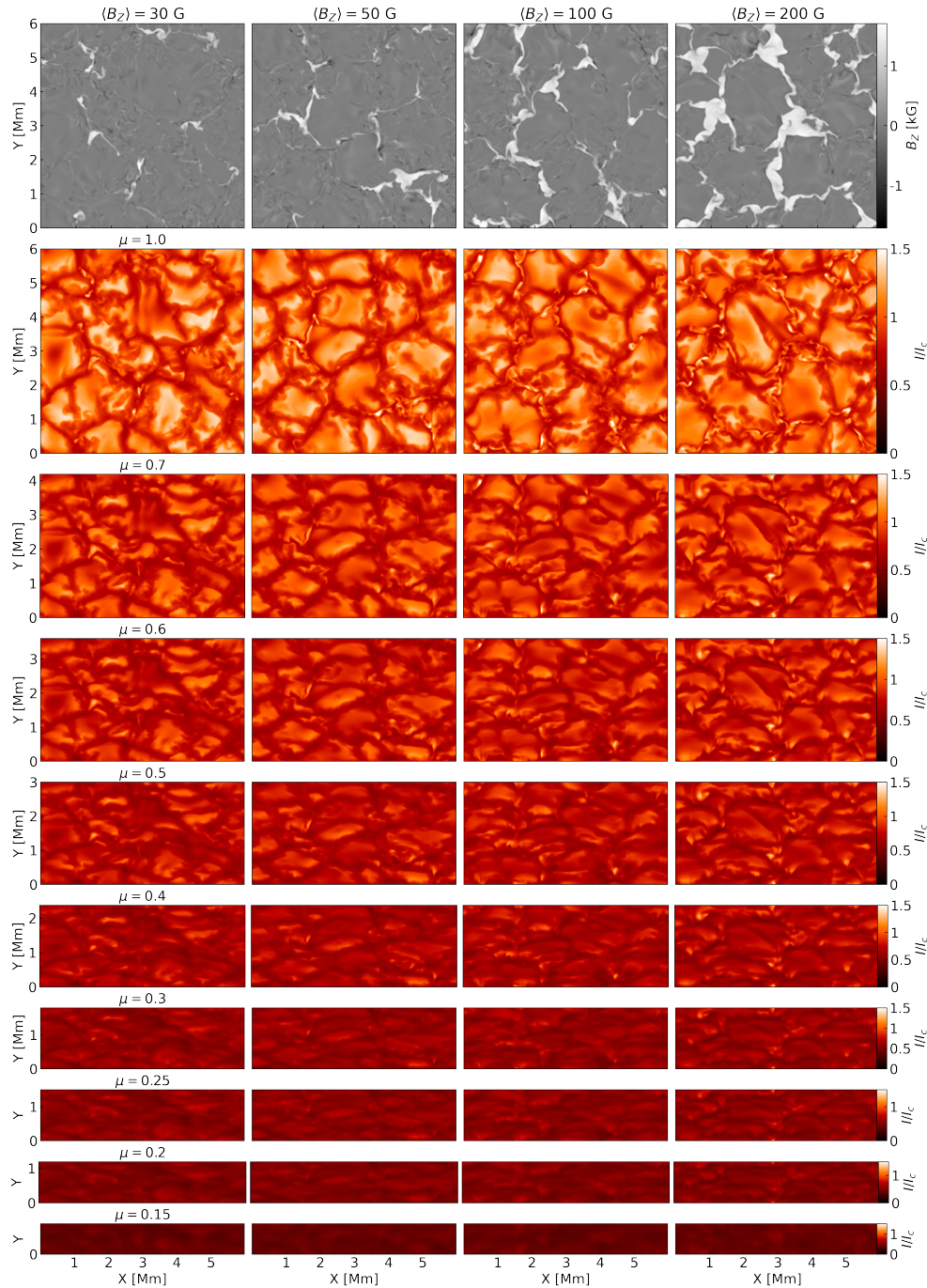


Figure 5.1: MHD simulations and the corresponding synthetic Stokes I maps. Top row:  $B_z$  in kG of the MURaM simulations at a height of  $z = 0.85$  Mm above the bottom layer of the simulation box, which approximately corresponds to the visible surface layer. From left to right snapshots of simulations with different initially imposed mean vertical magnetic fields of  $\langle B_z \rangle = 30, 50, 100$  and  $200$  G. Second row to bottom row: Synthetic Stokes  $I/I_c$  maps at  $d\lambda = -0.35$  Å for the Fe I 6173.3 Å absorption line for  $\mu = \cos(\theta)$  decreasing from  $\mu = 1.0$  to  $\mu = 0.15$ . For  $\mu < 1$  the y axis is foreshortened. The  $I/I_c$  maps are saturated from 0 to 1.5 units of the average continuum intensity,  $I_c$ , at  $\mu = 1$ . The maps at  $\mu = 0.9$  and  $0.8$  are omitted for brevity.

grey radiative transfer under local thermodynamic equilibrium (LTE) and the equation of state takes into account partial ionisation. The simulation box has physical dimensions of  $6 \times 6 \times 1.4$  Mm ( $x, y, z$ ), where  $z$  is the vertical axis, and has periodic horizontal boundary conditions. The box roughly covers 800 km below the visible surface and 600 km above. The horizontal extent of the simulation domain is sufficient in size, as at  $\mu = 0.15$ , the extent of the foreshortened axis is 900 km, which equates to just over two SDO/HMI pixels, just under 9 SO/PHI-HRT pixels, and more than one SO/PHI-FDT pixel when SO/PHI is at perihelion. The grid size is  $288 \times 288 \times 100$  cells resulting in cell sizes of 20.8 km in the horizontal directions and 14 km in the vertical axis.

The simulation box has a free in- and outflow lower boundary condition and a closed top boundary, while conserving the total mass. A non-grey radiative energy transfer with four opacity bins is included. The simulation box was first initialised under hydrodynamic conditions following which a homogeneous, unipolar vertical magnetic field was introduced. The outputs of simulations with initially imposed mean vertical fields of 30, 50, 100 and 200 G were included in this investigation. Analysing MHD cubes with such a range of fields allows us to determine the effect of a variety of solar environments on the determined magnetic flux density, from the weakest quiet Sun, to a strong plage region. Once the simulation had evolved to a statistically stationary state, after approximately 18 hours of solar time, snapshots were taken every 3–7 minutes, approximately the granule turnover time, allowing for sufficient evolution such that each snapshot is statistically independent. These simulations were produced in the initial stages of investigation for the Riethmüller et al. (2014a) study, where they were shown to be highly consistent with observations.

To improve the statistics, we considered 20 snapshots each for 30 G and 50 G, 19 for 100 G and 14 for 200 G. Less snapshots were required for  $\langle B_z \rangle = 200$  G as the results did not change when more than 10 snapshots were considered. A single snapshot for each  $\langle B_z \rangle$  is shown in the top row of Fig. 5.1. It is clear that as the mean vertical flux in the domain increases more, larger and stronger flux concentrations appear. These simulated unipolar regions represent different features on the solar surface:  $\langle B_z \rangle = 30, 50$  G represent conditions that are similar to the unipolar very quiet and the average quiet Sun, respectively (i.e. typical of coronal holes). These quiet Sun simulations well reproduce observations from the Sunrise mission (Riethmüller et al. 2014a). Meanwhile the simulations with  $\langle B_z \rangle = 100$  G represent the network field, and  $\langle B_z \rangle = 200$  G a plage region as found within active regions. Due to flux conservation and the periodic boundary conditions, the horizontally averaged (over the X-Y plane) vertical flux density,  $\langle B_z \rangle$ , remains constant with geometric height in all snapshots with a numerical accuracy of 0.02%. This simulation setup allows us to have a known value of the flux within the simulation domain, to which we can compare the retrieved line-of-sight magnetic flux via our methods outlined in Sect. 5.6 and Sect. 5.7.3 (the actual comparisons are between spatially averaged flux density, which is equivalent). The situation does not change in principle when computing the radiation emerging at an angle from the simulation box (smaller  $\mu$ ), except that it is more complex because the rays often pass through multiple magnetic structures as well as the space in between (see Solanki et al. 1998, for a description in a much more idealised version of the same geometry).

## 5.4 Spectral Synthesis

The SPINOR code (Frutiger et al. 2000, Frutiger 2000) was used to generate the synthetic Stokes profiles using the STOPRO routines (Solanki 1987) for the 6173.3 Å and 5250.2 Å Fe I absorption lines. The 6173.3 Å line was selected as it is sampled by both the SDO/HMI and SO/PHI vector magnetographs. The 5250.2 Å line was chosen for comparison with earlier works such as Solanki et al. (1998) and because both IMAx on the first two flights of Sunrise and the TuMAG instrument, a further development of the IMAx instrument, sample this line; TuMAG is scheduled to fly on the balloon-borne SUNRISE III mission in 2024 (Álvarez Herrero et al. 2022).

For both spectral lines, the profiles were synthesised over a wavelength range of  $\pm 350$  mÅ from the reference line core wavelength  $\lambda_0$ , which corresponds to a cut-off velocity of approximately  $\pm 17$  km/s for 6173.3 Å and  $\pm 20$  km/s for 5250.2 Å. This range was chosen to exclude contributions from nearby spectral lines, such as 6172.7 Å. For the 5250.2 Å case, neighbouring lines such as the strong Fe I 5250.6 Å line, were not synthesised as this would impact the retrieval of  $B_{LOS}$  via standard methods such as a Milne-Eddington inversion. The spectral sampling of the synthesis for both lines is 14 mÅ.

For synthesis of Stokes profiles off disc centre, the grid is adapted by the SPINOR code such that the slanted LOS (line-of-sight) becomes the new ‘vertical’. This is achieved by shifting the horizontal layers by  $n \times D_z \tan(\theta)$ , where  $n$  is the layer index,  $D_z = 14$  km is the vertical grid resolution and  $\theta$  is the angle of incidence, the heliocentric angle. However this shift is rarely an integer value of pixels, resulting in residuals of sub-pixel shifts. To compensate, a 2D linear interpolation is performed horizontally. Furthermore, the vertical grid spacing is increased to reflect the longer path travelled through each cell:  $\Delta z = D_z / \cos(\theta)$ . Next an atmosphere is built using 5000 Å as the default reference continuum wavelength to create the optical depth scale. Each column, is converted into vertical units of  $\log(\tau_{5000})$ , where  $\tau_{5000}$  is the optical depth at 5000 Å continuum. When  $\mu = \cos(\theta)$  is very low, the increased vertical grid spacing, now in  $\log(\tau_{5000})$ , becomes very large, such that the vertical change in temperature can be quite large. To mitigate this, the  $\log(\tau_{5000})$  grid is also interpolated in the vertical direction.

Additionally, the horizontally averaged solar surface, the layer where  $\langle \tau_{5000} \rangle = 1$ , is computed before the synthesis. This surface is set as the reference height layer,  $n = 0$ , such that it is not shifted horizontally. All other layers are shifted with respect to this reference layer. This layer is chosen to be fiducial because the continuum is formed near this layer. This choice thus mitigates unwanted artefacts from the interpolation and horizontal shifting near the height of formation of the spectral line. Stokes profiles are synthesised from  $\mu = 1.0 \dots 0.15$  with a step size of 0.1 in  $\mu$ . Below  $\mu = 0.3$ , the step size is reduced to 0.05.

To improve the statistics, the profiles were synthesised from two opposite viewing directions for the full range of  $\mu < 1$  values. Because the simulation snapshots are not symmetric, in general the results differ somewhat for the two viewing angles.

We now consider some of the limitations of our analysis. Firstly, the synthesis of the spectral lines did not consider any non-LTE effects, which have been shown to be

significant for the Fe I 6173.3 Å line (Smitha et al. 2023). It is unclear, however, how large this neglect has on the results presented here. Smitha et al. (2020) studied the effect of neglecting NLTE effects when inverting lines computed in NLTE. They found average errors in the field strength of around 10 G, corresponding to an average relative error of about 5% at the node with the largest signal (their Fig. 9). Although their result applies to the Fe I 6301.5 and 6302.5 Å line pair, which react somewhat differently to NLTE effects, it still suggests that uncertainty due to neglecting NLTE is considerably smaller than the effects we find here.

Secondly, at extreme low  $\mu$ , the curvature of the Sun should also be considered. Here we estimate if neglecting curvature could significantly affect our results. For a ray travelling from the bottom to the top of the solar atmosphere, the change in intensity  $I$  can be described by:

$$\frac{dI}{ds} = -\kappa_\nu I + \epsilon_\nu, \quad (5.1)$$

where  $ds$  is directed along the ray and  $\kappa_\nu$  and  $\epsilon_\nu$  are the absorption and emission coefficients at a wavelength  $\nu$  (Rutten et al. 2003). When assuming a plane parallel atmosphere, as we do here, we can transform  $ds$  to a function of the vertical distance  $z$  and  $\mu$  the cosine of the angle of the ray between the vertical axis:  $dz = \mu ds$ :

$$\mu \frac{dI}{dz} = -\kappa_\nu I + \epsilon_\nu. \quad (5.2)$$

To estimate the error by neglecting the curvature of the Sun we can transform the above into spherical coordinates, with radius  $r$  and  $\mu$ :

$$\mu \frac{\partial I}{\partial r} + \frac{1 - \mu^2}{r} \frac{\partial I}{\partial \mu} = -\kappa_\nu I + \epsilon_\nu. \quad (5.3)$$

This extra term,  $\frac{1 - \mu^2}{r} \frac{\partial I}{\partial \mu}$ , is the error we introduce by ignoring the Sun's curvature. When comparing the order of magnitudes of the first two terms we find an upper estimate for this term:

$$\frac{1 - \mu^2}{R_\odot} \frac{Z}{\mu}, \quad (5.4)$$

where  $r$  has become  $R_\odot = 696$  Mm, the solar radius, and  $Z = 1.4$  Mm is the length scale of  $\partial r$  of the considered simulation domain. This is an upper estimate as the key length scale for  $\partial r$  is the vertical height over which the majority of the spectral line is formed, which is hundreds of km for photospheric lines rather than the entire vertical extent that we have considered here. For  $\mu = 0.15$ , this fraction is 1.3%, and therefore we can safely neglect the Sun's curvature. Only below  $\mu = 0.05$  does this second term become significant (>5%).

Maps of Stokes  $I/I_c$ , where  $I_c$  is the average Stokes  $I$  in the continuum at  $\mu = 1$ , are shown in the native MURaM resolution from the second row to the bottom row in Fig.5.1 for  $\mu = 1.0 \dots 0.15$  for different  $\langle B_Z \rangle$ . The viewing angle is such that  $y = 0$  is nearer to disc centre, while the top of each image is located nearer to the limb. We define this viewing direction as 'positive', while viewing from the opposite side is 'negative'. The CLV of Stokes  $I$  can be seen, with the map becoming darker as  $\mu$  approaches the limb. The profiles are spatially foreshortened to represent the projection effect.

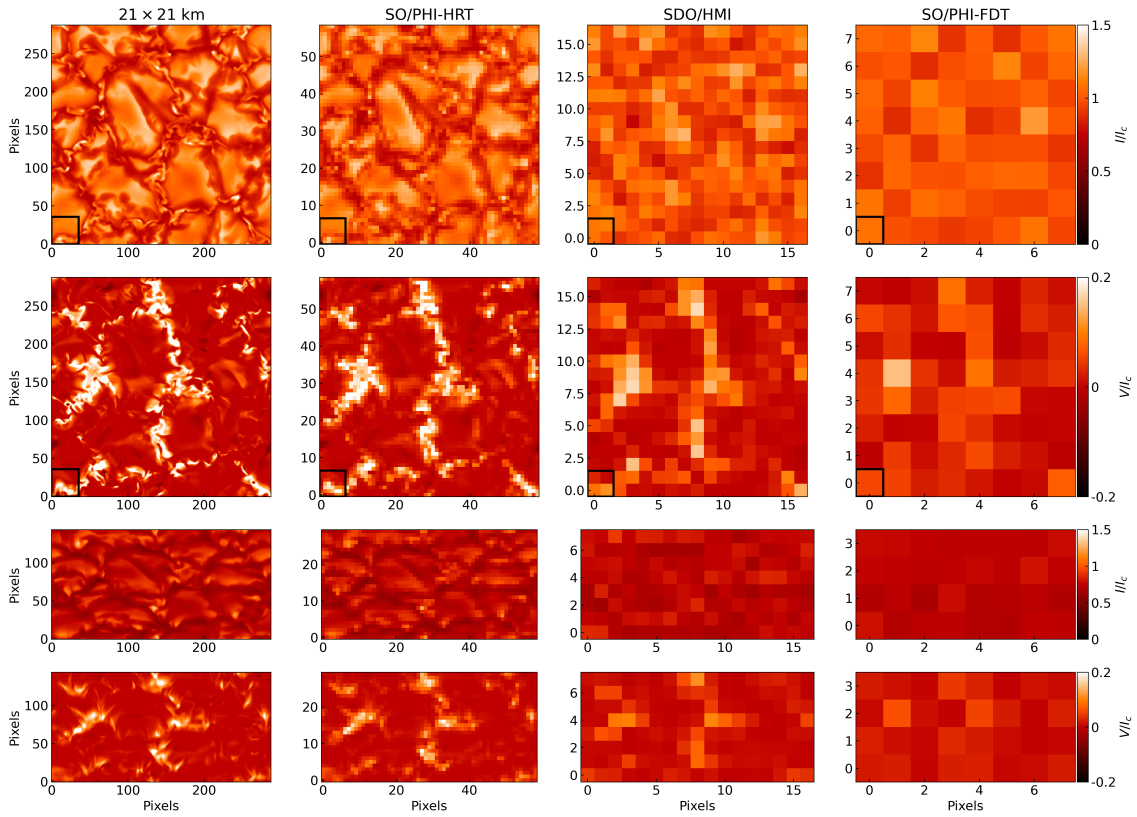


Figure 5.2: Maps of synthesised Stokes  $I/I_c$  and  $V/I_c$  profiles for the  $\lambda_0 = 6173.3 \text{ \AA}$  absorption line for one snapshot at  $\langle B_Z \rangle = 200 \text{ G}$  at different spatial resolutions. Left to right columns: Original MURaM resolution, resolution of SO/PHI-HRT at perihelion, SDO/HMI resolution, and resolution of SO/PHI-FDT at perihelion. Top two rows: maps at  $\mu = 1$ . Bottom two rows: maps at  $\mu = 0.5$  in the ‘positive viewing’ direction with spatial foreshortening applied. Top and third row: Stokes  $I/I_c$  at  $d\lambda = -0.35 \text{ \AA}$ . Second and fourth row: Stokes  $V/I_c$  at  $d\lambda = -0.07 \text{ \AA}$ . The black squares outline the region that is considered in Fig. 5.7.

## 5.5 Stokes processing

The Stokes profiles, regardless of  $\mu$ , are synthesised on the original  $288 \times 288$  grid of the MURaM simulations. As stated, we wish to investigate the CLV for different spatial resolutions: pixel sizes of the entire domain (6 Mm), SDO/HMI (362.5 km), SO/PHI-FDT (761.5 km), SO/PHI-HRT (101.5 km), and the original MURaM resolution (20.8 km). For the two SO/PHI telescopes, these correspond to the spatial resolution achieved when Solar Orbiter is at closest perihelion: 0.28 au. The Hinode SOT/SP pixel size is 116 km, very close to that of SO/PHI-HRT at perihelion (Tsuneta et al. 2008b), so that the results for SO/PHI-HRT should also be approximately valid for Hinode SOT/SP, although the spectral lines used are different.

For the  $\mu = 1$  case, with no spatial foreshortening, the maps are composed of the following number of (binned) pixels (rounded to the nearest pixel): the entire domain (one pixel), SO/PHI-FDT ( $8 \times 8$  pixels), SDO/HMI ( $17 \times 17$  pixels), SO/PHI-HRT ( $59 \times 59$

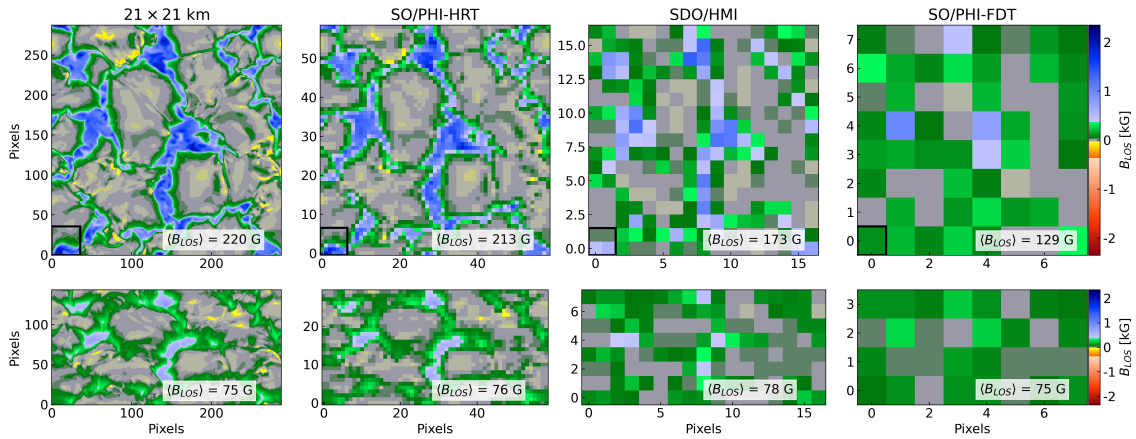


Figure 5.3:  $B_{LOS}$ , derived via MILOS inversions, from the Stokes profiles shown in Fig. 5.2. Top row:  $\mu = 1$ , bottom row:  $\mu = 0.5$  in the ‘positive viewing’ direction with spatial foreshortening applied. The  $B_{LOS}$  maps are shown at the original MURaM resolution, SO/PHI-HRT resolution at perihelion, SDO/HMI resolution and SO/PHI-FDT resolution, also at perihelion. The spatially averaged value of  $B_{LOS}$  is inscribed at the lower-right in each panel. The black squares outline the region considered in Fig. 5.7.

pixels), and the original MURaM ( $288 \times 288$  pixels). The binning is performed via a local mean down-sampling.

We note that for simplicity we do not consider the spatial PSFs of the various instruments when binning to different pixel sizes. Nor do we take into account that the magnetographs sample the observed spectral line at only a very limited number of wavelength points, or the spectral PSF (i.e. filter profile).

For  $\mu < 1$ , the pixel count, for a desired resolution, along the foreshortened  $y$ -axis, is calculated by dividing the foreshortened length,  $6 \times \mu$  Mm, by the instrument pixel resolution. The  $x$ -axis pixel count remains constant independent of  $\mu$ . For either axis, if the desired pixel count is not an integral factor of the original 288, the Stokes grid is first interpolated linearly in the spatial dimensions\* to a pixel count, nearest to the original 288, that is a multiple of the desired instrument pixel count, after which the local mean down-sampling is applied. In the case of one pixel over the entire domain, the Stokes maps are spatially averaged over its entirety, regardless of the  $\mu$  value. The negative viewing angles are treated as independent measurements from the positive angle, because a snapshot can present a rather different picture when observed from the two directions.

An example of these processed Stokes profiles is displayed in Fig. 5.2. Here we show maps of  $I/I_c$  and  $V/I_c$  in the  $6173.3 \text{ \AA}$  spectral line for four different resolutions at  $\mu = 1$ . Also displayed are the maps for  $\mu = 0.5$  with foreshortening applied. The  $I/I_c$  maps are shown at  $d\lambda = -0.35 \text{ \AA}$ , i.e. basically in the continuum, while the  $V/I_c$  maps are at  $d\lambda = -0.07 \text{ \AA}$ , i.e. in the flank of the line. It is clear that as the resolution decreases beyond that of SO/PHI-HRT the fine structure is lost. The black rectangular outline denotes the physical extent of one SO/PHI-FDT pixel at the origin at  $\mu = 1$ . The

\*<https://scikit-image.org/docs/stable/api/skimage.transform.html#skimage.transform.resize>

profiles from this region are investigated in Sect. 5.7.

## 5.6 Inference of the line-of-sight magnetic field

We inferred the LOS magnetic field with an inversion code: MILOS<sup>†</sup> (Orozco Suárez and Del Toro Iniesta 2007b, Orozco Suárez 2024). This inversion technique solves the radiative transfer equation by assuming a Milne Eddington atmosphere. This atmosphere assumes that the physical parameters ( $\mathbf{B}$ ,  $v_{LOS}$ ,  $\eta_0$ ,  $\Delta\lambda_D$ : i.e. magnetic field vector, LOS velocity, ratio of absorption coefficient at line core, continuum, and Doppler width of the spectral line) are independent of optical depth, while the source function is linear in optical depth. While we know this not to be case in the solar atmosphere, this assumption enables an analytic solution to be found, resulting in a simple and fast method to infer the physical conditions. Furthermore Milne-Eddington inversion codes have been shown to be very reliable (Borrero et al. 2014b) and therefore widely used. This code is currently employed by the SO/PHI instrument (Solanki et al. 2020) and SDO/HMI employs a similar Milne-Eddington inversion code: VFISV (Borrero et al. 2011a). As input the complete Stokes vector:  $I, Q, U, V$  was used with the full spectral sampling of 14 mÅ. The LOS magnetic field,  $B_{LOS}$ , was determined via  $B \cos(\gamma)$ , where  $\gamma$  is the magnetic field inclination relative to the line-of-sight. A filling factor of unity was used, the same as in the inversion routines of SO/PHI and SDO/HMI.

When inferring the LOS magnetic field, we have neglected all other instrumental effects, such as filter profiles, discrete wavelength sampling and photon noise. The wavelength sampling and range in particular affect the retrieval of strong split profiles. To fully understand all these effects, end-to-end simulations are required, such as a study already completed for the GONG telescopes (Plowman and Berger 2020a,b,c). An end-to-end simulator for SO/PHI exists (SOPHISM, see Blanco Rodríguez et al. 2018), but results from tests across a range of  $\mu$  values has not been reported yet.

As validation of the method and its behaviour when inverting Stokes profiles with inclined lines of sight, a test case with a 1D plane parallel atmosphere with a homogeneous vertical field of 200 G was used. The CLV of the inferred  $B_{LOS}$  followed the expected  $200 \times \mu$  G straight line very closely: the mean (vertical) separation from the  $200 \times \mu$  line is  $1.0 \pm 0.3$  G. For more details see Appendix A.1.

Maps of the retrieved  $B_{LOS}$ , via the MILOS inversion, from the Stokes profiles underlying the images displayed in Fig. 5.2, are shown in Fig. 5.3. As illustrated by the spatially averaged  $B_{LOS}$  values overlaid on each panel, one notes that the spatial average decreases with decreasing resolution at  $\mu = 1$ . The same, however, is not the case at  $\mu = 0.5$ , where  $\langle B_{LOS} \rangle$  is approximately independent of the pixel resolution. The analysis of this behaviour is presented in Sect. 5.7.

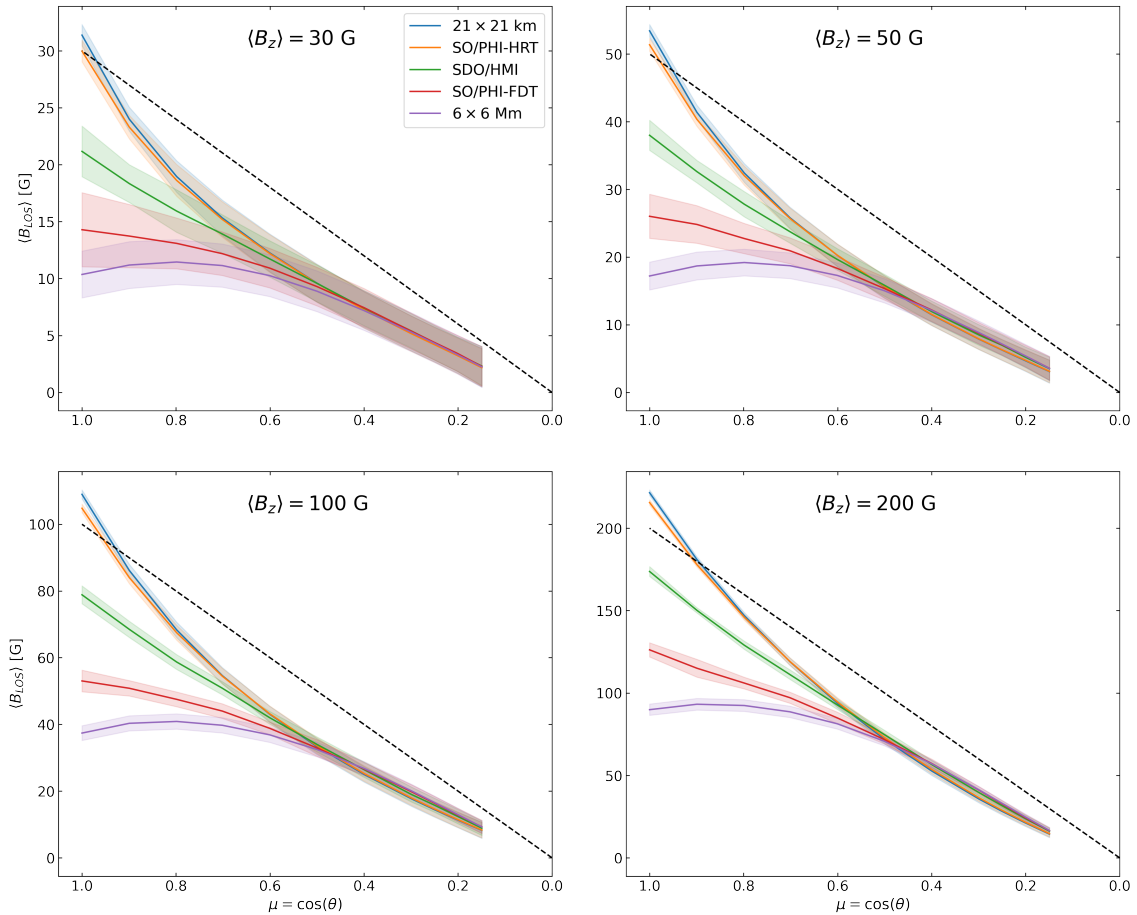


Figure 5.4:  $\langle B_{LOS} \rangle(\mu)$  retrieved from the  $\lambda_0 = 6173.3 \text{ \AA}$  line at the five tested resolutions. From the top left panel clockwise: results for simulations with  $\langle B_Z \rangle = 30, 50, 100, 200 \text{ G}$  respectively. At each  $\mu$  the retrieved  $\langle B_{LOS} \rangle$  quantities are averaged over all snapshots and the two employed viewing directions. The shaded regions denote the standard deviation over the range of snapshots. The legend in the upper left panel is valid for all panels. The dashed black lines indicate the expected  $\mu$ -dependence under the assumption that the ‘ground truth’  $\langle B_Z \rangle$  is retrieved at  $\mu = 1$ .

## 5.7 $\langle B_{LOS} \rangle$ centre-to-limb variation

### 5.7.1 Fe I 6173.3 $\text{\AA}$

We determined the mean LOS magnetic field,  $\langle B_{LOS} \rangle$ , for the different spatial resolutions to compare how accurately the known ‘ground-truth’  $\langle B_Z \rangle$  in the MHD simulation is retrieved. Importantly, this was done for the full range of  $\mu$  values. The centre-to-limb variation of  $\langle B_{LOS} \rangle$  for the 6173.3  $\text{\AA}$  spectral line is illustrated in Fig. 5.4. The 4 separate panels show that the  $\langle B_{LOS} \rangle$  CLV is strikingly similar regardless of the mean vertical field strength in the MHD simulation (the main difference is that the standard deviation of points becomes smaller as the average strength of the field in a simulation box increases). The most obvious point that one draws is that the CLV, irrespective of the resolution, is

<sup>†</sup><https://gitlab.com/SOPHI1/milos>

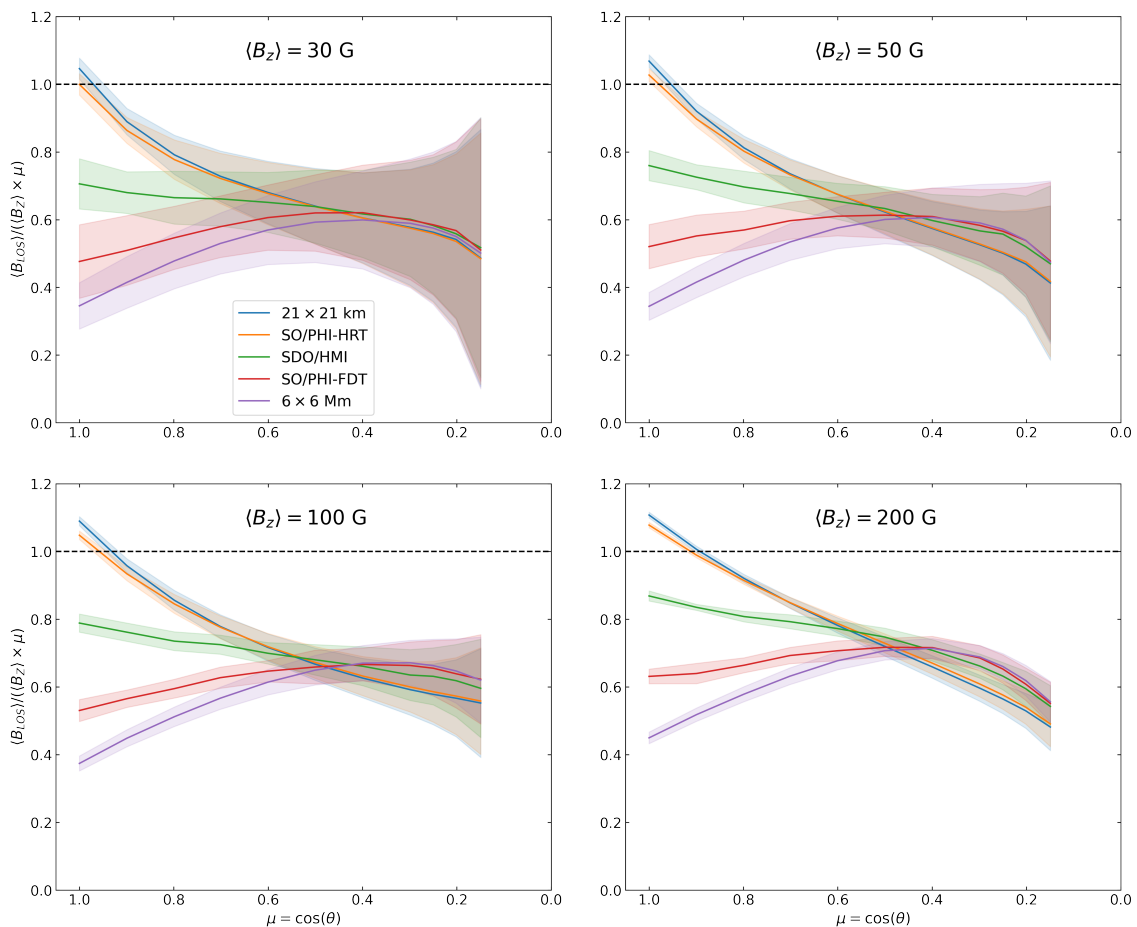


Figure 5.5: Same as Fig. 5.4 but for  $\langle B_{LOS} \rangle / (\langle B_Z \rangle \times \mu)$  instead of  $\langle B_{LOS} \rangle$  plotted vs.  $\mu$ . The dashed black line indicates the result if the  $B_{LOS}$  CLV is linear with  $\mu$  and the ‘ground truth’  $\langle B_Z \rangle$  was retrieved at  $\mu = 1$ .

almost entirely below the  $\langle B_Z \rangle \times \mu$  curve, indicated by the black dashed lines, that is expected by the radial field assumption. This is further illustrated in Fig. 5.5, which displays the same curves in Fig. 5.4 but divided by the  $\langle B_Z \rangle \times \mu$  dashed black line also shown in Fig. 5.4, to clearly indicate the fraction of the magnetic flux density that is underestimated.

Fig. 5.4 and Fig. 5.5 imply that there is almost always an underestimation of flux density from unipolar regions when inferred via the  $\mu$ -correction, regardless of the  $\mu$  value,  $\langle B_Z \rangle$  in the MHD simulation, or spatial resolution. For  $\mu > 0.5$  the amount by which  $\langle B_Z \rangle$  is underestimated increases with decreasing spatial resolution, whereas at  $\mu \leq 0.5$  the resolution plays a smaller role. Below  $\mu = 0.6$  at least 25% of the flux density is ‘missing’ when the  $\mu$ -correction is applied. the amount of missed flux increases to at least 40% as we consider simulation snapshots with lower average flux (more representative of coronal holes).

At or near disc centre, at SO/PHI-HRT and the native MURaM resolution,  $\langle B_{LOS} \rangle$  exceeds  $\langle B_Z \rangle$  by approximately 3 – 10%: at the MURaM resolution the values are:  $221 \pm 2$ ,  $109 \pm 1$ ,  $53 \pm 1$ ,  $31 \pm 1$  G for  $\langle B_Z \rangle = 200, 100, 50, 30$  G, respectively. This increase can be attributed to the fact that we observe the photosphere on an optical depth surface,

instead of a geometric one. In regions of high magnetic flux, the plasma is evacuated such that we can ‘see’ deeper into the Sun, into regions where the magnetic field is enhanced. Schlichenmaier et al. (2023) presented a similar effect; Milic et al. (2024) reported a 10% increase for  $\langle B_Z \rangle = 30$  G at  $\mu = 1$ , compared to the 3% increase we find, but this small difference is most likely due to the somewhat different formation heights of the 6301.5 Å and 6302.5 Å line pair that they investigated and 6173.2 Å.

Above  $\mu = 0.5$ ,  $\langle B_{LOS} \rangle$  decreases as the spatial resolution decreases, which was already visible in the  $\langle B_{LOS} \rangle$  values written in Fig. 5.3. This appears to be caused by two effects. The first is flux cancellation: for example, in the top left quadrant of Fig. 5.3 for  $\mu = 1$ , there are several patches with negative  $B_{LOS}$  close to positive, i.e. upward pointing, flux concentrations. When the pixel size increases, and these positive and negative flux patches are included in the same pixel, the Stokes  $V$  profiles partially cancel, such that an overall lower flux density is inferred. In order to minimise this well-known and expected behaviour, we have started the simulations with purely unipolar field initial conditions. Therefore we assume that this is a minor effect compared to the other factor: as the pixel sizes increase, the strongest field regions (magnetic elements or flux tubes) are no longer adequately resolved. It is due to the non-linear behaviour of radiative transfer and the differences in properties, such as the thermal profile, between structures with and without magnetic fields, that when they are considered together in a low spatial resolution element, the inferred magnetic field does not accurately represent the true underlying physical structures.

An extreme example of this effect is illustrated in Fig. 5.6. A pixel from a snapshot with  $\langle B_Z \rangle = 200$  G was selected with a  $B_{LOS}$  of approximately 2000 G and low inclination ( $< 0.1^\circ$  to the vertical) at the solar surface. The Stokes  $I$  and  $V$  profiles arising at  $\mu = 1$  from this pixel are shown in blue in the top and middle panels of Fig. 5.6, respectively. In orange the profile of an atmosphere with a  $B_{LOS}$  of 100 G (and low inclination of  $< 0.1^\circ$ ) at  $\tau = 1$  is also depicted. Doppler shifts were removed for simplicity. When the profiles from these two atmospheres, strong and weak, are combined with equal weights (i.e. with a filling factor of 0.5 each), the inferred  $B_{LOS}$  is only 274 G, just under 4 times less than the true  $B_{LOS}$  in the area from which the combined profiles arise: approximately 1035 G. This is an extreme case, as the 1970 G profile is strongly split, so much so that the dips in Stokes  $I$  lie almost outside the wings of the weak field Stokes  $I$  profile, and hence are largely ignored by MILOS when inferring  $B_{LOS}$ . The fact that strong concentrations of magnetic field are typically hot leads to weaker line profiles, at least of neutral atomic lines (e.g. Solanki 1986). This weakening also contributes to underestimating  $B_{LOS}$ . Another effect that helps explain the underestimate of the retrieved  $B_{LOS}$  from the combined profile is the presence of Zeeman saturation for strongly split spectral lines (Stenflo 1973). The removal of the Doppler shifts shows that this discrepancy is not a result of Doppler shifts, in agreement with the findings of Milic et al. (2024). Tests were also completed where the strong fields considered were weaker, 1000 G and 500 G. Here too the discrepancy remained although it was lessened. Using completely independent techniques, similar results for the different spatial resolutions near  $\mu = 1$  are found (see Sect. 5.7.3 and Appendix A.3& A.4)

This suppression of the strong fields, and how this changes with spatial resolution is clearly observed in our results. In Fig. 5.7 the Stokes  $I$  and  $V$  profiles from the region

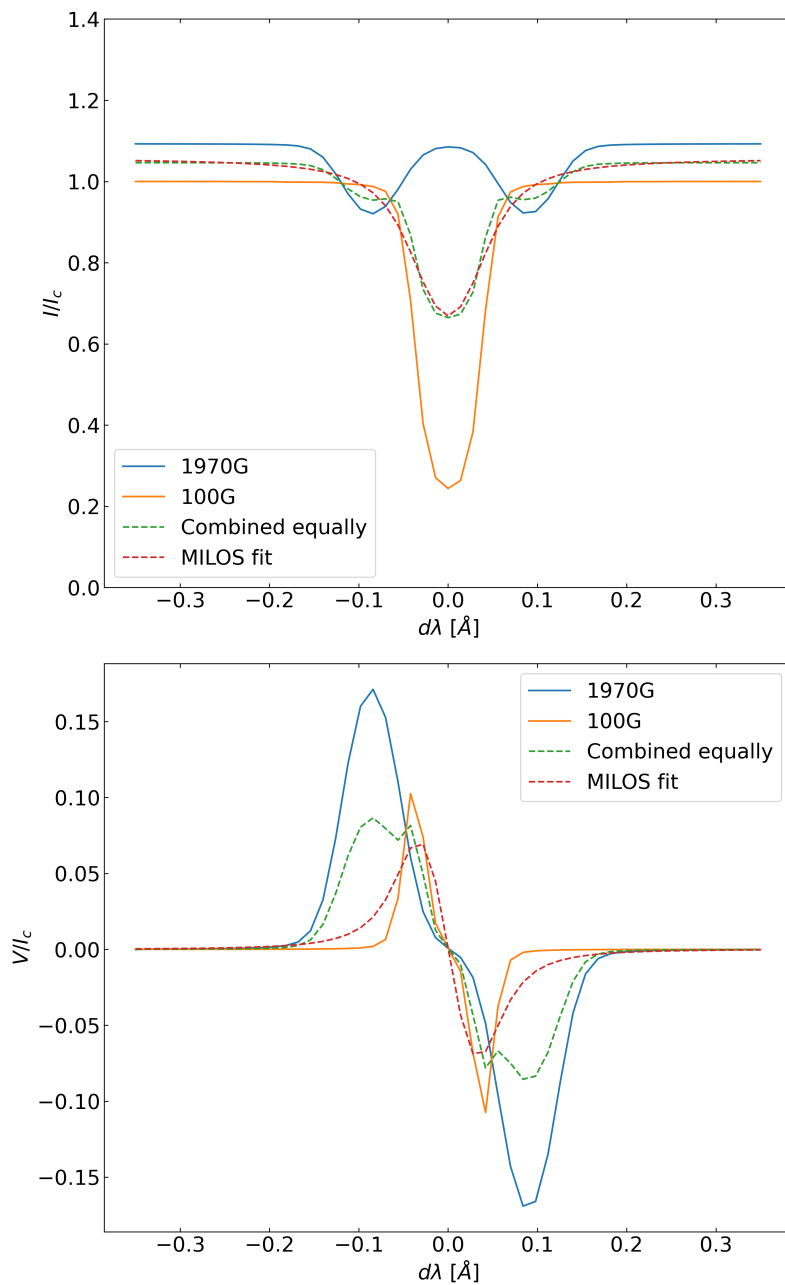


Figure 5.6: Combination of Stokes signals from weak and strong magnetic regions for  $\lambda_0 = 6173.3 \text{ \AA}$ . Top panel: Stokes  $I$  profiles for a  $\approx 2000 \text{ G}$  pixel and a  $100 \text{ G}$  pixel. The combined profile, a simple average of the individual profiles, is depicted by the dashed green line, while the fit to the combined profile is the dashed red line. Bottom panel: same as the top but for Stokes  $V$ .

outlined in black in Fig. 5.2 and Fig. 5.3 is shown for 4 different resolutions. This region is equivalent in area to one pixel at SO/PHI-FDT resolution, but 1296 pixels at the original MURaM resolution. The profiles spatially averaged over the region are shown by solid thick black lines. If we are at original resolution, then we retrieve a  $B_{LOS}$  value for the area considered that corresponds to the average of the  $B_{LOS}$  values obtained from the individual pixels. This  $\langle B_{LOS} \rangle$  is written in the lower right of the top panels of Fig. 5.7, while the averaged Stokes  $I$  and  $V$  profiles (in black) are much weaker and result in a significantly lower retrieved  $B_{LOS}$ , which is given in the lowest panels of the same figure. As indicated in Fig. 5.7, the spatial average of  $B_{LOS}$  from the constituent pixels decreases with decreasing pixel resolution, with the  $B_{LOS}$  retrieved at SO/PHI-FDT pixel resolution being a factor of 4 lower than at the original MURaM resolution. The spatially averaged  $B_Z$  in this region, close to the average height of formation, is 415 G<sup>‡</sup>. This shows that MILOS retrieves the vertical magnetic field well at high spatial resolution, while at low resolutions it does not. This difference of the average profile to that from any one pixel in the underlying area is consistent with the discussion by Leka and Barnes (2012) and a worse spatial resolution is expected to dilute the polarisation signal such that a lower magnetic field strength is inferred Leka (1999), Orozco Suárez et al. (2007).

We have explained the reason why a much lower LOS flux density is inferred when the spatial resolution is low at high  $\mu$  but the curves converge at  $\mu = 0.5$ , and the LOS flux density is always below the expected linear dependence, even when the spatial resolution is at the native MURaM resolution. We believe that this is due to a combination of mainly two factors, which have been already mentioned in Sect. 5.2. Firstly, the passage of the inclined rays through both magnetic and non-magnetic regions significantly affects the inferred LOS flux density. Audic (1991) and Solanki et al. (1998) described the effect on the polarised profiles by the absorption in both magnetic and non-magnetic regions, and concluded that it is highly dependent on the temperature difference between the magnetic flux tubes and the non-magnetic surroundings, and at what geometrical height the absorption takes place. Especially if the magnetic concentrations are hotter than their surroundings, which is generally the case, then the lines get more strongly absorbed in the field-free or weak-field surroundings than in the concentrations themselves. Absorption in the field-free region leads to the reduction in the strength of the polarised Stokes profiles relative to Stokes  $I$ . This reduces the signal of the magnetic field and mimics a weaker field, leading MILOS to underestimate  $B_{LOS}$ . Because this reduction is due to effects happening along each line-of-sight, it is independent of the spatial resolution of the observations. The same figure but for  $\mu = 0.5$  is shown in Appendix A.2 and demonstrates the lack of dependence on the spatial resolution. Solanki et al. (1998) also found that Stokes  $V$  amplitudes were more strongly reduced at  $\mu < 1$  for narrower flux tubes. This could explain the larger underestimation at smaller  $\mu$  of regions with low  $\langle B_Z \rangle$  visible in Figs. 5.4 and 5.5 as such regions tend to have narrower magnetic concentrations. Furthermore, narrow flux concentrations have a stronger tendency to be hidden behind a neighbouring granule, further reducing the polarised Stokes signals.

---

<sup>‡</sup>The average  $B_Z$  in this sub-region of the MURaM cube was found by converting geometrical height to optical depth and averaging over both the spatial  $(x, y)$  and 21 optical depth planes ( $\log(\tau) = -2$  to  $\log(\tau) = 0$ , with a step size of 0.1  $\log(\tau)$  and all optical depth planes weighted equally). We used response functions to the magnetic field to guide this choice. We note that this step is undertaken only for the purpose of illustration and applied only to the small sub-region of the simulation cube.

The second reason why we suspect the curves to converge is due to the projection effect. As  $\mu$  decreases, the extent of the Sun's surface that is covered by a pixel, even at the native MURaM resolution, increases to the point that little to no strong field regions are resolved, and for those that are, the LOS component is diminished. Indeed we find that at  $\mu = 0.5$  at the MURaM resolution and  $\langle B_Z \rangle = 200$  G, no pixels in any snapshot or viewing direction have an inferred LOS field larger than 950 G.

The shaded areas in Fig. 5.4, colour matched with the corresponding  $\langle B_{LOS} \rangle$  CLV curve, indicate one standard deviation of  $\langle B_{LOS} \rangle$  from the distribution of the multiple MURaM snapshots and two viewing directions. These shaded areas reveal that the lower the  $\langle B_Z \rangle$ , the larger the spread in  $\langle B_{LOS} \rangle$  from one snapshot to the next, and from one viewing direction to the other. This large spread in the low mean field regions could be because there are fewer and smaller flux concentrations, thus leading to more relative variation between each granule turnover time. Furthermore, as these flux concentrations are smaller the viewing geometry also has a larger impact on the inferred  $\langle B_{LOS} \rangle$ , as from one viewing point a flux concentration might not be visible behind a neighbouring granule, but it may well be from another. This larger variation also validates our consideration of a longer time series for the lower field strength cases.

An extreme example is found for one quiet Sun snapshot,  $\langle B_Z \rangle = 30$  G, 'observed' at  $\mu = 0.15$ . While, as expected, a positive  $\langle B_{LOS} \rangle$  was retrieved when viewing from the positive direction, a negative  $\langle B_{LOS} \rangle$  is retrieved when viewing from the 'negative' direction regardless of the spatial resolution, illustrating the high variability of observing the weakest quiet Sun at extreme angles. Such an apparent change in polarity may be produced by the fact that in the quiet Sun even the strong-field magnetic features are not quite vertical, so that they can be pointing towards or away from an observer observing at very small  $\mu$ . When there are few magnetic features in the FOV, their random inclinations need not average out.

From Fig. 5.5 we find a tendency at low  $\mu$  that at high resolutions approximately 2 – 10% lower  $\langle B_{LOS} \rangle$  is inferred than at low resolutions. This is the opposite behaviour to the much more striking dependence on resolution seen at large  $\mu$ . The dependence on resolution increases with  $\langle B_Z \rangle$  and only becomes statistically significant for  $\langle B_Z \rangle = 200$  G, since at lower  $\langle B_Z \rangle$  the shaded regions associated with the curves for various resolutions overlap significantly. We suspect that this difference arises as the Stokes profiles in the resolved pixels become increasingly anomalous at low  $\mu$ , for instance the Stokes  $V$  profiles often have more than two lobes, and do not exhibit the 'normal' opposite polarity between the lobes: for example some profiles only have a positive signal. When MILOS then fits a profile to these anomalous profiles,  $\langle B_{LOS} \rangle$  inferred from these anomalous pixels is lower than that obtained when it fits profiles corresponding to a low spatial resolution, which tend to be more normal in shape. Then the contribution of these anomalous profiles are averaged out or at least suppressed, and hence MILOS fits profiles that infer a larger  $B_{LOS}$ .

One more finding is the maximum of  $\langle B_{LOS} \rangle$  for the lowest resolution, for the  $6 \times 6$  Mm case is at  $\mu = 0.8$  and not at  $\mu = 1$  (see Fig. 5.4). Naively, one would expect  $\langle B_{LOS} \rangle$  to decrease with  $\mu$  as is the case for the other resolutions. We also find that the area and amplitude asymmetry of the Stokes  $V$  profile, averaged over the entire domain, is largest at  $\mu = 1$ , and decreases with  $\mu$ . It is due to this asymmetry, which is positive

in both amplitude ( $\approx 15\%$ ) and area ( $\approx 3\%$ ) at  $\mu = 1$  (positive in the sense that the blue lobe is larger than the red lobe, see Solanki and Stenflo (1984) and Solanki (1993) for a definition), and the inability of a Milne-Eddington inversion to fit asymmetric profiles that this maximum in  $\langle B_{LOS} \rangle$  at  $\mu = 0.8$  exists. As the asymmetry decreases, the retrieved  $B_{LOS}$  increases, but this is offset by the overall decrease in the polarisation signal as  $\mu$  decreases, such that a maximum exists. This is a well known limitation of Milne-Eddington inference schemes and the resulting differences of the retrieved physical parameters with the ground truth from MHD simulations has already been presented (e.g. Borrero et al. 2014b).

We take away several key results from our work so far: the retrieved  $\langle B_{LOS} \rangle$  is much lower than expected everywhere on the solar disc except for the very highest resolution observations. Close to disk centre the retrieved  $\langle B_{LOS} \rangle$  depends strongly on spatial resolution, such that at low spatial resolution, the true  $\langle B_Z \rangle$  is not retrieved at  $\mu = 1$ . This result has also been reported by Milic et al. (2024), although restricted strictly to  $\mu = 1$ , who synthesised the line pair sampled by Hinode SOT/SP. This dependence on spatial resolution decreases as away from disc centre and is very weak for  $\mu < 0.5$ . Nonetheless, also at smaller  $\mu$  the  $\langle B_{LOS} \rangle$  is significantly underestimated.

### 5.7.2 5250.2 Å versus 6173.3 Å

In Fig. 5.8 the relative difference, in %, between the 6173.3 Å  $\langle B_{LOS} \rangle$  CLV curves presented in Fig. 5.4 and those for the 5250.2 Å line are shown for the four different initial vertical magnetic fields in the MHD simulations. Across all four panels, we see a similar trend; at high  $\mu$ , compared to Fe I 6173.3 Å, up to 9% lower mean LOS field is retrieved from Fe I 5250.2 Å. The converse is true at low  $\mu$ : a larger mean LOS field is inferred from Fe I 5250.2 Å, between 10% and 23% at the very lowest  $\mu$  values.

We see little dependence on the difference between the spectral lines due to the spatial resolution, only at high  $\mu$  do the spatial resolutions deviate, and even in this regime the difference is only a few per cent. It is difficult to ascertain a trend in spatial resolution in this regime, especially with the large shaded areas that indicate one standard deviation of the differences across all snapshots<sup>§</sup>. Consistent with the previous figures, such as Fig. 5.5, the statistical spread of the results across all the snapshots increases with decreasing  $\langle B_Z \rangle$  in the MHD simulations.

There are various physical factors to consider here when comparing these two spectral lines, which becomes increasingly complex when inclined viewing angles are included. The Fe I 5250.2 Å spectral line has a larger absorption coefficient in the quiet Sun and it probes slightly higher in the atmosphere when viewing at disc centre (Quintero Noda et al. 2021). This could explain the slightly lower retrieved values at high  $\mu$ , due to the higher temperature contrast between magnetic features and the non-magnetic atmosphere at these layers. Finally, due to the much lower first excitation potential of Fe I 5250.2 Å, there is a large difference in temperature sensitivity of the two spectral lines. As mentioned in Sect. 5.7.1, when viewing at inclined angles the polarised profiles are highly affected by the temperature difference between the magnetic flux concentrations and the non-magnetic surroundings. Therefore, the difference in the temperature

---

<sup>§</sup>Using the standard error propagation formula for  $y = f(a, b, \dots)$ :  $\sigma_y^2 = (\partial y / \partial a)^2 \sigma_a^2 + (\partial y / \partial b)^2 \sigma_b^2 + \dots$

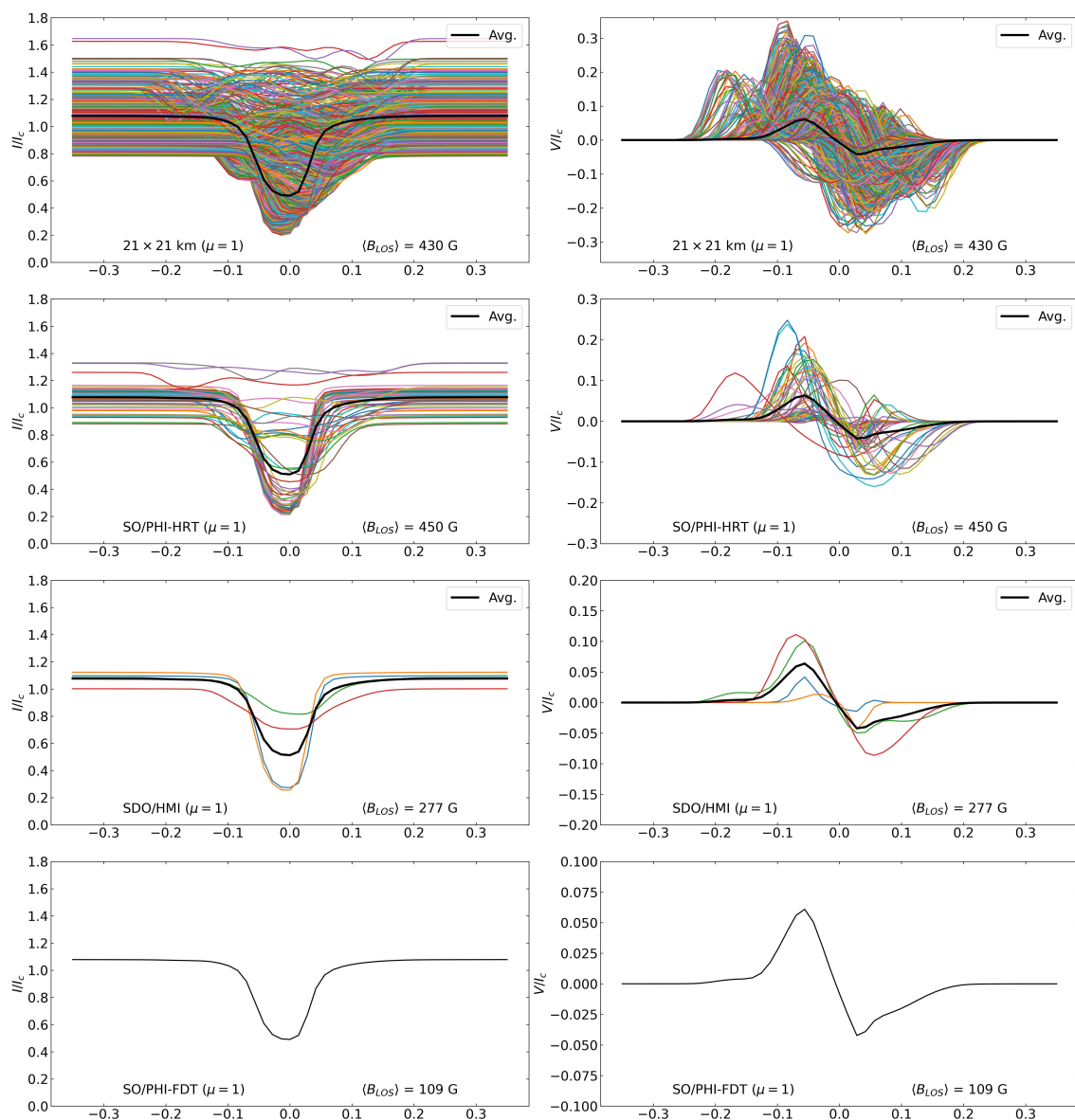


Figure 5.7: Stokes profiles, normalised to the spatially averaged disk centre  $I_c$ , from the physical region that is encompassed by the single SO/PHI-FDT pixel at  $[0, 0]$  at  $\mu = 1$ , as outlined by the black square in Fig. 5.3. First column: Stokes  $I/I_c$ , second column: Stokes  $V/I_c$ . From top row down: the original MURaM resolution, SO/PHI-HRT resolution, SDO/HMI resolution, SO/PHI-FDT resolution. The number of considered pixel(s) in this region for the original MURaM resolution are 1296, SO/PHI-HRT: 49, SDO/HMI: 4 and SO/PHI-FDT: 1. The average line-of-sight magnetic field of the pixels in this region,  $\langle B_{LOS} \rangle$ , is shown for each resolution.

## 5 Magnetograms underestimate even unipolar magnetic flux nearly everywhere on the solar disk

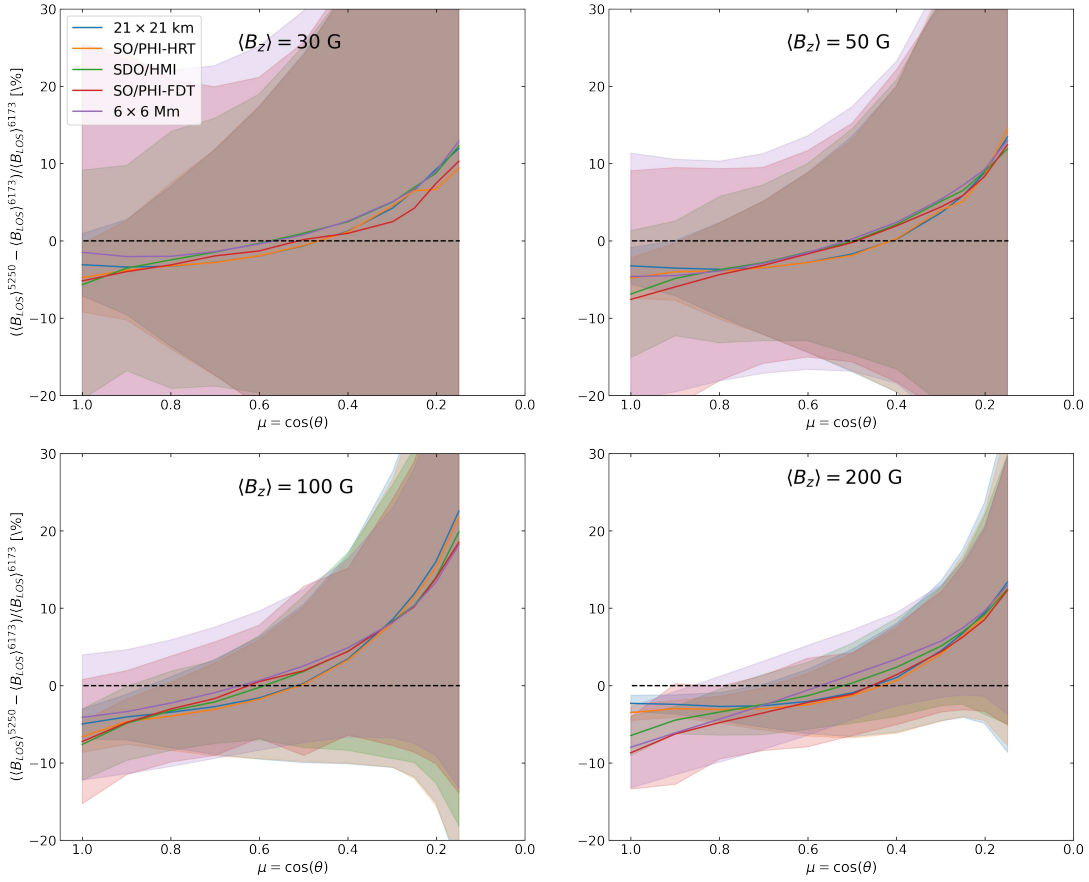


Figure 5.8: Relative differences of  $\langle B_{LOS} \rangle$ , in %, between the 5250.2 and 6173.3 Å spectral lines. From the top left panel clockwise: for  $\langle B_Z \rangle = 30, 50, 100, 200$  G respectively. At each  $\mu$  the retrieved  $\langle B_{LOS} \rangle$  quantities are averaged over all snapshots and viewing directions. The shaded regions denote the propagated standard deviation of the difference. The y axis is saturated from  $-20\%$  to  $+30\%$ . The legend in the upper left panel is valid for all panels. The dashed black line indicates the zero level.

sensitivity of these two spectral lines may contribute to a difference in the Stokes profiles and hence the inferred LOS magnetic field. The challenge lies in disentangling all these effects to understand the behaviour we find here: to do so properly requires further study which is out of scope for this paper. Nonetheless the centre-to-limb variation of  $\langle B_{LOS} \rangle$  retrieved via Fe I 5250.2 Å is qualitatively the same:  $\langle B_{LOS} \rangle$  is underestimated at all  $\mu$  values, at high  $\mu$  it is more strongly underestimated if the spatial resolution of the synthetic observations is lower, while for  $\mu < 0.5$  there is little dependence on spatial resolution.

### 5.7.3 Other $B_{LOS}$ retrieval methods

To avoid that the obtained results are distorted by any bias inherent to the Milne-Eddington inversion or the MILOS code, other methods to retrieve the  $B_{LOS}$  were also investigated. These included the MDI-like algorithm (a Fourier Tachometer technique used by the Michelson Doppler Imager on board the Solar and Heliospheric Observatory Couvidat et al. 2012a), currently also employed for the production of the LOS observ-

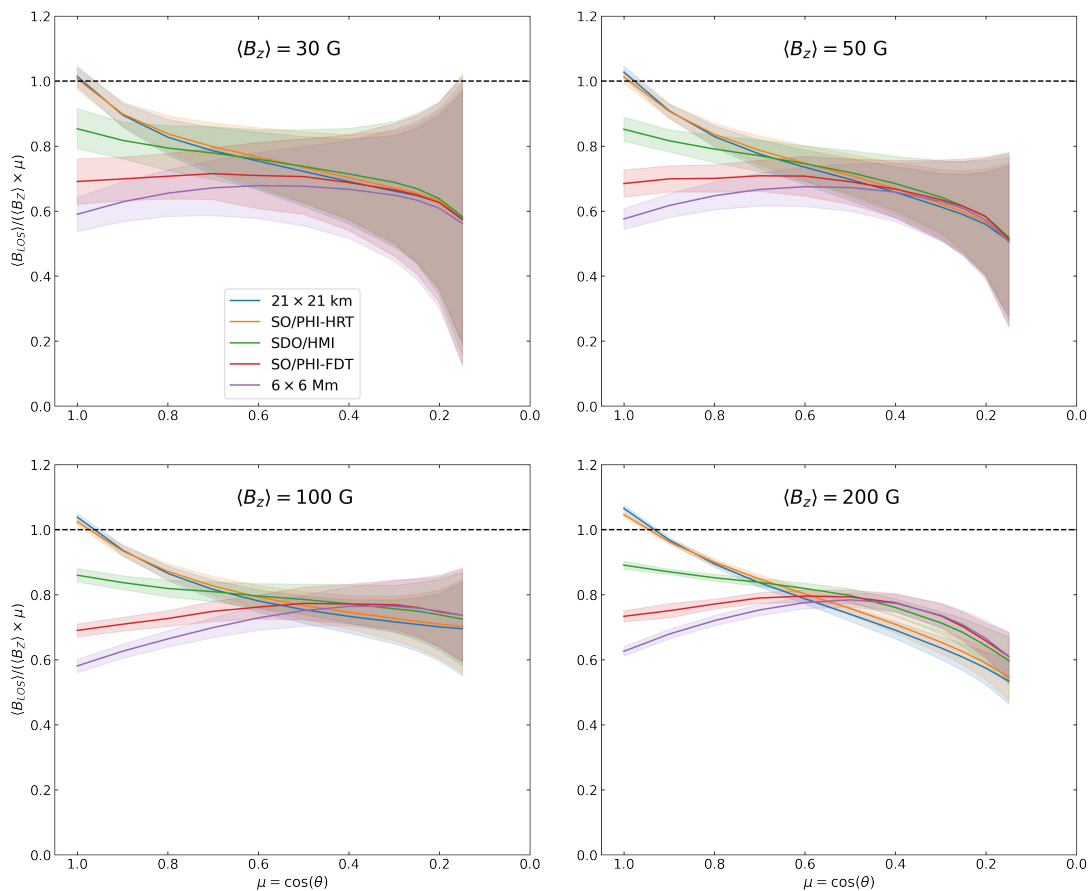


Figure 5.9: Same as Fig. 5.5 but derived via the MDI-like algorithm instead of with MILOS.

ables by SDO/HMI, the weak-field approximation (WFA) (e.g. Landi Degl’Innocenti and Landolfi 2004) and the centre-of-gravity (COG) method (Rees and Semel 1979, Stenflo 1994). The WFA is implemented via a linear least-squares minimisation method following Martínez González and Bellot Rubio (2009). These methods were validated on a one dimensional plane parallel atmosphere, as was done for MILOS, and the results of the validation are shown for  $\lambda_0 = 6173.3 \text{ \AA}$  in Appendix A.1.

When applied to the synthetic Stokes profiles from the MURaM simulations, the WFA method retrieves results most similar to those obtained via MILOS inversion. However, the approximation breaks down as expected when applied to the Stokes profiles at higher spatial resolutions at high  $\mu$ , as the method fails to retrieve physically sensible results in pixels with the strongest fields ( $B_{LOS} > 1000 \text{ G}$ ). The COG technique and MDI-like algorithm retrieved very comparable results to each other, both of which were akin to those retrieved via MILOS: with  $\langle B_{LOS} \rangle$  underestimated for all  $\mu$ . However the underestimation is less (i.e. the retrieved  $\langle B_{LOS} \rangle$  values are larger), particularly at low resolution and high  $\mu$  values. The COG technique struggled in cases where the profiles were particularly anomalous, i.e. mainly at low  $\langle B_Z \rangle$  and low  $\mu$ . The results obtained by applying the WFA and COG method are given in Appendix A.3 and A.4 for the two spectral lines.

Given this smaller underestimation of  $\langle B_{LOS} \rangle$  by the COG and MDI-like technique, and that the MDI-like algorithm performed more robustly, we present the  $\langle B_{LOS} \rangle$  CLV derived by the MDI-like algorithm for the 6173.3 Å line in Fig. 5.9. The MDI-like algorithm infers 30 – 60% more  $\langle B_{LOS} \rangle$  compared to MILOS for the low resolution cases at high  $\mu$ . Nevertheless it exhibits the same trend as in Fig. 5.4, with a convergence of the different spatial resolution-based curves around  $\mu = 0.5$  and larger variance for the lower  $\langle B_z \rangle$  simulations.

As described in Hoeksema et al. (2014), the MDI-like algorithm estimates the first Fourier coefficients, and from their phase derives the Doppler velocity (as they are proportional) for both circularly polarised components. From the difference of the Doppler velocity of these two components the line-of-sight magnetic field can be determined. This method makes several assumptions, chief among which is that the iron spectral lines are Gaussian, which we know to be only approximately correct leading to errors in the results. However, we stress that a correction for the known Fe I line profile (see Couvidat et al. 2012a) is implemented in the SDO/HMI LOS pipeline, which we have not considered. The MDI-like method does not appear to be as sensitive to the Stokes V asymmetry as MILOS, with no maximum for the  $6 \times 6$  Mm pixel resolution at  $\mu = 0.8$ .

## 5.8 Discussion

In this section we discuss implications regarding the work presented in this study. One of our main results is that, even for relatively vertical unipolar fields organised in flux tubes, we infer the wrong magnetic flux density at disc centre, with the derived flux density being clearly too low for synthetic observations having spatial resolutions worse than 200 km on the Sun.

This result has also been reported by Milic et al. (2024), but our work is complementary and goes beyond what those authors have presented. We can confirm this result for multiple flux densities ranging from the very quiet Sun to a reasonably strong active region plage, while Milic et al. (2024) only investigated one flux density. We find very similar behaviour across all tested flux densities, but with less variance between different MHD simulation snapshots at higher flux densities. Additionally, unlike Milic et al. (2024), we did not solely rely upon the retrieval of the line-of-sight magnetic field by a Milne-Eddington inversion. We also investigated three additional widely used techniques, the weak-field approximation (linear least-squares minimisation implementation), an MDI-like algorithm and the centre-of-gravity technique. The weak-field approximation generally gave results closest to the Milne-Eddington inversion, but, unsurprisingly, broke down at locations where strong fields were spatially resolved. With the MDI-like algorithm and centre-of-gravity technique the inferred flux density was found to be somewhat closer to the ground truth, but it was still significantly underestimated at low spatial resolutions. Finally, we demonstrated that this result holds also for two widely used spectral lines Fe I 6173.3 Å (used e.g. in SDO/HMI and SO/PHI) and Fe I 5250.2 Å (used e.g. by Mt. Wilson and Kitt Peak observatories and the IMAx, TuMag instruments on the Sunrise balloon-borne observatory), which were not investigated by Milic et al. (2024).

Another key result is that we retrieve LOS magnetic fields that are much lower

than expected by the radial field assumption also off disc centre, in fact at any angle down to  $\mu = 0.15$ . The centre-of-gravity technique struggled at low  $\mu$  due to the increasingly anomalous profiles, while the other methods were more robust. These results have strong implications for total flux measurements, of both open and closed magnetic field regions, irrespective of the technique used to infer the magnetic field. The Fe I 5250.2 Å and Fe I 6173.3 Å spectral lines have both been extensively employed by past and present observatories. Hence our results support the case that a significant amount of magnetic flux is missed by Zeeman-effect based flux measurements. This includes magnetic fluxes reported by long term monitoring programs such as Mount Wilson and Kitt Peak (Arge et al. 2002, Wallace et al. 2019), which have relatively low spatial resolution, but also more recent observations by, for example the widely used SDO/HMI instrument. This applies also to regions such as unipolar plage within active regions and coronal holes.

In the final paper of a series of papers that describe the end-to-end simulation of the GONG telescopes, Plowman and Berger (2020c) report that GONG too underestimates the magnetic flux, although they sample a different line: Ni I 6768 Å. As mentioned in Sect. 5.2, they explain their results through convective blue-shift, in contrast with our argument at disc centre of the non-linear behaviour of the spectral lines in the combination of structures with and without magnetic fields (thermal effects, Zeeman saturation, and details of the fitting of complex line profiles), which is qualitatively in agreement with Milic et al. (2024). Near the limb, we attribute the decrease to the strong absorption in the nearly field-free gas between magnetic flux concentrations through which each ray passes, even those that pierce the magnetic concentrations, an effect proposed by Audic (1991) and Solanki et al. (1998). Since the latter effect acts along individual rays, it is expected to be almost independent of spatial resolution, which is what our computations show. Gosain and Uitenbroek (2024) also reported an underestimation of the magnetic flux across a range of  $\mu$  values down to 0.3, when synthesising Stokes profiles from the Ni I 6768 Å spectral line from MHD simulations.

Together, our work, that of Plowman and Berger (2020c) and of Milic et al. (2024) suggest that the underestimation of magnetic flux due to low spatial resolution near disc centre is independent of the spectral line sampled, although this needs to be confirmed in future work. Whether the difference in result between our work and that of Plowman and Berger (2020c) is partly due to the different spectral lines studied, needs further analysis.

We have restricted ourselves to unipolar regions for two reasons. Firstly, we expected the spatial resolution of observations to play a much smaller role for unipolar fields than for mixed polarity fields, where flux cancellation is known to play a large role in reducing the deduced magnetic flux for lower spatial resolution (at all  $\mu$ ). Secondly, unipolar fields are associated with coronal holes and open magnetic flux. Hence our study may shed some light on whether effects such as Zeeman saturation, thermal line weakening in magnetic features, saturation effects due to radiative transfer along rays passing through both magnetic concentrations and the nearly field-free gas in between, and spatial resolution effects could help explain the mismatch between the open magnetic flux seen in coronal holes and the heliospheric magnetic flux measured in situ (Linker et al. 2017).

Our analysis is valid for unipolar regions on the Sun, that is for typical coronal

holes (for relatively low  $\langle B_z \rangle$ ) and plage (larger  $\langle B_z \rangle$ ). Near the boundaries of such features, however,  $\langle B_z \rangle$  is generally not independent of height, so that although qualitatively correct, we expect there to be quantitative departures from our results.

Since at activity minimum the coronal holes are mainly found in the polar regions, and hence are located close to the solar limb as seen from Earth, it is important to not just restrict such a study to  $\mu = 1$ , but to consider the full centre-to-limb-variation. Here we do not aim to provide a quantitative estimate of how much of the observed mismatch can be explained by the effects we have found. That will be the topic of a follow-up investigations.

Combined observations by the SO/PHI instrument and SDO/HMI may provide a route to observationally test the results of the present study for  $\mu < 1$ . This will also be the subject of a future study.

## 5.9 Conclusions

We have used MHD simulations of unipolar magnetic regions representing a range of solar features from the quiet Sun to active region plage in the photosphere to test how reliably various methods retrieve the LOS magnetic field from Stokes profiles. To this end, Stokes profiles of two commonly used spectral lines, Fe I 6173.3 Å and Fe I 5250.2 Å, were synthesised in sets of simulation snapshots covering a range of magnetic flux densities. The synthesis was repeated for a range of viewing angles corresponding to synthetic observations ranging from solar disc centre down to  $\mu = 0.15$ . We have binned these Stokes profiles to different spatial resolutions and inferred the line of sight magnetic field using a variety of techniques. We have shown that the mean line-of-sight magnetic field is underestimated in nearly all cases at all  $\mu$ . The only exception is close to disc centre, where high resolution observations that resolve the strongest field regions, which return roughly the correct averaged magnetic flux density. We also find that for  $\mu$  less than  $\approx 0.5$  the retrieved averaged flux density is nearly independent of spatial resolution of the synthetic observations and is always well below the expected value. This underestimation was consistently found regardless of the inference method used.

Our results also suggest the inferred line-of-sight flux density does not depend linearly on  $\mu$ , but rather shows a more complex dependence and lies too low. Hence, when applying the  $\mu$ -correction (i.e. dividing  $B_{LOS}$  by  $\mu$ ), there is a significant discrepancy between the inferred radial magnetic field and the true radial field in the simulation. This discrepancy is enhanced with low resolution for  $\mu > 0.5$ , as the mixing of the strongest flux regions with neighbouring weak flux regions results in a much lower than expected inferred flux density (due to effects such as thermal line weakening in the magnetic features and Zeeman saturation, etc.).

At or below  $\mu = 0.5$  there is little to no variance in the inferred mean magnetic flux density with spatial resolution. This is due to radiative transfer effects that act on individual light rays passing through both magnetic and non-magnetic regions. The large projection effect overwhelming any possibility of resolving the strongest field features may also play a role.

We do find non-negligible differences between the two spectral lines, Fe I 6173.3 Å and 5250.2 Å, considered in this study. At high  $\mu$ , an up to 9% lower mean line-of-sight flux density is inferred from Fe I 5250.2 Å relative to Fe I 6173.3 Å. The difference is particularly striking at low spatial resolution. At low  $\mu$ , however, the opposite is true where instead an up to 23% larger mean flux density is inferred from Fe I 5250.2 Å. Nonetheless, this line significantly underestimates  $B_{LOS}$  everywhere as well.

These results were consistently found for all  $\mu$  values irrespective of the exact employed magnetic field inference technique and of the mean vertical flux density of the simulated region. A small dependence on the mean flux density in the MHD simulations is found, with the synthetic measurements applied to simulations with lower magnetic flux typically falling short more severely. All this suggests that the main results are robust, and hence have significant implications for a broad range of reported solar observations.

The results presented here have a potential to contribute substantially to the resolution of the open flux problem (Linker et al. 2017), as the magnetic flux is underestimated everywhere on the solar disk in unipolar fields such as those underlying coronal holes, even at the spatial resolution of SDO/HMI. Turning this into estimates of the amount of "missing" magnetic flux will be the subject of a follow-up paper.



## 6 Conclusions and Outlook

The Polarimetric and Helioseismic Imager on Solar Orbiter (SO/PHI) is providing the first ever opportunity to infer the photospheric magnetic field from a new vantage point. Of interest for this thesis is the first direct opportunity to test the hypothesis whether part or all of the missing open magnetic flux arises from an underestimation of the magnetic field when observing near the limb and the poles. I have focused on the High Resolution Telescope (HRT) of SO/PHI, which due to the combination of its high spatial resolution and close approaches to the Sun, provides incredibly rich information of the photospheric magnetic field. To exploit this opportunity the first three chapters of my thesis cover crucial steps to make the analysis of SO/PHI-HRT data possible:

- The development and implementation of a data reduction pipeline for the SO/PHI-HRT instrument applicable to raw data that is downlinked to Earth.
- A comparison between the magnetic field data products of SO/PHI-HRT with its very similar space-based counterpart that orbits Earth: SDO/HMI, when the two host spacecraft are at a near identical viewing position.
- An evaluation of the pointing information of the SO/PHI-HRT data, and first attempt of comparing magnetograms from two different positions with different instruments.

The development of the SO/PHI-HRT data reduction pipeline, Chapter 2, yielded these results from raw data taken during the commissioning phase and early part of the nominal mission phase:

- Through unsharp masking artefacts in the flat fields could be removed when quiet Sun regions are observed.
- With a flat field created near the observation date, the polarimetric ghosts are reduced to below the  $10^{-3}I_c$  level.
- With ideal calibration files SO/PHI-HRT achieves a polarimetric noise of  $10^{-3}I_c$  or better. The noise is limited by the compression of the raw data before transmission to Earth.
- The first SO/PHI-HRT data products of the quiet Sun and an active region containing a sunspot were produced, highlighting the instruments performance.
- The noise in the magnetograms ranges between 6.5 – 8.5 G dependent on the cadence and modulation scheme of each observation. The lowest magnetogram noise is achieved with a cadence of 96 – 100 seconds and [4, 5] modulation scheme.

On 7 March 2022, Solar Orbiter crossed the Sun-Earth line and allowed for an opportunity to compare the inference of the photospheric magnetic field with Earth-based assets such as SDO/HMI. On this date SO/PHI-HRT observed an active region and the line-of-sight magnetic field as well as the vector magnetic field were compared with those from SDO/HMI, presented in Chapter 3, obtaining the following results:

- The line-of-sight component of the vector magnetic field inferred by SO/PHI-HRT, on a 60-second cadence, agreed remarkably closely with the line-of-sight magnetic field inferred by SDO/HMI via a Fourier tachometer technique. This close agreement was consistent for both the 45-second and 12-minute cadence data product produced by SDO/HMI, with offsets below 1 G and a slope and Pearson correlation coefficient of 0.97.
- The vector magnetic field inferred by both however did not agree as closely:
  - SO/PHI-HRT inferred a stronger magnetic field strength in the weak-field regime ( $|\mathbf{B}| < 600$  G), while it inferred weaker field strengths in the strong-field regime compared to SDO/HMI. This was consistent when compared to both the 90-second and 12-minute data products produced by SDO/HMI. There were also offsets of 118 G and 178 G respectively when compared to the two different cadence products from SDO/HMI.
  - SO/PHI-HRT inferred magnetic fields which were more horizontally inclined, however a closer agreement was found with the 90-second data product from SDO/HMI. When only comparing the inclination in the strong field regime with the 90-second SDO/HMI data, the agreement was much closer, with a Pearson correlation coefficient of 0.98.
  - Restricting the comparison of the azimuth to strong-field pixels to avoid influence from noise, a close agreement was found between SO/PHI-HRT and the SDO/HMI azimuth data products at both cadences, with a few degrees of offset. Part or all of the offset could be attributed to the  $3^\circ$  angle between the two spacecraft.
  - When comparing the line-of-sight component of the two instrument’s vector magnetic fields, the offset remained minimal at 1 G, while slopes of 0.83 were determined when comparing to both the 90-second and 12-minute SDO/HMI data products.

Hoeksema et al. (2014) reported that the  $B_{LOS}$  determined via the Fourier tachometer technique is underestimated when compared to the  $B_{LOS}$  determined from the Milne-Eddington inversion. With the  $B_{LOS}$  from SO/PHI-HRT as an intermediary the a similar inconsistency between the two  $B_{LOS}$  products from SDO/HMI was found, regardless of the cadence of SDO/HMI. The reason why the LOS components of the two instrument’s vector magnetic field differs is mainly due to the observed difference in  $|\mathbf{B}|$ , as the inclination is well correlated for strong fields. All these results from comparing the vector magnetic fields suggest that any differences are mainly due to differences in noise in the data from the two instruments. Given SO/PHI-HRT observed at a much faster cadence, the photon noise was greater, and was further increased by the pointing inaccuracy of the spacecraft which unfortunately could not to be compensated. Therefore, much closer

agreement was found when comparing SO/PHI-HRT data to the non-standard 90-second data as opposed to the readily available 12-minute data from SDO/HMI.

In Chapter 4 a first attempt at comparing magnetograms from vastly different viewing angles in the ecliptic plane was made with data taken two weeks after the Sun-Earth alignment presented in Chapter 3:

- Six dates of co-temporal co-spatial observations were selected across a range of Earth-Sun-Solar Orbiter angles from  $28^\circ$  to  $51^\circ$ , with a broad range of photospheric features covered, including an active region with two sunspots, plage and quiet Sun. SO/PHI-HRT observed these features near disc centre, with the exception of one day of observations, while these features were observed closer to the limb by SDO/HMI.
- The standard reprojection algorithm used by the Python solar physics community (DeForest 2004) was found to be inappropriate when reprojecting and down-sampling magnetograms, as the algorithm is designed to achieve good photometric performance when applied to filtergrams. Unable to overcome these shortcomings through different input parameters to the algorithm, I was restricted to use the algorithm to purely evaluate the alignment of the respective magnetograms after reprojection.
- Using SDO/HMI as a reference the pointing information of the SO/PHI-HRT magnetograms could be corrected to first order. After reprojecting the SO/PHI-HRT magnetograms onto the SDO/HMI coordinate frame and down-sampling to account for the different pixel sizes and foreshortening, a good alignment was found with residual shifts in the plane of the sky on the order of 1 or 2 SDO/HMI pixels. These residual shifts however increased when the viewing angle between the two host spacecraft increased and when one or both instruments were viewing very close to the limb.
- Restricting the comparison to the umbrae from one set of co-observations mitigated the unwanted effects of the reprojection algorithm, and a cautious comparison of the LOS magnetic flux was made:
  - Due to viewing the sunspots closer to disc centre SO/PHI-HRT inferred more unsigned LOS magnetic flux compared to SDO/HMI
  - After applying the  $\mu$ -correction the unsigned LOS magnetic flux agreed remarkably well, which remained consistent throughout the 1 hour time series.
- Analysis of umbral fluxes revealed complex details. First near the centre of the umbrae, SO/PHI-HRT inferred much greater  $B_{LOS}/\mu$  values, up to 530 G more. This is most likely due to the spectral line forming at greater depth for SO/PHI-HRT, where the magnetic field is stronger, as it viewed the sunspots closer to disc centre. Secondly, as the underlying SO/PHI-HRT magnetograms have a greater spatial resolution, SO/PHI-HRT was able to better determine the umbral boundary, and hence several pixels in fact lay outside the umbra in SO/PHI-HRT, where it inferred much weaker LOS fields. These two effects offset each other after the  $\mu$ -correction was applied. The differences found between the two  $B_{LOS}/\mu$  values

likely also stem from the fact that umbral magnetic fields are not perfectly radial. In some areas the magnetic field will be preferentially inclined to one of the two instruments.

In Chapter 5, I carried out a theoretical exploration into the radiative transfer effects of inferring the photospheric magnetic field at an inclined viewing angle, such as the change in formation height of the spectral line alluded to in Chapter 4. I synthesised Stokes profiles from  $\mu = 1$  to  $\mu = 0.15$  of two commonly used photospheric spectral lines from 3D MHD simulations. These simulations had mean vertical magnetic fields of different strengths which represented unipolar regions in the quiet Sun, network and plage. I applied several commonly used methods to infer the line-of-sight magnetic field from the synthetic Stokes profiles. These synthetic Stokes profiles were additionally resampled to different spatial resolutions to test the impact on the LOS magnetic field inference. This simulation-driven work produced the following results:

- The spatially averaged LOS magnetic field is underestimated in nearly all cases (vertical magnetic field strength in the simulation and spatial resolution of the synthetic Stokes profiles) at all  $\mu$  values. Only at  $\mu = 1$ , and at a high spatial resolution, was roughly the ‘ground truth’ spatially averaged LOS magnetic field retrieved from the simulation.
- At  $\mu \leq 0.5$  the spatial resolution had little to no effect on the underestimation of the spatially averaged LOS magnetic field.
- The retrieved spatially averaged LOS magnetic field clearly did not exhibit the expected linear dependence on  $\mu$ .
- These results were consistently found for four different methods of inferring the LOS magnetic field: a Milne-Eddington Inversion code, the Fourier tachometer technique used by SDO/HMI, centre-of-gravity method and weak-field approximation. The weak-field approximation did produce erratic results near disc centre as the approximation broke down for the strong fields present in magnetic concentrations.
- We found non-negligible differences between the two spectral lines. At high  $\mu$  the 5250.2 Å spectral line inferred a lower flux density compared to 6173.3 Å, while this was reversed at low  $\mu$  where the 5250.2 Å spectral line inferred significantly more spatially averaged LOS magnetic flux density.

The underestimation of the spatially averaged LOS magnetic field was due to a combination of effects. One large effect was the passage of inclined rays through both magnetic and non-magnetic regions. Another effect was the combination polarimetric signals from strong and weak magnetic features. It was shown that the Milne-Eddington inversion code, which is the method primarily used by current space-based magnetographs, could not extract the true average field of neighbouring strong and weak magnetic features. This played a role at low spatial resolutions and when the photosphere is foreshortened due to inclined viewing angles.

## 6.1 Implications and further work

The work presented in this thesis is motivated by the desire to investigate if there are inaccuracies in magnetograms which are input as the boundary condition for models that calculate the total solar open magnetic flux. Most of these models rely on synoptic photospheric magnetograms; these capture a picture of the entire photospheric magnetic field during one rotation. This is achieved by combining vertical cutouts around the central meridian from magnetograms over the 27 days, and performing large-scale temporal averaging (and often spatial down sampling). In these synoptic magnetograms the high latitudes are therefore the region where magnetograms could suffer from inclined viewing angles.

I have shown from the results in Chapter 5 that the flux from unipolar regions, which is representative of open flux regions in coronal holes, is indeed greatly underestimated when viewing at an inclined angle. This however would mostly contribute to missing open magnetic flux near solar minimum when coronal holes are near the poles and could not explain missing open flux near solar maximum, where the coronal holes are closer to the equator. The results from Chapter 5 however also indicate that the LOS magnetic flux is underestimated in unipolar regions everywhere on the disc where we do not observe at high spatial resolution and even then only at  $\mu \geq 0.9$ . Hence there may also be open magnetic flux missing when the coronal holes are closer to the equator. Furthermore, I have made a first attempt of comparing magnetograms from two different directions and compared the total unsigned magnetic flux from the umbrae of two sunspots and found a close agreement after applying the  $\mu$ -correction. However while the total  $\mu$ -corrected fluxes agreed, large differences in the  $B_{LOS}/\mu$  distributions were found. These mostly stemmed from preferential inclination of the magnetic field, different spectral line formation heights and the Wilson depression.

These results, and their possible implications, provide compelling evidence to investigate the possible underestimation of the photospheric magnetic field further. Starting from the results of this thesis, there are several avenues that can be explored. First, as the orbital conditions of Solar Orbiter change, such as moving out of the ecliptic, the data reduction pipeline must be continually updated and refined to produce data of the highest quality possible. Secondly, there are several SO/PHI-HRT campaigns suitable for stereoscopic analysis that have been successfully carried out, with more planned in future operations. One such campaign is the active region long term tracking SOOP performed in October 2023. In Fig. 6.1 the orbital conditions of Solar Orbiter during this period are indicated in Geocentric Solar Ecliptic coordinates. Solar Orbiter orbited the Sun from right to left, and the co-observation campaign started after quadrature. For 5.5 days from 12 October until 17 October 2022, SO/PHI-HRT and SDO/HMI observed an active region that emerged a few days earlier on the back side of the Sun.

Continuum intensity images and magnetograms from both SO/PHI-HRT and SDO/HMI from each day (successive rows from top to bottom) are shown in Fig. 6.2. The continuum images and magnetograms from SDO/HMI are cropped to display only the active region that was observed by SO/PHI-HRT. The magnetograms are saturated between  $\pm 2$  kG and the continuum images are saturated between 0 and  $1.4 I_c$ , where  $I_c$  is the average continuum intensity at disc centre. Additionally, the  $\mu$  value of the sunspot

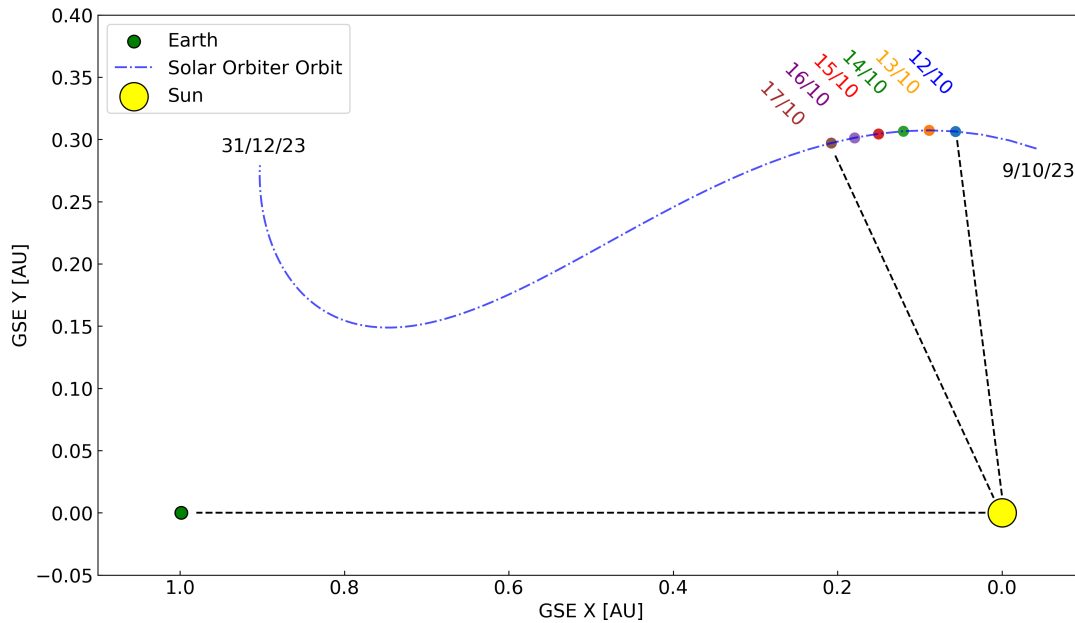


Figure 6.1: The orbital configuration of Earth, the Sun and Solar Orbiter from October 2023 until December 2023 in Geocentric Solar Ecliptic (GSE) coordinates. The orbit of Solar Orbiter is indicated in the dashed blue line. It starts from the top right and moves towards the top left. The 6 dates of Solar Orbiter observations during the Active Region Long Term SOOP are highlighted in different colours.

for the two instruments are overlaid in text, as well as the UTC time of both observations. SO/PHI-HRT observed throughout this campaign at a 1 hour cadence, providing excellent temporal coverage. The SO/PHI-HRT data are reduced to a preliminary state with further improvements to be made. This figure indicates that this active region was at the very edge of the limb for SDO/HMI at the start; conversely it is at almost disc centre for SO/PHI-HRT. As the co-observations progress, the active region moves across the solar disc such that on the last day, SDO/HMI now observed the region at disc centre while it is near the limb for SO/PHI-HRT. This dataset uniquely provides both cases of observing conditions that are perfect to investigate the effect of inclined viewing angles.

Investigations are not restricted to only comparing SO/PHI-HRT and SDO/HMI data. This active region was also observed by Hinode/SOT-SP, another space-based magnetograph, that like SDO/HMI orbits Earth. Like SO/PHI-HRT, Hinode/SOT-SP observes at a high spatial resolution and with a limited field of view. Hence comparisons with data from these two instruments are another intriguing opportunity for future investigations. However, as discussed in Chapter 4, to accurately align and account for foreshortening an algorithm dedicated to the reprojection and resampling of magnetograms must first be developed.

Finally, the simulation work from Chapter 5 can also be extended. For one, the inference of the LOS magnetic field at  $\mu < 0.15$  can be investigated. At such low  $\mu$  values the Sun's curvature will become more important and hence this should be appropriately considered. The total missing open magnetic flux that the results from Chapter 5 imply, can be estimated by applying those results to synoptic magnetograms.

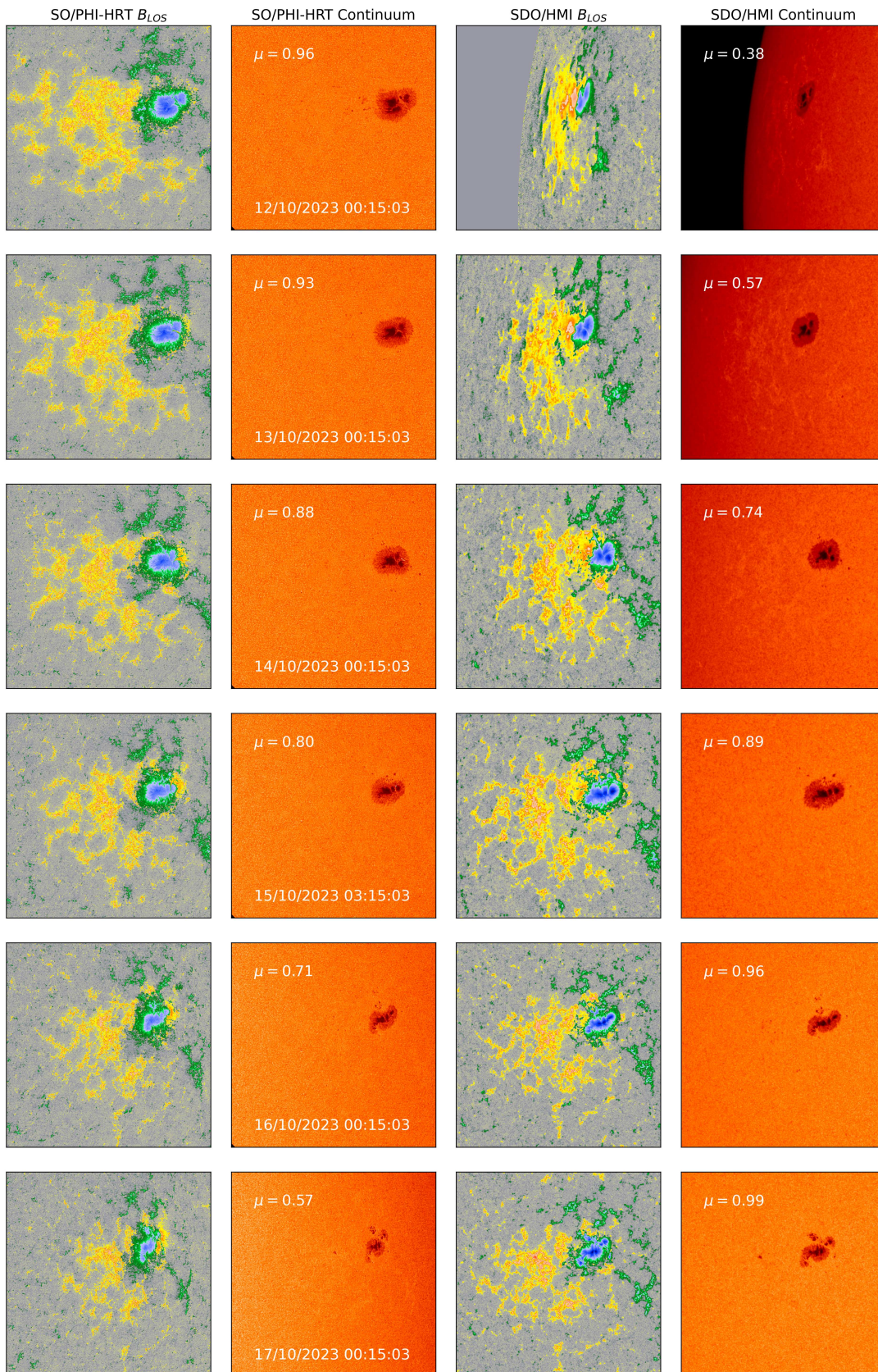


Figure 6.2: SO/PHI-HRT (preliminary) and SDO/HMI  $B_{LOS}$  and continuum images in October 2023 during the Active Region Long Term SOOP. See text for details.



# Bibliography

- Albert, K., Hirzberger, J., Kolleck, M., Jorge, N. A., Busse, D., Rodríguez, J. B., Carrascosa, J. P. C., Fiethe, B., Gandorfer, A., Germerott, D., Guan, Y., Guerrero, L., Gutierrez-Marques, P., Expósito, D. H., Lange, T., Michalik, H., Suárez, D. O., Schou, J., Solanki, S. K., del Toro Iniesta, J. C., Woch, J., 2020, Autonomous on-board data processing and instrument calibration software for the Polarimetric and Helioseismic Imager on-board the Solar Orbiter mission, *Journal of Astronomical Telescopes, Instruments, and Systems*, 6, 048004
- Alvarez-Herrero, A., García Parejo, P., Laguna, H., Villanueva, J., Barandiarán, J., Bastide, L., Reina, M., Sánchez, A., Gonzalo, A., Navarro, R., Vera, I., Royo, M., 2015, Polarization modulators based on liquid crystal variable retarders for the Solar Orbiter mission, in *Polarization Science and Remote Sensing VII*, (Eds.) J. A. Shaw, D. A. LeMaster, vol. 9613 of *Society of Photo-Optical Instrumentation Engineers (SPIE) Conference Series*, p. 96130I
- Álvarez Herrero, A., Fernández-Medina, A., Cebollero, M., Garranzo-García, D., Núñez, A., Gonzalo, A., Sánchez, A., Villanueva, J., García Parejo, P., Campos-Jara, A., Silva-López, M., San Julián, R., Laguna, H., 2022, TuMag for SUNRISE III mission: development of the optical unit of an imaging spectropolarimeter, in *Ground-based and Airborne Instrumentation for Astronomy IX*, (Eds.) C. J. Evans, J. J. Bryant, K. Motohara, vol. 12184 of *Society of Photo-Optical Instrumentation Engineers (SPIE) Conference Series*, p. 121842G
- Arge, C. N., Hildner, E., Pizzo, V. J., Harvey, J. W., 2002, Two solar cycles of nonincreasing magnetic flux, *Journal of Geophysical Research: Space Physics*, 107, SSH–16
- Arge, C. N., Leisner, A., Antiochos, S. K., Wallace, S., Henney, C. J., 2024, Proposed Resolution to the Solar Open Magnetic Flux Problem, *ApJ*, 964, 115, 2304.07649
- Aschwanden, M. J., Winebarger, A., Tsiklauri, D., Peter, H., 2007, The coronal heating paradox, *The Astrophysical Journal*, 659, 1673
- Audic, S., 1991, Radiative transfer across a magnetic flux tube, *Sol. Phys.*, 135, 275–297
- Badman, S. T., Bale, S. D., Rouillard, A. P., Bowen, T. A., Bonnell, J. W., Goetz, K., Harvey, P. R., MacDowall, R. J., Malaspina, D. M., Pulupa, M., 2021, Measurement of the open magnetic flux in the inner heliosphere down to 0.13 AU, *A&A*, 650, A18, 2009.06844

- Balbus, S. A., Hawley, J. F., 1998, Instability, turbulence, and enhanced transport in accretion disks, *Reviews of Modern Physics*, 70, 1–53
- Barthol, P., Gandorfer, A., Solanki, S. K., Schüssler, M., Chares, B., Curdt, W., Deutsch, W., Feller, A., Germerott, D., Grauf, B., Heerlein, K., Hirzberger, J., Kolleck, M., Meller, R., Müller, R., Riethmüller, T. L., Tomasch, G., Knölker, M., Lites, B. W., Card, G., Elmore, D., Fox, J., Lecinski, A., Nelson, P., Summers, R., Watt, A., Martínez Pillet, V., Bonet, J. A., Schmidt, W., Berkefeld, T., Title, A. M., Domingo, V., Gasent Blesa, J. L., del Toro Iniesta, J. C., López Jiménez, A., Álvarez-Herrero, A., Sabau-Graziati, L., Widani, C., Haberler, P., Härtel, K., Kampf, D., Levin, T., Pérez Grande, I., Sanz-Andrés, A., Schmidt, E., 2011, The Sunrise Mission, *Sol. Phys.*, 268, 1–34, 1009.2689
- Bello González, N., Yelles Chaouche, L., Okunev, O., Kneer, F., 2009, Dynamics of small-scale magnetic fields on the Sun: observations and numerical simulations, *A&A*, 494, 1091–1106
- Bellot Rubio, L., Orozco Suárez, D., 2019, Quiet Sun magnetic fields: an observational view, *Living Reviews in Solar Physics*, 16, 1
- Bellot Rubio, L. R., 1998, Structure of solar magnetic elements from inversion of Stokes spectra, Ph.D. thesis, University of La Laguna, Spain
- Berkefeld, T., Schmidt, W., Soltau, D., Bell, A., Doerr, H. P., Feger, B., Friedlein, R., Gerber, K., Heidecke, F., Kentischer, T., v. d. Lühe, O., Sigwarth, M., Wälde, E., Barthol, P., Deutsch, W., Gandorfer, A., Germerott, D., Grauf, B., Meller, R., Álvarez-Herrero, A., Knölker, M., Martínez Pillet, V., Solanki, S. K., Title, A. M., 2011, The Wave-Front Correction System for the Sunrise Balloon-Borne Solar Observatory, *Sol. Phys.*, 268, 103–123, 1009.3196
- Blanco Rodríguez, J., del Toro Iniesta, J. C., Orozco Suárez, D., Martínez Pillet, V., Bonet, J. A., Feller, A., Hirzberger, J., Lagg, A., Piqueras, J., Gasent Blesa, J. L., 2018, SOPHISM: An End-to-end Software Instrument Simulator, *ApJS*, 237, 35
- Borrero, J. M., Ichimoto, K., 2011, Magnetic Structure of Sunspots, *Living Reviews in Solar Physics*, 8, 4, 1109.4412
- Borrero, J. M., Kobel, P., 2011, Inferring the magnetic field vector in the quiet Sun. I. Photon noise and selection criteria, *A&A*, 527, A29, 1011.4380
- Borrero, J. M., Tomczyk, S., Kubo, M., Socas-Navarro, H., Schou, J., Couvidat, S., Bogart, R., 2011a, VFISV: Very Fast Inversion of the Stokes Vector for the Helioseismic and Magnetic Imager, *Sol. Phys.*, 273, 267–293, 0901.2702
- Borrero, J. M., Tomczyk, S., Kubo, M., Socas-Navarro, H., Schou, J., Couvidat, S., Bogart, R., 2011b, VFISV: Very Fast Inversion of the Stokes Vector for the Helioseismic and Magnetic Imager, *Sol. Phys.*, 273, 267–293, 0901.2702

- Borrero, J. M., Lites, B. W., Lagg, A., Rezaei, R., Rempel, M., 2014a, Comparison of inversion codes for polarized line formation in MHD simulations. I. Milne-Eddington codes, *A&A*, 572, A54, 1409.3376
- Borrero, J. M., Lites, B. W., Lagg, A., Rezaei, R., Rempel, M., 2014b, Comparison of inversion codes for polarized line formation in MHD simulations. I. Milne-Eddington codes, *A&A*, 572, A54, 1409.3376
- Bumba, V., Howard, R., 1969, Solar Activity and Recurrences in Magnetic-Field Distribution, *Sol. Phys.*, 7, 28–38
- Cameron, R., Schüssler, M., 2007, Solar Cycle Prediction Using Precursors and Flux Transport Models, *ApJ*, 659, 801–811, astro-ph/0612693
- Carmona, M., Gómez, J. M., Roma, D., Casas, A., López, M., Bosch, J., Herms, A., Sabater, J., Volkmer, R., Heidecke, F., Maue, T., Nakai, E., Schmidt, W., 2014, System model of an image stabilization system, in *Modeling, Systems Engineering, and Project Management for Astronomy VI*, (Eds.) G. Z. Angeli, P. Dierickx, vol. 9150 of Society of Photo-Optical Instrumentation Engineers (SPIE) Conference Series, p. 91501U
- Castellanos Durán, J. S., 2023, Strong magnetic fields and unusual flows in sunspots, Ph.D. thesis, Georg-August-Universität-Göttingen
- Castellanos Durán, J. S., Lagg, A., Solanki, S. K., van Noort, M., 2020, Detection of the Strongest Magnetic Field in a Sunspot Light Bridge, *ApJ*, 895, 129, 2003.12078
- Centeno, R., Milić, I., Rempel, M., Nitta, N. V., Sun, X., 2023, Limitations and Biases in the Retrieval of the Polar Magnetic Field. I. The Role of the Magnetic Filling Factor in Milne-Eddington Inversions of Simulated Hinode/SP Data, *ApJ*, 951, 23, 2305.00924
- Charbonneau, P., 2020, Dynamo models of the solar cycle, *Living Reviews in Solar Physics*, 17, 1–104
- Chatzistergos, T., Usoskin, I. G., Kovaltsov, G. A., Krivova, N. A., Solanki, S. K., 2017, New reconstruction of the sunspot group numbers since 1739 using direct calibration and “backbone” methods, *A&A*, 602, A69, 1702.06183
- Chitta, L. P., Peter, H., Solanki, S. K., Barthol, P., Gandorfer, A., Gizon, L., Hirzberger, J., Riethmüller, T. L., van Noort, M., Blanco Rodríguez, J., Del Toro Iniesta, J. C., Orozco Suárez, D., Schmidt, W., Martínez Pillet, V., Knölker, M., 2017, Solar Coronal Loops Associated with Small-scale Mixed Polarity Surface Magnetic Fields, *ApJS*, 229, 4, 1610.07484
- Cobos Carrascosa, J. P., Aparicio del Moral, B., Ramos Mas, J. L., Balaguer, M., López Jiménez, A. C., del Toro Iniesta, J. C., 2016, The RTE inversion on FPGA aboard the solar orbiter PHI instrument, in *Software and Cyberinfrastructure for Astronomy IV*, (Eds.) G. Chiozzi, J. C. Guzman, vol. 9913 of Society of Photo-Optical Instrumentation Engineers (SPIE) Conference Series, p. 991342

- Couvidat, S., Rajaguru, S. P., Wachter, R., Sankarasubramanian, K., Schou, J., Scherrer, P. H., 2012a, Line-of-Sight Observables Algorithms for the Helioseismic and Magnetic Imager (HMI) Instrument Tested with Interferometric Bidimensional Spectrometer (IBIS) Observations, *Sol. Phys.*, 278, 217–240
- Couvidat, S., Schou, J., Shine, R. A., Bush, R. I., Miles, J. W., Scherrer, P. H., Rairden, R. L., 2012b, Wavelength Dependence of the Helioseismic and Magnetic Imager (HMI) Instrument onboard the Solar Dynamics Observatory (SDO), *Sol. Phys.*, 275, 285–325
- Couvidat, S., Schou, J., Hoeksema, J. T., Bogart, R. S., Bush, R. I., Duvall, T. L., Liu, Y., Norton, A. A., Scherrer, P. H., 2016, Observables Processing for the Helioseismic and Magnetic Imager Instrument on the Solar Dynamics Observatory, *Sol. Phys.*, 291, 1887–1938, 1606.02368
- Cranmer, S. R., 2009, Coronal holes, *Living Reviews in Solar Physics*, 6, 1–66
- Crutcher, R. M., Kembell, A. J., 2019, Review of zeeman effect observations of regions of star formation, *Frontiers in Astronomy and Space Sciences*, 6, 66
- Dang, T., Li, X., Luo, B., Li, R., Zhang, B., Pham, K., Ren, D., Chen, X., Lei, J., Wang, Y., 2022, Unveiling the Space Weather During the Starlink Satellites Destruction Event on 4 February 2022, *Space Weather*, 20, e2022SW003152
- de la Cruz Rodríguez, J., 2019, A method for global inversion of multi-resolution solar data, *A&A*, 631, A153, 1909.02604
- De Moortel, I., Browning, P., 2015, Recent advances in coronal heating, *Philosophical Transactions of the Royal Society A: Mathematical, Physical and Engineering Sciences*, 373, 20140269
- DeForest, C. E., 2004, On Re-sampling of Solar Images, *Sol. Phys.*, 219, 3–23
- del Toro Iniesta, J. C., 2003, Introduction to Spectropolarimetry
- Del Toro Iniesta, J. C., Martínez Pillet, V., 2012, Assessing the Behavior of Modern Solar Magnetographs and Spectropolarimeters, *ApJS*, 201, 22, 1205.4845
- Dominguez-Tagle, C., Appourchaux, T., Ruiz de Galarreta, C., Fourmond, J.-J., Philippon, A., Le Clec’h, J.-C., Bouzit, M., Bommier, V., Le Cocquen, R., Crussaire, D., Malherbe, J.-M., 2014, Optical characterization of the breadboard narrowband pre-filters for Solar Orbiter PHI, in *Space Telescopes and Instrumentation 2014: Optical, Infrared, and Millimeter Wave*, (Eds.) J. Oschmann, Jacobus M., M. Clampin, G. G. Fazio, H. A. MacEwen, vol. 9143 of *Society of Photo-Optical Instrumentation Engineers (SPIE) Conference Series*, p. 91435G
- Elkins-Tanton, L. T., 2006, *The Sun, Mercury, and Venus*, Infobase Publishing
- Evershed, J., 1909, Radial movement in sun-spots, *MNRAS*, 69, 454

- Felipe, T., Collados, M., Khomenko, E., Rajaguru, S. P., Franz, M., Kuckein, C., Asensio Ramos, A., 2017, Signatures of the impact of flare-ejected plasma on the photosphere of a sunspot light bridge, *A&A*, 608, A97, 1708.06133
- Fligge, M., Solanki, S. K., Unruh, Y. C., 2000, Modelling irradiance variations from the surface distribution of the solar magnetic field, *A&A*, 353, 380–388
- Fouhey, D. F., Higgins, R. E. L., Antiochos, S. K., Barnes, G., DeRosa, M. L., Hoeksema, J. T., Leka, K. D., Liu, Y., Schuck, P. W., Gombosi, T. I., 2023, Large-scale Spatial Cross-calibration of Hinode/SOT-SP and SDO/HMI, *ApJS*, 264, 49, 2209.15036
- Freytag, B., Steffen, M., Wedemeyer-Böhm, S., Ludwig, H.-G., Leenaarts, J., Schaffenberger, W., Allard, F., Chiavassa, A., Höfner, S., Kamp, I., Steiner, O., 2010, CO5BOLD: COnservative COde for the COmputation of COmpressible COnvection in a BOx of L Dimensions with  $l=2,3$ , *Astrophysics Source Code Library*, record ascl:1011.014
- Freytag, B., Steffen, M., Ludwig, H. G., Wedemeyer-Böhm, S., Schaffenberger, W., Steiner, O., 2012, Simulations of stellar convection with CO5BOLD, *Journal of Computational Physics*, 231, 919–959, 1110.6844
- Frutiger, C., 2000, Inversions of Zeeman split Stokes profiles, Ph.D. thesis, Institute of Astronomy, ETH Zürich, Switzerland, No. 13896
- Frutiger, C., Solanki, S. K., Fligge, M., Bruls, J. H. M. J., 2000, Properties of the solar granulation obtained from the inversion of low spatial resolution spectra, *A&A*, 358, 1109–1121
- Galsgaard, K., Nordlund, Å., 1996, Heating and activity of the solar corona 1. Boundary shearing of an initially homogeneous magnetic field, *J. Geophys. Res.*, 101, 13 445–13 460
- Gandorfer, A., Grauf, B., Barthol, P., Riethmüller, T. L., Solanki, S. K., Chares, B., Deutsch, W., Ebert, S., Feller, A., Germerott, D., Heerlein, K., Heinrichs, J., Hirche, D., Hirzberger, J., Kolleck, M., Meller, R., Müller, R., Schäfer, R., Tomasch, G., Knölker, M., Martínez Pillet, V., Bonet, J. A., Schmidt, W., Berkefeld, T., Feger, B., Heidecke, F., Soltau, D., Tischenberg, A., Fischer, A., Title, A., Anwand, H., Schmidt, E., 2011, The Filter Imager SuFI and the Image Stabilization and Light Distribution System ISLiD of the Sunrise Balloon-Borne Observatory: Instrument Description, *Sol. Phys.*, 268, 35–55, 1009.1037
- Gandorfer, A., Grauf, B., Staub, J., Bischoff, J., Woch, J., Hirzberger, J., Solanki, S. K., Álvarez-Herrero, A., García Parejo, P., Schmidt, W., Volkmer, R., Appourchaux, T., del Toro Iniesta, J. C., 2018, The High Resolution Telescope (HRT) of the Polarimetric and Helioseismic Imager (PHI) onboard Solar Orbiter, in *Space Telescopes and Instrumentation 2018: Optical, Infrared, and Millimeter Wave*, (Eds.) M. Lystrup, H. A. MacEwen, G. G. Fazio, N. Batalha, N. Siegler, E. C. Tong, vol. 10698 of *Society of Photo-Optical Instrumentation Engineers (SPIE) Conference Series*, p. 106984N

- García, R. A., Turck-Chièze, S., Jiménez-Reyes, S. J., Ballot, J., Pallé, P. L., Eff-Darwich, A., Mathur, S., Provost, J., 2007, Tracking solar gravity modes: the dynamics of the solar core, *Science*, 316, 1591–1593
- Gomez, D. O., 1990, Heating of the Solar Corona, *Fund. Cosmic Phys.*, 14, 131–233
- Gosain, S., Uitenbroek, H., 2024, Estimation of projection effects in the polar magnetic field measurements from the ecliptic view, [2407.09010](#)
- Gosic, M., 2015, The solar internetwork, Ph.D. thesis, University of Granada, Spain
- Gošić, M., Bellot Rubio, L. R., Orozco Suárez, D., Katsukawa, Y., del Toro Iniesta, J. C., 2014, The Solar Internetwork. I. Contribution to the Network Magnetic Flux, *ApJ*, 797, 49, [1408.2369](#)
- Gudiksen, B. V., Carlsson, M., Hansteen, V. H., Hayek, W., Leenaarts, J., Martínez-Sykora, J., 2011, The stellar atmosphere simulation code Bifrost. Code description and validation, *A&A*, 531, A154, [1105.6306](#)
- Guizar-Sicairos, M., Thurman, S. T., Fienup, J. R., 2008, Efficient subpixel image registration algorithms, *Optics Letters*, 33, 156
- Hagenaar, H. J., 2001, Ephemeral Regions on a Sequence of Full-Disk Michelson Doppler Imager Magnetograms, *ApJ*, 555, 448–461
- Hale, G. E., 1908, The zeeman effect in the sun, *Publications of the Astronomical Society of the Pacific*, Vol. 20, No. 123, p. 287, 20, 287
- Hale, G. E., Nicholson, S. B., 1925, The Law of Sun-Spot Polarity, *ApJ*, 62, 270
- Hale, G. E., Ellerman, F., Nicholson, S. B., Joy, A. H., 1919, The Magnetic Polarity of Sun-Spots, *ApJ*, 49, 153
- Hathaway, D. H., 2015, The Solar Cycle, *Living Reviews in Solar Physics*, 12, 4, [1502.07020](#)
- Hoeksema, J. T., Liu, Y., Hayashi, K., Sun, X., Schou, J., Couvidat, S., Norton, A., Bobra, M., Centeno, R., Leka, K. D., Barnes, G., Turmon, M., 2014, The Helioseismic and Magnetic Imager (HMI) Vector Magnetic Field Pipeline: Overview and Performance, *Sol. Phys.*, 289, 3483–3530, [1404.1881](#)
- Hoeksema, J. T., Baldner, C. S., Bush, R. I., Schou, J., Scherrer, P. H., 2018, On-Orbit Performance of the Helioseismic and Magnetic Imager Instrument onboard the Solar Dynamics Observatory, *Sol. Phys.*, 293, 45, [1802.01731](#)
- Ito, H., Tsuneta, S., Shiota, D., Tokumaru, M., Fujiki, K., 2010, Is the Polar Region Different from the Quiet Region of the Sun?, *ApJ*, 719, 131–142, [1005.3667](#)
- Jin, C. L., Wang, J. X., Song, Q., Zhao, H., 2011, The Sun’s Small-scale Magnetic Elements in Solar Cycle 23, *ApJ*, 731, 37, [1102.3728](#)

- Kahil, F., Gandorfer, A., Hirzberger, J., Orozco Suárez, D., Albert, K., Albelo Jorge, N., Appourchaux, T., Álvarez-Herrero, A., Blanco Rodríguez, J., Germerott, D., Guerrero, L., Gutierrez Marquez, P., Sinjan, J., Calchetti, D., Kolleck, M., Solanki, S. K., del Toro Iniesta, J. C., Volkmer, R., Woch, J., Fiethe, B., Gómez Cama, J. M., Pérez-Grande, I., Sanchis Kilders, E., Balaguer Jiménez, M., Bellot Rubio, L. R., Carmona, M., Deutsch, W., Fernandez-Rico, G., Fernández-Medina, A., García Parejo, P., Gasent Blesa, J. L., Gizon, L., Grauf, B., Heerlein, K., Korpi-Lagg, A., Lange, T., López Jiménez, A., Maue, T., Meller, R., Michalik, H., Moreno Vacas, A., Müller, R., Nakai, E., Schmidt, W., Schou, J., Schühle, U., Staub, J., Strecker, H., Torralbo, I., Valori, G., 2022, Image quality of data products of the high resolution telescope of the polarimetric and helioseismic imager, in *Space Telescopes and Instrumentation 2022: Optical, Infrared, and Millimeter Wave*, (Eds.) L. E. Coyle, S. Matsuura, M. D. Perrin, vol. 12180 of *Society of Photo-Optical Instrumentation Engineers (SPIE) Conference Series*, p. 121803F
- Kahil, F., Gandorfer, A., Hirzberger, J., Calchetti, D., Sinjan, J., Valori, G., Solanki, S. K., Van Noort, M., Albert, K., Albelo Jorge, N., Alvarez-Herrero, A., Appourchaux, T., Bellot Rubio, L. R., Blanco Rodríguez, J., Feller, A., Fiethe, B., Germerott, D., Gizon, L., Guerrero, L., Gutierrez-Marques, P., Kolleck, M., Korpi-Lagg, A., Michalik, H., Moreno Vacas, A., Orozco Suárez, D., Pérez-Grande, I., Sanchis Kilders, E., Schou, J., Schühle, U., Staub, J., Strecker, H., del Toro Iniesta, J. C., Volkmer, R., Woch, J., 2023, Wavefront error of PHI/HRT on Solar Orbiter at various heliocentric distances, *A&A*, 675, A61, 2306.00163
- Kippenhahn, R., Moellenhoff, C., 1975, *Elementare Plasmaphysik*
- Krieger, A. S., Timothy, A. F., Roelof, E. C., 1973, A Coronal Hole and Its Identification as the Source of a High Velocity Solar Wind Stream, *Sol. Phys.*, 29, 505–525
- Krivova, N. A., Solanki, S. K., 2004, Effect of spatial resolution on estimating the Sun's magnetic flux, *A&A*, 417, 1125–1132
- Kuhn, J. R., Lin, H., Loran, D., 1991, Gain calibrating NonUniform Image-Array Data Using Only the Image Data, *PASP*, 103, 1097
- Lagg, A., Woch, J., Krupp, N., Solanki, S. K., 2004, Retrieval of the full magnetic vector with the He I multiplet at 1083 nm. Maps of an emerging flux region, *A&A*, 414, 1109–1120
- Lagg, A., Ishikawa, R., Merenda, L., Wiegmann, T., Tsuneta, S., Solanki, S. K., 2009, Internetwork Horizontal Magnetic Fields in the Quiet Sun Chromosphere: Results from a Joint Hinode/VTT Study, in *The Second Hinode Science Meeting: Beyond Discovery-Toward Understanding*, (Eds.) B. Lites, M. Cheung, T. Magara, J. Mariska, K. Reeves, vol. 415 of *Astronomical Society of the Pacific Conference Series*, p. 327
- Landi Degl'Innocenti, E., Landolfi, M., 2004, *Polarization in Spectral Lines*, vol. 307
- Lange, T., Fiethe, B., Michel, H., Michalik, H., Albert, K., Hirzberger, J., 2017, On-board processing using reconfigurable hardware on the solar orbiter PHI instrument, in *2017 NASA/ESA Conference on Adaptive Hardware and Systems (AHS)*, pp. 186–191

- Leka, K. D., 1999, On the value of  $\alpha$  from vector magnetograph data-ii. spatial resolution, field of view, and validity, *Solar Physics*, 188, 21–40
- Leka, K. D., Barnes, G., 2012, Modeling and interpreting the effects of spatial resolution on solar magnetic field maps, *Solar Physics*, 277, 89–118
- Lemen, J. R., Title, A. M., Akin, D. J., Boerner, P. F., Chou, C., Drake, J. F., Duncan, D. W., Edwards, C. G., Friedlaender, F. M., Heyman, G. F., Hurlburt, N. E., Katz, N. L., Kushner, G. D., Levay, M., Lindgren, R. W., Mathur, D. P., McFeaters, E. L., Mitchell, S., Rehse, R. A., Schrijver, C. J., Springer, L. A., Stern, R. A., Tarbell, T. D., Wuelser, J.-P., Wolfson, C. J., Yanari, C., Bookbinder, J. A., Cheimets, P. N., Caldwell, D., Deluca, E. E., Gates, R., Golub, L., Park, S., Podgorski, W. A., Bush, R. I., Scherrer, P. H., Gumm, M. A., Smith, P., Auken, G., Jerram, P., Pool, P., Soufli, R., Windt, D. L., Beardsley, S., Clapp, M., Lang, J., Waltham, N., 2012, The Atmospheric Imaging Assembly (AIA) on the Solar Dynamics Observatory (SDO), *Sol. Phys.*, 275, 17–40
- Lepping, R. P., Acuña, M. H., Burlaga, L. F., Farrell, W. M., Slavin, J. A., Schatten, K. H., Mariani, F., Ness, N. F., Neubauer, F. M., Whang, Y. C., Byrnes, J. B., Kennon, R. S., Panetta, P. V., Scheifele, J., Worley, E. M., 1995, The Wind Magnetic Field Investigation, *Space Sci. Rev.*, 71, 207–229
- Linker, J. A., Caplan, R. M., Downs, C., Riley, P., Mikic, Z., Lionello, R., Henney, C. J., Arge, C. N., Liu, Y., DeRosa, M. L., et al., 2017, The open flux problem, *The Astrophysical Journal*, 848, 70
- Lites, B., Casini, R., Garcia, J., Socas-Navarro, H., 2007, A suite of community tools for spectro-polarimetric analysis, *Mem. Soc. Astron. Italiana*, 78, 148
- Liu, Y., Hoeksema, J. T., Scherrer, P. H., Schou, J., Couvidat, S., Bush, R. I., Duvall, T. L., Hayashi, K., Sun, X., Zhao, X., 2012, Comparison of Line-of-Sight Magnetograms Taken by the Solar Dynamics Observatory/Heliioseismic and Magnetic Imager and Solar and Heliospheric Observatory/Michelson Doppler Imager, *Sol. Phys.*, 279, 295–316
- Liu, Y., Baldner, C., Bogart, R., Duvall, T., Hoeksema, J. T., Norton, A., Scherrer, P., Schou, J., 2016, Hmi sci. nuggets, #56, a new observing scheme for hmi vector field measurements: Mod-1
- Livingston, W., 2002, Sunspots Observed to Physically Weaken in 2000-2001, *Sol. Phys.*, 207, 41–45
- Löschl, P., Valori, G., Hirzberger, J., Schou, J., Solanki, S. K., Orozco Suárez, D., Albert, K., Albelo Jorge, N., Appourchaux, T., Alvarez-Herrero, A., Blanco Rodríguez, J., Gandorfer, A., Germerott, D., Guerrero, L., Gutierrez-Marques, P., Kahil, F., Kolléck, M., del Toro Iniesta, J. C., Volkmer, R., Woch, J., Fiethe, B., Pérez-Grande, I., Sanchis Kilders, E., Balaguer Jiménez, M., Bellot Rubio, L. R., Calchetti, D., Carmona, M., Deutsch, W., Feller, A., Fernandez-Rico, G., Fernández-Medina, A., García Parejo, P., Gasent Blesa, J. L., Gizon, L., Grauf, B., Heerlein, K., Korpi-Lagg, A., Lange, T., López Jiménez, A., Maue, T., Meller, R., Moreno Vacas, A., Müller, R., Nakai, E.,

- Schmidt, W., Schühle, U., Sinjan, J., Staub, J., Strecker, H., Torralbo, I., 2024, A first rapid synoptic magnetic field map using SDO/HMI and SO/PHI data, *A&A*, 681, A59
- Martínez González, M. J., Bellot Rubio, L. R., 2009, Emergence of small-scale magnetic loops through the quiet solar atmosphere, *The Astrophysical Journal*, 700, 1391
- Martínez Pillet, V., del Toro Iniesta, J. C., Álvarez-Herrero, A., Domingo, V., Bonet, J. A., González Fernández, L., López Jiménez, A., Pastor, C., Gasent Blesa, J. L., Mellado, P., Piqueras, J., Aparicio, B., Balaguer, M., Ballesteros, E., Belenguer, T., Bellot Rubio, L. R., Berkefeld, T., Collados, M., Deutsch, W., Feller, A., Girela, F., Grauf, B., Heredero, R. L., Herranz, M., Jerónimo, J. M., Laguna, H., Meller, R., Menéndez, M., Morales, R., Orozco Suárez, D., Ramos, G., Reina, M., Ramos, J. L., Rodríguez, P., Sánchez, A., Uribe-Patarroyo, N., Barthol, P., Gandorfer, A., Knoelker, M., Schmidt, W., Solanki, S. K., Vargas Domínguez, S., 2011, The Imaging Magnetograph eXperiment (IMaX) for the Sunrise Balloon-Borne Solar Observatory, *Sol. Phys.*, 268, 57–102, 1009.1095
- Mathew, S. K., Solanki, S. K., Lagg, A., Collados, M., Borrero, J. M., Berdyugina, S., 2004, Thermal-magnetic relation in a sunspot and a map of its Wilson depression, *A&A*, 422, 693–701
- Maunder, E. W., 1904, Note on the Distribution of Sun-spots in Heliographic Latitude, 1874-1902, *MNRAS*, 64, 747–761
- Metcalf, T. R., 1994, Resolving the 180-degree ambiguity in vector magnetic field measurements: The ‘minimum’ energy solution, *Sol. Phys.*, 155, 235–242
- Metcalf, T. R., Leka, K. D., Barnes, G., Lites, B. W., Georgoulis, M. K., Pevtsov, A. A., Balasubramaniam, K. S., Gary, G. A., Jing, J., Li, J., Liu, Y., Wang, H. N., Abramenko, V., Yurchyshyn, V., Moon, Y. J., 2006, An Overview of Existing Algorithms for Resolving the 180 Ambiguity in Vector Magnetic Fields: Quantitative Tests with Synthetic Data, *Sol. Phys.*, 237, 267–296
- Milic, I., Centeno, R., Sun, X., Rempel, M., de la Cruz Rodriguez, J., 2024, Spatial resolution effects on the solar open flux estimates, *arXiv e-prints*, arXiv:2402.02486, 2402.02486
- Modestov, M., Khomenko, E., Vitas, N., de Vicente, A., Navarro, A., González-Morales, P. A., Collados, M., Felipe, T., Martínez-Gómez, D., Hunana, P., Luna, M., Koll Pistarini, M., Popescu Braileanu, B., Perdomo García, A., Liakh, V., Santamaria, I., Gomez Miguez, M. M., 2024, MANCHA3D Code: Multipurpose Advanced Non-ideal MHD Code for High-Resolution Simulations in Astrophysics, *Sol. Phys.*, 299, 23, 2312.04179
- Moreno Vacas, A., Orozco Suárez, D., Strecker, H., del Toro Iniesta, J. C., Borrero, J. M., Albert, K., Solanki, S. K., Bailén, F. J., Bellot Rubio, L. R., Hirzberger, J., Sinjan, J., Santamarina Guerrero, P., Valori, G., Albelo Jorge, N., Alvarez-Herrero, A., Appourchaux, T., Blanco Rodríguez, J., Calchetti, D., Feller, A., Fiethe, B., Gandorfer, A., Germerott, D., Gizon, L., Gómez Cama, J. M., Guerrero, L., Gutierrez-Marques,

- P., Kahil, F., Kolleck, M., Korpi-Lagg, A., Michalik, H., Pérez-Grande, I., Sanchis Kilders, E., Schou, J., Schühle, U., Staub, J., Volkmer, R., Woch, J., 2024, Comparison of magnetic data products from Solar Orbiter SO/PHI-FDT and SDO/HMI, *A&A*, 685, A28
- Müller, D., Marsden, R. G., St. Cyr, O. C., Gilbert, H. R., Solar Orbiter Team, 2013, Solar Orbiter . Exploring the Sun-Heliosphere Connection, *Sol. Phys.*, 285, 25–70, 1207.4579
- Müller, D., Nicula, B., Felix, S., Verstringe, F., Bourgoignie, B., Csillaghy, A., Berghmans, D., Jiggins, P., García-Ortiz, J., Ireland, J., et al., 2017, Jhelioviewer-time-dependent 3d visualisation of solar and heliospheric data, *Astronomy & Astrophysics*, 606, A10
- Müller, D., St. Cyr, O. C., Zouganelis, I., Gilbert, H. R., Marsden, R., Nieves-Chinchilla, T., Antonucci, E., Auchère, F., Berghmans, D., Horbury, T. S., Howard, R. A., Krucker, S., Maksimovic, M., Owen, C. J., Rochus, P., Rodriguez-Pacheco, J., Romoli, M., Solanki, S. K., Bruno, R., Carlsson, M., Fludra, A., Harra, L., Hassler, D. M., Livi, S., Louarn, P., Peter, H., Schühle, U., Teriaca, L., del Toro Iniesta, J. C., Wimmer-Schweingruber, R. F., Marsch, E., Velli, M., De Groof, A., Walsh, A., Williams, D., 2020, The Solar Orbiter mission. Science overview, *A&A*, 642, A1, 2009.00861
- Murray, N., 1992, On the Inclination of Photospheric Solar Magnetic Fields, *ApJ*, 401, 386
- Ngampoopun, N., Long, D. M., Baker, D., Green, L. M., Yardley, S. L., James, A. W., To, A. S. H., 2023, The Merging of a Coronal Dimming and the Southern Polar Coronal Hole, *ApJ*, 950, 150, 2305.06106
- Orozco Suárez, D., Del Toro Iniesta, J. C., 2007a, The usefulness of analytic response functions, *A&A*, 462, 1137–1145, 1211.1502
- Orozco Suárez, D., Del Toro Iniesta, J. C., 2007b, The usefulness of analytic response functions, *A&A*, 462, 1137–1145, 1211.1502
- Orozco Suárez, D., Bellot Rubio, L., Del Toro Iniesta, J. C., Tsuneta, S., Lites, B., Ichimoto, K., Katsukawa, Y., Nagata, S., Shimizu, T., Shine, R. A., et al., 2007, Strategy for the inversion of hinode spectropolarimetric measurements in the quiet+ n, *Publications of the Astronomical Society of Japan*, 59, S837–S844
- Orozco Suárez, D., 2024, The milos milne-eddington inversion code
- Owens, M. J., Arge, C. N., Crooker, N. U., Schwadron, N. A., Horbury, T. S., 2008, Estimating total heliospheric magnetic flux from single-point in situ measurements, *Journal of Geophysical Research (Space Physics)*, 113, A12103
- Paschen, F. v., Back, E., 1912, Normale und anomale zeemaneffekte, *Annalen der Physik*, 344, 897–932

- Paxman, R. G., Schulz, T. J., Fienup, J. R., 1992, Joint estimation of object and aberrations by using phase diversity, *Journal of the Optical Society of America A*, 9, 1072–1085
- Pence, W. D., Chiappetti, L., Page, C. G., Shaw, R. A., Stobie, E., 2010, Definition of the Flexible Image Transport System (FITS), version 3.0, *A&A*, 524, A42
- Pereira, T. M. D., Uitenbroek, H., 2015, RH 1.5D: a massively parallel code for multi-level radiative transfer with partial frequency redistribution and Zeeman polarisation, *A&A*, 574, A3, 1411.1079
- Pesnell, W. D., Thompson, B. J., Chamberlin, P. C., 2012, The Solar Dynamics Observatory (SDO), *Sol. Phys.*, 275, 3–15
- Petrie, G., Ettinger, S., 2017, Polar Field Reversals and Active Region Decay, *Space Sci. Rev.*, 210, 77–108
- Petrie, G. J. D., 2015, Solar Magnetism in the Polar Regions, *Living Reviews in Solar Physics*, 12, 5
- Petrovay, K., 2020, Solar cycle prediction, *Living Reviews in Solar Physics*, 17, 2
- Pietarila Graham, J., Danilovic, S., Schüssler, M., 2009, Turbulent Magnetic Fields in the Quiet Sun: Implications of Hinode Observations and Small-Scale Dynamo Simulations, *ApJ*, 693, 1728–1735, 0812.2125
- Plowman, J. E., Berger, T. E., 2020a, Calibrating GONG Magnetograms with End-to-end Instrument Simulation I: Background, the GONG Instrument, and End-to-end Simulation, *Sol. Phys.*, 295, 143, 2002.02489
- Plowman, J. E., Berger, T. E., 2020b, Calibrating GONG Magnetograms with End-to-End Instrument Simulation II: Theory of Calibration, *Sol. Phys.*, 295, 142, 2002.02490
- Plowman, J. E., Berger, T. E., 2020c, Calibrating GONG Magnetograms with End-to-End Instrument Simulation III: Comparison, Calibration, and Results, *Sol. Phys.*, 295, 144, 2002.02486
- Prabhu, A., Lagg, A., Hirzberger, J., Solanki, S. K., 2020, The magnetic fine structure of the sun’s polar region as revealed by sunrise, *Astronomy & Astrophysics*, 644, A86
- Priest, E. R., 1982, *Solar magneto-hydrodynamics.*, vol. 21
- Przybylski, D., Cameron, R., Solanki, S. K., Rempel, M., Leenaarts, J., Anusha, L. S., Witzke, V., Shapiro, A. I., 2022, Chromospheric extension of the MURaM code, *A&A*, 664, A91, 2204.03126
- Quintero Noda, C., Barklem, P., Gafeira, R., Cobo, B. R., Collados, M., Carlsson, M., Martínez Pillet, V., Orozco Suárez, D., Uitenbroek, H., Katsukawa, Y., 2021, Diagnostic capabilities of spectropolarimetric observations for understanding solar phenomena. i. zeeman-sensitive photospheric lines, *Astronomy & Astrophysics*, 652, A161

- Quintero Noda, C., Barklem, P. S., Gafeira, R., Ruiz Cobo, B., Collados, M., Carlsson, M., Martínez Pillet, V., Orozco Suárez, D., Uitenbroek, H., Katsukawa, Y., 2021, Diagnostic capabilities of spectropolarimetric observations for understanding solar phenomena. I. Zeeman-sensitive photospheric lines, *A&A*, 652, A161, 2106.05084
- Rachkovsky, D. N., 1962, Magnetic rotation effects in spectral lines, *Izvestiya Ordena Trudovogo Krasnogo Znameni Krymskoj Astrofizicheskoj Observatorii*, 28, 259–270
- Rachkovsky, D. N., 1967, The reduction for anomalous dispersion in the theory of absorption line formation in a magnetic field, *Izvestiya Ordena Trudovogo Krasnogo Znameni Krymskoj Astrofizicheskoj Observatorii*, 37, 56–61
- Rees, D. E., Semel, M. D., 1979, Line formation in an unresolved magnetic element: a test of the centre of gravity method., *A&A*, 74, 1–5
- Régnier, S., 2013, Magnetic Field Extrapolations into the Corona: Success and Future Improvements, *Sol. Phys.*, 288, 481–505, 1307.3844
- Rempel, M., Bhatia, T., Bellot Rubio, L., Korpi-Lagg, M. J., 2023, Small-Scale Dynamos: From Idealized Models to Solar and Stellar Applications, *Space Sci. Rev.*, 219, 36, 2305.02787
- Rempel, M. D., Cheung, M., 2016, Coronal extension of the MURaM radiative MHD code: From quiet sun to flare simulations, in *AAS/Solar Physics Division Abstracts #47*, vol. 47 of *AAS/Solar Physics Division Meeting*, p. 208.03
- Riethmüller, T. L., Solanki, S. K., Berdyugina, S. V., Schüssler, M., Martínez Pillet, V., Feller, A., Gandorfer, A., Hirzberger, J., 2014a, Comparison of solar photospheric bright points between Sunrise observations and MHD simulations, *A&A*, 568, A13, 1406.1387
- Riethmüller, T. L., Solanki, S. K., Berdyugina, S. V., Schüssler, M., Martínez Pillet, V., Feller, A., Gandorfer, A., Hirzberger, J., 2014b, Comparison of solar photospheric bright points between Sunrise observations and MHD simulations, *A&A*, 568, A13, 1406.1387
- Rieutord, M., Rincon, F., 2010, The Sun's Supergranulation, *Living Reviews in Solar Physics*, 7, 2, 1005.5376
- Rochus, P., Auchere, F., Berghmans, D., Harra, L., Schmutz, W., Schühle, U., Addison, P., Appourchaux, T., Cuadrado, R. A., Baker, D., et al., 2020, The solar orbiter eui instrument: the extreme ultraviolet imager, *Astronomy & Astrophysics*, 642, A8
- Romero Avila, A., Inhester, B., Hirzberger, J., Solanki, S. K., 2024, Photospheric Stereoscropy: Direct Estimation of Solar Surface-Height Variations, *Sol. Phys.*, 299, 41
- Ruiz Cobo, B., del Toro Iniesta, J. C., 1992, Inversion of Stokes Profiles, *ApJ*, 398, 375
- Rutten, R. J., 1988, The NLTE formation of iron lines in the solar photosphere, in *IAU Colloq. 94: Physics of Formation of Fe II Lines Outside LTE*, (Eds.) R. Viotti, A. Vittone, M. Friedjung, vol. 138 of *Astrophysics and Space Science Library*, pp. 185–210

- Rutten, R. J., et al., 2003, Radiative transfer in stellar atmospheres, Sterrekundig Instituut Utrecht, 8 edn.
- Sainz Dalda, A., 2017, A Statistical Comparison between Photospheric Vector Magnetograms Obtained by SDO/HMI and Hinode/SP, *ApJ*, 851, 111, 1801.07374
- Sanchez Almeida, J., Lites, B. W., 1992, Observation and Interpretation of the Asymmetric Stokes Q, U, and V Line Profiles in Sunspots, *ApJ*, 398, 359
- Sarvaiya, J. N., Patnaik, S., Bombaywala, S., 2009, Image registration by template matching using normalized cross-correlation, in 2009 international conference on advances in computing, control, and telecommunication technologies, pp. 819–822, IEEE
- Schatten, K. H., Scherrer, P. H., Svalgaard, L., Wilcox, J. M., 1978, Using Dynamo Theory to predict the sunspot number during Solar Cycle 21, *Geophys. Res. Lett.*, 5, 411–414
- Scherrer, P. H., Schou, J., Bush, R. I., Kosovichev, A. G., Bogart, R. S., Hoeksema, J. T., Liu, Y., Duvall, T. L., Zhao, J., Title, A. M., Schrijver, C. J., Tarbell, T. D., Tomczyk, S., 2012, The Helioseismic and Magnetic Imager (HMI) Investigation for the Solar Dynamics Observatory (SDO), *Sol. Phys.*, 275, 207–227
- Schlichenmaier, R., Collados, M., 2002, Spectropolarimetry in a sunspot penumbra. Spatial dependence of Stokes asymmetries in Fe I 1564.8 nm, *A&A*, 381, 668–682
- Schlichenmaier, R., Pitters, D., Borrero, J. M., Schubert, M., 2023, Effects of solar evolution on finite acquisition time of fabry–perot interferometers in high resolution solar physics, *Astronomy & Astrophysics*, 669, A78
- Schou, J., Scherrer, P. H., Bush, R. I., Wachter, R., Couvidat, S., Rabello-Soares, M. C., Bogart, R. S., Hoeksema, J. T., Liu, Y., Duvall, T. L., Akin, D. J., Allard, B. A., Miles, J. W., Rairden, R., Shine, R. A., Tarbell, T. D., Title, A. M., Wolfson, C. J., Elmore, D. F., Norton, A. A., Tomczyk, S., 2012, Design and Ground Calibration of the Helioseismic and Magnetic Imager (HMI) Instrument on the Solar Dynamics Observatory (SDO), *Sol. Phys.*, 275, 229–259
- Schwabe, H., 1844, Sonnenbeobachtungen im jahre 1843. von herrn hofrath schwabe in dessau, *Astronomische Nachrichten*, volume 21, issue 15, p. 233, 21, 233
- Semel, M., 1967, Contribution à l'étude des champs magnétiques dans les régions actives solaires, *Annales d'Astrophysique*, 30, 513–513
- Sinjan, J., Calchetti, D., Hirzberger, J., Suárez, D. O., Albert, K., Jorge, N. A., Appourchaux, T., Alvarez-Herrero, A., Rodríguez, J. B., Gandorfer, A., et al., 2022, The on-ground data reduction and calibration pipeline for so/phi-hrt, in *Software and Cyberinfrastructure for Astronomy VII*, vol. 12189, pp. 612–628, SPIE
- Sinjan, J., Calchetti, D., Hirzberger, J., Kahil, F., Valori, G., Solanki, S. K., Albert, K., Albelo Jorge, N., Alvarez-Herrero, A., Appourchaux, T., Bellot Rubio, L. R., Blanco Rodríguez, J., Feller, A., Gandorfer, A., Germerott, D., Gizon, L., Gómez Cama,

- J. M., Guerrero, L., Gutierrez-Marques, P., Kolleck, M., Korpi-Lagg, A., Michalik, H., Moreno Vacas, A., Orozco Suárez, D., Pérez-Grande, I., Sanchis Kilders, E., Balaguer Jiménez, M., Schou, J., Schühle, U., Staub, J., Strecker, H., del Toro Iniesta, J. C., Volkmer, R., Woch, J., 2023, Magnetic fields inferred by Solar Orbiter: A comparison between SO/PHI-HRT and SDO/HMI, *A&A*, 673, A31, 2303. 16771
- Siu-Tapia, A., Lagg, A., van Noort, M., Rempel, M., Solanki, S. K., 2019, Superstrong photospheric magnetic fields in sunspot penumbrae, *A&A*, 631, A99, 1909. 13619
- Smith, E. J., Balogh, A., 1995, Ulysses observations of the radial magnetic field, *Geophys. Res. Lett.*, 22, 3317–3320
- Smitha, H. N., Holzreuter, R., van Noort, M., Solanki, S. K., 2020, The influence of NLTE effects in Fe I lines on an inverted atmosphere. I. 6301 Å and 6302 Å lines formed in 1D NLTE, *A&A*, 633, A157, 1912. 07007
- Smitha, H. N., van Noort, M., Solanki, S. K., Castellanos Durán, J. S., 2023, Non-LTE formation of the Fe I 6173 Å line in the solar atmosphere, *A&A*, 669, A144, 2211. 10236
- Solanki, S. K., 1986, Velocities in solar magnetic fluxtubes, *Astronomy and Astrophysics*, 168, 311–329
- Solanki, S. K., 1987, The photospheric layers of solar magnetic fluxtubes, Ph.D. thesis, Institute of Astronomy, ETH Zürich, Switzerland, No. 8309
- Solanki, S. K., 1993, Smallscale Solar Magnetic Fields - an Overview, *Space Sci. Rev.*, 63, 1–188
- Solanki, S. K., 2003, Sunspots: An overview, *A&A Rev.*, 11, 153–286
- Solanki, S. K., Stenflo, J. O., 1984, Properties of solar magnetic fluxtubes as revealed by Fe I lines, *A&A*, 140, 185–198
- Solanki, S. K., Steiner, O., Bunte, M., Murphy, G., Ploner, S. R. O., 1998, On the reliability of Stokes diagnostics of magnetic elements away from solar disc centre, *A&A*, 333, 721–731
- Solanki, S. K., Barthol, P., Danilovic, S., Feller, A., Gandorfer, A., Hirzberger, J., Riethmüller, T. L., Schüssler, M., Bonet, J. A., Martínez Pillet, V., del Toro Iniesta, J. C., Domingo, V., Palacios, J., Knölker, M., Bello González, N., Berkefeld, T., Franz, M., Schmidt, W., Title, A. M., 2010, SUNRISE: Instrument, Mission, Data, and First Results, *ApJ*, 723, L127–L133, 1008. 3460
- Solanki, S. K., del Toro Iniesta, J., Woch, J., Gandorfer, A., Hirzberger, J., Alvarez-Herrero, A., Appourchaux, T., Pillet, V. M., Pérez-Grande, I., Kilders, E. S., et al., 2020, The polarimetric and helioseismic imager on solar orbiter, *Astronomy & Astrophysics*, 642, A11

- Solanki, S. K., del Toro Iniesta, J. C., Woch, J., Gandorfer, A., Hirzberger, J., Alvarez-Herrero, A., Appourchaux, T., Martínez Pillet, V., Pérez-Grande, I., Sanchis Kilders, E., Schmidt, W., Gómez Cama, J. M., Michalik, H., Deutsch, W., Fernandez-Rico, G., Grauf, B., Gizon, L., Heerlein, K., Kolleck, M., Lagg, A., Meller, R., Müller, R., Schühle, U., Staub, J., Albert, K., Alvarez Copano, M., Beckmann, U., Bischoff, J., Busse, D., Enge, R., Frahm, S., Germerott, D., Guerrero, L., Löptien, B., Meierdierks, T., Oberdorfer, D., Papagiannaki, I., Ramanath, S., Schou, J., Werner, S., Yang, D., Zerr, A., Bergmann, M., Bochmann, J., Heinrichs, J., Meyer, S., Monecke, M., Müller, M. F., Sperling, M., Álvarez García, D., Aparicio, B., Balaguer Jiménez, M., Bellot Rubio, L. R., Cobos Carracosa, J. P., Girela, F., Hernández Expósito, D., Herranz, M., Labrousse, P., López Jiménez, A., Orozco Suárez, D., Ramos, J. L., Barandiarán, J., Bastide, L., Campuzano, C., Cebollero, M., Dávila, B., Fernández-Medina, A., García Parejo, P., Garranzo-García, D., Laguna, H., Martín, J. A., Navarro, R., Núñez Peral, A., Royo, M., Sánchez, A., Silva-López, M., Vera, I., Villanueva, J., Fourmond, J. J., de Galarreta, C. R., Bouzit, M., Hervier, V., Le Clec'h, J. C., Szwec, N., Chaigneau, M., Buttice, V., Dominguez-Tagle, C., Philippon, A., Boumier, P., Le Cocquen, R., Baranjuk, G., Bell, A., Berkefeld, T., Baumgartner, J., Heidecke, F., Maue, T., Nakai, E., Scheiffelen, T., Sigwarth, M., Soltau, D., Volkmer, R., Blanco Rodríguez, J., Domingo, V., Ferreres Sabater, A., Gasent Blesa, J. L., Rodríguez Martínez, P., Osorno Caudel, D., Bosch, J., Casas, A., Carmona, M., Herms, A., Roma, D., Alonso, G., Gómez-Sanjuan, A., Piqueras, J., Torralbo, I., Fiethe, B., Guan, Y., Lange, T., Michel, H., Bonet, J. A., Fahmy, S., Müller, D., Zouganelis, I., 2020, The Polarimetric and Helioseismic Imager on Solar Orbiter, *A&A*, 642, A11, 1903 . 11061
- Sporer, G., 1894, Number 32. Zehnten Bandes Erstes Stuck. Beobachtungen von Sonnenflecken in den Jahren 1885 bis 1893, Publikationen des Astrophysikalischen Observatoriums zu Potsdam, 10, 3–147
- Steiner, O., Vigeesh, G., Krieger, L., Wedemeyer-Böhm, S., Schaffenberger, W., Freytag, B., 2007, First local helioseismic experiments with CO<sup>5</sup>BOLD, *Astronomische Nachrichten*, 328, 323, [astro-ph/0701029](https://arxiv.org/abs/astro-ph/0701029)
- Stenflo, J., 1994, *Solar Magnetic Fields: Polarized Radiation Diagnostics*, vol. 189
- Stenflo, J. O., 1973, Magnetic-field structure of the photospheric network, *Solar Physics*, 32, 41–63
- Stenflo, J. O., 1985, Measurements of Magnetic Fields and the Analysis of Stokes Profiles, *Sol. Phys.*, 100, 189
- Stenflo, J. O., Solanki, S., Harvey, J. W., Brault, J. W., 1984, Diagnostics of solar magnetic fluxtubes using a Fourier transform spectrometer, *A&A*, 131, 333–346
- Stephenson, F. R., Willis, D. M., 1999, The earliest drawing of sunspots, *Astronomy and Geophysics*, 40, 21
- Stone, E. C., Frandsen, A. M., Mewaldt, R. A., Christian, E. R., Margolies, D., Ormes, J. F., Snow, F., 1998, The Advanced Composition Explorer, *Space Sci. Rev.*, 86, 1–22

- Temmer, M., 2021, Space weather: the solar perspective, *Living Reviews in Solar Physics*, 18, 4, 2104.04261
- Thompson, W. T., 2006, Coordinate systems for solar image data, *A&A*, 449, 791–803
- Trosseille, C., Appourchaux, T., Fourmond, J.-J., 2008, Design of a Fabry-Perot interferometer for the SO/PHI instrument on Solar Orbiter, in *Space Telescopes and Instrumentation 2008: Optical, Infrared, and Millimeter*, (Eds.) J. Oschmann, Jacobus M., M. W. M. de Graauw, H. A. MacEwen, vol. 7010 of *Society of Photo-Optical Instrumentation Engineers (SPIE) Conference Series*, p. 701017
- Tsuneta, S., Ichimoto, K., Katsukawa, Y., Lites, B. W., Matsuzaki, K., Nagata, S., Orozco Suárez, D., Shimizu, T., Shimojo, M., Shine, R. A., Suematsu, Y., Suzuki, T. K., Tarbell, T. D., Title, A. M., 2008a, The Magnetic Landscape of the Sun's Polar Region, *ApJ*, 688, 1374–1381, 0807.4631
- Tsuneta, S., Ichimoto, K., Katsukawa, Y., Nagata, S., Otsubo, M., Shimizu, T., Suematsu, Y., Nakagiri, M., Noguchi, M., Tarbell, T., Title, A., Shine, R., Rosenberg, W., Hoffmann, C., Jurcevich, B., Kushner, G., Levay, M., Lites, B., Elmore, D., Matsushita, T., Kawaguchi, N., Saito, H., Mikami, I., Hill, L. D., Owens, J. K., 2008b, The Solar Optical Telescope for the Hinode Mission: An Overview, *Sol. Phys.*, 249, 167–196, 0711.1715
- Uitenbroek, H., 2001, Multilevel Radiative Transfer with Partial Frequency Redistribution, *ApJ*, 557, 389–398
- Unno, W., 1956, Line Formation of a Normal Zeeman Triplet, *PASJ*, 8, 108
- Valori, G., Löschl, P., Stansby, D., Pariat, E., Hirzberger, J., Chen, F., 2022, Disambiguation of Vector Magnetograms by Stereoscopic Observations from the Solar Orbiter (SO)/Polarimetric and Helioseismic Imager (PHI) and the Solar Dynamic Observatory (SDO)/Helioseismic and Magnetic Imager (HMI), *Sol. Phys.*, 297, 12, 2112.10650
- Valori, G., Calchetti, D., Moreno Vacas, A., Pariat, É., Solanki, S. K., Löschl, P., Hirzberger, J., Parenti, S., Albert, K., Albelo Jorge, N., Álvarez-Herrero, A., Appourchaux, T., Bellot Rubio, L. R., Blanco Rodríguez, J., Campos-Jara, A., Feller, A., Gandorfer, A., García Parejo, P., Germerott, D., Gizon, L., Gómez Cama, J. M., Guerrero, L., Gutierrez-Marques, P., Kahil, F., Kolleck, M., Korpi-Lagg, A., Orozco Suárez, D., Pérez-Grande, I., Sanchis Kilders, E., Schou, J., Schühle, U., Sinjan, J., Staub, J., Strecker, H., del Toro Iniesta, J. C., Volkmer, R., Woch, J., 2023, Stereoscopic disambiguation of vector magnetograms: First applications to SO/PHI-HRT data, *A&A*, 677, A25, 2307.09907
- Vögler, A., 2003, Three-dimensional simulations of magneto-convection in the solar photosphere, Ph.D. thesis, Georg August University of Göttingen, Germany
- Vögler, A., Shelyag, S., Schüssler, M., Cattaneo, F., Emonet, T., Linde, T., 2005, Simulations of magneto-convection in the solar photosphere. Equations, methods, and results of the MURaM code, *A&A*, 429, 335–351

- Voigt, W., 1912, Über das gesetz der intensitätsverteilung innerhalb der linien eines gasspektrums, Königlich Bayerischen Akademie der Wissenschaften, Heft III, November- und Dezembersitzung, 603
- Volkmer, R., Bosch, J., Feger, B., Gomez, J. M., Heidecke, F., Schmidt, W., Scheiffelen, T., Sigwarth, M., Soltau, D., 2012, Image stabilisation system of the photospheric and helioseismic imager, in Space Telescopes and Instrumentation 2012: Optical, Infrared, and Millimeter Wave, (Eds.) M. C. Clampin, G. G. Fazio, H. A. MacEwen, J. Oschmann, Jacobus M., vol. 8442 of Society of Photo-Optical Instrumentation Engineers (SPIE) Conference Series, p. 84424P
- Wallace, S., Arge, C. N., Pattichis, M., Hock-Mysliwiec, R. A., Henney, C. J., 2019, Estimating total open heliospheric magnetic flux, *Solar Physics*, 294, 1–20
- Wang, Y. M., Sheeley, N. R., 2009, Understanding the Geomagnetic Precursor of the Solar Cycle, *ApJ*, 694, L11–L15
- Wang, Y.-M., Sheeley Jr., N. R., 1995, Solar Implications of ULYSSES Interplanetary Field Measurements, *ApJ*, 447, L143
- Wiegelmann, T., Solanki, S. K., 2004, Similarities and Differences between Coronal Holes and the Quiet Sun: Are Loop Statistics the Key?, *Sol. Phys.*, 225, 227–247, 0802.0120
- Wiegelmann, T., Petrie, G. J. D., Riley, P., 2017, Coronal Magnetic Field Models, *Space Sci. Rev.*, 210, 249–274
- Wiehr, E., 1985, Spatial and temporal variation of circular Zeeman profiles in isolated solar Ca(+) K structures, *A&A*, 149, 217–220
- Wolf, R., 1861, Abstract of his latest Results, *MNRAS*, 21, 77
- Xiahong Li, 2024, private communication
- Yadav, R., Díaz Baso, C. J., de la Cruz Rodríguez, J., Calvo, F., Morosin, R., 2021, Stratification of physical parameters in a C-class solar flare using multiline observations, *A&A*, 649, A106, 2011.02953
- Yeo, K. L., 2014, Analysis and modeling of solar irradiance variations, Ph.D. thesis, Technischen Universität Carolo-Wilhelmina zu Braunschweig
- Zeeman, P., 1897a, Vii. doublets and triplets in the spectrum produced by external magnetic forces, *The London, Edinburgh, and Dublin Philosophical Magazine and Journal of Science*, 44, 55–60
- Zeeman, P., 1897b, Xxxii. on the influence of magnetism on the nature of the light emitted by a substance, *The London, Edinburgh, and Dublin Philosophical Magazine and Journal of Science*, 43, 226–239

- Zeeman, P., 1897c, Xxxiii. doublets and triplets in the spectrum produced by external magnetic forces.—(ii.), *The London, Edinburgh, and Dublin Philosophical Magazine and Journal of Science*, 44, 255–259
- Zirker, J. B., 1993, Coronal heating: Invited review paper, *Solar physics*, 148, 43–60
- Zouganelis, I., De Groof, A., Walsh, A. P., Williams, D. R., Müller, D., St Cyr, O. C., Auchère, F., Berghmans, D., Fludra, A., Horbury, T. S., Howard, R. A., Krucker, S., Maksimovic, M., Owen, C. J., Rodríguez-Pacheco, J., Romoli, M., Solanki, S. K., Watson, C., Sanchez, L., Lefort, J., Osuna, P., Gilbert, H. R., Nieves-Chinchilla, T., Abbo, L., Alexandrova, O., Anastasiadis, A., Andretta, V., Antonucci, E., Appourchaux, T., Aran, A., Arge, C. N., Aulanier, G., Baker, D., Bale, S. D., Battaglia, M., Bellot Rubio, L., Bemporad, A., Berthomier, M., Bocchialini, K., Bonnin, X., Brun, A. S., Bruno, R., Buchlin, E., Büchner, J., Bucik, R., Carcaboso, F., Carr, R., Carrasco-Blázquez, I., Cecconi, B., Cernuda Cangas, I., Chen, C. H. K., Chitta, L. P., Chust, T., Dalmasse, K., D’Amicis, R., Da Deppo, V., De Marco, R., Dolei, S., Dolla, L., Dudok de Wit, T., van Driel-Gesztelyi, L., Eastwood, J. P., Espinosa Lara, F., Etesi, L., Fedorov, A., Félix-Redondo, F., Fineschi, S., Fleck, B., Fontaine, D., Fox, N. J., Gandorfer, A., Génot, V., Georgoulis, M. K., Gissot, S., Giunta, A., Gizon, L., Gómez-Herrero, R., Gontikakis, C., Graham, G., Green, L., Grundy, T., Haberreiter, M., Harra, L. K., Hassler, D. M., Hirzberger, J., Ho, G. C., Hurford, G., Innes, D., Issautier, K., James, A. W., Janitzek, N., Janvier, M., Jeffrey, N., Jenkins, J., Khotyaintsev, Y., Klein, K. L., Kontar, E. P., Kontogiannis, I., Krafft, C., Krasnoselskikh, V., Kretzschmar, M., Labrosse, N., Lagg, A., Landini, F., Lavraud, B., Leon, I., Lepri, S. T., Lewis, G. R., Liewer, P., Linker, J., Livi, S., Long, D. M., Louarn, P., Malandraki, O., Maloney, S., Martinez-Pillet, V., Martinovic, M., Masson, A., Matthews, S., Matteini, L., Meyer-Vernet, N., Moraitis, K., Morton, R. J., Musset, S., Nicolaou, G., Nindos, A., O’Brien, H., Orozco Suarez, D., Owens, M., Pancrazzi, M., Papaioannou, A., Parenti, S., Pariat, E., Patsourakos, S., Perrone, D., Peter, H., Pinto, R. F., Plainaki, C., Plettemeier, D., Plunkett, S. P., Raines, J. M., Raouafi, N., Reid, H., Retino, A., Rezeau, L., Rochus, P., Rodriguez, L., Rodriguez-Garcia, L., Roth, M., Rouillard, A. P., Sahraoui, F., Sasso, C., Schou, J., Schühle, U., Sorriso-Valvo, L., Soucek, J., Spadaro, D., Stangalini, M., Stansby, D., Steller, M., Strugarek, A., Štverák, Š., Susino, R., Telloni, D., Terasa, C., Teriaca, L., Toledo-Redondo, S., del Toro Iniesta, J. C., Tsiropoula, G., Tsounis, A., Tziotziou, K., Valentini, F., Vaivads, A., Vecchio, A., Velli, M., Verbeek, C., Verdini, A., Verscharen, D., Vilmer, N., Vourlidis, A., Wicks, R., Wimmer-Schweingruber, R. F., Wiegmann, T., Young, P. R., Zhukov, A. N., 2020, The Solar Orbiter Science Activity Plan. Translating solar and heliospheric physics questions into action, *A&A*, 642, A3, 2009.10772

# A Appendix to Chapter 5

## A.1 Validation of $B_{LOS}$ retrieval methods for a 1D atmosphere for all $\mu$

The SPINOR synthesis and  $B_{LOS}$  retrieval methods were validated by first generating Stokes profiles for a 1D plane parallel atmosphere (PPA), where  $B_X, B_Y = 0$  and  $B_Z = 200$  G everywhere. The atmosphere was calculated by averaging a snapshot of the  $B_Z = 200$  G MURaM simulation (Riethmüller et al. 2014a), over the horizontal  $(x, y)$  dimensions, and setting  $v_x, v_y = 0$  km/s. Under these conditions one expects to retrieve exactly  $B_{LOS}(\mu) = 200 \times \mu$ . As shown in Fig. A.1 all tested methods retrieve the input field well, with MILOS doing somewhat better than the other techniques. The average (vertical) separation of the retrieved CLV from the expected  $200 \times \mu$  for the 4 methods are as follows: MILOS  $1.0 \pm 0.3$  G, MDI-like algorithm  $5 \pm 2$  G, WFA  $4 \pm 1$  G and COG  $6 \pm 2$  G. All panels demonstrate that the SPINOR synthesis code generated the negative angles correctly as they lie on top of the positive viewing angle curves. This proves that any difference between negative and positive viewing direction presented in this study are purely the result of the anisotropic nature of the features in the generated photospheres. This figure also validates the correct implementation of methods and also demonstrates that any deviation from the dashed line arises from radiative transfer effects.

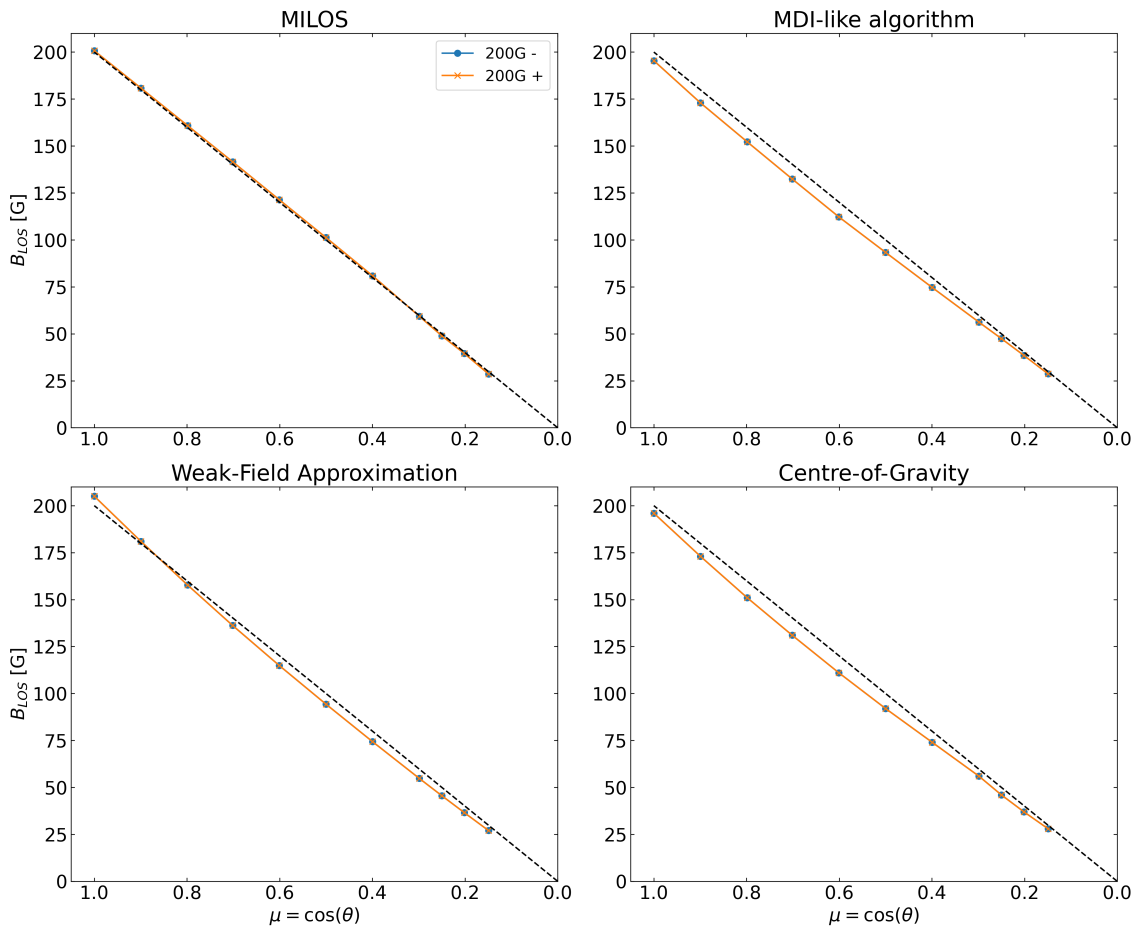


Figure A.1:  $B_{LOS}$  CLV retrieved through 4 different methods when applied to a 1D plane parallel atmosphere, where  $B_Z = 200$  G everywhere, for both positive and negative viewing directions. Clockwise from top left: MILOS, MDI-like algorithm, linear least squares weak-field approximation and the centre-of-gravity method.

## A.2 Stokes Profiles at $\mu = 0.5$

At  $\mu = 0.5$ , this region (the SO/PHI-FDT pixel at the origin) is no longer the same physical area as that considered in Fig. 5.7. This is due to the foreshortening, which means that at  $\mu = 0.5$ , a larger physical region is sampled. At this  $\mu$  value, the region is twice as large in the  $y$  dimension, equal to two SO/PHI-FDT pixels at disc centre. The spatially averaged magnetic field along the line of sight in the MURaM simulation from this larger area, between  $\log(\tau) = -2$  and 0, is 54 G.

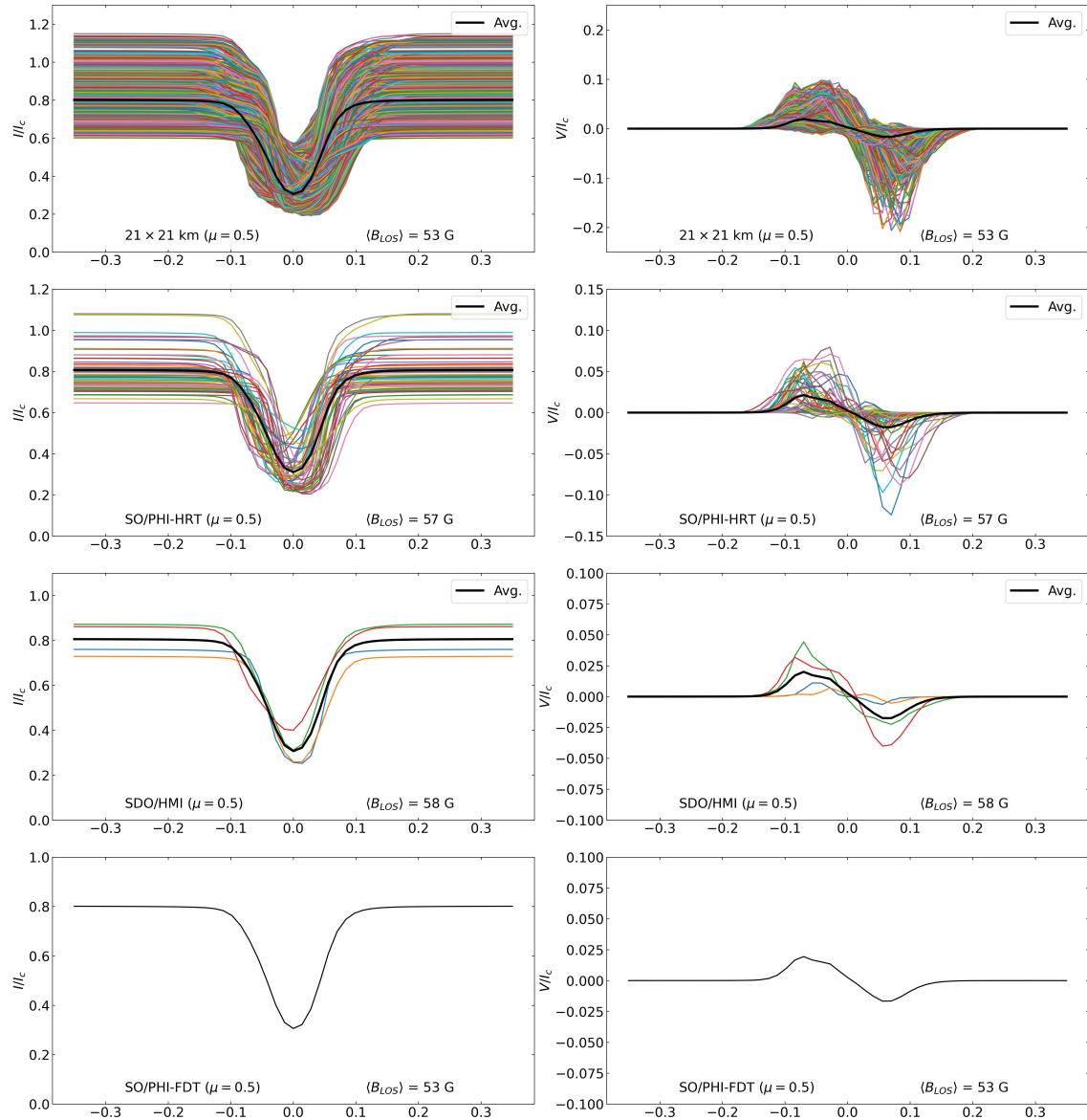


Figure A.2: Same as Fig. 5.7 but for  $\mu = 0.5$ . The physical region encompassed by this region, due to the foreshortening, however is not the same. See text for details.

### A.3 $\langle B_{LOS} \rangle$ centre-to-limb variation for Fe I 6173.3 Å derived by the weak-field approximation and centre-of-gravity technique.

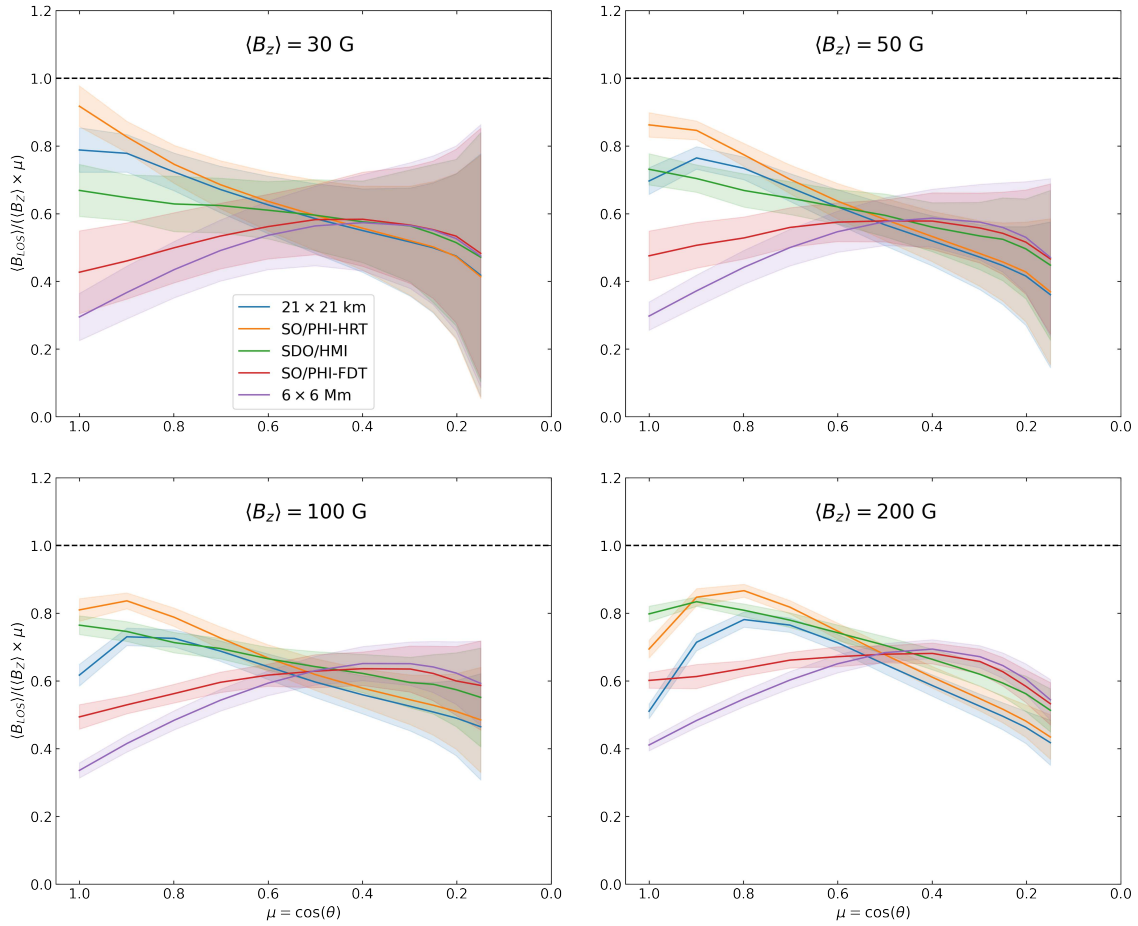


Figure A.3: Same as Fig. 5.5 but  $B_{LOS}$  is inferred by the weak-field approximation.

A.3  $\langle B_{LOS} \rangle$  centre-to-limb variation for Fe I 6173.3 Å derived by the weak-field approximation and centre-of-gravity technique.

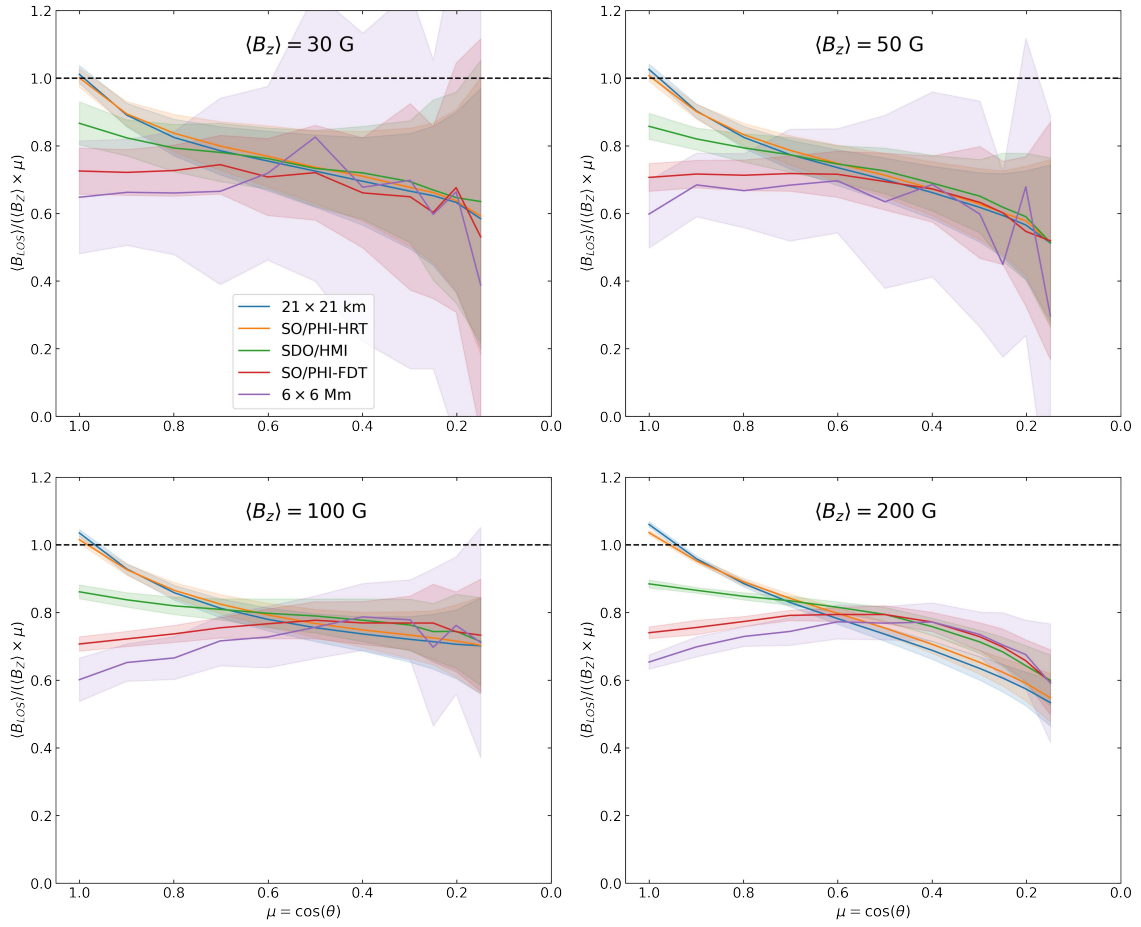


Figure A.4: Same as Fig. 5.5 but  $B_{LOS}$  is inferred by the centre-of-gravity technique.

### A.4 $\langle B_{LOS} \rangle$ centre-to-limb variation for Fe I 5250.2 Å derived by the MDI-like algorithm, weak-field approximation and centre-of-gravity technique.

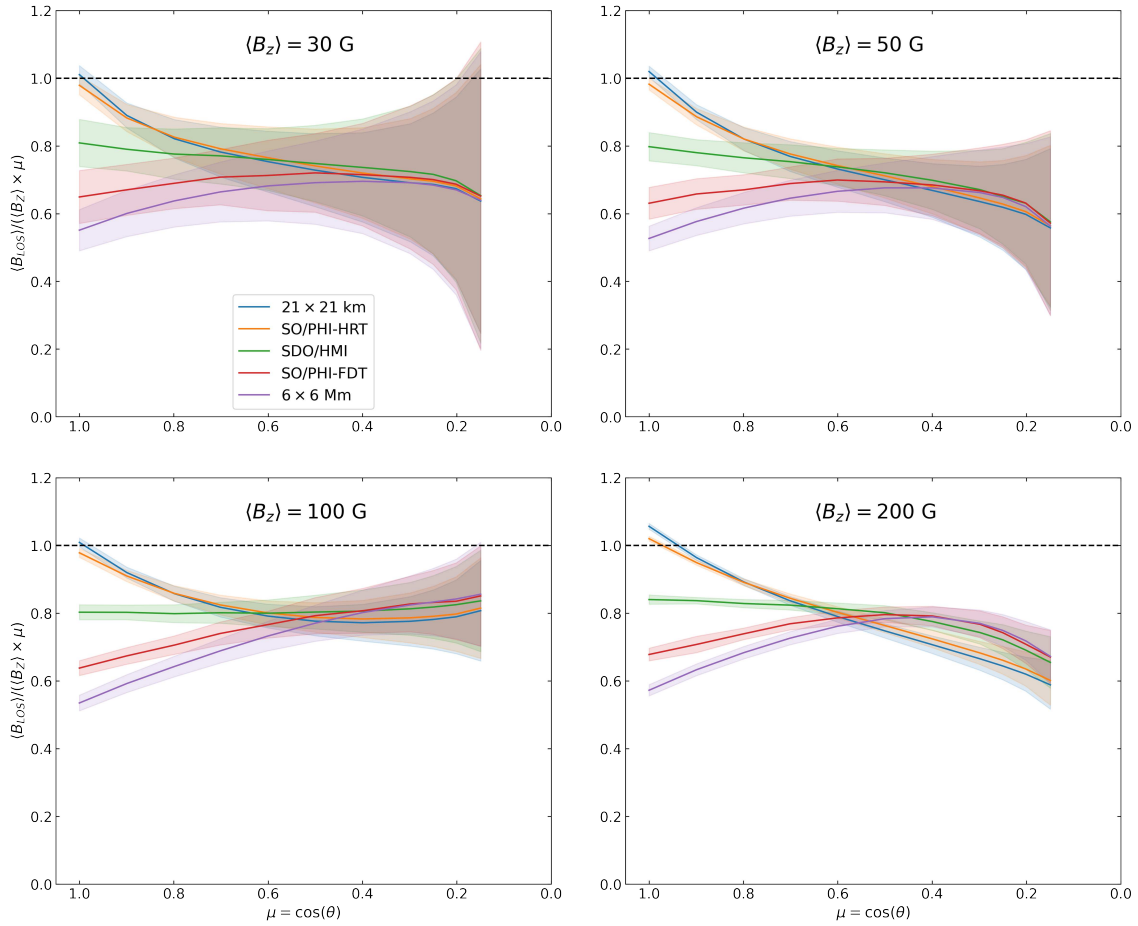


Figure A.5: Same as Fig. 5.9 but Fe I 5250.2 Å and  $B_{LOS}$  is inferred by the MDI-like algorithm.

A.4  $\langle B_{LOS} \rangle$  centre-to-limb variation for Fe I 5250.2 Å derived by the MDI-like algorithm, weak-field approximation and centre-of-gravity technique.

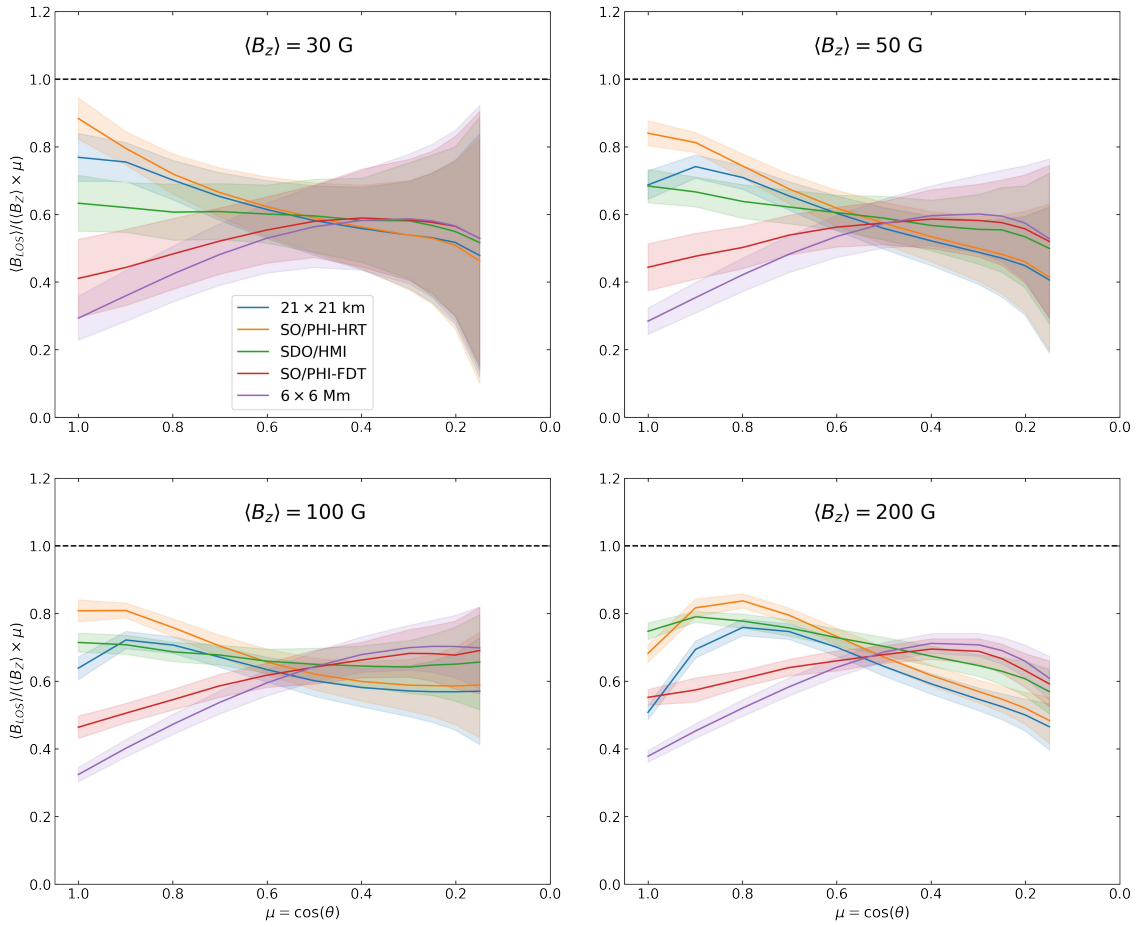


Figure A.6: Same as Fig. 5.5 but Fe I 5250.2 Å and  $B_{LOS}$  is inferred by the weak-field approximation.

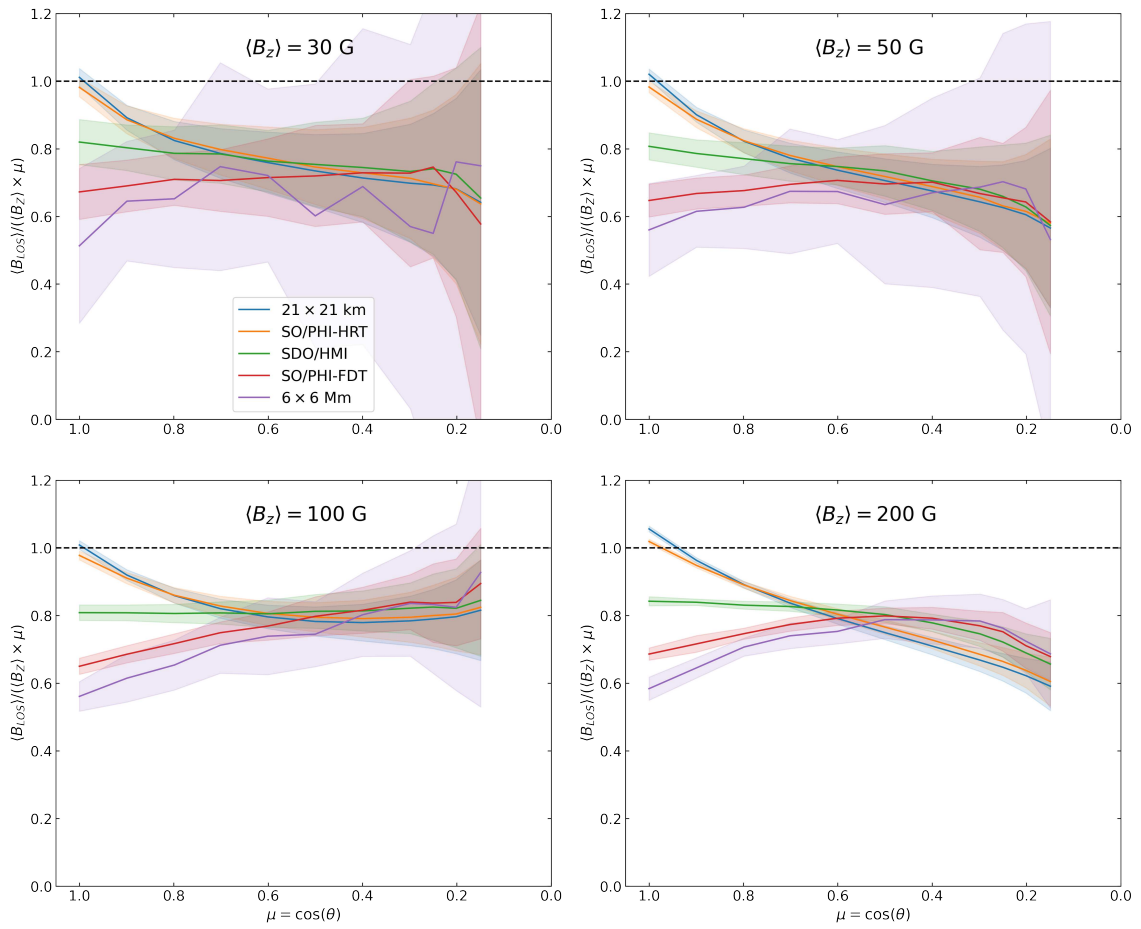


Figure A.7: Same as Fig. 5.5 but Fe I 5250.2 Å and  $B_{LOS}$  is inferred by the centre-of-gravity technique.

# Publications

## First Author Refereed publications

**J. Sinjan**, D. Calchetti, J. Hirzberger, F. Kahil, G. Valori, S. K. Solanki, K. Albert et al.  
Magnetic fields inferred by Solar Orbiter: A comparison between SO/PHI-HRT and SDO/HMI  
A&A 673, A31 (2023) <https://doi.org/10.1051/0004-6361/202245830>

**J. Sinjan**, S. K. Solanki, J. Hirzberger, T. L. Riethmüller and D. Przybylski  
Magnetograms underestimate even unipolar magnetic flux nearly everywhere on the solar disk  
A&A, in press (2024) <https://doi.org/10.1051/0004-6361/202450267>

For a complete list of co-authored refereed publications see:  
<https://orcid.org/0000-0002-5387-636X>

## Conference proceedings

**J. Sinjan**, D. Calchetti, J. Hirzberger, D. Orozco Suárez, K. Albert et al.  
The on-ground data reduction and calibration pipeline for SO/PHI-HRT  
SPIE, Proceedings Volume 12189, Software and Cyberinfrastructure for Astronomy VII;  
121891J (2022) <https://doi.org/10.1117/12.2629323>

F Kahil, A Gandorfer, J Hirzberger, D. Orozco Suárez, K. Albert, ..., **J. Sinjan** et. al.  
Image quality of data products of the high resolution telescope of the polarimetric and helioseismic imager  
SPIE, Proceedings Volume 12180, Software and Cyberinfrastructure for Astronomy VII;  
121803F (2022) <https://doi.org/10.1117/12.2628942>



# Acknowledgements

I want to thank my supervisors, Johann Hirzberger, Sami K. Solanki and Ansgar Reiners for their support as they guided me through this journey. I thank them for providing the opportunities to contribute to this scientific space mission. Highlights include the many PHI team meetings, especially those in Granada, where I felt very welcome. A huge bucket of thanks goes to all members of the PHI team spread across Europe, the engineers, the secretaries, the scientists...it goes on. Particular thanks go to Daniele Calchetti and Gherardo Valori, on the close collaboration on the pipeline development, and of course the evenings enjoying what Granada and Madrid have to offer.

Thank you to the other PhDs (or Doctoral Researchers as we should properly call ourselves) for their support and laughs as we experience this sometimes turbulent journey together. Particular shout outs go to Paula (my student rep in crime), Dušan, Tanayveer, Neelanchal and Ilse for the many bike rides and hikes together. Thank you for the times spent in Gartenlaube, which I think we can now christen as the MPS bar of choice. Thank you to my office mates, Nikolina and Patrick, for putting up with me hitting your feet under the desk, smelly banana peels and sneezing. I hope my music was never too loud...

Of course the biggest thanks goes to those closest in my life. To Rabea, for your constant love and support, your unwavering attempts to bring out the positives and things I do well as I battle myself as my own worst critic, I say the greatest thanks. For the walks, gym sessions, and countless bike rides together, sometimes even in the snow with our fingers and toes flirting with frostbite. For travelling back and forth and for helping me get my confidence back. I love you.

Next, to my parents for supporting me every step of the way, providing a wonderful education and most importantly creating an atmosphere of care and love, especially when the hardest cards were dealt. To my sister Helena, for the witty comments and general good vibes whenever we are all able to be together. To my grandparents for showing how proud they are for all the things Helena and I do. In particular I say thank you to Jef, for showing such an interest in the research I do, reading my master's thesis and first publications. It is a shame that I could not share this thesis with you, as you have started your next journey beyond this life.

Finally, I dedicate this thesis to Simon, my brother who passed away the year before I started this PhD. His never ending happiness and ability to see the funny side of things is something I miss dearly everyday. His smile and twinkle in his eyes truly shone like a star. I personally like to think that he directly contributes to some of the photons that PHI records as we observe the star that provides the energy for all life as we know it.